

NASA Contractor Report 4709

# Computational Analysis of Semi-Span Model Test Techniques

---

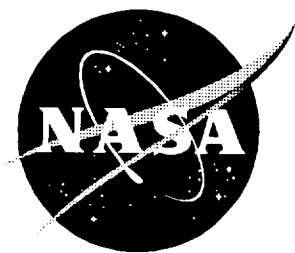
*William E. Milholen II and Ndaona Chokani*

Cooperative Agreement NCC1-169  
Prepared for Langley Research Center

---

March 1996





NASA Contractor Report 4709

# Computational Analysis of Semi-Span Model Test Techniques

---

*William E. Milholen II and Ndaona Chokani  
North Carolina State University • Raleigh, North Carolina*

National Aeronautics and Space Administration  
Langley Research Center • Hampton, Virginia 23681-0001

Prepared for Langley Research Center  
under Cooperative Agreement NCC1-169

March 1996

**Printed copies available from the following:**

**NASA Center for AeroSpace Information**  
800 Elkridge Landing Road  
Linthicum Heights, MD 21090-2934  
(301) 621-0390

**National Technical Information Service (NTIS)**  
5285 Port Royal Road  
Springfield, VA 22161-2171  
(703) 487-4650

## Abstract

A computational investigation was conducted to support the development of a semi-span model test capability in the NASA Langley Research Center's National Transonic Facility. This capability is required for the testing of high-lift systems at flight Reynolds numbers. A three-dimensional Navier-Stokes solver was used to compute the low-speed flow over both a full-span configuration, and a semi-span configuration mounted on the wind tunnel sidewall. The computational results were found to be in good agreement with the experimental data, and demonstrate that the Navier-Stokes solver is a practical tool to aid in the development of semi-span model test techniques.

The computational results indicate that the stand-off height has a strong influence on the flow over a semi-span model. The semi-span model adequately replicates the aerodynamic characteristics of the full-span configuration when a small stand-off height, approximately twice the tunnel empty sidewall boundary layer displacement thickness, is used. Several active sidewall boundary layer control techniques were examined including: upstream blowing, local jet blowing, and sidewall suction. Both upstream tangential blowing, and sidewall suction were found to minimize the separation of the sidewall boundary layer ahead of the semi-span model. The required mass flow rates are found to be practicable for testing in the National Transonic Facility. For the configuration examined, the active sidewall boundary layer control techniques were found to be necessary only near the maximum lift conditions.

## Acknowledgements

The work presented here was the basis of the first authors Ph.D. dissertation. This research was supported by Cooperative Agreement NCC1-169 between North Carolina State University and the Research Facilities Branch at NASA Langley Research Center. L. Elwood Putnam and Jassim A. Al-Saadi of NASA Langley Research Center served as technical monitors, and the authors are grateful for their support and technical advice.

The authors are also grateful to several colleagues and groups at the NASA Langley Research Center for their contributions in this work: Jerry C. South; Zachary T. Applin; Greg M. Gatlin; William G. Johnson; Robert J. McGhee; Lee Pollard; Christopher L. Rumsey; and Veer N. Vatsa. The support of Stuart E. Rogers of the NASA Ames Research Center and William K. Londenbergh of ViGYAN Inc. was greatly appreciated.

The computations were performed on the North Carolina Supercomputing Center's Cray Y-MP, and the Numerical Aerodynamic Simulation Facility's Cray C-90.

# Table of Contents

<b>List of Symbols</b>	<b>vii</b>
<b>1 Introduction</b>	<b>1</b>
<b>2 Numerical Procedure</b>	<b>8</b>
2.1 Experimental Database . . . . .	8
2.2 Geometry Definition . . . . .	9
2.3 Grid Generation . . . . .	11
2.4 Governing Equations . . . . .	13
2.5 Computational Code Evaluation . . . . .	13
2.5.1 Computational codes . . . . .	15
2.5.2 Rectangular wing computations . . . . .	17
2.5.3 Transport wing-body computations . . . . .	20
2.6 Computational Code Selection . . . . .	22
<b>3 Analysis of Baseline Configurations</b>	<b>24</b>
3.1 Full-span computations . . . . .	24
3.1.1 Boundary conditions . . . . .	24
3.1.2 Grid refinement study . . . . .	24
3.1.3 Influence of turbulence model . . . . .	25
3.1.4 Influence of angle-of-attack . . . . .	27
3.2 Semi-span computations . . . . .	28
3.2.1 Boundary conditions . . . . .	28
3.2.2 Influence of angle-of-attack . . . . .	28
<b>4 Comparison of Full-span and Semi-span Configuration Flow Fields</b>	<b>31</b>
4.1 Comparison of aerodynamic loadings . . . . .	31
4.2 Comparison of near surface streamline patterns . . . . .	33
4.3 Comparison of wing boundary layer characteristics . . . . .	36
4.4 High angle-of-attack aerodynamic characteristics . . . . .	37
<b>5 Development of Semi-span Test Techniques</b>	<b>40</b>
5.1 Influence of stand-off geometry . . . . .	40
5.1.1 Influence of stand-off height . . . . .	40
5.1.2 Influence of stand-off shaping . . . . .	46
5.1.3 Influence of stand-off boundary layer fence . . . . .	47
5.2 Influence of boundary layer control techniques . . . . .	48
5.2.1 Influence of juncture region blowing jets . . . . .	49

5.2.2	Influence of upstream tangential blowing . . . . .	52
5.2.3	Influence of active sidewall suction . . . . .	57
<b>6</b>	<b>Conclusions</b>	<b>61</b>
<b>7</b>	<b>Recommendations for future work</b>	<b>64</b>
	<b>References</b>	<b>65</b>
	<b>Appendices</b>	<b>69</b>
<b>A</b>	<b>Metric stand-off Mounting Technique</b>	<b>70</b>
<b>B</b>	<b>Tangential Blowing Simulation</b>	<b>74</b>
<b>C</b>	<b>Active Suction Simulation</b>	<b>76</b>
	<b>Tables</b>	<b>79</b>
	<b>Figures</b>	<b>81</b>



# List of Symbols

$A_j$	cross sectional area of blowing jet
$A_s$	cross sectional area of blowing slot
B-L	Baldwin-Lomax turbulence model
$b$	wingspan, $b = 79.50$ inches
$C_D$	drag coefficient
$C_L$	lift coefficient
$C_M$	pitching moment coefficient
$C_p$	surface static pressure coefficient
$C_q$	surface transpiration coefficient, $\frac{(\rho U)_w}{(\rho U)_\infty}$
$C_\mu$	blowing coefficient, $\frac{(\dot{m}U)_j + (P_j - P_1)A_j}{q_\infty S}$
$\Delta C_p$	$(C_p)_{ss} - (C_p)_{fs}$
$c$	local chord length
$\bar{c}$	mean geometric chord, 8.40 inches
$c_n$	sectional normal force coefficient
$h$	stand-off height
$h_f$	boundary layer fence height
$L$	fuselage length, 75.0 inches
$M$	Mach number
$\dot{m}$	mass flow rate
$n$	surface unit normal vector
$P$	static pressure
$q$	dynamic pressure
$Re$	Reynolds number based on mean geometric chord
$S$	full-span wing reference area
S-A	Spalart-Allmaras turbulence model
$U$	total velocity
$u, v, w$	velocity components in the x,y,z directions
$x, y, z$	Cartesian coordinate system
$y^+$	law of the wall coordinate, $u_\tau y / \nu$
$\alpha$	angle-of-attack, degrees
$\gamma$	ratio of specific heats
$\delta^*$	boundary layer displacement thickness
$\zeta$	normal coordinate to wing surface
$\eta$	non dimensional semi-span fraction
$\nu$	kinematic viscosity
$\rho$	density
$\tau$	local shear stress

**Subscripts:**

<b>f</b>	final value
<b>fs</b>	full-span
<b>j</b>	jet value
<b>l</b>	local value
<b>ss</b>	semi-span
<b>w</b>	wall value
<b><math>\infty</math></b>	free stream value

# 1 Introduction

The objective of wind tunnel testing is to simulate the flight conditions experienced by a full-scale configuration in a ground based test facility using a scale model. For commercial transport aircraft, it is necessary to duplicate both the flight Mach number and Reynolds number. The operating envelopes of several transonic wind tunnels are shown in Figure 1. For comparison, the cruise conditions of several commercial transport aircraft [1] are also shown. The commercially available wind tunnels, represented by the four lower curves, duplicate the flight Mach number at a significantly reduced Reynolds number. As a result, transport designers face a dilemma of extrapolating low Reynolds number test data to flight conditions. The extrapolation of low Reynolds number wind tunnel data to flight conditions can be problematic [2]. Figure 2 compares an upper wing surface pressure distribution obtained in a wind tunnel at low Reynolds number to full-scale flight data. The full-scale configuration experienced significantly higher wing loading than expected. As a consequence, the full-scale configuration required an expensive and extensive redesign of the wing structure, and retrofit to existing aircraft. The problems of extrapolation of low Reynolds number wind tunnel data are not limited to cruise conditions, but can also occur on high-lift configurations.

A two-dimensional comparison of a cruise configuration and a high-lift configuration is presented in Figure 3. The high-lift configuration is comprised of three

elements: the slat; the main element; and the flap. The high-lift devices are deployed to improve the low-speed performance of a configuration, which is important during take-off and landing. The Reynolds number effects for a high-lift system can be significant. A schematic diagram of the flow over a similar configuration is shown in Figure 4. The flow over a high-lift system is dominated by viscous effects, such as the development of confluent boundary layers, separation, and reattachment [3]. A confluent boundary layer develops when the wake shed from an upstream element merges with a boundary layer on a downstream element. Flow separation can occur in such regions as the cove on the slat and main element. All three phenomena are influenced by the Reynolds number of the flow. As a result, the variation of maximum lift coefficient with Reynolds number has been seen to be highly non-linear [1, 4]. For this reason, it is necessary to design and test high-lift systems at flight Reynolds numbers.

As shown in Figure 1, only the NASA Langley Research Center's National Transonic Facility (NTF) has the potential to provide the capability of testing high-lift systems at full-scale Reynolds numbers. However, a conventional full-span model is not well suited for high-lift testing due to the relatively small size of the leading and trailing edge devices. Inaccurate positioning of these components can result in poor repeatability of the test data. In addition, aeroelastic deformations may introduce significant errors into the test data. Thus, a semi-span model test technique has been proposed for the NTF. Figure 5 shows a comparison between a conventional full-span

model, mounted in the center of the test section, and a semi-span model mounted on the test-section sidewall. The primary advantage of semi-span model testing is the increased Reynolds number capability due to the larger model size. The increased model size also allows for more accurate positioning of the model components, improved model fidelity, and increased model stiffness; all these features improve the data quality [2, 5]. In spite of these advantages, the use of a semi-span model introduces additional difficulties which must be addressed in the semi-span test procedure. These difficulties include the effects of increased wind-tunnel wall interference due to the increased model size [5, 6], and the effects of the semi-span model mounting. The latter is the focus of the present research. The presence of the boundary layer on the wind-tunnel sidewall results in the loss of symmetry about the model centerplane. Previous research [7] has shown that even when the sidewall boundary layer remains attached, it may strongly influence the flow over the semi-span model. An improved understanding of the interactions between the sidewall boundary layer and the flow over the semi-span model is a key to the successful implementation of the semi-span model test technique in the NTF. However, an examination of the few available references reveals that the influence that a sidewall boundary layer has on the flow over a semi-span model is largely unknown.

*Franz* [8] examined various semi-span mounting techniques to remove the semi-span model from the influence of the sidewall boundary layer. The first approach taken was to mount the semi-span model on a splitter plate as shown in Figure 6a. The

splitter plate was offset from the sidewall, and spanned the entire tunnel height. This approach was abandoned early, due largely to the difficulty in maintaining uniform flow over the model. In addition, the boundary layer growth rate on the splitter plate was found to be excessive, due to the adverse pressure gradients imposed by the semi-span model. A second method examined involved mounting the semi-span model directly on the sidewall as shown in Figure 6b. The model was offset from the sidewall by the use of a non-metric stand-off geometry. The stand-off geometry had a constant profile shape, which was identical to that of the fuselage centerline. The height of the stand-off geometry was equal to the tunnel empty sidewall boundary layer thickness. Unfortunately, few details were provided regarding the success of this mounting strategy. Furthermore, the understanding of the sidewall boundary layer influence is incomplete. *Franz* proposed that the sidewall boundary layer only influences the flow over the fuselage, and does not influence the flow over the wing. Conversely, it is proposed that the flow over the wing does not influence the sidewall boundary layer.

The research of *Boersen* [5] is significant in two respects. First, comparisons of full-span and semi-span data were presented for several different configurations. Over a wide range of conditions, the aerodynamic characteristics of the semi-span model were found to be quite different from those of the corresponding full-span model. This was particularly true at high angles-of-attack. The semi-span models tended to stall at lower angles-of-attack, and the stall patterns were often quite different. The

semi-span models typically experienced inboard stalls, whereas the full-span models typically stalled outboard. The second significant contribution is the realization that model blockage effects for a semi-span model can be significant, and need to be properly addressed. The understanding of the sidewall boundary layer influence is again however incomplete. It was proposed that the sidewall boundary layer only influences the flow over the fuselage, and that the flow over the wing does not influence the sidewall boundary layer.

The recent research by *Earnshaw et. al.* [9] demonstrates an improved understanding of the influence of the sidewall boundary layer. They recognized that the interactions between the sidewall boundary layer and the flow over the semi-span model are closely coupled. The stand-off height was shown to have a significant effect on the semi-span data. However, few details were presented, and the influence of the stand-off height on the flow field is still largely unknown. A sidewall boundary layer control technique was also employed in an attempt to minimize the influence of the sidewall boundary layer. An upstream tangential blowing nozzle was used to reenergize the sidewall boundary layer. The semi-span results were found to be in much better agreement with the full-span results. Again, few details were provided, and the effect of the upstream blowing on the flow over the semi-span model is largely unknown.

The studies discussed above were experimental in nature. One limitation of an experimental approach is the difficulty in obtaining detailed flow field measurements.

On the other hand, previous research conducted by the author [7] has demonstrated the capability of Computational Fluid Dynamics (CFD) methods to provide such data. The transonic flow over a semi-span wing mounted on a wind-tunnel sidewall was simulated. The validated computational results were interrogated to document the complex flow physics thus providing information unobtainable in the wind tunnel. The computational method was also used to efficiently perform a number of parametric studies. Although the geometry was simple and the flow transonic, the strategy can be used to examine more complex configurations, and lower speed flows.

Thus, the objectives of the present research are: (a) to develop a computational approach to support semi-span model test techniques in the NTF; and (b) to integrate this approach with the conduct of an experimental test program. To meet these objectives, the following approach is taken. A state-of-the-art three-dimensional Navier-Stokes solver is employed to compute the flow over both a full-span configuration and a semi-span configuration mounted on the sidewall of the tunnel. The computations are validated by making direct comparisons to experimental data. The semi-span computational results are then compared to the full-span results, to document how the flow over the semi-span configuration differs from that over the full-span configuration. Next, a parametric study is conducted to systematically examine the influence of stand-off geometry on the flow over the semi-span model. Finally two sidewall boundary layer control techniques, tangential blowing and suction, are examined. The results of this research will be used to provide a conceptual framework



within which a semi-span model test technique may be implemented in the NTF.

## 2 Numerical Procedure

### 2.1 Experimental Database

The 3.6% full-span EET model was tested extensively in the NASA Ames Research Center's 12-Foot Pressure Tunnel [10]. The aspect ratio of the wing was 10.0, with a quarter-chord sweep angle of  $27.0^\circ$ , and a dihedral angle of  $5.0^\circ$ . The wing was constructed of supercritical airfoil sections, with a nonlinear twist distribution. The model was tested through a Reynolds number range of  $0.91 \times 10^6$  to  $4.2 \times 10^6$  at a freestream Mach number of 0.20. Force and moment data were acquired along with wing pressure data at three spanwise stations.

After the full-span configuration testing, the full-span model was modified to become the NTF semi-span [11] model. The flow conditions examined were identical to those of the previous full-span testing. Figure 7 shows a schematic diagram of the semi-span cruise configuration which was examined in the NTF. A non-metric stand-off geometry was used to support the model away from the wind-tunnel sidewall. The profile shape of the stand-off was identical to that of the full-span fuselage symmetry plane. The height of the stand-off geometry was approximately four inches, which corresponds to the maximum tunnel empty sidewall boundary layer thickness [12]. Surface pressure data on the stand-off and fuselage were obtained in the experiment to document the flow in the near-wall region. In addition, surface pressure data at two spanwise locations on the wing, and force and moment data were also obtained.

## 2.2 Geometry Definition

The first step in the research was the development of a surface geometry definition suitable for generating structured multiblock grids. The wing definition for the EET model is described in detail in Reference [10]. Tabulated theoretical non-dimensional coordinates were available for six spanwise stations, which included the proper twist distribution. However, the resulting planform shape had one significant deficiency; the wing tip leading edge was straight, whereas the wind tunnel model had a rounded-off leading edge. During the model construction, the straight leading edge was contoured as specified by model blueprints. The resulting leading edge was then hand rounded to give a leading edge radius equal to half the local wing thickness. The following steps were taken to simulate the rounded leading edge geometry. The leading edge planform definition from the blueprint was reproduced using a second order polynomial. The leading edge modification began at  $\eta = 0.9660$ , and intersected the original tip station at 21.0% chord. Figure 8a shows a schematic diagram of how the new leading edge radius was formed. The vertical line shows the new leading edge location as obtained from the second order polynomial. Next, a circle was drawn which would approximate the new leading edge. With the circle drawn, the intersection points for the upper and lower surface were determined. This information was used along with a polynomial function to generate the new leading edge radius. The polynomial function was designed to have an infinite slope at the new leading edge position, and maintain slope continuity at the intersection points with the original airfoil. Figure 8b

shows the resulting modified tip airfoil. This procedure was repeated to generate six additional input stations in the tip region. Care was taken to preserve the correct twist and thickness distribution.

A second modification to the wing geometry was the closing of the blunt trailing edge, to provide a single wake attachment line for the grid generation. This was accomplished using two simple exponential blending functions [13]. The functions have the following form:

$$(y/c)_{upper} = (y/c)_{upper} - \frac{\epsilon}{2} \exp[20. \{(x/c)_{upper} - (x/c)_{te}\}] \quad (2.1)$$

$$(y/c)_{lower} = (y/c)_{lower} + \frac{\epsilon}{2} \exp[20. \{(x/c)_{lower} - (x/c)_{te}\}] \quad (2.2)$$

where the subscript  $te$  represents the trailing edge location, and  $\epsilon$  is the trailing edge thickness. Figure 9 shows how these functions have modified the root airfoil shape and slope distributions. Only small differences are noted near the trailing edge. Similar observations were made at the other spanwise stations.

The fuselage geometry was obtained from the full-scale blueprint used by the model builders to construct the fuselage. The blueprint included cross sectional views of the available fuselage stations, as well as complete top and side views which were used to generate analytic sections in the nose and tail regions. Each fuselage station was scanned onto a workstation and digitized. The cross sections were then plotted, and visually inspected for smoothness. In the apex of the nose, circular cross sections were found to give near exact agreement with the blueprint. In the tail region, elliptic cross sections were found to be in good agreement with the blueprint. In addition,

several cross sections were generated to adequately define the wing-fuselage fillet. A close inspection of the semi-span model verified that the additional sections provided an accurate representation.

The last piece of the semi-span model to be defined was the stand-off geometry. Since the stand-off has a constant profile shape, only two sections are required to uniquely define this model piece. The first section is the profile shape of the fuselage centerline. The second section is defined by translating this section a distance equal to the stand-off height.

The sectional definitions of the three model components were input into various CAD packages to generate the final surface geometry definition suitable for use with grid generation software. Figure 10 shows an oblique view of the resulting surface geometry. For clarity, the model components have been separated.

## 2.3 Grid Generation

Figure 11 shows partial views of the C-O grid topologies generated for both the full-span and semi-span configurations. The multiblock structured grids were generated using GRIDGEN [14]. Grid points have been clustered in the streamwise, normal, and spanwise directions to resolve the expected large flow gradients. The far-field boundaries are located six semi-span lengths from the model, which corresponds to approximately 18 root chord lengths. The grid for the full-span model is comprised of 2 blocks, while the semi-span grid has 6 blocks.

A novel approach was taken to generate the grid for the full-span configuration.

When a C-O grid is used to represent a wing-body type configuration, a singular grid line is often formed in the wake region directly behind the fuselage. As a result, computational cells are generated with zero volume. The definition of the surface normal vector becomes ambiguous in this region, and computational difficulties can arise. In order to avoid the formation of a singular line, a small cylindrical “sting” was generated which extended aft from the end of the fuselage. Figure 12 shows a view of the aft fuselage surface grid, along with the sting. The ratio of sting diameter to maximum fuselage diameter was approximately 0.01. Given the small size of the sting, it was anticipated that this modification would have negligible effect on the flow field.

The grid for the semi-span configuration was generated as follows. The grids used to represent the stand-off geometry were generated separately. In the region aft of the stand-off, a small cylindrical grid was generated, to replace the sting used in the full-span grid. To create a semi-span grid, the stand-off grids were abutted to the original full-span grid. This approach allowed alternate stand-off geometries to be examined with ease. Figure 13a shows a spanwise slice through the semi-span grid at the trailing edge of the wing, looking downstream. Figure 13b shows the corresponding block boundaries. At all block boundary interfaces, continuous grid spacings have been used to avoid introducing numerical errors. Care has been taken to produce a smooth grid which maintains the specified grid point clustering. Finally, Figure 14 shows a typical streamwise slice through the wing grid. The normal spacing

was generated using a geometric progression.

## 2.4 Governing Equations

The equations which govern viscous fluid flow in the continuum regime are the Navier-Stokes equations. In three-dimensions, the equation set is comprised of five equations representing the conservation of mass, momentum, and energy. The numerical integration of the full equation set is a formidable task. This is particularly true for high Reynolds numbers, where turbulent flow is likely. For practicality, a reduced set of equations are often used. The unsteady, three-dimensional, thin-layer, compressible Reynolds averaged Navier-Stokes equations are used in the present research. In a Cartesian coordinate system, the equation set is written in conservation law form as:

$$\frac{\partial U}{\partial t} + \frac{\partial E}{\partial x} + \frac{\partial F}{\partial y} + \frac{\partial G}{\partial z} = \frac{\partial E_\nu}{\partial x} + \frac{\partial F_\nu}{\partial y} + \frac{\partial G_\nu}{\partial z} \quad (2.3)$$

The vector  $U$  contains the conserved quantities:  $\rho$ ,  $\rho u$ ,  $\rho v$ ,  $\rho w$ ,  $\rho E$ . The vectors  $E$ ,  $F$ , and  $G$  represent the inviscid fluxes, while  $E_\nu$ ,  $F_\nu$ , and  $G_\nu$  represent the viscous shear flux vectors. Reference [15] gives a full description of these vectors. To simulate turbulent flow, a turbulence model is required to obtain closure of the set of equations.

## 2.5 Computational Code Evaluation

As discussed above, the flow fields of interest are typical of take-off and landing conditions, with freestream Mach numbers of approximately 0.20. Even though the freestream Mach numbers of interest are low, the flow around a transport wing with

high-lift devices deployed may contain regions of supersonic flow [3]. Thus to properly model the flow physics, a compressible flow solver may be required. However, the application of a compressible flow solver at low Mach numbers can be problematic.

At low freestream Mach numbers, it may be expected that the performance of a compressible flow solver will degrade to the point where either the solver becomes inefficient, or accurate solutions may be unobtainable [16, 17]. The inefficiency stems from the fact that the allowable local time step is inversely proportional to the local speed of sound [15]. As the freestream Mach number decreases, the speed of sound increases, and the allowable time step decreases. As a result, solution times increase. Also, it can be shown that in the limit as the freestream Mach number goes to zero, the solution of the compressible flow equations becomes singular [18]. For these reasons, it is necessary to examine the low Mach number performance of a particular flow solver, to determine where it becomes inefficient or inaccurate.

Recently, several researchers have investigated the performance of compressible flow solvers at low freestream Mach numbers [16, 17]. While quite informative, the geometries used for the computations were two-dimensional. In the present work, the low Mach number performance of two widely used three-dimensional compressible Navier-Stokes solvers is compared. The compressible Navier-Stokes solvers chosen, TLNS3D-MB [19] (TLNS3D) and CFL3D [20], developed at NASA Langley Research Center, represent the current state-of-the-art of compressible 3-D Navier-Stokes solvers. For comparison, the results from the incompressible Navier-Stokes



solver, INS3D-UP [21] (INS3D), developed recently at NASA Ames Research Center are also presented. The performance of the two compressible flow solvers is evaluated using two geometries of practical engineering interest. The first geometry is an untwisted rectangular wing [22]. The second geometry is the full-span EET cruise configuration [10]. The accuracy of the computational results is examined by making direct comparison to available experimental data.

### **2.5.1 Computational codes**

The three computational codes examined are briefly discussed below. Both compressible flow solvers, TLNS3D and CFL3D, were developed at NASA Langley Research Center. The incompressible flow solver, INS3D, was developed at NASA Ames Research Center. Both TLNS3D and CFL3D are finite volume codes, while INS3D is a finite difference code.

TLNS3D solves the three-dimensional, time dependent, thin-layer compressible Navier-Stokes equations for a body fitted coordinate system [19]. The equations are discretized in a central difference, finite volume formulation. The solution is advanced to steady state using an explicit Runge-Kutta time stepping scheme, which is second order accurate. Artificial dissipation, in the form of blended second and fourth differences is added for stability. The artificial dissipation can be added in either scalar or matrix form. For the evaluation, only the matrix form of artificial dissipation is employed. Fuller details of the code are found in Reference [19]. CFL3D solves the time dependent, thin-layer, compressible Navier-Stokes equations for a body

fitted coordinate system [20]. The equations are discretized using an upwind biased, finite volume formulation. The convective and pressure terms are upwind biased using the flux-difference splitting scheme of Roe. The shear stress and heat transfer terms are centrally differenced. The solution is implicitly advanced to steady state by use of a 3-factor approximate factorization which is second order accurate. For steady state solutions, both TLNS3D and CFL3D take advantage of several acceleration techniques including multigriding, grid sequencing, and local time stepping. Reference [20] gives fuller details of CFL3D. INS3D solves the incompressible Navier-Stokes equations for a body fitted coordinate system, using the method of artificial compressibility [21]. The equations are discretized using an upwind biased finite difference formulation. The convective, pressure, and shear stress terms are treated similar to those of CFL3D. The solution is implicitly advanced to steady state using a Gauss-Seidel type line relaxation scheme. The resulting solution is second order accurate. Fuller details of the code are found in Reference [21].

All three Navier-Stokes solvers discussed above offer several turbulence modeling options. For the present research, only the one-equation model of Spalart-Allmaras [23] is used to simulate the effects of fine scale turbulence. For all test cases presented, fully turbulent flow was simulated.

The lift coefficient was monitored to consistently compare the convergence characteristics of the codes. When the lift coefficient converged to four decimal places, the solutions were considered converged. In addition, the computational time was

also monitored to compare the computational efficiency.

## 2.5.2 Rectangular wing computations

Figure 15 shows a partial view of the C-O grid used to represent the rectangular wing geometry. The wing has an aspect ratio of 6.0, with the wing cross section being defined by the NACA 0012 airfoil [22]. An algebraic grid generation algorithm based on transfinite interpolation was used to generate the three-dimensional grid. Grid points have been clustered to resolve the large flow gradients in the chordwise, spanwise, and normal directions. For this wing geometry, the upstream and downstream boundaries extend eight root chord lengths from the leading and trailing edges of the wing respectively. Since no side slip was considered, symmetry conditions were applied at the root plane of the grid.

A grid refinement study was conducted for the simple wing configuration using all three codes. Figure 16 compares computed pressure distributions obtained from three representative grids to experimental data at one spanwise location. The flow conditions for this test case are:  $M_\infty = 0.14$ ,  $\alpha = 10.01^\circ$ ,  $Re = 3.17 \times 10^6$ . These computations simulated fully turbulent flow, using the Spalart-Allmaras turbulence model. The grid dimensions, such as  $193 \times 49 \times 49$ , represent the number of grid points in the streamwise, normal, and spanwise directions respectively. Refinement of the grid clearly improves the agreement with experimental data, particularly in the leading edge region. The results obtained using the  $289 \times 73 \times 73$  grid are identical within plotting accuracy to those obtained using the  $193 \times 49 \times 49$  grid for all three codes.

Figure 17 shows the influence of grid refinement on the computed lift and drag coefficients. Here  $N$  represents the total number of grid points in a particular grid. On the two finest grids, the maximum variation in lift coefficient for both compressible flow solvers is 1.1%, while for INS3D, the variation is only 0.1%. The maximum variation in drag coefficient for both compressible flow solvers is 2.0%, while for INS3D, the variation is approximately 4.3%. Figure 18 shows the influence of grid refinement on upper surface streamwise velocity profiles at the 50% chord location at the same spanwise location. Here  $\zeta$  is the normal distance from the wing surface. Again, the results from the two finer grids are nearly identical. From this grid refinement study, it is evident that the  $193 \times 49 \times 49$  grid is capable of adequately resolving the features of the flow field. With this grid, typical values of  $y^+$  for the first grid point off of the wing surface were in the range of 1-5, with approximately 25 grid points clustered in the wing boundary layer.

Figure 19 compares computed lift and drag coefficients to experimental data. The computations were performed at the following angles-of-attack:  $10.01^\circ$ ,  $16.00^\circ$ , and  $18.10^\circ$ . In general, the agreement with the experimental data is good. Both compressible flow solvers have predicted the break in the lift curve at  $16.00^\circ$ . In contrast, INS3D underpredicts the flow separation, and the computed lift value at the highest angle-of-attack does not agree well with the experimental data. Subsequent computations with INS3D have shown that the choice of turbulence model has a strong impact on the predicted flow separation. Thus, detailed comparison of the

computational results from all three flow solvers will only be presented at the lower angle-of-attack, where all three codes have predicted an attached flow.

Figure 20 compares predicted pressure distributions to experimental data at three spanwise stations for  $\alpha = 10.01^\circ$ . Across the span of the wing, all three flow solvers accurately predict the leading edge suction peaks, and their associated adverse pressure gradients. At the two inboard stations, the computational results are nearly identical, and agree quite well with the experimental data. At the outboard station, the influence of the tip vortex on the upper surface is consistently underpredicted. The computations, however, are still in good agreement with the data. To further illustrate the similarities between the predicted flow fields, the computed spanwise load distributions are compared in Figure 21. Here  $c_n$  is the local sectional normal force coefficient, obtained by integrating the surface pressure distribution. All three codes predict similar spanwise load distributions, with the results from the two compressible flow solvers being nearly identical.

Figure 22 compares the computed upper surface streamwise velocity profiles at 50% chord, and  $\eta = 0.6084$ . The similarities between the profiles is encouraging. Outside of the boundary layer, all codes predict nearly identical flow acceleration over the wing. This is not surprising, given the agreement in the computed pressure distributions, as discussed above. Inside the boundary layer, some differences are observed. Over the entire wing surface, the profiles predicted by INS3D are slightly fuller, and thus more resistant to flow separation. At the higher angles-of-attack,

this may partially account for the underprediction of flow separation by INS3D, as discussed above. It should be noted that similar observations were made at other locations.

Finally, Figure 23 compares the convergence histories of lift and drag coefficients from all three flow solvers. The normalized coefficients are plotted versus Cray Y-MP CPU time in hours. The arrows indicate where the lift coefficient has converged to 99.5% of its final value. It should be noted that using this criterion, the drag coefficient is also similarly converged. The computational time of CFL3D is approximately 60% higher than that of INS3D, while the computational time of TLNS3D is approximately double that of INS3D.

The influence of freestream Mach number on the accuracy and efficiency of both compressible flow solvers was also examined in detail [24]. For this study, the angle-of-attack and Reynolds number were held constant, while the freestream Mach number was varied from 0.40 to 0.14. Both compressible flow solvers were found to accurately predict the variation of lift and drag coefficients with freestream Mach number. As the freestream Mach number decreased, the flow fields changed significantly, ranging from compressible to largely incompressible. As a result, the computational times increased noticeably, on the order of 75%.

### **2.5.3 Transport wing-body computations**

Figure 11 shows a partial view of the single block C-O grid topology used for the wing-body configuration. The grid was generated using GRIDGEN [14], as discussed

above. Since no side slip was considered, symmetry conditions were again applied at the root plane of the grid. A grid refinement study was conducted using only TLNS3D. From this grid refinement study, it was clear that a  $241 \times 65 \times 81$  grid was capable of resolving the features of the flow field. The resulting wing grid is  $145 \times 61$ . With this grid, typical values of  $y^+$  for the first grid point off the wing surface *and* fuselage surface were in the range of 1-5, with approximately 25 grid points clustered in the boundary layer.

Figure 24 compares the computed pressure distributions to experimental data at three spanwise locations. The flow conditions for this test case are:  $M_\infty = .20$ ,  $\alpha = 4.43^\circ$ ,  $Re = 4.2 \times 10^6$ . These computations simulated fully turbulent flow, using the Spalart-Allmaras turbulence model. The computations agree quite well with the experimental data. Across the span of the wing, all three flow solvers again accurately predict the leading edge suction peaks, and the subsequent adverse pressure gradients. The predicted lower surface pressure distributions are identical to within plotting accuracy. On the upper wing surface, small differences are observed. At all stations, INS3D predicts stronger adverse pressure gradients, giving slightly better agreement with the experimental data. Figure 25 compares the computed spanwise load distributions. The fuselage wing juncture occurs at  $\eta = 0.1095$ . Again, the spanwise load distributions are quite similar, with each code predicting loss of lift on the inboard portion of the wing due to fuselage interference.

Figure 26 compares the predicted upper surface streamwise velocity profiles at 50%

chord, and  $\eta = 0.6234$ . Again, the profiles are quite similar. INS3D predicts that the external flow is slightly decelerated, as compared to the results from both compressible flow solvers. This is consistent with the stronger adverse pressure gradients predicted by INS3D, as discussed above. Inside the boundary layer, INS3D again predicts a slightly fuller profile. Again, it should be noted that similar observations were made at other locations.

For this test case, the computational times required for the lift coefficient to converge to 99.5% of its final value were quite similar. On a Cray C-90 supercomputer, TLNS3D required 1.9 hours; CFL3D required 2.1 hours; while INS3D required 2.7 hours. This is in sharp contrast to the rectangular wing computational times discussed above, where both compressible flow solvers required significantly more computational time. For this test case, INS3D required approximately 40% more computational time than TLNS3D. These results clearly show that the relative computational times are case dependent.

## 2.6 Computational Code Selection

Both compressible flow solvers were found to accurately predict the low speed flow over both geometries. The computed pressure distributions were nearly identical, and agreed quite well with the experimental data. For the EET configuration, both compressible flow solvers required approximately 35% less computational time than INS3D. It was apparent that the use of a compressible flow solver would not introduce numerical difficulties. At the time the code evaluation was conducted, only TLNS3D



offered generalized boundary conditions. That is, each grid cell on a surface can have a different boundary condition specified. This approach allows complex configurations to be examined with relative ease, and thus TLNS3D was used for all subsequent computations.

# 3 Analysis of Baseline Configurations

In this chapter, the aerodynamic characteristics of both the full-span and semi-span configurations are examined using TLNS3D. The computational results are validated by making direct comparison to experimental data for both configurations.

## 3.1 Full-span computations

### 3.1.1 Boundary conditions

The boundary conditions used to simulate the flow over the full-span configuration are as follows. The far-field outer boundary is treated using characteristic boundary conditions. The properties at the downstream boundary are obtained using a zeroth-order extrapolation from the interior. The fuselage and wing surfaces are treated as adiabatic, no-slip surfaces, with the normal pressure gradient set to zero at the surface. The final boundary condition is the root plane. Since no sideslip was considered, symmetry boundary conditions are used, resulting in a “free-air” simulation.

### 3.1.2 Grid refinement study

Initially, computations were carried out with four grids simulating fully turbulent flow using the Baldwin-Lomax turbulence model. Figure 27 shows a comparison of the computational results with experimental data for  $M_\infty = .20$ ,  $\alpha = 4.43^\circ$ , and  $Re = 4.2 \times 10^6$ . The grid dimensions, such as  $241 \times 65 \times 81$ , represent the number

of grid points in the streamwise, normal, and spanwise directions respectively. It is seen that refinement of the grid improves the agreement with experimental data, particularly in the leading edge region. Further streamwise refinement up to 481 points was examined; the results obtained were identical within plotting accuracy to those obtained with the  $241 \times 65 \times 81$  grid. Figure 28 shows the influence of grid refinement on the wing boundary layer, at  $\eta = .9066$ . These results are representative of those obtained across the entire wing. In Figure 28a, the streamwise velocity profiles at  $x/c = .50$  are plotted. The results obtained using the two finest grids are nearly identical. Figure 28b compares the skin friction distributions, while Figure 28c compares the  $y^+$  distributions. Again, the results from the two finest grids are nearly identical. The results obtained using the  $481 \times 65 \times 81$  grid were again identical to within plotting accuracy to those obtained using the  $241 \times 65 \times 81$  grid. Thus the  $241 \times 65 \times 81$  grid was used in the following computations. For this grid, the wing surface grid dimensions were  $145 \times 61$ . The typical values of  $y^+$  for the first grid point off the wing and fuselage surfaces were in the range of 1-5. However as shown in Figure 28c, the typical values of  $y^+$  on the wing were essentially in the range of 1-2, with approximately 25 grid points clustered in the wing boundary layer.

### 3.1.3 Influence of turbulence model

The predicted pressure distributions with the zero-equation Baldwin-Lomax and one-equation Spalart-Allmaras turbulence models are plotted in Figure 29 for  $\alpha = 4.43^\circ$ . It can be seen that the computations using the one-equation model are in

better agreement with the experimental data. At all three stations, the suction peak level is more accurately predicted, as is the subsequent adverse pressure gradient. It is also evident that the pressure distribution over the *whole* wing is influenced by the turbulence model. Two higher angles of attack ( $8.58^\circ$  and  $12.55^\circ$ ) were also investigated, and also confirmed that the one-equation model consistently gave better predictions.

To further demonstrate the influence of the turbulence model, Figure 30 compares the near surface streamline patterns obtained using both turbulence models at  $\alpha = 12.55^\circ$ . Zero mass particles have been released one grid point above the surface, to simulate the oil flow visualization technique. It is important to note that the particles have been released at identical locations for both cases. Significant differences in the streamline patterns are observed. The result obtained using the Baldwin-Lomax turbulence model predicts attached flow over the entire wing, with little spanwise flow. In sharp contrast, the result obtained using the Spalart-Allmaras turbulence model predicts flow separation near the outboard trailing edge. Considerable spanwise flow is observed across the entire span. It should be noted that the Baldwin-Lomax turbulence model tends to underpredict flow separation [25]. The predicted fuselage streamline patterns are also quite different, particularly in the wing-fuselage juncture region. Here, the Spalart-Allmaras turbulence model predicts noticeably higher streamline curvature. A detailed examination of both solutions has shown that the streamline pattern in the wing-fuselage juncture region is influenced by the vortex

shed from the nose region of the fuselage. The forebody vortex predicted using the Baldwin-Lomax turbulence model was much weaker than that obtained using the Spalart-Allmaras turbulence model. As a result, the induced downwash on the fuselage was significantly reduced. This result is not surprising, given the tendency of the Baldwin-Lomax turbulence model to dissipate off-body vortical flows [26]. Similar differences were observed at the lower angles-of-attack. The one-equation turbulence model of Spalart-Allmaras was thus used in the following computations.

#### **3.1.4 Influence of angle-of-attack**

Figure 31 shows a comparison of the computed lift and pitching moment coefficients with experimental data. The computations were performed at  $\alpha = 4.43^\circ$ ,  $8.58^\circ$ , and  $12.55^\circ$ . Overall, the agreement between the experiment and computations is quite good. Figures 32 - 34 compare the predicted pressure distributions to experimental data for all three angles-of-attack. At  $4.43^\circ$ , the agreement between the computations and experimental data is excellent. Across the span of the wing, the computations accurately predict the leading edge suction peaks, and subsequent strong adverse pressure gradients. For the  $8.58^\circ$  case, the computations are again in excellent agreement with the data. As the angle-of-attack is increased further, to  $12.55^\circ$ , the computations are observed to slightly underpredict the leading edge suction peaks. Overall, the agreement is still quite good. Given such agreement, the Navier-Stokes solver was then used to compute the flow over the semi-span configuration.

## 3.2 Semi-span computations

### 3.2.1 Boundary conditions

The boundary conditions used for the semi-span computations are as follows. The far-field outer boundary is treated using characteristic boundary conditions. The properties at the downstream boundary are obtained using a zeroth-order extrapolation from the interior. The stand-off, fuselage, and wing surfaces are treated as adiabatic, no-slip surfaces, with the normal pressure gradient set to zero at the surface. It should be noted that the stand-off surface is *not* included in the force and moment calculations, since it is non-metric in the experiment. To simulate the wind tunnel sidewall, the root plane is treated as a no-slip surface. For the given flow conditions, an initial inflow boundary layer profile was not required to duplicate the characteristics of the sidewall boundary layer.

### 3.2.2 Influence of angle-of-attack

A fully turbulent boundary layer representative of that measured in a recent NTF experiment [12] was predicted along the sidewall of the semi-span configuration. The results of a grid refinement study showed that 33 points clustered in the sidewall boundary layer were adequate to resolve the details of the flow in the near wall region. Figure 35 presents a comparison of computed lift and pitching moment coefficients with *uncorrected* data from the NTF tests. The computations were performed at the same angles-of-attack as discussed above, and agree well with the experimental data. It should again be emphasized that consistent with the experimental method,

the force and moment coefficients are computed *only* on the wing and fuselage. That is, the stand-off is non-metric. The potential benefits of using a metric stand-off are discussed in Appendix A.

Figure 36 shows a comparison of the computed pressure distributions with uncorrected experimental data at two spanwise locations on the wing for the case  $\alpha = 8.24^\circ$ . The computations show good qualitative agreement with the experimental data. Across the span, the leading edge suction peaks and strong adverse pressure gradients are well predicted. The mismatch in pressures suggests that the computational and experimental angles-of-attack differ. It should be noted that the experimental data has not been corrected for the effects of the wind-tunnel wall interference, which may account for the apparent difference in angle-of-attack. The capabilities of the Navier-Stokes solver are further demonstrated from the comparison of the predicted pressure distribution at the midspan section of the stand-off geometry and *uncorrected* experimental data shown in Figure 37. For reference, the location of the wing root is shown. Again, the qualitative agreement between the pressure distributions is quite good. The multiple adverse pressure gradients along the stand-off have been adequately predicted. Since the stand-off is immersed in the sidewall boundary layer, this comparison indicates that the Navier-Stokes solver is capable of predicting the near-wall behavior resulting from the interaction of the sidewall boundary layer and the flow over the semi-span model. In the following chapter, the semi-span computational results are compared with the full-span results, to de-

termine in detail how the flows over the semi-span and full-span configurations differ.



## 4 Comparison of Full-span and Semi-span Configuration Flow Fields

In the following sections, the semi-span computational results are compared to the full-span results to document how the flow over the semi-span configuration differs from that over the full-span configuration.

### 4.1 Comparison of aerodynamic loadings

Figure 38 shows a comparison of the computed and experimental lift and pitching moment coefficients for both configurations. The full-span and semi-span results differ in several aspects. Firstly, the lift coefficients are higher for the semi-span configuration. Secondly, the lift curve slope for the semi-span configuration is greater than that of the full-span. And finally, the semi-span pitching moment curve has been shifted upward. These observations suggest that the stand-off distance from the sidewall is too large [9]. Although the computed values are slightly off-set from the experimental data, the computations correctly predict the incremental shifts observed in the data. Since the semi-span configuration generates more lift for a given angle-of-attack, one may conclude that the semi-span model is at an effective higher angle-of-attack. An examination of the computed pressure distributions, however shows that this is incorrect.

In general, when the angle-of-attack is increased, the pressure distribution on *both* the upper and lower wing surface changes. The  $C_p$  values on the upper surface become more negative, while the  $C_p$  values on the lower surface become more positive. The computed pressure distributions for both configurations at  $\alpha = 4.43^\circ$  are plotted in Figure 39. It is observed that the pressure distribution on the lower surface of the wing is *not* significantly altered. In contrast, the upper surface pressure distribution for the semi-span model has been altered. The flow over the upper surface of the semi-span wing is accelerated more, thus decreasing the pressure. It is also important to note that the flow acceleration on the upper wing surface is not limited to the leading edge region, but extends up to the trailing edge at all 3 stations. The net result of this flow acceleration is that the lift on the semi-span configuration is increased. At the higher angles-of-attack, Figures 40 - 41, the same effect of the flow acceleration is observed. This effect is more clearly illustrated in Figure 42, where the difference between the full-span and semi-span pressure coefficients is plotted. As the angle-of-attack is increased, the maximum difference between the full-span and semi-span upper surface pressure coefficients is also increased. At the highest angle-of-attack,  $\alpha = 12.55^\circ$ , the maximum difference is found to be on the order of 0.70.

Figure 43 shows a comparison of the predicted spanwise load distributions for both configurations at all three angles-of-attack. The wing-fuselage juncture occurs at  $\eta = .1095$ . This comparison demonstrates how the flow acceleration over the upper wing surface of the semi-span configuration results in an increased wing loading across the

entire span. Clearly, the influence of the stand-off geometry and sidewall boundary layer is not limited to the inboard portion of the wing. Further flow field comparisons also show that the flow acceleration over the semi-span model is not limited to the wing alone.

The predicted pressure distributions along the centerline of the fuselage for all three angles-of-attack are compared in Figure 44. For all three cases, the semi-span configuration experiences significant flow acceleration over the upper surface of the fuselage. As with the wing, the flow acceleration is not limited to the nose region alone, but extends downstream to the wing-fuselage juncture region. In contrast to the wing, the lower surface pressure distribution along the fuselage of the semi-span configuration is altered noticeably. The flow along the lower fuselage surface has been accelerated as compared to the full-span configuration. Further examination of the semi-span computational results shows that the stand-off geometry behaves as a lifting surface. Even though the lift generated by the stand-off geometry is *not* included in the force and moment calculations, the circulation of the entire flow is increased. As a result, a flow acceleration is induced over the upper surface of the semi-span configuration.

## **4.2 Comparison of near surface streamline patterns**

The near surface streamline patterns are examined to further demonstrate how the flow over the semi-span configuration differs from that over the full-span. The upper

wing surface streamline patterns for all three cases are compared in Figures 45. At  $\alpha = 4.43^\circ$ , both streamline patterns are quite similar. As the angle-of-attack is increased to  $8.58^\circ$ , noticeable differences are observed on the inboard portion of the wing. The semi-span configuration experiences increased cross flow, especially near the trailing edge. As the angle-of-attack is increased to  $12.55^\circ$ , significant differences in the streamline patterns are observed. Both solutions predict flow separation along the outboard trailing edge of the wing. The location and extent of the separation is quite similar for both configurations. On the inboard portion of the wing, the streamline patterns are vastly different. The semi-span configuration experiences significantly increased cross flow, particularly near the trailing edge. It may be anticipated that such an increase in cross flow on the inboard portion of the semi-span wing may adversely affect the stall characteristics.

The increased cross flow on the inboard portion of the semi-span wing suggests that the fuselage streamline pattern has also been altered. Figure 46 compares the fuselage streamline patterns at  $\alpha = 12.55^\circ$ . The streamline patterns are indeed quite different. Ahead of the wing, the flow over the semi-span fuselage flows inboard toward the wall, crossing the fuselage centerline. Such a flow pattern is not possible for the full-span configuration, due to symmetry. In the wing-fuselage juncture region, the full-span computation predicts flow separation near the trailing edge of the fillet. In sharp contrast, the semi-span computation predicts attached flow. Over the aft portion of the fuselage, the semi-span computation predicts that the streamlines are

displaced away from the fuselage centerline. Further insight into this flow pattern can be gained by examining Figure 47. Here, a planform view of the semi-span configuration is presented. Particles have been released in the nose region of the stand-off. In the nose region, the flow moves spanwise from the stand-off onto the fuselage. Further downstream, the flow migrates from the fuselage onto the stand-off. Near the trailing edge of the wing, the flow migrates spanwise, spilling onto the aft portion of the fuselage. It is seen that the symmetry about the fuselage centerline has been lost. Similar flow patterns were observed at the lower angles-of-attack.

Figures 48 - 50 compare the predicted streamline patterns at the root plane of each configuration. For the full-span configuration this is the centerline of the fuselage, while for the semi-span configuration, this is the simulated wind tunnel sidewall. For all angles-of-attack, the full-span computations predict smooth flow over the fuselage, exhibiting little streamline curvature. In sharp contrast, the semi-span computations predict that the sidewall boundary layer separates upstream of the stand-off, and rolls up to form a horseshoe vortex in the juncture region. As a result, significant streamline curvature occurs. Figure 50c shows details of the predicted flow patterns on the sidewall in the nose region of the stand-off at  $12.55^\circ$ . The saddle point and dividing streamlines of the separation are clearly visible, along with the subsequent flow reversal near the nose of the stand-off. Similar results were obtained at the other angles-of-attack. This again demonstrates that the flow over the semi-span model differs markedly from the flow over the full-span configuration.

Figure 51 presents a comparison of computed sidewall streamline patterns and experimental tuft visualization results for  $\alpha = 8.24^\circ$ . The agreement is excellent. The location of the saddle point and subsequent flow reversal in the nose region are well predicted by the computation. It should be noted that the computational results were used to determine the location of tufts on the wind-tunnel sidewall. This comparison further demonstrates the capabilities of the Navier-Stokes solver to aid in the development of semi-span model test techniques in the NTF.

### 4.3 Comparison of wing boundary layer characteristics

As discussed above, the semi-span configuration experiences an induced flow acceleration over the upper surface of the wing. The streamwise and spanwise velocity profiles are examined to document what influence this has on the development of the wing boundary layer. For this comparison, the  $\alpha = 8.58^\circ$  case is used as the illustrative example, since similar observations were made at the other angles-of-attack.

Figure 52 compares upper surface streamwise and spanwise velocity profiles at the 50% chord location, at all three stations. The streamwise profiles consistently show the flow acceleration experienced by the semi-span configuration. In general, the flow acceleration alters the entire profile shape. The spanwise profiles give further insight into the increased cross flow experienced by the semi-span model. Here, positive values of  $w$  indicate flow toward the wingtip. At the inboard station, the increased spanwise migration is readily seen. The peak spanwise velocity near the surface has

increased by nearly 50%. These observations are consistent with the near surface wing streamline patterns discussed above. At each spanwise station, several other chordwise locations were examined. The results obtained were quite similar to those observed at the 50% chord location.

The characteristics of the wakes shed from the wings of both configurations were examined at the three locations shown in Figure 53. The horizontal line indicates the location where the wake profiles were examined. The choice of a streamwise location for such a comparison is somewhat arbitrary. For the present comparison, the streamwise location was chosen based on grid quality in the wake region. Figure 54 compares wake shapes for both configurations at  $\alpha = 8.58^\circ$ . The wake shapes are quite similar. At each station, the location of the maximum velocity deficit is nearly identical for both configurations. This tends to indicate that the downwash distribution for both configurations is quite similar. The wake spreading rates were also found to be nearly identical for both configurations. Again, the induced flow acceleration experienced by the semi-span configuration is evident. Similar observations were also made at other streamwise locations and angles-of-attack.

#### **4.4 High angle-of-attack aerodynamic characteristics**

A post stall case was simulated to examine the characteristics of both configurations at high angles-of-attack. The angle-of-attack chosen was  $18.25^\circ$ , due to the availability of experimental pressure data for the semi-span model. Unfortunately,

pressure data for the full-span model is unavailable above  $\alpha = 12.55^\circ$ .

Figure 55 compares computed and experimental semi-span pressure distributions at two spanwise locations. At the inboard station, the computations show good qualitative agreement with the experimental data. On the outboard portion of the wing however, the agreement is poor. These differences are attributed largely to aeroelastic deformations which occur experimentally at high angles-of-attack. Figure 56 compares the computed and experimental lift and pitching moment coefficients for both configurations. Even though the computations neglect aeroelastic deformations, the agreement with the experimental data is quite similar to that obtained at the lower angles-of-attack.

Figure 57 compares the computed pressure distributions for both configurations at three spanwise stations. Significant differences are again observed. The flow over the upper surface of the semi-span model has been largely decelerated as compared to that over the full-span. As with the lower angles-of-attack, the lower surface pressure distributions are nearly identical. At the inboard station, the differences between the upper surface pressure distributions near the trailing edge suggest that the semi-span model experiences an increased flow separation. The differences are more clearly seen in Figure 58, where the differential pressure distributions are plotted. The differences over the forward 50% of the wing are significant. A comparison of the fuselage centerline pressure distributions, Figure 59, shows that the flow over the semi-span fuselage has again been greatly accelerated.



The comparison of the upper wing surface streamline patterns, Figure 60, shows that the stall patterns for both configurations are vastly different. For the full-span configuration, the flow inboard of the trailing edge break is attached, with a strong cross flow near the trailing edge. Outboard of the trailing edge break, massive flow separation is predicted, with the separation line visible near the leading edge. In stark contrast, the semi-span model experiences flow separation across the *entire* span. Only a small region of attached flow is predicted near the inboard leading edge. Figure 61 compares the predicted root plane streamline patterns for both configurations. The extent of the sidewall boundary layer separation has increased dramatically, as compared to the lower angles-of-attack. The resulting streamline curvature has also increased significantly.

## **5 Development of Semi-span Test Techniques**

In the previous chapter, the comparison of full-span and semi-span computational results showed that the flow over the semi-span configuration was vastly different from that over the full-span. In this chapter, the Navier-Stokes solver is used to examine methods to improve the flow over the semi-span configuration. First, the code is used to examine alternate strategies for mounting the semi-span model. The code is then used to examine methods to manipulate the sidewall boundary layer, and thus minimize its influence on the flow over the semi-span model.

### **5.1 Influence of stand-off geometry**

The following studies were conducted to examine the influence of the stand-off geometry. First, a parametric study was conducted to systematically examine the influence of the stand-off height. Next, the influence of three-dimensional shaping of the stand-off geometry was examined. Finally, the effect of a boundary layer fence mounted between the fuselage and stand-off was examined.

#### **5.1.1 Influence of stand-off height**

The stand-off geometry used in the experiments had a height of 4.50 inches. As previously discussed, this height was chosen to remove the semi-span model from the sidewall boundary layer. However, the analysis presented in the previous chapter in-

dicated that this stand-off height was too large. A family of smaller stand-off heights was thus considered. Since the sidewall boundary layer has a strong influence on the flow over the semi-span model, the stand-off heights were based on a characteristic length scale of the sidewall boundary layer. The length scale chosen was the displacement thickness,  $\delta^*$ . For the given flow conditions, both the experimental [12] and theoretical [27] tunnel empty sidewall boundary layer displacement thickness values were approximately 0.30 inches, at a streamwise location corresponding to the midpoint of the fuselage. Thus, the original stand-off had a non-dimensional height ratio,  $h/\delta^*$ , equal to 15. Three smaller stand-offs were generated, with  $h/\delta^*$  values of 1.0, 2.0, and 5.0. Figure 62 shows a frontal view of all four stand-offs, plotted in physical coordinates. It should be noted that a zero-height stand-off configuration was not examined, due to the extensive grid modifications which would be required to adequately resolve the sidewall boundary layer.

Figure 63 shows the influence of the stand-off height on the lift and pitching moment coefficients. The full-span values are also shown for comparison. As anticipated, the stand-off height has a strong influence on the semi-span coefficients. As the stand-off height is initially decreased from  $15\delta^*$  to  $2\delta^*$ , the agreement with the full-span values improves significantly. The shortest stand-off is observed to slightly underpredict the full-span values. An extrapolation of the results shows that decreasing the stand-off height further would result in poorer agreement with the full-span values. From this comparison, a stand-off height of approximately  $1.5\delta^*$  would be

expected to match the full-span results exactly. These results are somewhat contrary to conventional thinking, in that partially immersing the semi-span model in the side-wall boundary layer improves the agreement with the full-span results. The following comparisons examine in detail how the stand-off height influences the flow over the semi-span model.

Figure 64 compares the differential pressure distributions for all four stand-off heights, at the three spanwise stations. As the height is decreased, the induced flow acceleration over the upper surface of the wing decreases dramatically. It is important to note that the stand-off height influences the pressure distribution across the entire span. Of the stand-off heights examined, the  $2\delta^*$  case appears to best replicate the full-span pressure distribution. Over the aft 75% of the upper wing surface, the  $\Delta C_p$  values are essentially zero. In contrast, the  $1\delta^*$  case shows that the  $\Delta C_p$  values have just become positive over the upper surface. This indicates that the flow field has been slightly decelerated as compared to the full-span configuration. Figure 65 compares the computed spanload distributions for the same cases. This further shows how the stand-off height alters the pressure distribution across the entire wing.

Figure 66 examines the influence of stand-off height on the fuselage centerline pressure distribution. For clarity, the upper and lower surface pressure distributions are plotted separately. The induced flow acceleration on the upper surface of the fuselage decreases greatly with stand-off height, especially in the nose region. The lower surface pressure distribution overall also improves as the height is decreased. It

should be noted that for each stand-off, the pressure distribution along the fuselage centerline is representative of that predicted at the root of the stand-off. Thus, this comparison demonstrates how the lift generated by the stand-off geometry decreases with the stand-off height. Again, the  $2\delta^*$  stand-off gives the best agreement with the full-span result.

The influence of stand-off height on the near surface streamline patterns is next examined. Figure 67 shows the influence of stand-off height on the upper wing surface streamline pattern. The streamline patterns obtained using the  $2\delta^*$  stand-off are compared to those obtained using the original  $15\delta^*$  stand-off, and the full-span results. As the stand-off height decreases, the cross flow on the inboard portion of the semi-span wing decreases. The  $2\delta^*$  case shows better agreement with the full-span result. Figure 68 compares the corresponding fuselage streamline patterns. It is seen that decreasing the stand-off height does improve the agreement with the full-span result, but the improvements are not as noticeable as on the upper wing surface. Ahead of the wing, the  $2\delta^*$  case again shows flow migration from the fuselage onto the stand-off. The streamline curvature in the wing-fuselage juncture region is now less than that observed on the full-span configuration. Over the aft portion of the fuselage, the streamlines are again displaced by the spanwise migration from the stand-off. Figure 69 compares the root plane streamline patterns. The semi-span computations predict that the sidewall boundary layer separates, and forms a horseshoe vortex in the juncture region. As the stand-off height decreases, the extent of the separation

decreases only slightly.

The performance of the  $2\delta^*$  stand-off was also examined at angles-of-attack of  $4.43^\circ$  and  $12.55^\circ$ . Figure 70 shows the influence of stand-off height on the lift and pitching moment curves. At all angles-of-attack, the  $2\delta^*$  stand-off shows marked improvements over the original stand-off height. The shift in the pitching moment curve is quite encouraging. The influence of stand-off height on the differential wing pressure distributions is shown in Figures 71-72. Again, the induced flow acceleration over the upper wing surface has been greatly reduced. Figures 73-74 show similar improvements in the fuselage centerline pressure distributions. The upper wing surface streamline patterns are compared in Figures 75-76. Consistently, the streamline pattern on the inboard portion of the wing has improved. This is particularly seen at  $12.55^\circ$ . Here, the cross flow on the inboard portion of the wing has actually decreased below the full-span result. On the outboard portion of the wing, the region of flow separation has decreased. The root plane streamline comparisons were quite similar to those shown in Figure 69, and are therefore not presented.

Next, the high angle-of-attack performance of the  $2\delta^*$  stand-off was examined. Figure 77 examines the influence of stand-off height on the differential wing pressure distributions at  $18.25^\circ$ . The  $2\delta^*$  stand-off again greatly improves the agreement with the full-span result. The improvements on both the upper and lower wing surfaces are significant. Only the second station,  $\eta = 0.6234$ , differs noticeably from the full-span result. The differences however, are limited to the forward 25% of the

upper surface. Decreasing the stand-off height again improves the fuselage centerline pressure distribution as shown in Figure 78. The upper surface pressure distribution is now nearly identical to the full-span result.

The effect of the stand-off height on the upper wing surface streamline patterns is examined in Figure 79. Decreasing the stand-off height has dramatically improves the streamline pattern. The  $2\delta^*$  semi-span result is very similar to the full-span results. This is in sharp contrast to the  $15\delta^*$  semi-span case. The flow over the inboard portion of the wing remains attached for the  $2\delta^*$  case. Outboard of the wing break station, the streamline patterns are essentially identical. The corresponding fuselage streamline patterns are shown in Figure 80. The improvements are again dramatic. The effect that the stand-off height has on the root plane streamline pattern is shown in Figure 81. Decreasing the stand-off height has noticeably improved the sidewall streamline pattern. This is in contrast to the lower angles-of-attack, where only minor improvements were observed.

These comparisons have shown that the  $2\delta^*$  stand-off greatly improves the aerodynamic loading on the semi-span model. The decrease in the stand-off height however, had little influence on the separation of the sidewall boundary layer. As a result, significant flow field differences still exist between the full-span and semi-span configurations. Further steps must clearly be taken to minimize the influence of the sidewall boundary layer on the flow over the semi-span configuration.

### 5.1.2 Influence of stand-off shaping

In the previous section, it was shown that the stand-off height has a strong influence on the flow over the semi-span model. The effect of three-dimensional shaping on the  $2\delta^*$  stand-off, which best improved the flow over the semi-span configuration, was next examined. The three-dimensional stand-off geometry examined represented a reflection of the fuselage about the centerplane. Figure 82 shows planform views of the nose and tail regions of the 2-D and 3-D stand-off geometries. The nose of the 3-D stand-off intersects the sidewall at an  $X/L$  location of 0.003, while the tail intersects the sidewall at an  $X/L$  location of 0.97. Even though the stand-off height is only 0.60 inches, the 3-D stand-off is indeed quite different.

Figure 83 shows the effect of three-dimensional shaping on the lift and pitching moment coefficients. Both the coefficients have decreased dramatically, and under predict the full-span results. The comparison of the differential pressure distributions, Figure 84, shows that the pressure distribution across the entire wing has been altered. The flow over the upper *and* lower wing surfaces has been decelerated as compared to the full-span configuration. This is in contrast to the influence of stand-off height, where essentially only the upper surface pressure distribution was altered. Figure 85 shows that the flow over the fuselage has also been decelerated. Finally, Figure 86 shows that the three-dimensional shaping of the stand-off has little influence on the separation of the sidewall boundary layer. The overall results however, suggest that a combination of stand-off height and three-dimensional shaping may yield an optimum



stand-off geometry.

### 5.1.3 Influence of stand-off boundary layer fence

In Figure 68 it was shown that even for a near optimal stand-off height,  $h = 2\delta^*$ , the streamline patterns on the fuselage were still quite different from those on the full-span configuration. The flow on the forward portion of the fuselage migrated toward the wall; in the aft region, the flow migrated from the stand-off onto the fuselage. One method which can be used to passively control spanwise flow migration is a boundary layer fence. The Navier-Stokes solver was used to examine the influence of a boundary layer fence placed between the  $2\delta^*$  stand-off and fuselage.

The following steps were taken to simulate boundary layer fences. As discussed previously, separate grid blocks are used to represent the various stand-off geometries. As a result, grid boundaries exist between the fuselage and stand-off as shown in Figure 13b. For all previous computations, these block boundaries have been treated using continuous flow boundary conditions. To simulate a boundary layer fence, a portion of the grid block boundary is treated as a solid surface. It should be noted that the boundary layer fences were treated as adiabatic *inviscid* surfaces, since significant grid modifications would be required to properly resolve a viscous flow past the fences.

Figure 87 shows a frontal view of the two boundary layer fences examined. The two fence heights are 4.00 and 0.75 inches respectively. Figure 88 shows an oblique view of the 4.00 inch boundary layer fence. Due to the fence height, the  $2\delta^*$  stand-off geometry is not visible. The effect of both fences was evaluated at an angle-of-attack

of  $12.55^\circ$ . The computations indicated that the addition of a boundary layer fence had negligible effect on the aerodynamic loading of the semi-span model. The wing *and* fuselage pressure distributions were identical to within plotting accuracy of the original  $2\delta^*$  results. Figure 89 compares the fuselage streamline pattern obtained with the 4.00 inch fence, to both the  $2\delta^*$  semi-span and full-span results. An examination of the streamline pattern reveals that the fence did eliminate the spanwise flow across the fuselage centerline as desired. The streamline pattern over the greater portion of the fuselage however, was not altered. Noticeable differences are still observed between the full-span and semi-span results. Further examination of the computational results indicated that the addition of a boundary layer fence had little effect on the separation of the sidewall boundary layer. For this configuration, it is apparent that the use of a boundary layer fence is not advantageous.

## **5.2 Influence of boundary layer control techniques**

In the following sections, the Navier-Stokes solver is used to examine the ability of three active boundary layer control techniques to minimize the influence of the sidewall boundary layer. First, the addition of tangential blowing jets in the juncture region between the stand-off geometry and the wind-tunnel sidewall is examined. This technique has been used successfully in two-dimensional high-lift testing [28]. Next, the influence of an upstream tangential blowing slot on the sidewall boundary layer is examined [9]. Finally, the influence of sidewall boundary layer suction [28, 29] is examined.

Figure 90 illustrates the effect of the active boundary layer control techniques in manipulating a boundary layer. In the baseline case, Figure 90a, a turbulent boundary layer experiences an adverse pressure gradient which leads to flow separation. Figure 90b shows how tangential blowing influences the boundary layer development. High velocity fluid is injected adjacent to the surface from a high pressure supply. The blowing reenergizes the boundary layer, allowing the flow to remain attached. As a result, the velocity profiles immediately downstream of the blowing location have a distinctive bulge. Figure 90c shows the effect of suction on the boundary layer development. As the boundary layer flows over the porous surface, the lower plenum pressure induces a transpiration through the surface, which removes the low momentum flow near the surface. The boundary layer thickness is decreased, and the resulting fuller velocity profile is more resistant to flow separation. The computational approaches used to simulate the tangential blowing and suction are described in Appendices B and C respectively.

### 5.2.1 Influence of juncture region blowing jets

The  $2\delta^*$  stand-off geometry was used to examine the influence of juncture region blowing jets. The angle-of-attack was fixed at  $12.55^\circ$ . Figure 91 shows the location of the jets considered. Following the approach in Reference [28], the first two jets in the upper juncture region were positioned to coincide with the adverse pressure gradients imposed on the sidewall boundary layer. Their respective  $X/L$  locations are 0.12 and 0.51. The two aft jets were positioned to influence the separation which occurs

aft of the stand-off. Their  $X/L$  locations were both 0.83. The jets were aligned to blow tangent to the stand-off shape. The jets were sized to simulate a 0.25 inch inner diameter exit area. Appendix B describes the details of the computational approach taken to simulate the blowing jets.

Figure 92 examines the influence of the jet blowing on the differential wing pressure distributions. The first blowing case,  $C_\mu = 0.008$ , simulates a choked exit condition with an exit Mach number of unity. The second case,  $C_\mu = 0.002$ , simulates an exit Mach number of 0.50. The  $C_\mu$  values shown characterize the mass flow rate for *each* individual jet, not the total mass flow rate. The jet blowing has slightly increased the flow acceleration over the inboard portion of the upper wing surface. The pressure distributions on the outer portion of the wing have not been noticeably affected. Figure 93 shows the effect of the jet blowing on the spanwise load distribution. Over the outer 70% of the wing, the loading is not affected. The lower blowing case is not shown, since it was identical to within plotting accuracy of the case shown. The influence of the jet blowing on the fuselage centerline pressure distribution is shown in Figure 94. Over the forward 90% of the fuselage, only minor differences are observed in the vicinity of the blowing jets. In contrast, significant differences occur downstream of the two aft blowing jets. The blowing jets have greatly accelerated the flow over the aft portion of the stand-off. At first, this was of concern. However, inspection of the pressure distributions revealed that the upper and lower surface pressure distributions were quite similar. Thus, the flow acceleration over the aft

fuselage has little effect on the semi-span force and moment coefficients.

Figure 95 shows the influence of the blowing jets on the upper surface fuselage streamline patterns. With no blowing, significant spanwise flow migration occurs. Even the flow adjacent to the wall crosses over the fuselage centerline. With the addition of the blowing jets, the streamline pattern is vastly improved. For the choked simulation,  $C_\mu = 0.008$ , only the flow adjacent to the centerline migrates onto the fuselage. As the blowing rate is decreased, the spanwise migration increases slightly. For this reason, even lower blowing rates were not examined. It should be noted that the upper wing surface streamline patterns for both blowing rates were identical to the no blowing case, which was previously shown in Figure 76c.

Figure 96 examines the influence of the blowing jets on the root plane streamline patterns. The blowing jets have no influence on the separation of the sidewall boundary layer ahead of the semi-span model. This is not surprising, since the blowing jets are located downstream of the separation. The blowing has however, improved the streamline pattern in the region aft of the model. These improvements are more clearly seen in Figure 97, where the streamline patterns in the aft region are compared. With no blowing, flow separation occurs on the aft portion of the stand-off geometry. The resulting streamline pattern is in sharp contrast to the smooth flow predicted over the aft portion of the full-span fuselage. The application of the blowing reenergizes the flow adjacent to the stand-off, allowing the flow to remain attached. The resulting streamline patterns are quite similar to the full-span result.

Further computational studies were conducted to examine the influence of additional blowing jets in the lower juncture region. Two blowing jets were added, giving a jet arrangement which is symmetric about the  $y$  axis. The results obtained for both blowing rates were identical to within plotting accuracy of those discussed above. This symmetric six jet configuration was then used to examine the high angle-of-attack performance of the blowing jets. Figure 98 examines the influence of the blowing jets on the differential wing pressure distribution at  $18.25^\circ$ . On the inboard station, the blowing has slightly accelerated the flow over the upper surface. Moving outboard, the blowing jets improve the agreement with the full-span result. The improvements realized at the second station are quite encouraging. This is in contrast to the previous results, where the blowing jets had little effect on the wing pressure distribution. The comparison of the fuselage centerline pressure distributions, Figure 99, shows that the blowing jets have again noticeably accelerated the flow over the aft fuselage region. Similar to the previous results, the blowing jets had little influence on the upper wing surface streamline pattern, and the separation of the sidewall boundary layer ahead of the model.

### **5.2.2 Influence of upstream tangential blowing**

In the previous section, the juncture blowing jets were seen to improve the flow over the aft portion of the semi-span model. The blowing jets however, had no influence on the separation of the sidewall boundary layer ahead of the semi-span model. It was thus decided to examine the influence of an upstream tangential blowing

slot. Some minor grid modifications were required to simulate a realistic blowing slot.

Figure 100 compares the original root plane grid, to the one used to simulate the upstream tangential blowing. The grid was modified such that a portion of the upstream grid was essentially perpendicular to the  $y$  axis. With this approach, a straight portion of the grid could be used to simulate a blowing slot, using the steps described in Appendix B. The blowing slot was located a distance of  $L/4$  upstream of the model. The resulting slot width in the  $y$  direction was approximately  $0.60L$ . The height of the slot, normal to the sidewall, was approximately  $1/8$  inch. The flow injected from the slot was tangent to both the sidewall and the approaching freestream. For this study, the angle-of-attack was held constant at  $12.55^\circ$ , while the blowing rate was varied. Again, the  $2\delta^*$  stand-off geometry was used.

Figure 101 shows the influence of the blowing slot on the root plane streamline patterns. The first case,  $C_\mu = 1.027$ , simulates a choked condition with an exit Mach number of unity. The second case,  $C_\mu = 0.257$ , represents an exit Mach number of 0.50. The streamline patterns have improved dramatically. Both blowing rates have weakened the horseshoe vortex. The resulting streamline patterns are quite similar to the full-span result. A blowing rate of  $C_\mu = 0.041$ , which represented an exit Mach number of 0.20 was also examined. This rate had little influence on the sidewall streamline pattern, and is thus considered a lower bound for effective blowing. The effects of the upstream tangential blowing on the sidewall boundary layer is examined in Figure 102, where representative streamwise velocity profiles along the  $y$  axis are

compared. Figure 102a compares velocity profiles at  $X/L = -.25$ , which corresponds to the location of the blowing slot. The blowing has reenergized the flow adjacent to the sidewall. The peak velocity is two and four times higher than the freestream velocity for the two blowing cases discussed above. Further downstream, Figure 102b, the peak velocity near the sidewall decreases due to mixing and viscous dissipation. The mixing does however, increase the velocity a considerable distance away from the sidewall. As a result of the slot blowing, the sidewall boundary layer is more resistant to separation.

The influence of the upstream tangential blowing on the upper surface fuselage streamline pattern is shown in Figure 103. This comparison shows that the influence of the upstream blowing is not limited to the forward portion of the semi-span model. The blowing has a strong effect on the aft fuselage streamline pattern, decreasing the spanwise migration. As the blowing rate is decreased, the spanwise migration increases. It should be noted that for both cases, the computations predict an attached flow over the aft portion of the stand-off geometry. In an attempt to further improve the fuselage streamline pattern, the juncture blowing jets discussed in the previous section were also included in the blowing simulation. The results indicated that in the presence of the upstream blowing, the juncture blowing jets have little effect. Figure 104 shows the influence of the upstream tangential blowing on the upper wing surface streamline patterns. The blowing has little effect. The only discernible differences occur near the inboard trailing edge, where the cross flow has decreased



slightly.

The influence of the upstream blowing on the semi-span lift and pitching moment coefficients is shown in Figure 105. Here, both coefficients are plotted versus the blowing coefficient. For comparison, the full-span values are also plotted. With the addition of blowing, the lift on the semi-span model increases. As the blowing rate is increased, the lift coefficient remains fairly constant. In practical applications, such a shift may not affect the overall data quality. The variation of the pitching moment coefficient however, is of concern. Even low blowing rates significantly increase the pitching moment coefficient. A comparison of the wing and fuselage pressure distributions provides considerable insight into this behavior.

Figure 106 compares the differential wing pressure distributions for all blowing rates. Across the entire span, the upstream blowing has accelerated the flow over the upper surface. As a result, the lift and pitching moment contributions of the wing increase. It is important to note that the pressure distributions for the two lowest blowing rates are nearly identical. Thus, the wing pitching moment contribution for both cases are nearly identical. This is in sharp contrast to Figure 105b, where the total pitching moment coefficients for both blowing rates were shown to be quite different. This indicates that the large variations in the total pitching moment coefficient are due largely to the fuselage, and not the wing. This is readily apparent when the fuselage centerline pressure distributions are compared in Figure 107. The upstream blowing significantly accelerates the flow over the forward portion of

the fuselage. Experimentally, it may be possible to correct the pitching moment coefficient by performing a blowing-off tare run. Even if the total pitching moment coefficient cannot be corrected, the above comparison shows that the wing pitching moment contribution varies little with the blowing rate. It would thus be anticipated that incremental shifts in the total pitching moment coefficient due to the deflection of a wing mounted control surface, would still be accurate.

The high angle-of-attack performance of the upstream tangential blowing was examined by considering an exit Mach number of 0.50 at  $\alpha = 18.25^\circ$ . Figure 108 shows the effect of the upstream blowing on the root plane streamline pattern. The horseshoe vortex has again been weakened. The resulting streamline pattern is quite similar to the full-span result. Figure 109 examines the influence of the upstream blowing on the upper wing surface streamline patterns. The upstream blowing decreases the cross flow near the inboard trailing edge. The streamline pattern however, is still quite similar to the full-span result. Figure 110 shows that the blowing has once again had a pronounced effect on the inboard pressure distribution. The flow has been noticeably accelerated, decreasing the cross flow. At the second station however, the improvements are significant. Figure 111 again shows that the upstream blowing has dramatically accelerated the flow over the forward portion of the fuselage.

Further computational studies were conducted to examine the influence of the blowing slot location. A second blowing slot was examined, located a distance of  $L/2$  upstream of the model. The slot width in the  $y$  direction was approximately  $1.10L$ .

The results indicated that this blowing slot had little effect on the separation of the sidewall boundary layer.

### 5.2.3 Influence of active sidewall suction

The third sidewall boundary layer control technique examined is active suction. The suction is simulated by specifying a constant normal velocity over a prescribed area. The implementation of the suction is discussed in detail in Appendix C. For this study, the angle-of-attack is held constant at  $12.55^\circ$ , while both the suction rate and suction area are varied. Again, the  $2\delta^*$  stand-off geometry is used.

Figure 112 shows a schematic diagram of the two suction areas examined. The suction has been concentrated near the semi-span model for maximum effect. In the first region, the suction area extends forward to approximately  $X/L = -.12$ , well ahead of the predicted flow separation. The second region represents an extension of the first, covering the entire juncture region. The second suction region extends outward from the stand-off an average distance of  $0.10L$ .

Figure 113 examines the influence of the first suction region on the root plane streamline pattern in the nose region. The suction dramatically improves the streamline pattern. As the suction rate increases, the separation point moves closer to the body. The highest suction rate,  $C_q = -.020$ , has weakened the horseshoe vortex. Figure 114 compares representative sidewall boundary layer profiles at  $Y/L = 0.00$ , and  $X/L = -.06$ . As the suction rate increases, the profiles become fuller, and thus more resistant to flow separation.

The influence of the suction on the semi-span lift and pitching moment coefficients is shown in Figure 115. Both coefficients are plotted versus the suction coefficient. Again, the full-span values are shown for comparison. The suction is observed to have little influence on the aerodynamic coefficients of the semi-span configuration. The comparison of the wing differential pressure distributions, Figure 116, shows that the suction has little effect on the wing loading. Similarly, Figure 117 shows that the suction does not significantly alter the fuselage pressure distribution. For clarity, the  $C_q = -.010$  result is not plotted.

Suction in the nose region alone however, does not improve the entire flow field. Significant differences in the root plane streamline patterns are still present, as shown in Figure 118. Downstream of the nose, the sidewall streamline pattern is quite similar to the original semi-span result. Although not evident in this figure, the upstream suction had no effect on the aft region separation. The suction was thus extended through the entire juncture region to further improve the flow field. The suction rate in the first region is held constant ( $C_q(1) = -.020$ ), while the suction rate in the second region is varied.

Figure 119 shows the effect of suction in the second region,  $C_q(2)$ , on the root plane streamline pattern. With the addition of the second suction region, Figure 119b, the streamline pattern in the lower juncture region is noticeably improved. In the upper juncture region however, the streamlines are slightly displaced away from the model. An examination of the flow field solution revealed that this occurs due to the suction

induced spanwise flow toward the sidewall. As the suction rate in the second region is decreased, the streamlines in the upper juncture region are drawn closer to the model. In the lower juncture region, the suction rate has little influence, which is encouraging. For all suction rates, attached flow was predicted over the aft portion of the stand-off. Figure 120 compares the latter case to the previous full-span and semi-span results. The segmented suction result is quite similar to the full-span result, and shows vast improvements over the no suction case. The influence of suction in the second region on the fuselage streamline pattern is examined in Figure 121. The suction had little effect. Only for the highest suction rate,  $C_q(2) = -.020$ , does the flow adjacent to the sidewall remain on the stand-off. It appears that a significantly higher suction rate would be required to minimize the spanwise migration. However, due to the large suction area of the second region, this would not be practical. As with the first suction region, the second suction region has no effect on the upper wing surface streamline pattern.

The influence of downstream suction on the semi-span lift and pitching moment coefficients is shown in Figure 122. The addition of the second suction region shifts both curves. The increase in the lift coefficient is small, while the increase in the pitching moment is more noticeable. Even though the coefficients have increased, their variation with  $C_q$  is minimal, which is quite encouraging. The comparison of the differential wing pressure distributions, Figure 123, shows that the suction in the second region has slightly increased the inboard wing loading. In contrast,

the downstream suction has improved the fuselage centerline pressure distribution as shown in Figure 124.

The high angle-of-attack performance of the active sidewall suction was examined using:  $C_q(1) = -.020$ ,  $C_q(2) = -.005$ . Figure 125 examines the influence of the suction on the root plane streamline pattern at  $\alpha = 18.25^\circ$ . The suction has again weakened the horseshoe vortex. The resulting streamline pattern is again quite similar to the full-span result. In the aft portion of the lower juncture region, the streamlines are displaced away from the semi-span model. This suggests that a higher suction rate may be appropriate in the lower juncture region. Figure 126 compares the upper wing surface streamline patterns. With the addition of the suction, the streamline pattern improves slightly. The effect that the suction has on the wing pressure distribution is shown in Figure 127. At the inboard station, the flow over the upper surface of the wing has been slightly accelerated. The improvements at the second station are again dramatic. Finally, Figure 128 shows that the suction has once again improved the fuselage centerline pressure distribution.

These comparisons have clearly shown that the sidewall suction has little adverse effect on the flow over the semi-span model. This is in sharp contrast to the adverse effects of the upstream tangential blowing discussed in the previous section.

## 6 Conclusions

A computational investigation was performed to support the development of a semi-span model test capability in the NASA Langley Research Center's National Transonic Facility. A state-of-the-art three-dimensional Navier-Stokes solver was used to compute the low-speed flow over both a full-span configuration, and a semi-span configuration mounted on the wind-tunnel sidewall. The computational results were validated by making direct comparison to experimental data for both configurations. The semi-span results were compared to the full-span results, to document how the flow over the semi-span configuration differs from that over the full-span. The Navier-Stokes solver was then used to examine several methods to improve the flow over the semi-span configuration. The conclusions which can be drawn from this investigation are:

1. The aerodynamic characteristics of the semi-span configuration were found to differ markedly from those of the full-span. The semi-span model produced higher lift coefficients, and its pitching moment curve was shifted upward. This was the result of an increased flow acceleration over the entire upper surface of the semi-span configuration. The flow acceleration was induced largely by the stand-off mounting geometry.
2. On the semi-span configuration, the sidewall boundary layer separated upstream of the model, and rolled up to form a horseshoe vortex in the juncture region

between the sidewall and the model. A significant streamline curvature thus occurred in the near wall region. The inboard portion of the semi-span wing was observed to experience more cross flow. These differences are suggested to be the source of the different stall characteristics observed on a semi-span model compared with a full-span model.

3. The aerodynamic characteristics of the semi-span configuration may be improved by decreasing the stand-off height. A stand-off height equal to twice the tunnel empty sidewall boundary layer displacement thickness was found to best replicate the characteristics of the full-span configuration. However, the smaller stand-off height had little effect on the separation of the sidewall boundary layer.
4. Blowing jets, placed in the sidewall/model juncture region, improved the flow over the aft portion of the semi-span model. The resulting near surface streamline patterns were quite similar to the full-span results. The blowing jets had little adverse effect on the semi-span force and moment coefficients. The blowing jets however, had no influence on the upstream separation of the sidewall boundary layer.
5. Tangential blowing through an upstream slot was found to be effective in minimizing the separation of the sidewall boundary layer. The horseshoe vortex was weakened, and the resulting near surface streamline patterns seen to be similar to the full-span results. The upstream blowing however, adversely affected



the pitching moment coefficient, due to significant flow acceleration over the forward portion of the fuselage.

6. An active segmented sidewall boundary layer suction technique was developed to minimize the separation of the sidewall boundary layer. The suction was concentrated near the semi-span model for maximum effect. The suction concentrated in the nose region weakened the horseshoe vortex. A significantly lower suction rate throughout the remainder of the juncture region improved the flow over the aft portion of the model. The near surface streamline patterns were greatly improved, and found to be quite similar to the full-span results. The active suction had negligible effect on the semi-span force and moment coefficients.

## 7 Recommendations for future work

The following recommendations are made to further develop the semi-span model test technique:

1. Further computational and experimental studies should be conducted to optimize the sidewall boundary layer control techniques. The Reynolds number range examined should cover the range obtainable in the NTF.
2. Wind tunnel testing of the metric stand-off mounting strategy is recommended. The testing should focus on demonstrating the accuracy of the correction strategy over a wide range of conditions.
3. The computational studies should be extended to include high-lift configurations.
4. An efficient computational method should be developed for designing and optimizing semi-span model stand-off geometries. The use of an optimally designed stand-off would remove the need for costly active sidewall boundary layer control techniques.

# References

- [1] Mack, M.D. and McMasters, J.H. , “High Reynolds Number Testing in Support of Transport Airplane Development (Invited Paper),” AIAA Paper 92-3982, July 1992.
- [2] Goldhammer, M.I. and Steinle Jr., F.W. , “Design and Validation of Advanced Transonic Wings Using CFD and Very High Reynolds Number Wind Tunnel Testing,” Proceedings of the 17<sup>th</sup> International Council of the Aeronautical Sciences, Paper 90-2.6.2, Sept. 1990, pp. 1028-1042.
- [3] Squire, L.C., “Interactions Between Wakes and Boundary-Layers,” Progress in Aerospace Sciences, Vol. 26, pp. 261-288, 1989.
- [4] Lynch, F.T., “Experimental Necessities for Subsonic Transport Configuration Development,” AIAA Paper 92-0158, Jan. 1992.
- [5] Boersen, S.J., “Half-Model Testing in NLR High-Speed Wind Tunnel HST, A 1981 Status Report,” NLR TR 82123 U, Aug. 1982.
- [6] Garriz, J.A., Newman, P.A., Vatsa, V.N., Haigler, K.J. and Burdges, K.P., “Evaluation of Transonic Wall Interference Assessment and Corrections for Semi-Span Wing Data,” AIAA Paper 90-1433, June 1990.

- [7] Milholen II, W.E. and Chokani, N., "Effect of Sidewall Boundary Layer on Transonic Flow over a Wing," *Journal of Aircraft*, Vol. 31, July 1994, pp. 986-988.
- [8] Franz, H.P., "The Half-Model Technique in the Wind Tunnel and its Employment in the Development of the Airbus Family," NASA TM-76970, Aug. 1982.
- [9] Earnshaw, P.B., Green, A.R., Hardy, B.C. and Jelly, A.H., "A Study of the Use of Half-Models in High-Lift Wind-Tunnel Testing," AGARD CP515, Oct. 1992, pp. 20.1-20.9.
- [10] Morgan Jr., H.L., "Model Geometry Description and Pressure Distribution Data From Tests of EET High-Lift Research Model Equipped with Full-Span and Part-Span Flaps," NASA TM 80048, Feb. 1979.
- [11] Johnson, W.G., Jr. , Private communication, June 1994.
- [12] Adcock, J.B., Private communication, June 1993.
- [13] Wedan, B.W., Private communication, June 1990.
- [14] Steinbrenner, J.P. and Chawner, J.R., "Incorporation of a Hierarchical Grid Component Structure into GRIDGEN," AIAA Paper 93-0429, Jan. 1993.
- [15] Anderson, D.A, Tannehill, J.C. and Pletcher, R.H., "Computational Fluid Mechanics and Heat Transfer," Hemisphere Publishing Corporation, New York, 1984.
- [16] Volpe, G., "Performance of Compressible Flow Codes at Low Mach Numbers," AIAA Journal, Vol. 31, Jan. 1993, pp. 49-56.

- [17] Choi, Y.H. and Merkle, C.L., "The Application of Preconditioning in Viscous Flows," *Journal of Computational Physics*, Vol. 105, pp. 207-223, 1993.
- [18] Pletcher, R.H. and Chen, K.H., "On Solving The Compressible Navier-Stokes Equations for Unsteady Flows at Very Low Mach Numbers," *AIAA Paper 93-3368-CP*, July 1993.
- [19] Vatsa, V.N., Sanetrik, M.D., and Parlette, E.B., "Development of a Flexible and Efficient Multigrid-Based Multiblock Flow Solver," *AIAA Paper 93-0677*, Jan. 1993.
- [20] Thomas, J.L., Taylor, S.L. and Anderson, W.K., "Navier-Stokes Computations of Vortical Flows Over Low Aspect Ratio Wings," *AIAA Paper 87-0207*, Jan. 1987.
- [21] Rogers, S.E., Kwak, D., and Kiris, C., "Numerical Solution of the Incompressible Navier-Stokes Equations for Steady-State and Time-Dependent Problems," *AIAA Journal*, Vol. 29, April 1991, pp. 603-610.
- [22] Applin, Z.T., "Pressure Distributions from Subsonic Tests of a NACA 0012 Semispan Wing Model," *NASA TM 110148*, Feb. 1995.
- [23] Spalart, P.R. and Allmaras, S.R., "A One-Equation Turbulence Model for Aerodynamic Flows," *AIAA Paper 92-0439*, Jan. 1992.

- [24] Milholen, W.E., II and Chokani, N., "A Comparison of Three-Dimensional Compressible Navier-Stokes Codes at Low Mach Numbers," AIAA Paper 95-0767, Jan. 1995.
- [25] Menter, F., "Performance of Popular Turbulence Models for Adverse Pressure Gradient Flows," AIAA Paper 91-1783, June 1991.
- [26] Degani, D. and Schiff, L.B., "Computation of Supersonic Viscous Flows Around Pointed Bodies at Large Incidence," AIAA Paper 83-0034, Jan. 1983.
- [27] White, F.M., "*Viscous Fluid Flow*," 1st ed., McGraw-Hill, New York, 1974.
- [28] Paschal, K., Goodman, W., McGhee, R., Walker, B., and Wilcox, P.A., "Evaluation of Tunnel Sidewall Boundary-Layer-Control Systems for High-Lift Airfoil Testing," AIAA Paper 91-3243, Sept. 1991.
- [29] Philips, D.B, Cimbala, J.M., and Treaster, A.L., "Suppression of the Wing-Body Junction Vortex by Body Surface Suction," *Journal of Aircraft*, Vol. 29, Jan. 1992, pp. 118-122.
- [30] Gatlin, G.M. and McGhee, R.J., "Private communication", Oct. 1995.

## **Appendices**

# A Metric stand-off Mounting Technique

The present semi-span model test methodology in the NTF incorporates the use of a non-metric stand-off geometry. A clearance gap is required between the metric semi-span model and non-metric stand-off to avoid mechanical fouling, and corruption of the data . The gap however, must be properly sealed, to avoid altering the flow over the semi-span model. Sealing such a gap is a formidable task. The recent NTF wind tunnel test experiences [11] illustrate that inadequate seal concepts are a source of frequent disruption, and hamper the ability to maintain a productive test schedule. The use of a metric stand-off configuration was thus examined using the computational results presented in Chapter 5.

The primary advantages of a metric stand-off configuration are shown in Figure 129, where a non-metric stand-off configuration is compared to a metric configuration. In the non-metric approach, a labyrinth type flow blocker is used in an attempt to seal the gap. Such an approach does not provide a complete seal, and internal flows have been documented [5]. The internal flows are quite problematic, because they introduce *unknown* pressure and viscous forces on the metric portion of the model. In addition, the possibility of mechanical fouling increases due to the small size and complex shape of the flow blocker. In contrast, the gap required in the metric configuration is relatively simple. This simpler gap is easier to manufacture,



and less susceptible to mechanical fouling. A second advantage of the gap in the metric configuration is that it is located in a lower momentum portion of the sidewall boundary layer. This gap is thus less susceptible to internal flows in comparison to the gap in the non-metric configuration. The metric stand-off approach ultimately improves both data quality and tunnel productivity.

The use of a metric stand-off does have one disadvantage. The measured forces and moments now include the forces and moments of the stand-off. For example, the measured normal force coefficient can be written as:

$$(C_N)_{\text{measured}} = (C_N)_{\text{model}} + (C_N)_{\text{stand-off}} \quad (\text{A.1})$$

The force and moment data must thus be corrected to remove the unwanted stand-off contribution. The computational results presented in Chapter 5 were analyzed to develop a simple, yet accurate, engineering method to correct the measured experimental data for the unwanted stand-off contribution.

An analysis of the computational results showed that for an engineering approach, the forces and moments on the stand-off are due largely to the pressure forces, and that the viscous contributions may be neglected. Thus, the normal force contribution of the stand-off can be approximated from the integrated pressure distribution:

$$(C_N)_{\text{stand-off}} \approx (C_N)_p = \frac{1}{S} \int_0^h \int_0^L C_p n_y dx dz \quad (\text{A.2})$$

The pitching moment and axial force contributions of the stand-off can be similarly approximated.

Equation A.1 can then be rewritten as:

$$(C_N)_{\text{model}} = (C_N)_{\text{measured}} - (C_N)_{\text{stand-off}} \quad (\text{A.3})$$

The corrected axial force, normal force, and pitching moment coefficients are then obtained as:

$$(C_A)_{\text{model}} \approx (C_A)_{\text{measured}} - (C_A)_p \quad (\text{A.4})$$

$$(C_N)_{\text{model}} \approx (C_N)_{\text{measured}} - (C_N)_p \quad (\text{A.5})$$

$$(C_M)_{\text{model}} \approx (C_M)_{\text{measured}} - (C_M)_p \quad (\text{A.6})$$

The accuracy of the corrected coefficients was then examined by comparing their predictions with the results of a Navier-Stokes computation with a metric stand-off. It should be noted that the computation included the contributions of the viscous forces in the calculation of the aerodynamic coefficients. Figure 130 compares the results of the non-metric computations with the metric computations with and without corrections. The metric lift and pitching moment coefficients are seen to be quite different without correction. On the otherhand, the present engineering correction method yields coefficients which are identical within plotting accuracy to the original non-metric results. This result also confirms that the viscous contributions have little effect on the engineering accuracy of the correction method.

The spanwise pressure distribution of all 2-D stand-off geometries were examined. A typical distribution is that shown in Figure 131 for the  $2\delta^*$  stand-off. Here the pressure distribution at the root (tunnel sidewall) and tip (fuselage centerline) are

compared. The pressure distributions are nearly identical, which indicates that the spanwise loading across the stand-off is essentially constant. The same observation was also made in the NTF wind tunnel experiments [11]. This result suggests that only a single chordwise row of pressure taps at the mid-span of the stand-off would be sufficient to provide a representative pressure distribution needed for evaluating equation A.2. This is further evidence that the proposed engineering correction method may be easily implemented.

A study was conducted to determine the number and location of the pressure taps required to resolve the stand-off pressure distribution. Figure 132 demonstrates that 100 pressure taps would adequately resolve the pressure distribution. The computational results were obtained with 209 total grid points. The integrated respective force and moment coefficients were found to differ only in the fourth decimal place. Table 1 lists the proposed  $X/L$  locations for the pressure taps. For a high-lift configuration, a finer distribution in the vicinity of the wing would be required. The cost of equipping the stand-off with these pressure taps is insignificant in comparison to an estimated cost of \$20,000 in lost nitrogen required to access the model only *once* during cryogenic operating mode [12].

It is suggested that the use of a metric stand-off and the proposed engineering correction method will yield improved data quality, and substantially increased testing productivity.

## B Tangential Blowing Simulation

The simulation of the tangential blowing using TLNS3D-MB is discussed in this appendix. Figure 133 presents a comparison of actual and simulated tangential blowing jets. For the numerical simulation, two simplifying approximations are made. First, the geometry of the blowing jet is neglected, since major grid modifications would otherwise be required. Second, the exit properties of the blowing jet are assumed to be constant across the jet height. For the small jet dimensions considered here, both approximations are valid.

The blowing jet at a prescribed location was then modeled as follows. The desired jet location was selected to coincide with a grid block boundary as shown in Figure 133b. Next, the grid block boundary was segmented into two parts; the first segment being the portion at the jet exit, and the second segment being that exterior to the jet. For the grid block upstream of the block boundary, both segments are treated in a straight forward manner. The first segment is treated as an out-flow boundary, while the second segment is treated using continuous flow boundary conditions. The second segment on the downstream block is also treated using a continuous flow boundary condition. However, the first segment on the downstream block is treated as an inflow boundary with a specified jet Mach number, stagnation pressure, stagnation temperature, and flow angle. The flow through the blowing jets

was assumed to be isentropic:

$$\frac{T_{oj}}{T_j} = 1 + \frac{\gamma - 1}{2} M_j^2 \quad (\text{B.1})$$

$$\frac{P_{oj}}{P_j} = \left( \frac{T_{oj}}{T_j} \right)^{\frac{\gamma}{\gamma-1}} \quad (\text{B.2})$$

The flow conditions considered ( $M_\infty = 0.20$ ,  $\text{Re} = 4.20 \times 10^6$ ) were for air mode in the NTF, with a freestream stagnation pressure of 5 atmospheres, and a freestream stagnation temperature of 110° F. The jet stagnation temperature was assumed to be constant at 70° F.

For the blowing jets and slots, the exit Mach numbers of 0.50 and 1.0 required stagnation supply pressures of 85 psi and 135 psi respectively. These pressures yielded mass flow rates for the blowing jets of 0.0023 slugs/second and 0.0049 slugs/second respectively, with the corresponding blowing coefficients of  $C_\mu = 0.002$  and 0.008. For the blowing slots the mass flow rates (and blowing coefficient) were 0.2944 slugs/second ( $C_\mu = 0.257$ ) and 0.6287 slugs/second ( $C_\mu = 1.027$ ) respectively. The availability of a high pressure air supply source in the NTF [11] indicates that these mass flow rates are achievable in practice.

## C Active Suction Simulation

The modifications to the TLNS3D-MB code to simulate the sidewall suction are described in this appendix. Figure 134 shows a partial view of a two-dimensional grid adjacent to a simulated porous surface. The suction over a surface is simulated by specifying a constant normal velocity,  $U_w$ , at the porous surface. Since TLNS3D-MB is a finite volume code, the flow quantities are specified and computed at cell centers. Thus it is necessary to modify the ghost cell values to properly simulate the flow through the porous surface.

The normal wall velocity is determined from the specified surface transpiration coefficient:

$$C_q = \frac{(\rho U)_w}{(\rho U)_\infty} \quad (\text{C.1})$$

where negative  $U_w$  denotes suction, and positive  $U_w$  denotes injection. The imposed normal wall velocity is obtained by rearranging equation C.1 to obtain:

$$U_w = \frac{C_q(\rho U)_\infty}{\rho_w} \quad (\text{C.2})$$

The density at the wall is set equal to the density at the first interior cell,  $j=2$ . The Cartesian velocity components are determined as:

$$u_w = U_w n_x \quad (\text{C.3})$$

$$v_w = U_w n_y \quad (\text{C.4})$$

where  $n_x$  and  $n_y$  are the Cartesian components of the normal vector  $n$ . Lastly, the

pressure at the surface is also set equal to that of the first interior cell. The ghost cell values are then related to the simulated porous surface values by the following expression:

$$\phi_w = \frac{1}{2}(\phi_{j=1} + \phi_{j=2}) \quad (\text{C.5})$$

where  $\phi$  represents any primitive flow variable. Equation C.5 is rearranged to obtain the ghost cell values:

$$\rho_{j=1} = \rho_{j=2} \quad (\text{C.6})$$

$$u_{j=1} = 2u_w - u_{j=2} \quad (\text{C.7})$$

$$v_{j=1} = 2v_w - v_{j=2} \quad (\text{C.8})$$

$$p_{j=1} = p_{j=2} \quad (\text{C.9})$$

The laminar flow over a porous flat plate with suction was computed to verify the correct implementation of the above approach. The results are compared to the analytic solution for incompressible laminar flow past an infinite flat plate with suction. The exact solution for the velocity profile can be written as [27]:

$$\frac{u}{U_\infty} = 1 - e^{\eta C_q (Re/\ell)} \quad (C_q < 0) \quad (\text{C.10})$$

where  $\eta$  is the coordinate normal to the plate, and  $Re/\ell$  is the unit Reynolds number of the flow. The exact solution is only valid asymptotically far downstream of the plate leading edge, at a distance given by [27]:

$$x \approx \frac{4.0}{C_q^2 (Re/\ell)} \quad (\text{C.11})$$

The following freestream conditions were used:  $M_\infty = 0.20$ ,  $Re/\ell = 0.1 \times 10^6$ . A unit length flat plate was examined, with grid dimensions of  $129 \times 33$ . Figure 135 compares the computed and Blasius [27] velocity profiles at the midpoint of the plate for zero suction. The agreement is excellent, and indicates sufficient grid resolution. For the given plate length and flow conditions, equation C.11 indicates that an asymptotic behavior would be expected at  $x \approx 0.4$  with  $C_q = -.01$ . Figure 136 compares the predicted velocity profile at the midpoint of the plate to the asymptotic solution given by equation C.10. The agreement is excellent, and provides validation of the implementation of the numerical boundary conditions. In addition, the convergence characteristics of the code were not affected by the suction boundary condition.

To further examine the performance of the suction boundary condition, turbulent two-dimensional flow over a backward facing sinusoidal ramp was examined. The freestream conditions considered were:  $M_\infty = 0.20$ ,  $Re/\ell = 2.0 \times 10^6$ . The one-equation Spalart-Allmaras turbulence model was employed. Figure 137 shows a partial view of the grid, with the leading edge of the forward flat plate at  $x = 0.00$ . The grid dimensions were  $145 \times 65$ . Figure 138 shows the effect of suction, applied *only* to the sinusoidal region. With no suction,  $C_q = 0.00$ , significant flow separation is predicted. With the addition of suction,  $C_q = -.005$ , the extent of separation decreases dramatically. Increasing the suction rate further,  $C_q = -.010$ , results in a wholly attached flow field. As with the laminar flow computations, the suction boundary condition did not introduce any numerical difficulties.



## Tables

Table 1: Metric stand-off pressure tap locations

tap number	X/L	tap number	X/L
1	0.00000	26	0.49245
2	0.00027	27	0.51337
3	0.00134	28	0.53195
4	0.00403	29	0.54820
5	0.00877	30	0.56220
6	0.01516	31	0.57405
7	0.02244	32	0.58388
8	0.03058	33	0.59186
9	0.04220	34	0.59816
10	0.05721	35	0.60293
11	0.07519	36	0.60634
12	0.09565	37	0.60859
13	0.11851	38	0.61321
14	0.14375	39	0.62921
15	0.17109	40	0.66074
16	0.20015	41	0.70894
17	0.23057	42	0.76976
18	0.26194	43	0.83390
19	0.29378	44	0.89094
20	0.32562	45	0.93440
21	0.35699	46	0.96311
22	0.38741	47	0.97963
23	0.41648	48	0.98834
24	0.44385	49	0.99500
25	0.46924	50	1.00000

## Figures

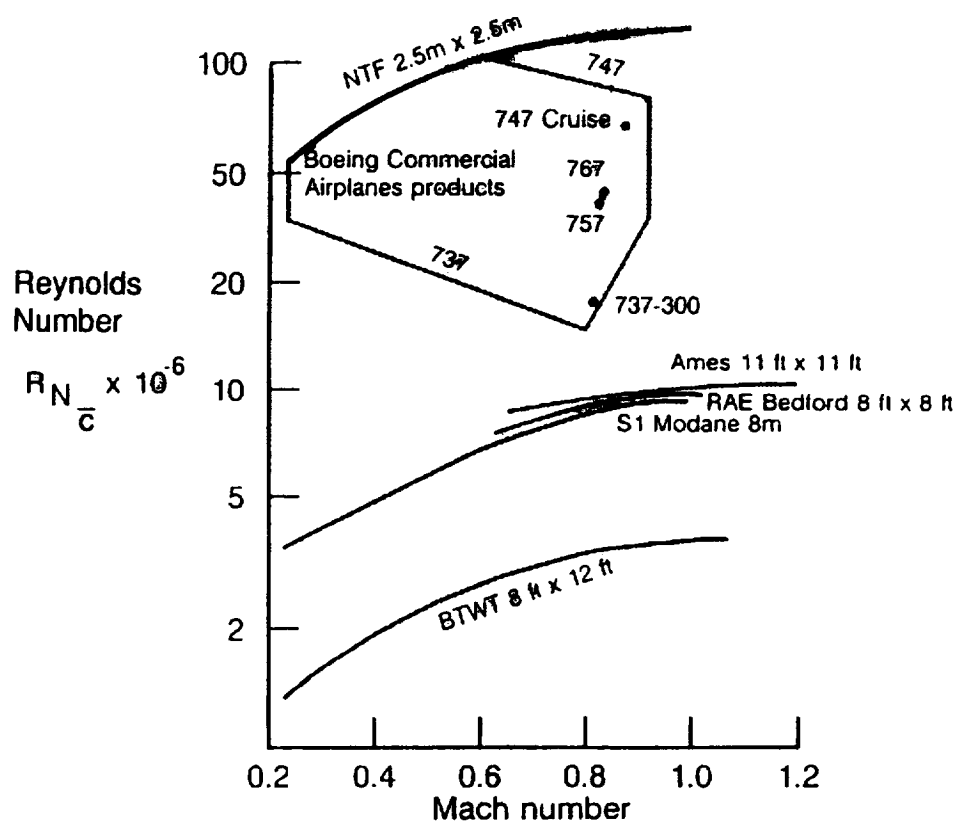


**Figure 1:** Operating envelopes of several transonic wind tunnels (Reference [1]).

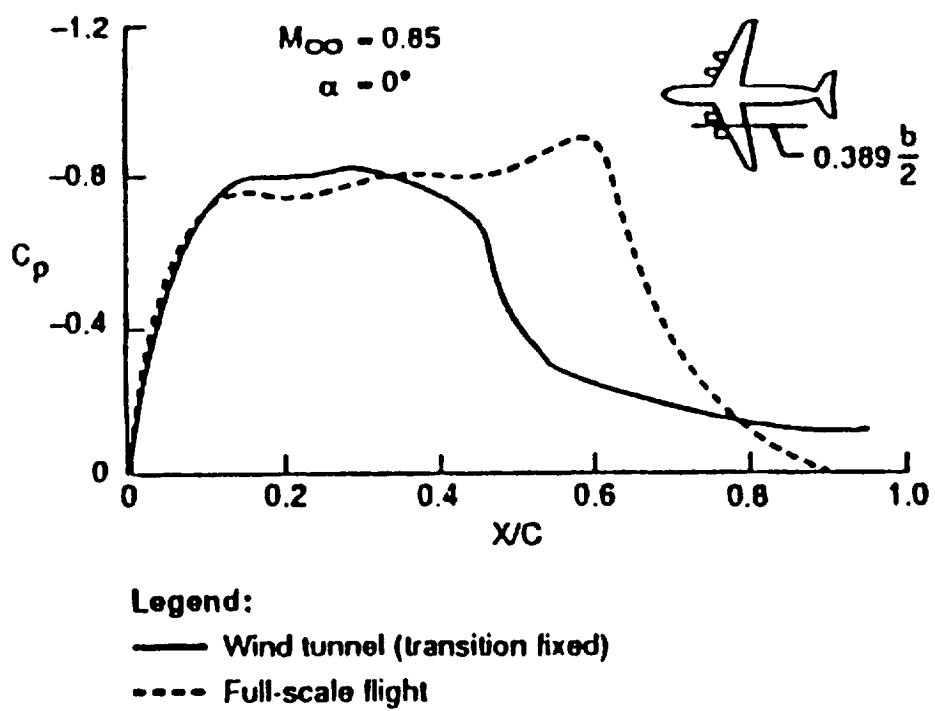


**Figure 2:** Comparison of wind tunnel and flight data (Reference [2]).

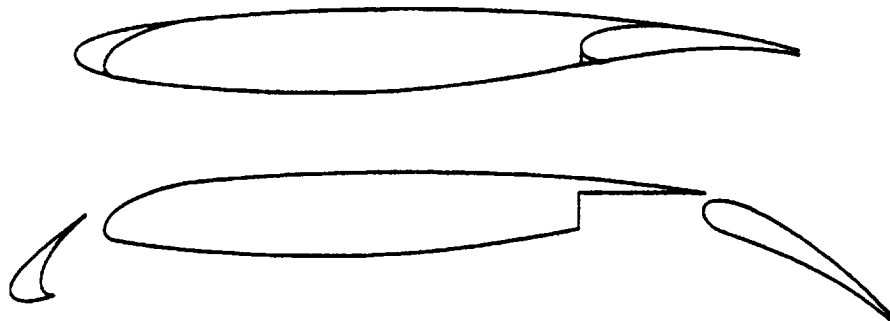


**Figure 3:** Comparison of cruise and high-lift configurations.

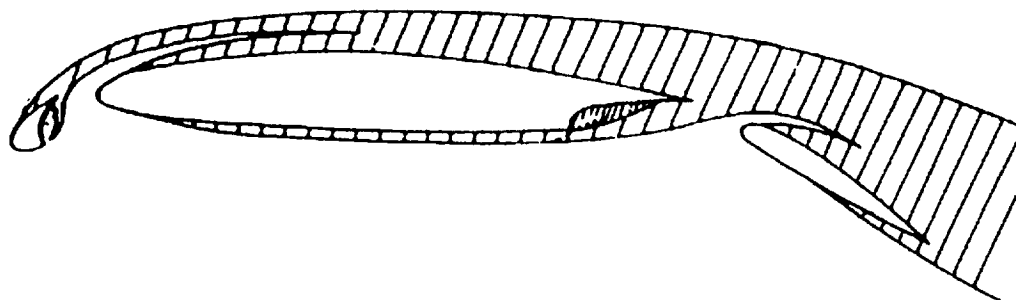


**Figure 4:** High-lift flow physics (Reference [3]).

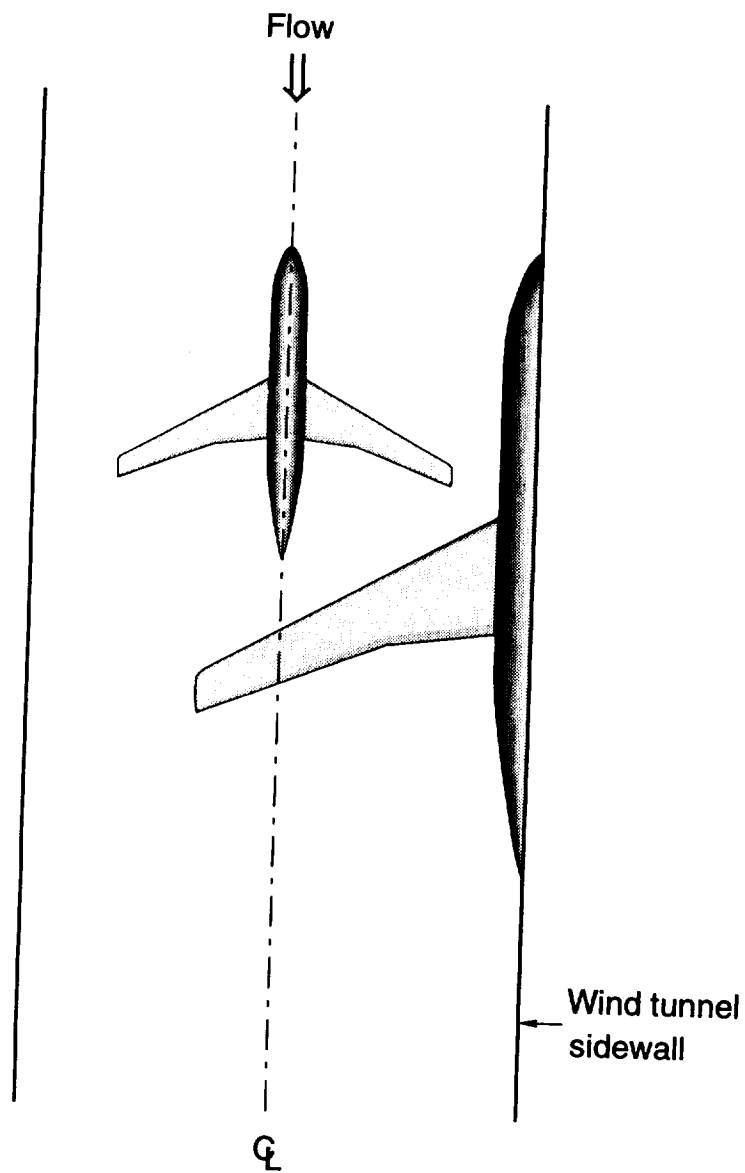
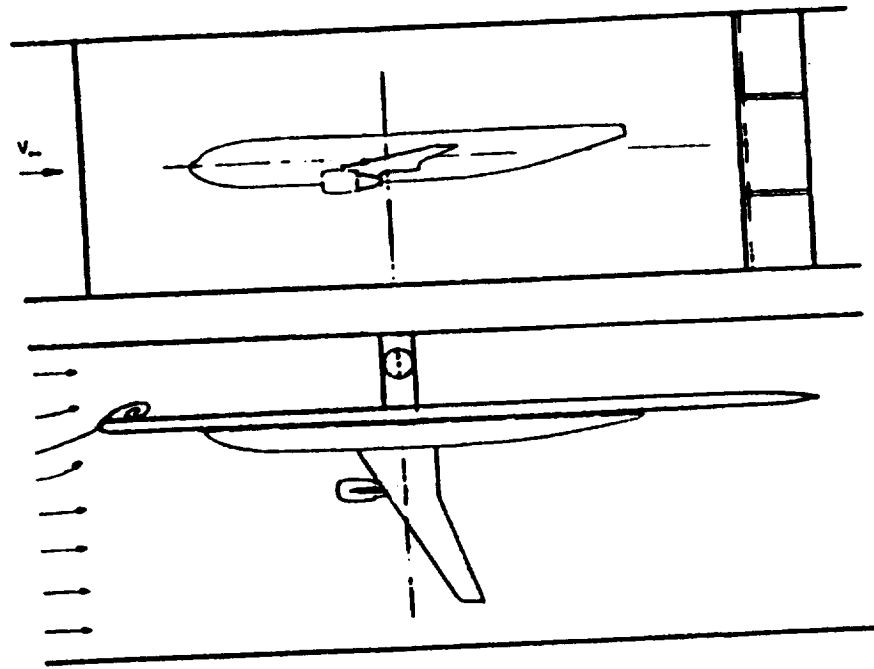
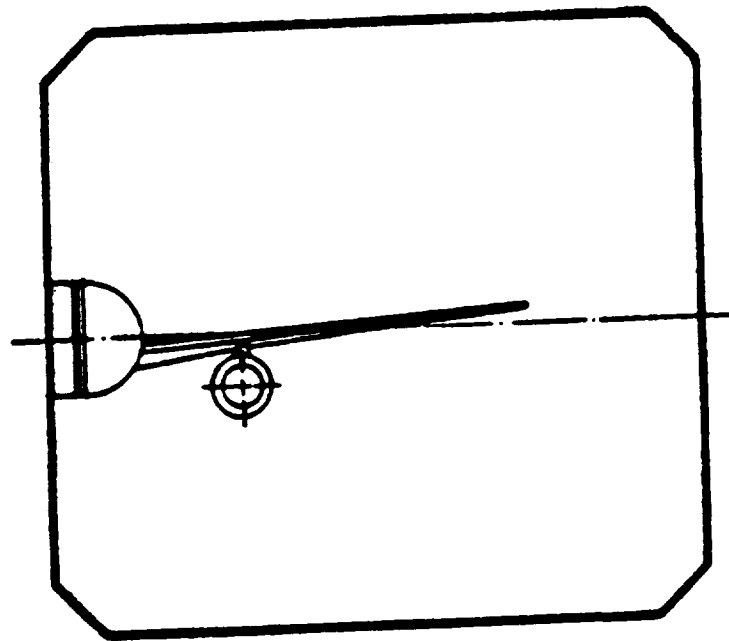


**Figure 5:** Comparison of full-span and semi-span models.



a) splitter plate mounting



b) sidewall mounting

**Figure 6:** Comparison of semi-span model mounting strategies (Reference [8]).



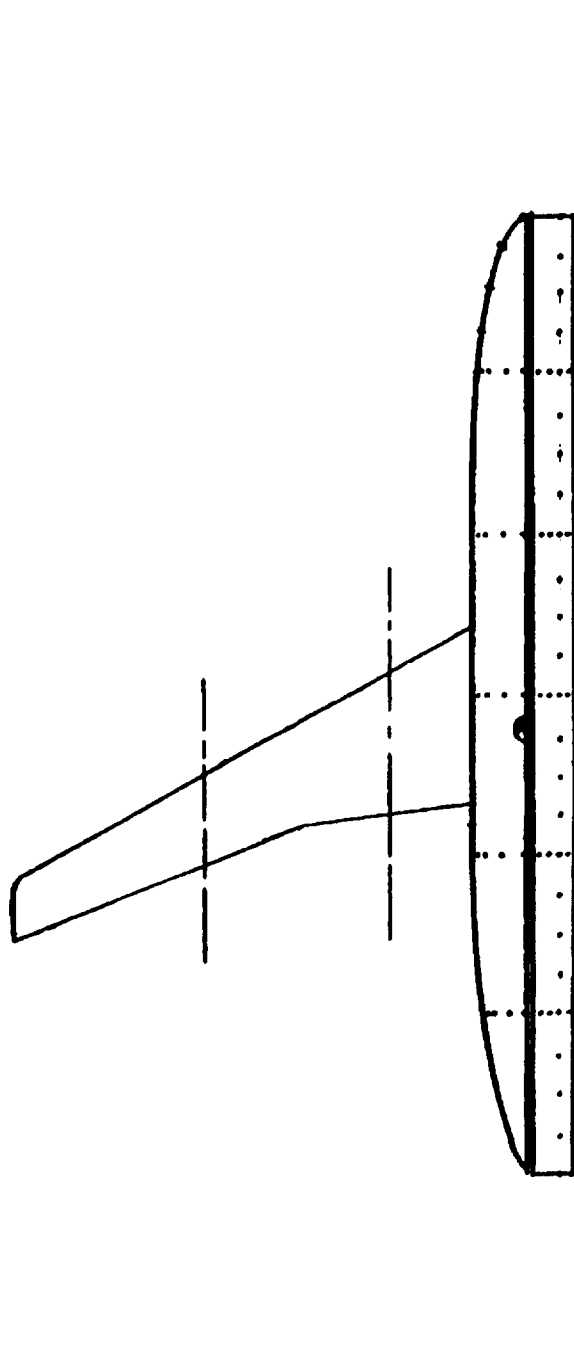
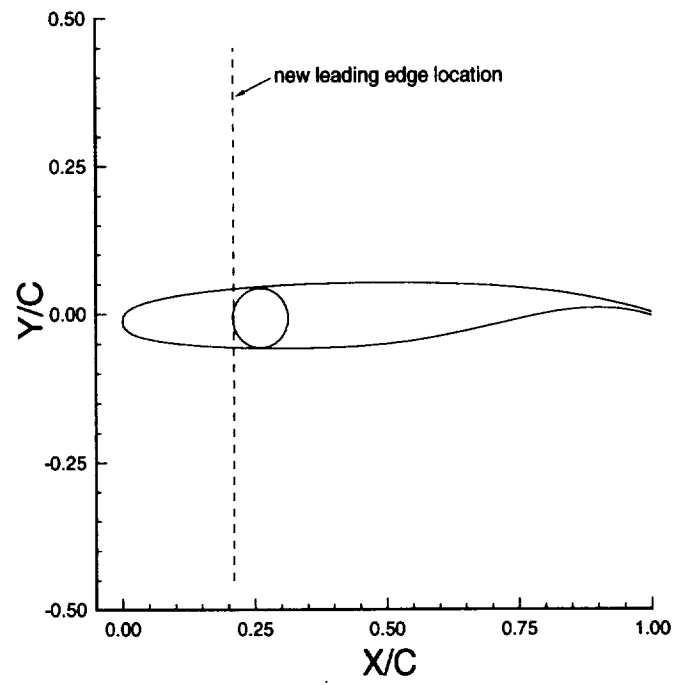
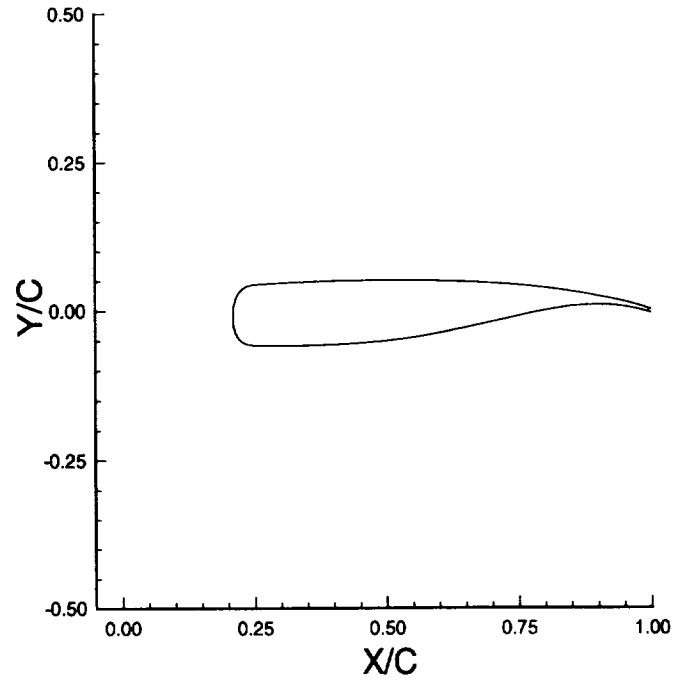


**Figure 7:** Planform view of semi-span model with stand-off geometry.

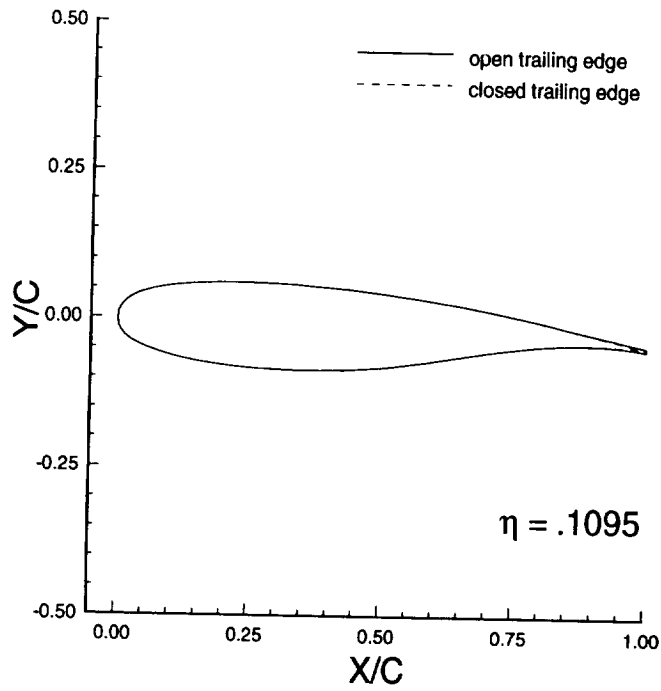


a) location of new leading edge

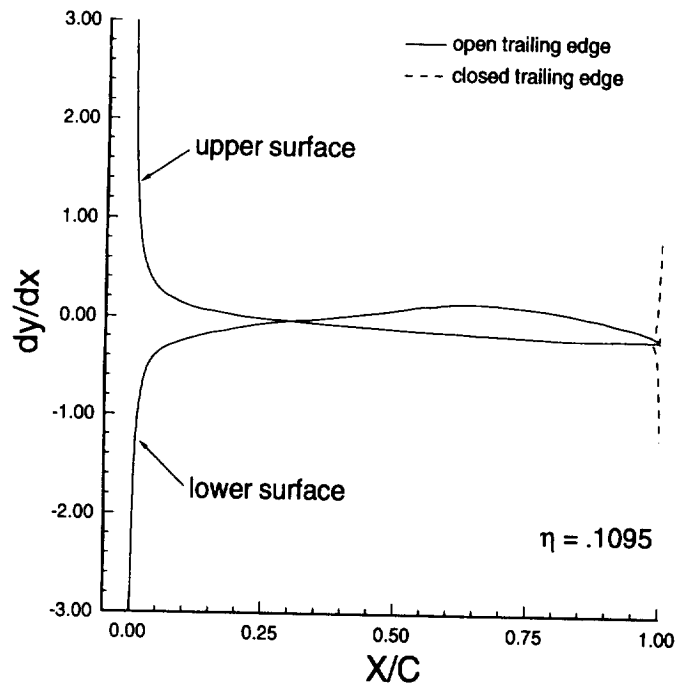


b) new tip airfoil

**Figure 8:** Construction of new tip airfoil.



a) airfoil geometry comparison



b) airfoil slope comparison

**Figure 9:** Influence of trailing edge closure on root airfoil.

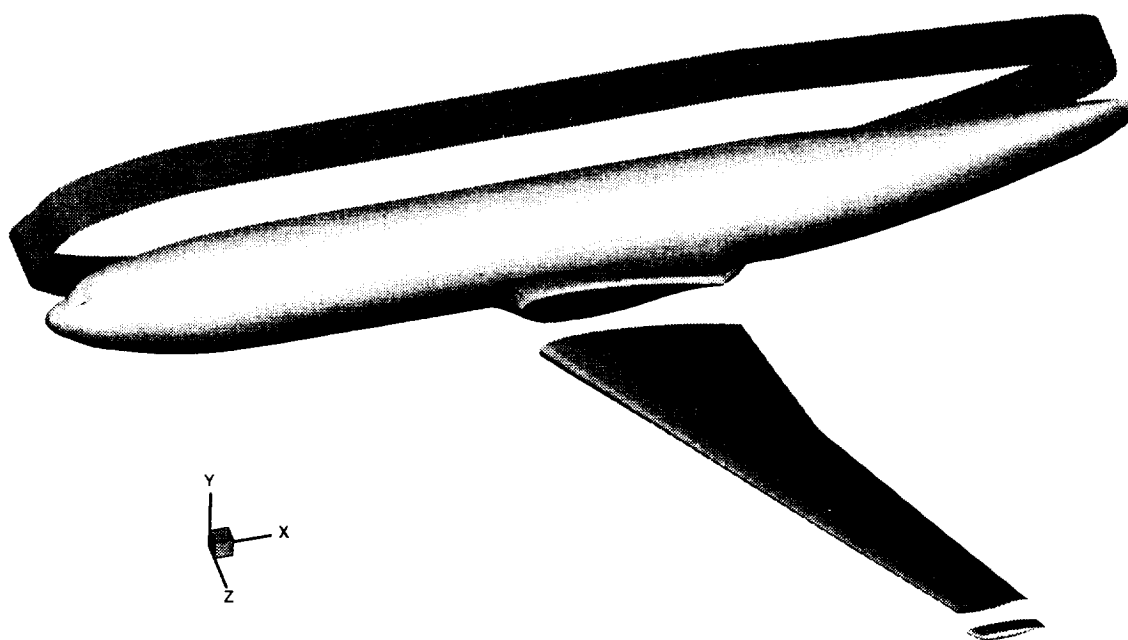


**Figure 10:** Oblique view of surface geometry.

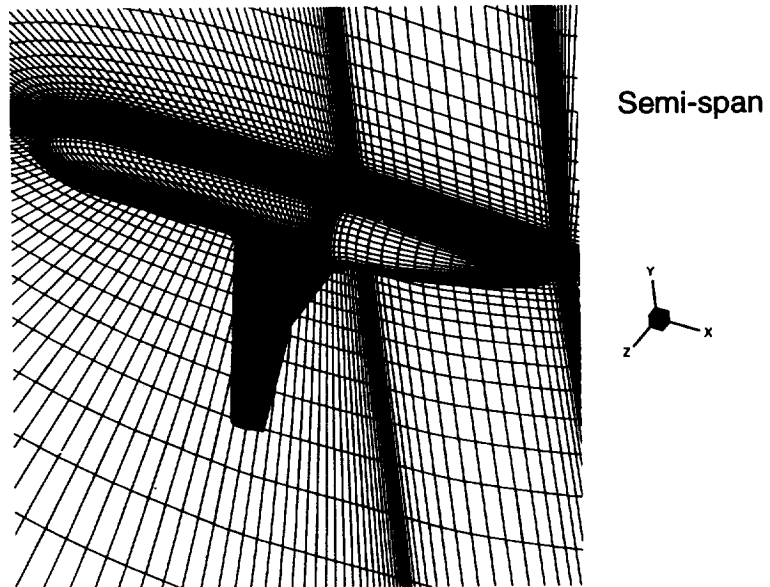
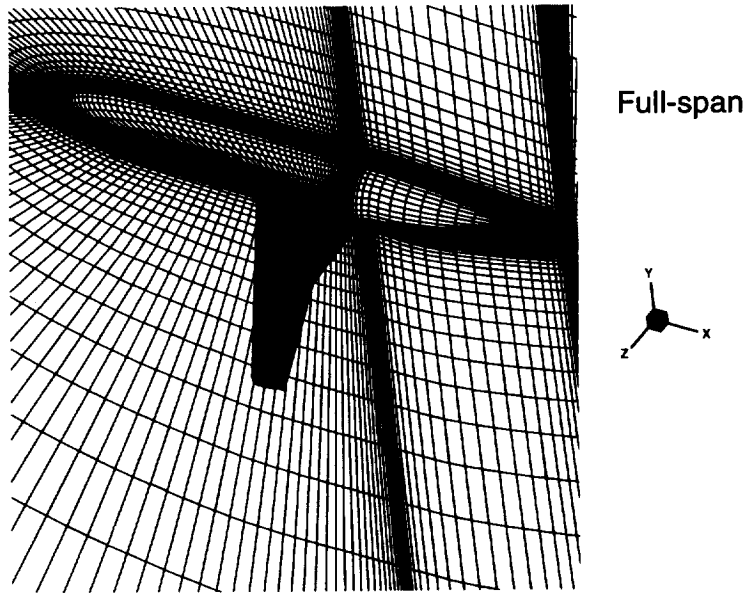


**Figure 11:** Partial view of C-O grid topologies.

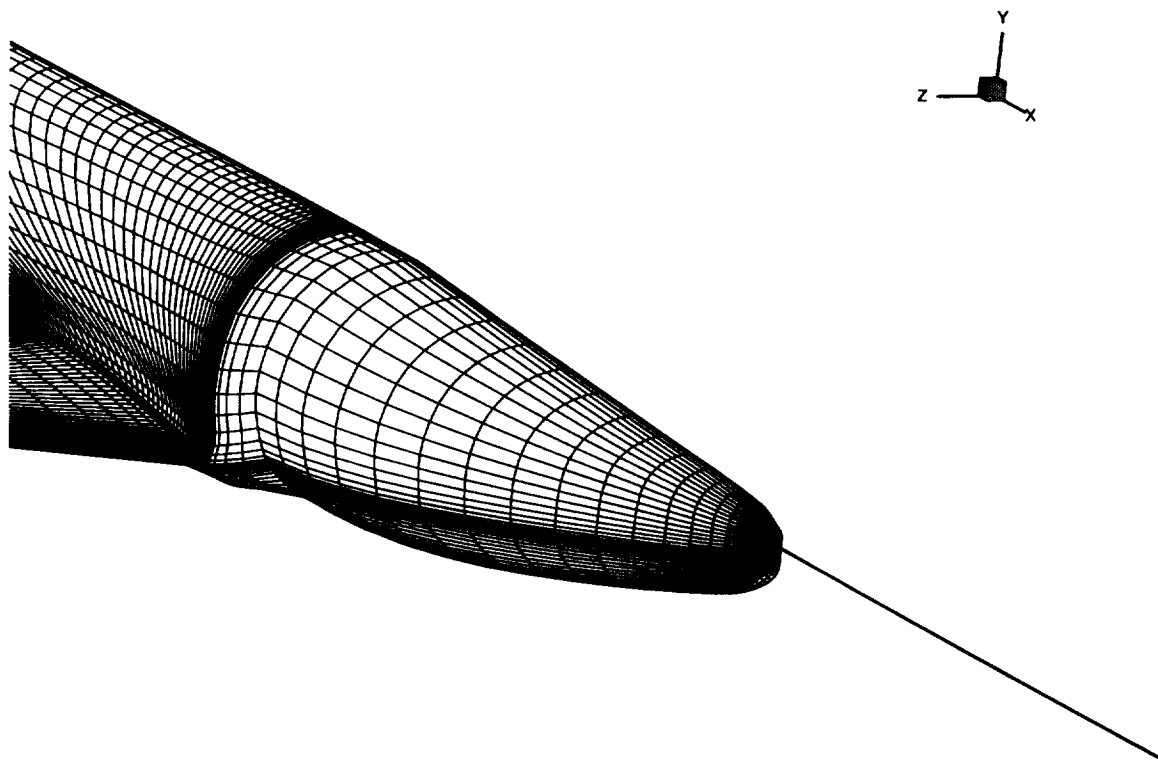
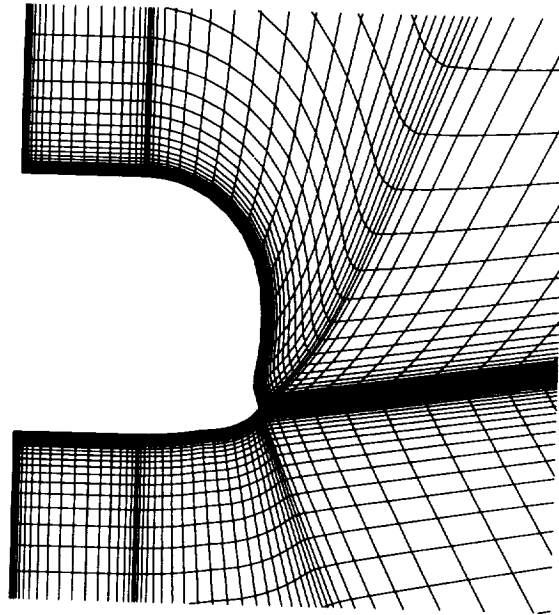
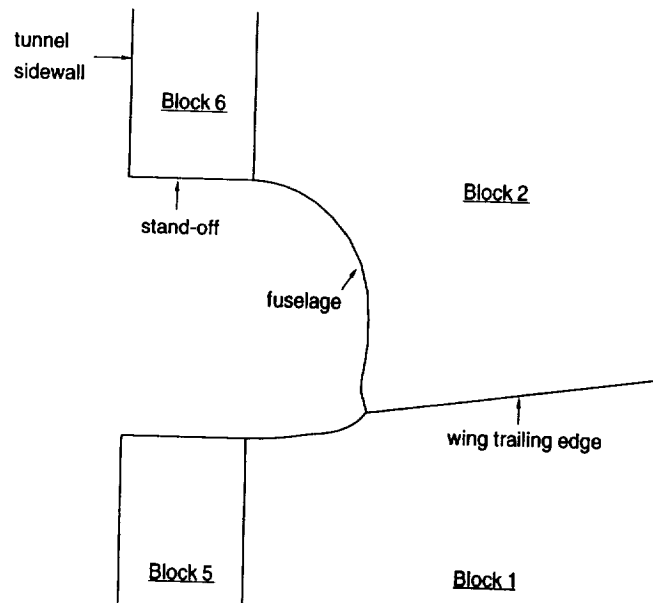


**Figure 12:** Aft fuselage surface grid with sting.



a) grid



b) block boundaries

**Figure 13:** Spanwise slice through semi-span grid at wing trailing edge, looking downstream.

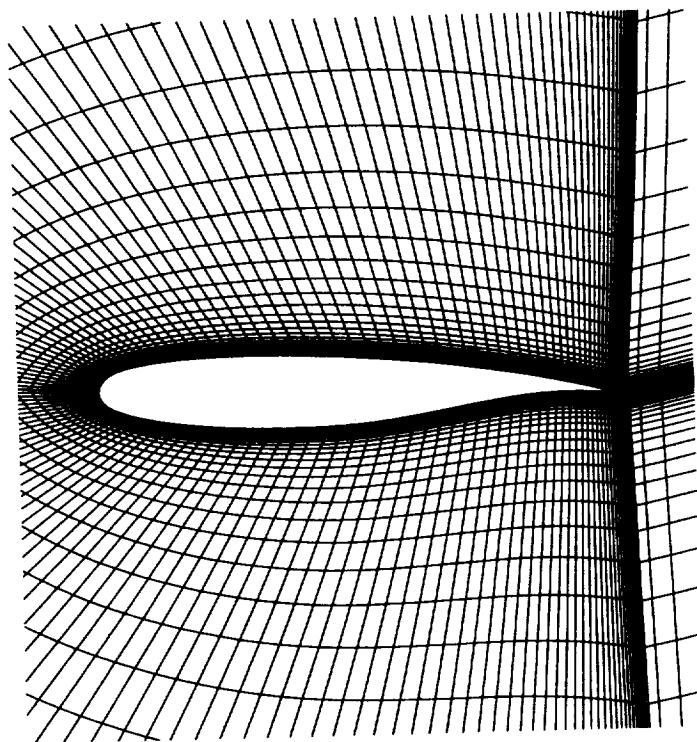


**Figure 14:** Streamwise slice through wing grid,  $\eta = .2665$ .



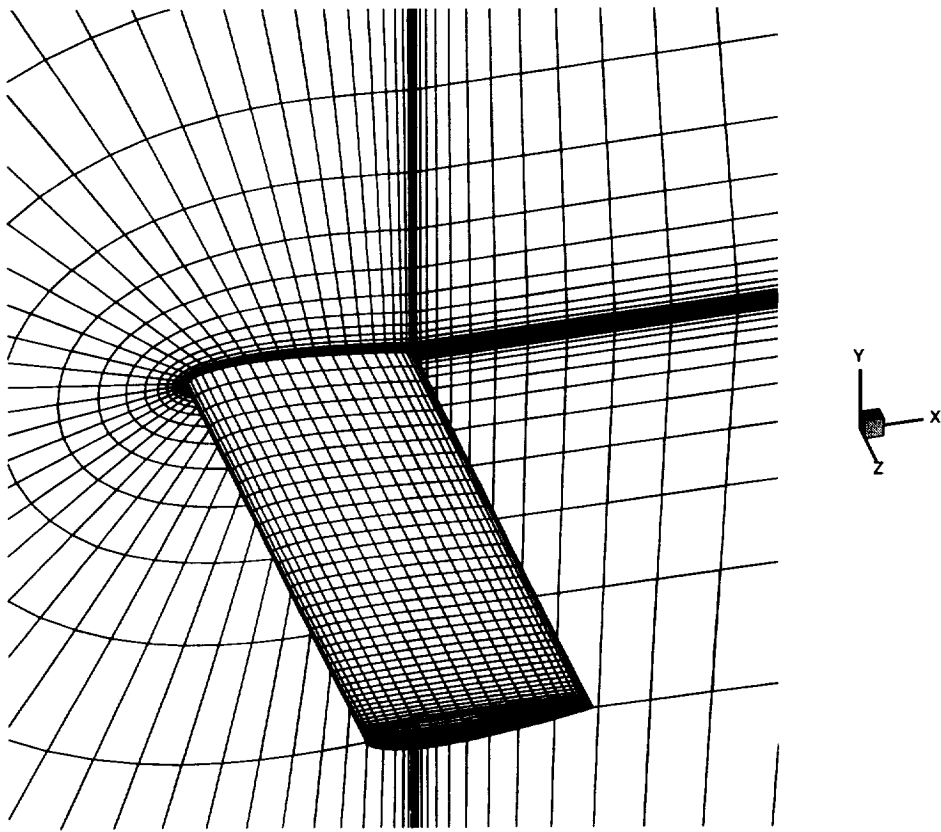


**Figure 15:** Partial view of rectangular wing C-O grid.

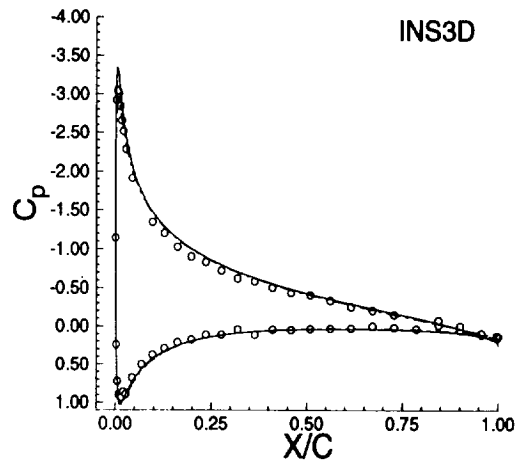
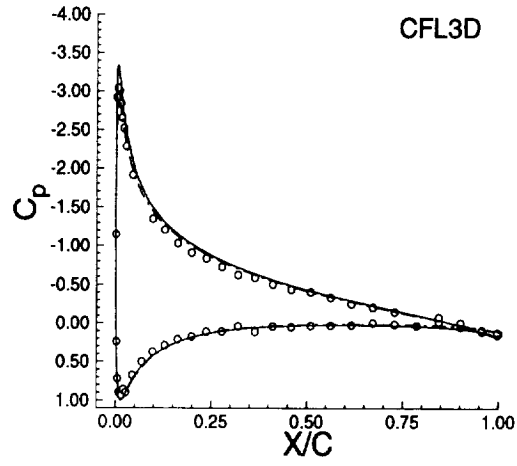
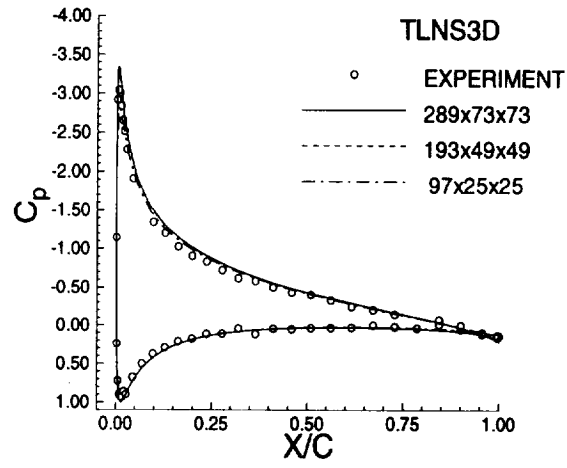
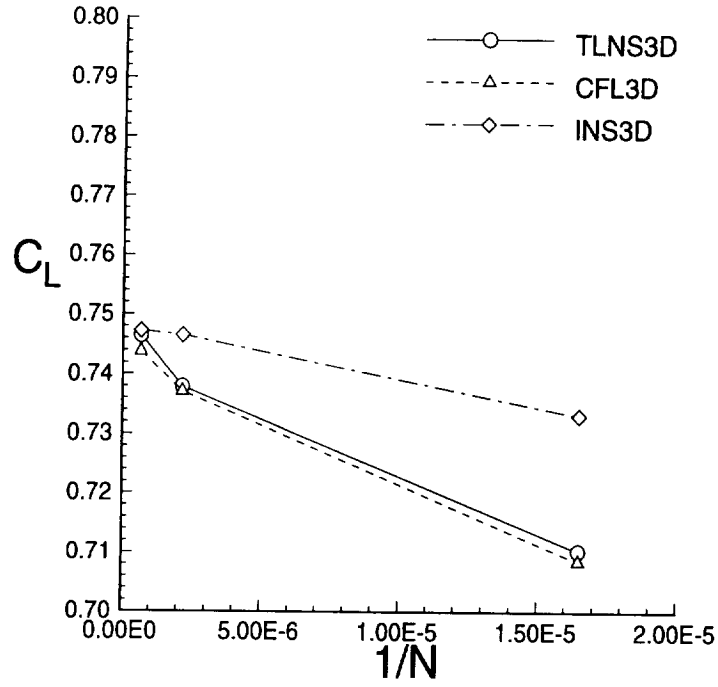
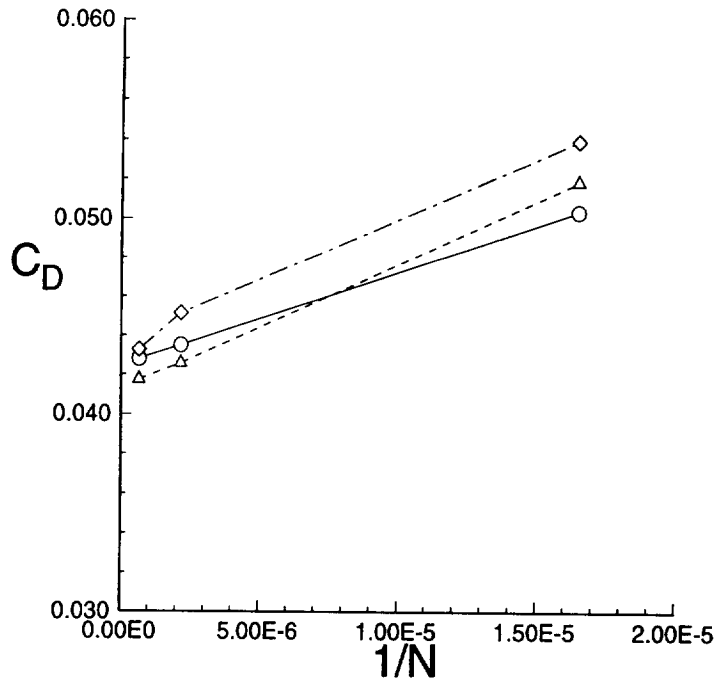


**Figure 16:** Influence of grid refinement on pressure distribution,  $\eta = 0.6084$  ( $M_\infty = 0.14$ ,  $\alpha = 10.01^\circ$ ,  $Re = 3.17 \times 10^6$ ).



a) lift coefficient



a) drag coefficient

**Figure 17:** Influence of grid refinement on lift and drag coefficients ( $M_\infty = 0.14$ ,  $\alpha = 10.01^\circ$ ,  $Re = 3.17 \times 10^6$ ).

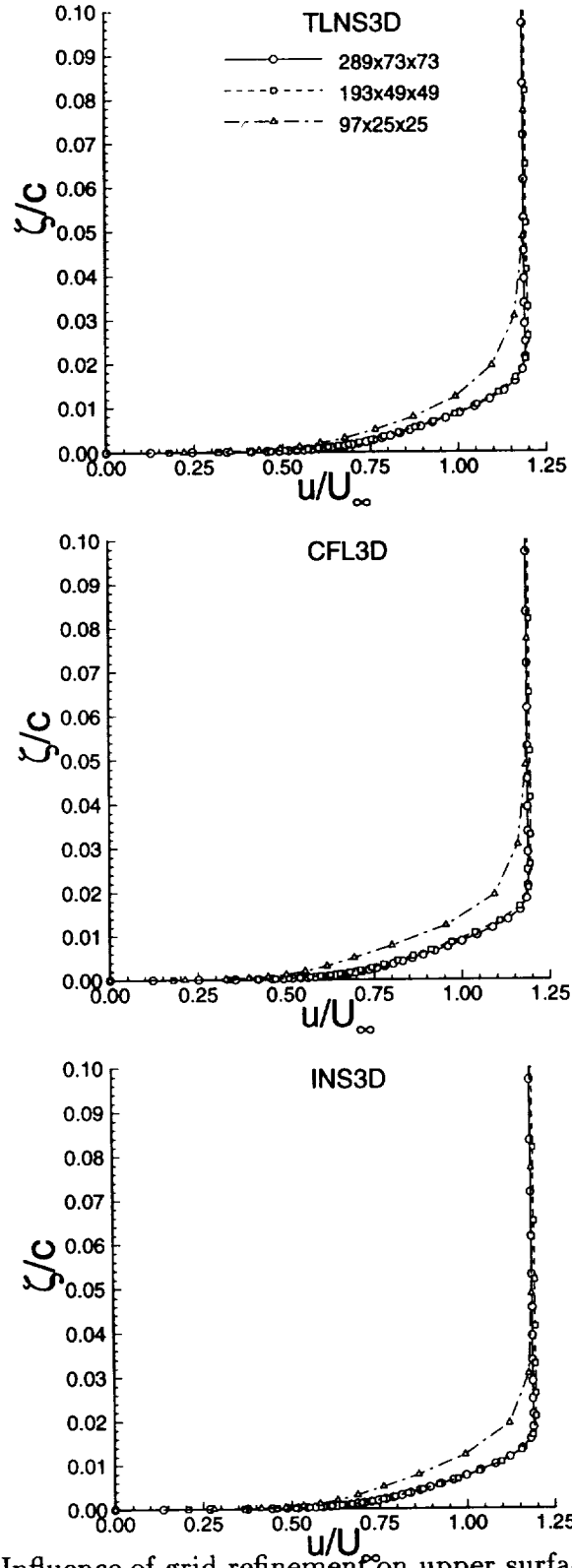


**Figure 18:** Influence of grid refinement on upper surface streamwise velocity profile at  $x/c = 0.50$ ,  $\eta = 0.6084$  ( $M_\infty = 0.14$ ,  $\alpha = 10.01^\circ$ ,  $Re = 3.17 \times 10^6$ ).

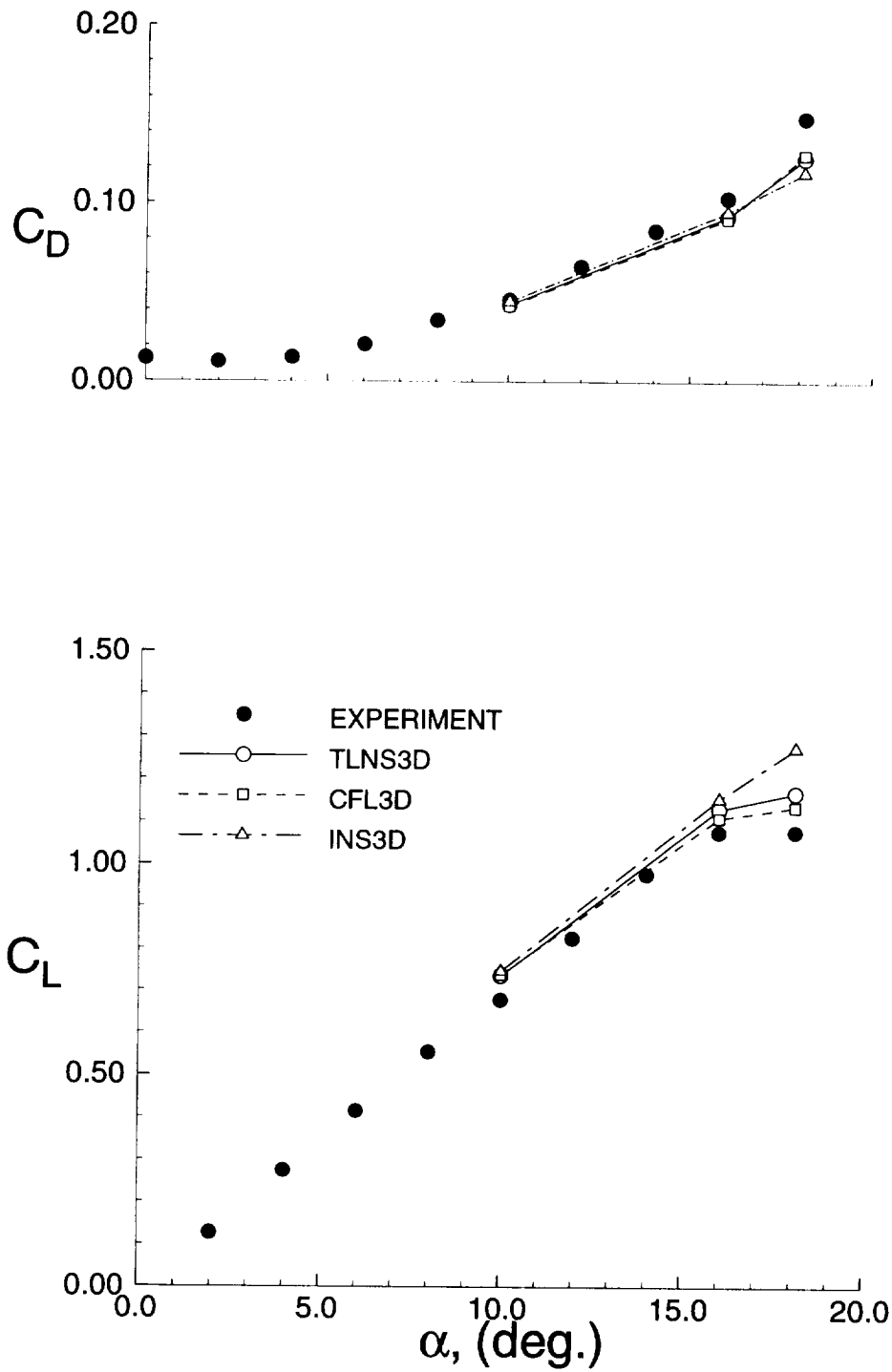


**Figure 19:** Comparison of predicted lift and drag coefficients to experimental data ( $M_\infty = 0.14$ ,  $Re = 3.17 \times 10^6$ ).

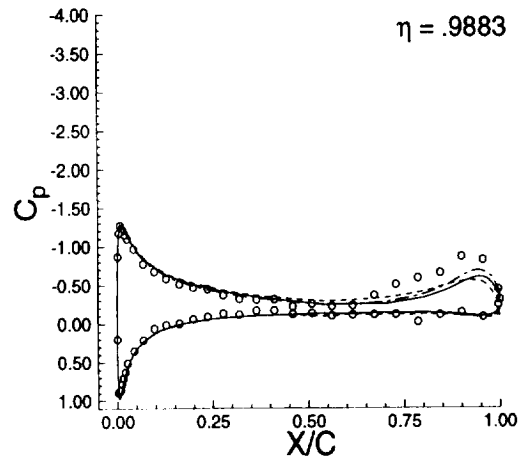
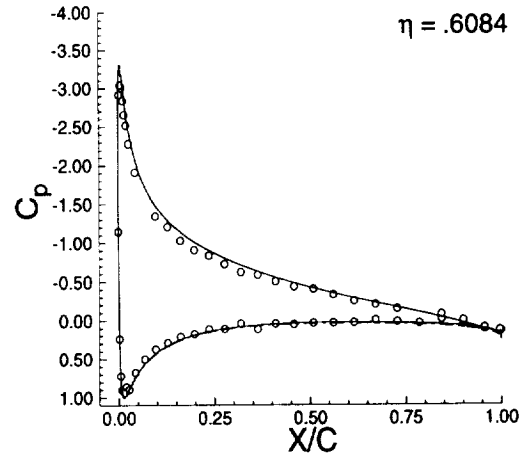
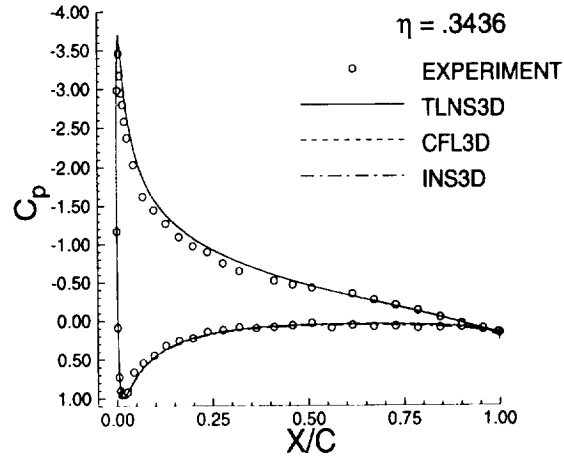


**Figure 20:** Comparison of predicted and experimental pressure distributions ( $M_\infty = 0.14$ ,  $\alpha = 10.01^\circ$ ,  $Re = 3.17 \times 10^6$ ).

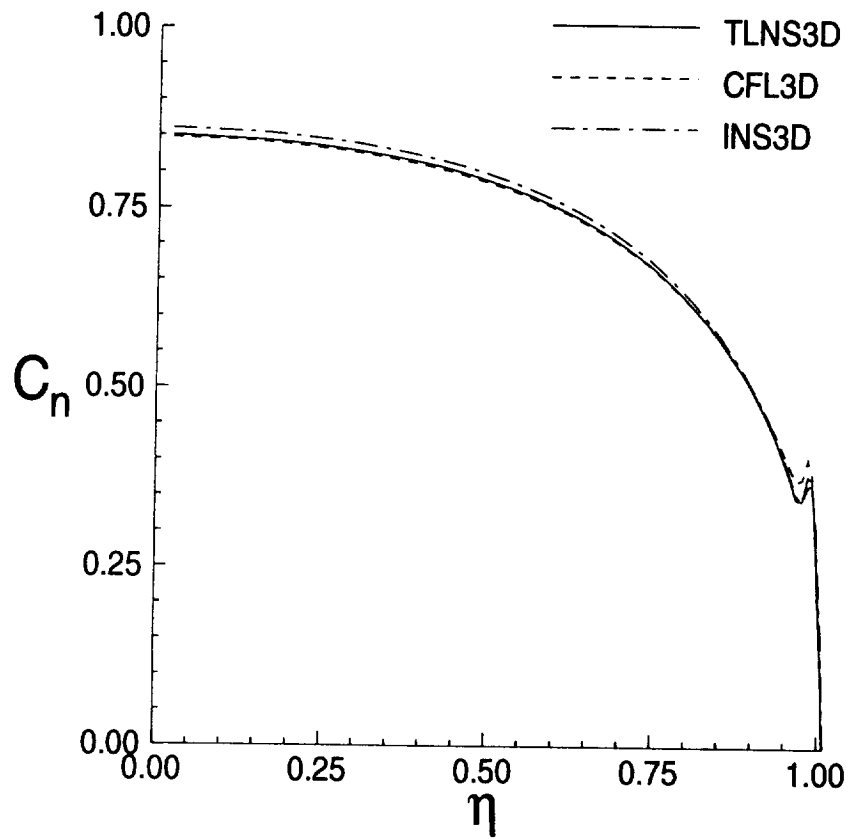


**Figure 21:** Comparison of predicted spanwise load distributions ( $M_\infty = 0.14$ ,  $\alpha = 10.01^\circ$ ,  $Re = 3.17 \times 10^6$ ).

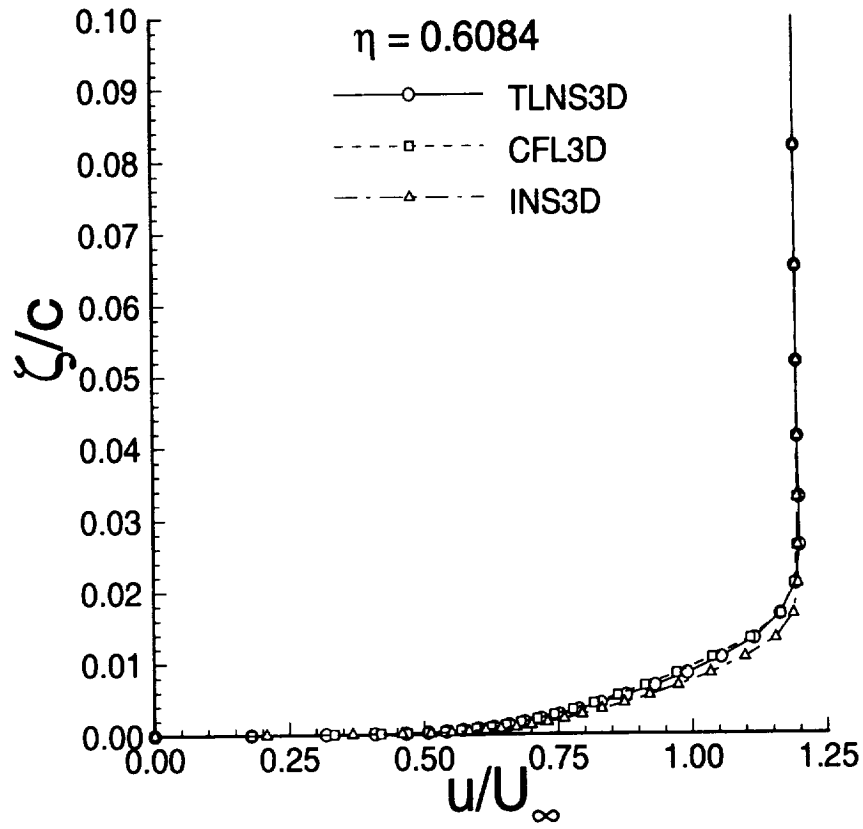


**Figure 22:** Comparison of upper surface streamwise velocity profiles at  $x/c = 0.50$  ( $M_{\infty} = 0.14$ ,  $\alpha = 10.01^{\circ}$ ,  $Re = 3.17 \times 10^6$ ).



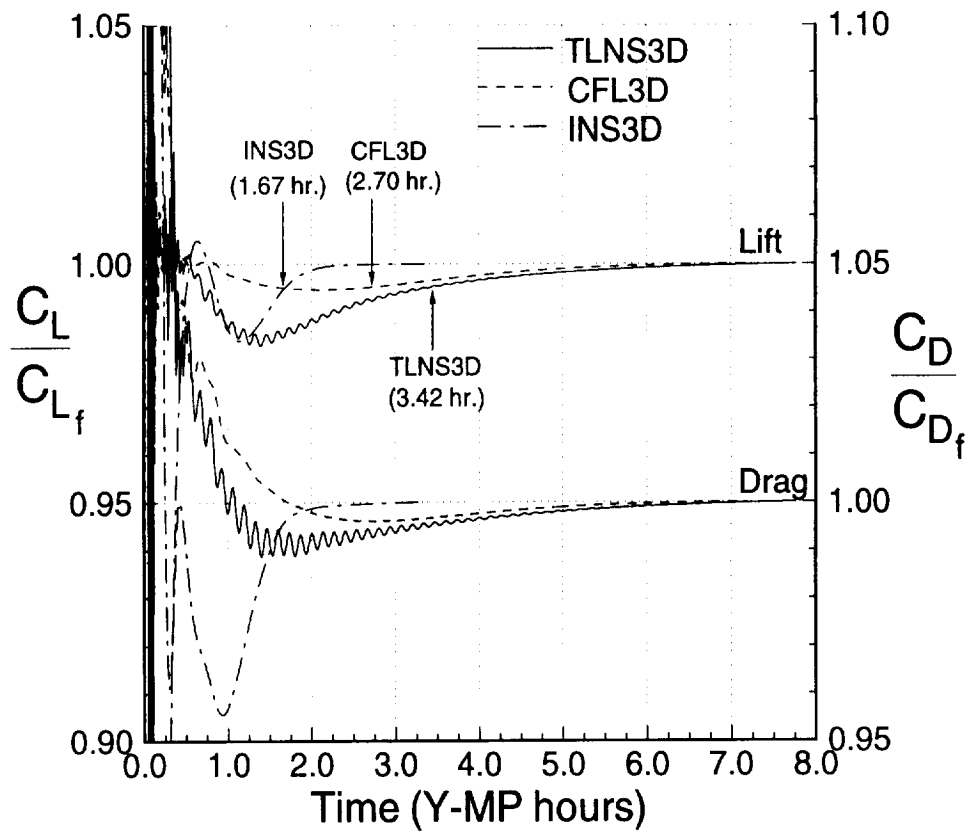


**Figure 23:** Comparison of convergence histories ( $M_\infty = 0.14$ ,  $\alpha = 10.01^\circ$ ,  $Re = 3.17 \times 10^6$ ).

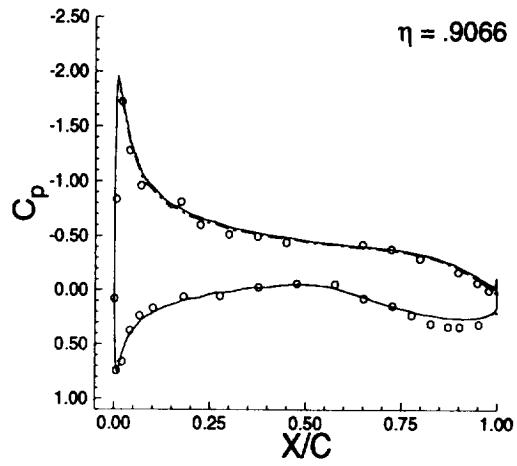
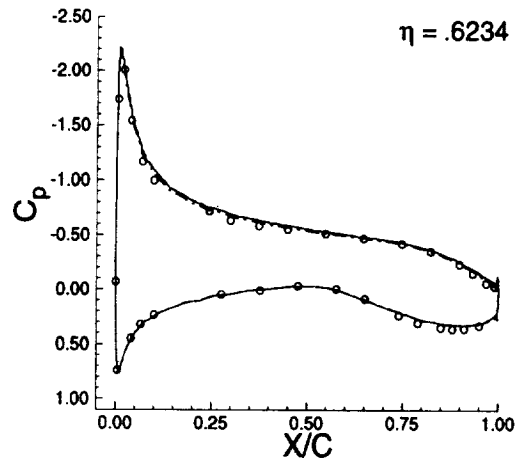
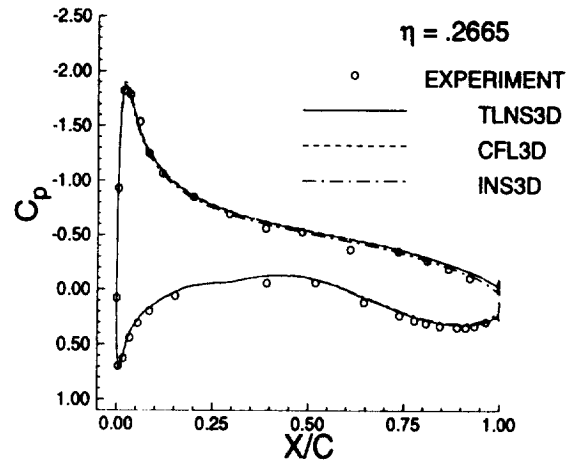


**Figure 24:** Comparison of predicted and experimental pressure distributions ( $M_\infty = 0.20$ ,  $\alpha = 4.43^\circ$ ,  $Re = 4.20 \times 10^6$ ).

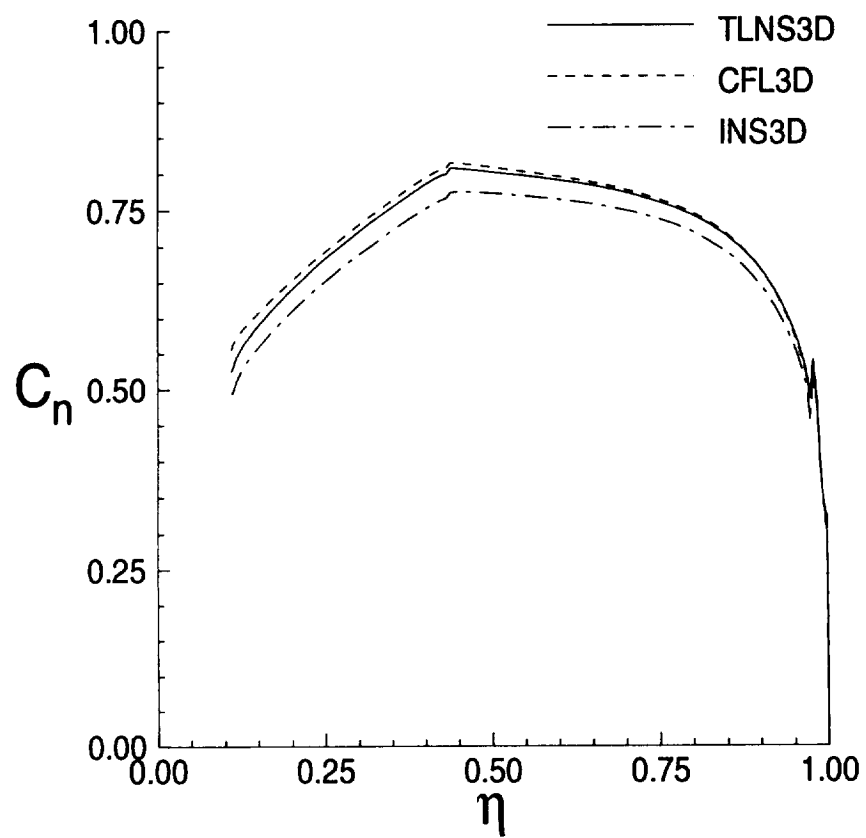


**Figure 25:** Comparison of predicted spanwise load distributions ( $M_\infty = 0.20$ ,  $\alpha = 4.43^\circ$ ,  $Re = 4.20 \times 10^6$ )

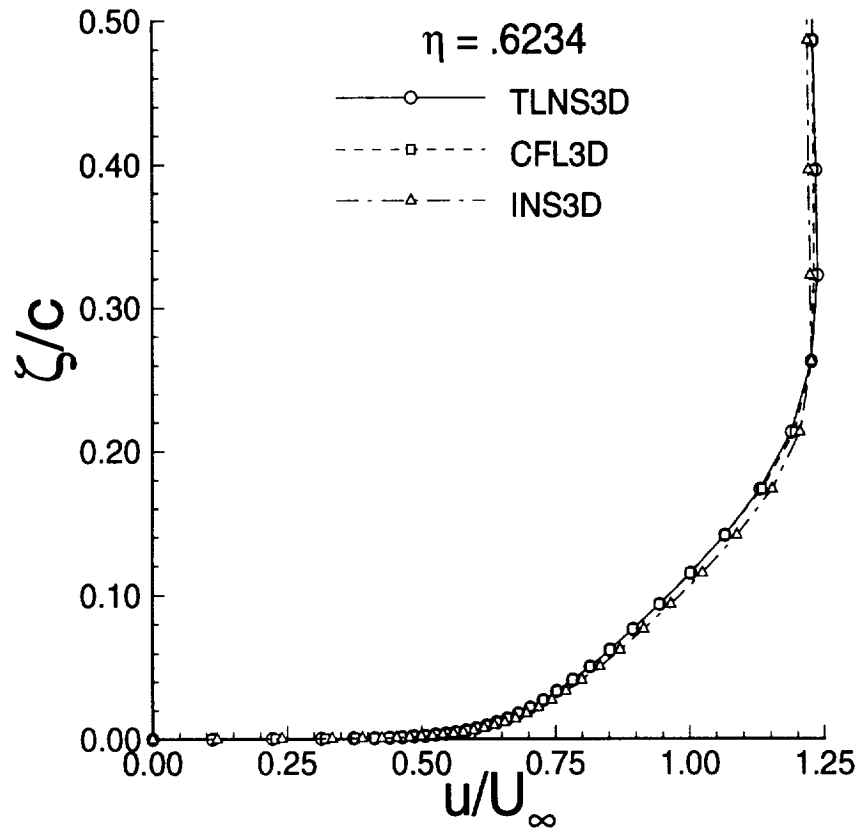


**Figure 26:** Comparison of upper surface streamwise velocity profiles at  $x/c = 0.50$  ( $M_\infty = 0.20$ ,  $\alpha = 4.43^\circ$ ,  $Re = 4.20 \times 10^6$ ).

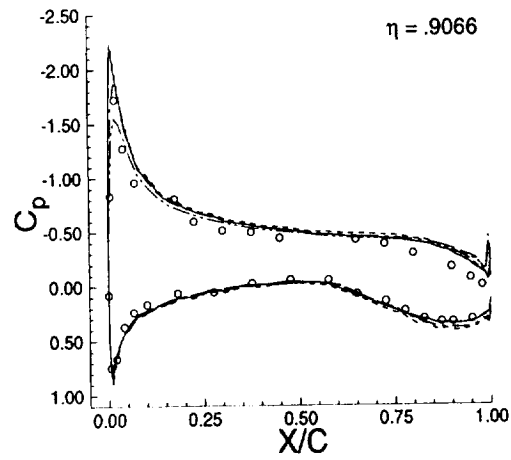
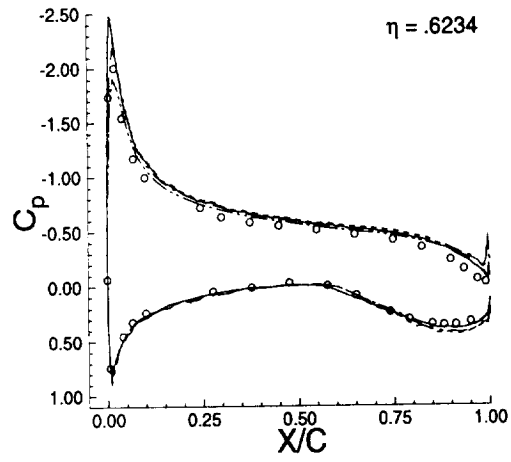
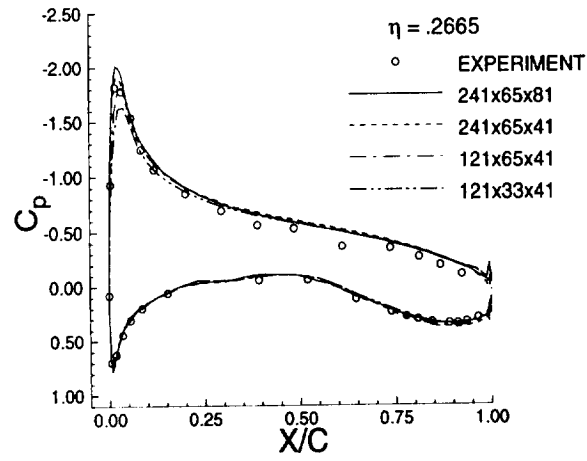
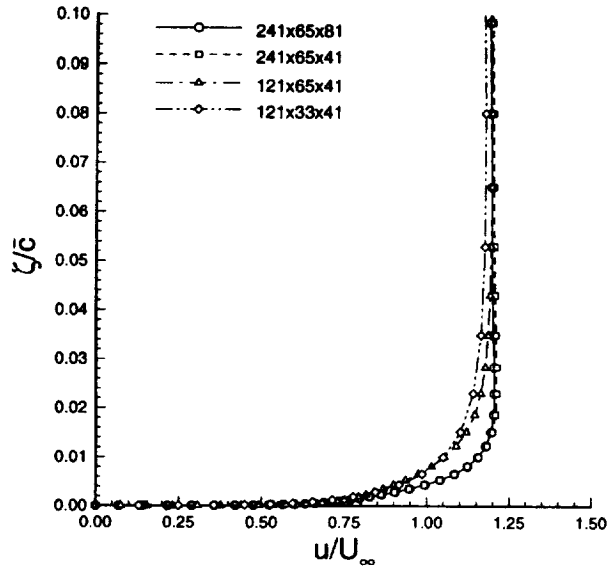
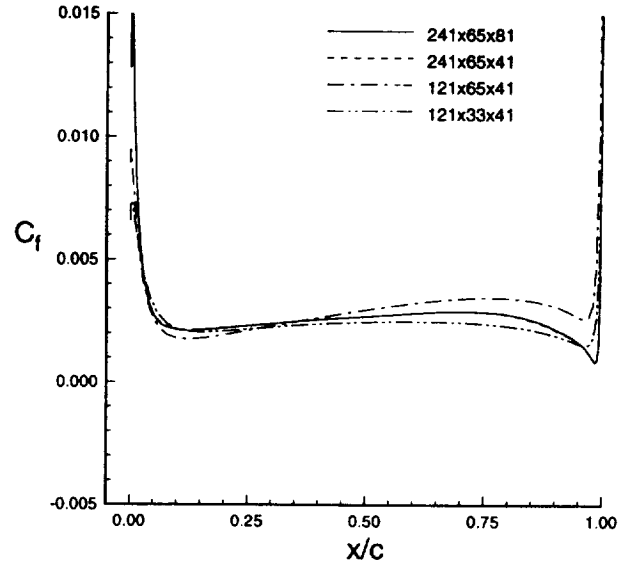


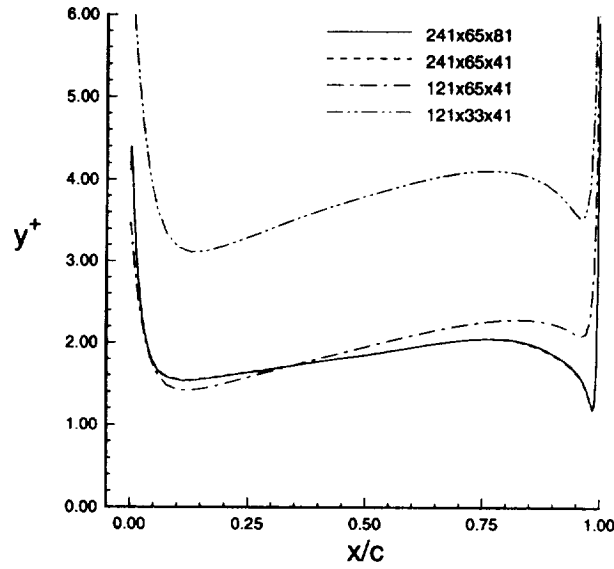
**Figure 27:** Comparison of computed pressure distributions with experimental data ( $M_\infty = .20$ ,  $\alpha = 4.43^\circ$ ,  $Re = 4.20 \times 10^6$ ).



a) velocity profile,  $x/c = 0.50$ .



b) skin friction distribution.



c)  $y^+$  distribution.

**Figure 28:** Influence of grid refinement on upper surface wing boundary layer,  $\eta = 0.9066$  ( $M_\infty = 0.20$ ,  $\alpha = 4.43^\circ$ ,  $Re = 4.20 \times 10^6$ ).

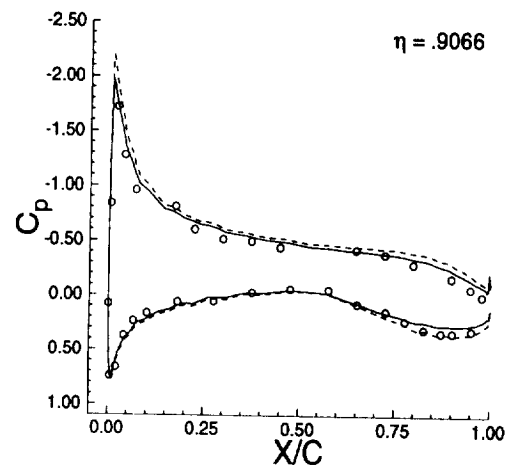
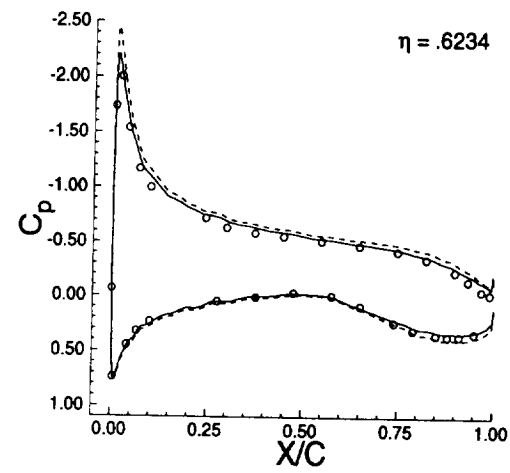
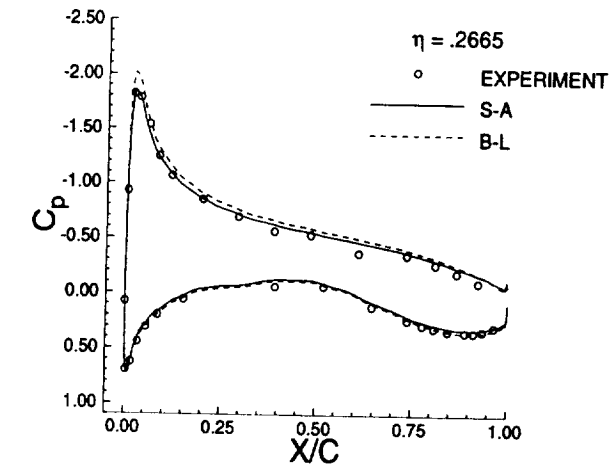
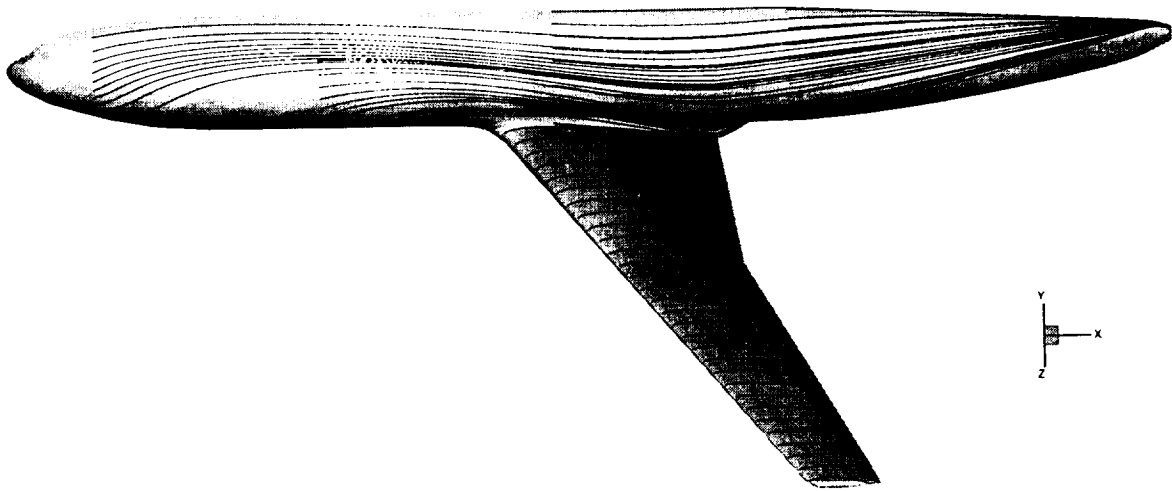
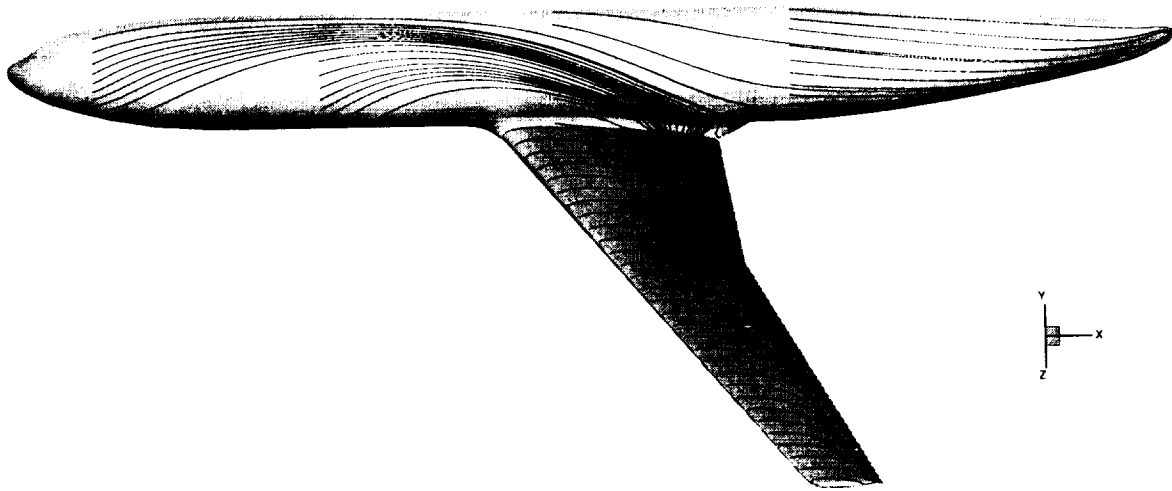


**Figure 29:** Influence of turbulence model on computed pressure distributions ( $M_\infty = .20$ ,  $\alpha = 4.43^\circ$ ,  $Re = 4.20 \times 10^6$ ).



a) Baldwin-Lomax



a) Spalart-Allmaras

**Figure 30:** Influence of turbulence model on near surface streamline patterns ( $M_\infty = 0.20$ ,  $\alpha = 12.55^\circ$ ,  $Re = 4.20 \times 10^6$ ).



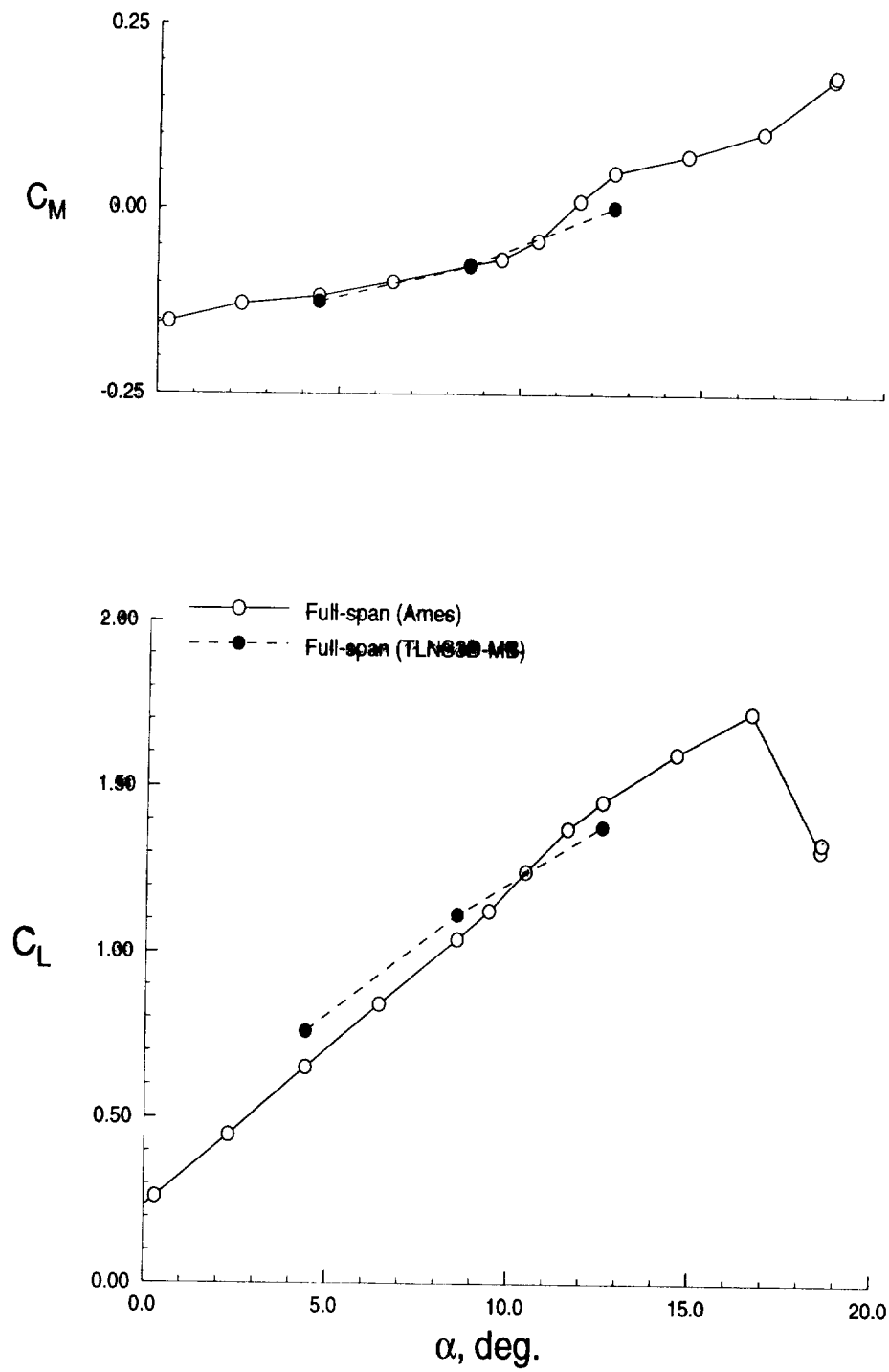


**Figure 31:** Comparison of computed and experimental full-span lift and pitching moment coefficients ( $M_\infty = .20$ ,  $Re = 4.20 \times 10^6$ ).

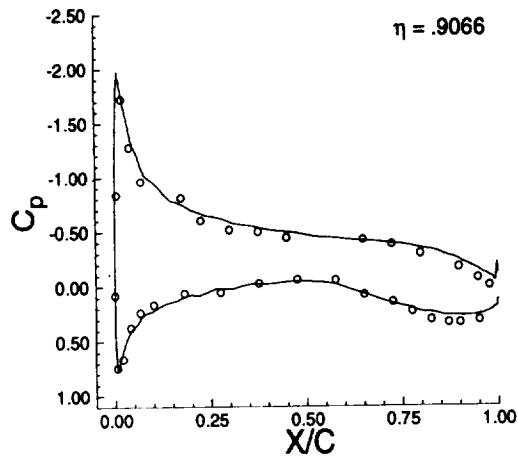
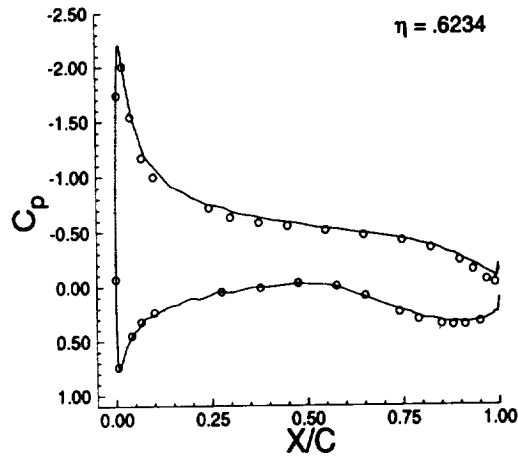
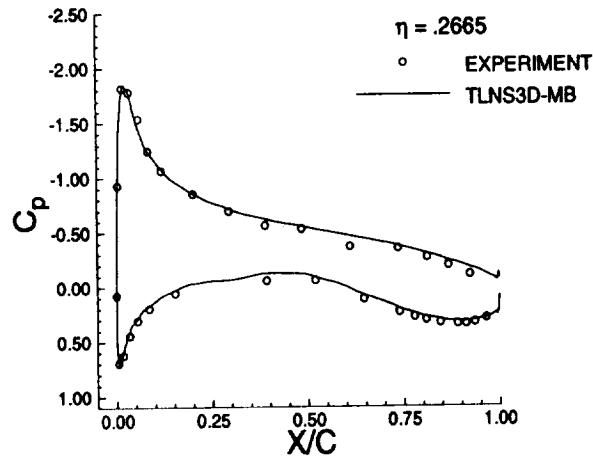


**Figure 32:** Comparison of computed and experimental full-span pressure distributions ( $M_\infty = .20$ ,  $\alpha = 4.43^\circ$ ,  $Re = 4.20 \times 10^6$ ).

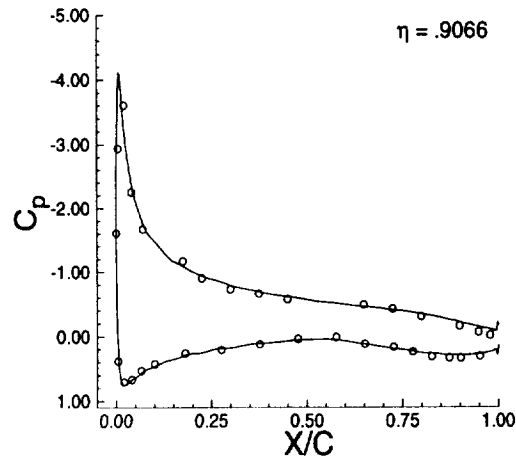
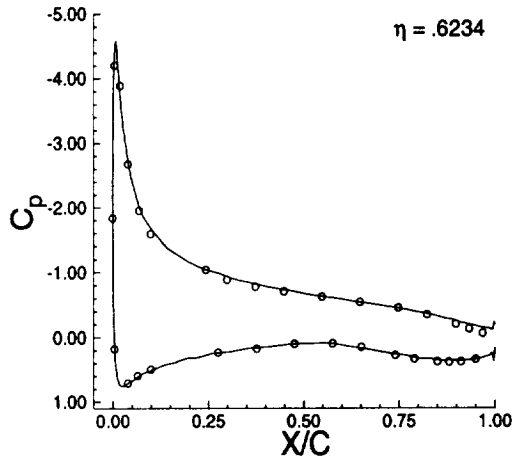
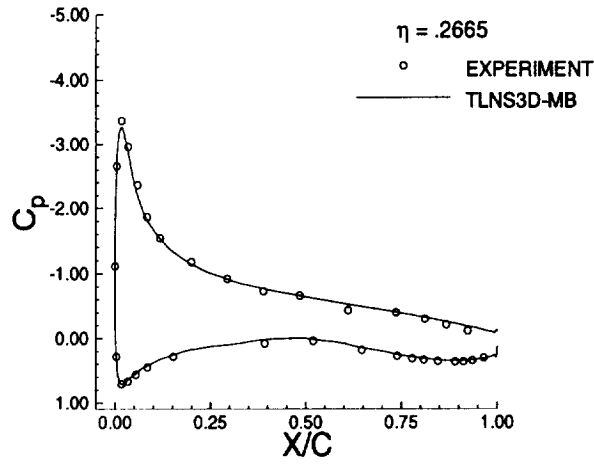


**Figure 33:** Comparison of computed and experimental full-span pressure distributions ( $M_\infty = .20$ ,  $\alpha = 8.58^\circ$ ,  $Re = 4.20 \times 10^6$ ).

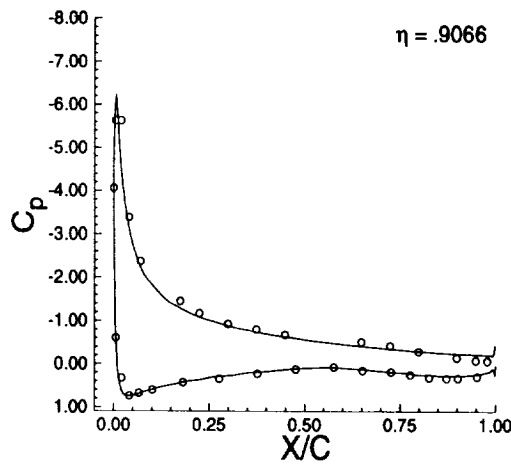
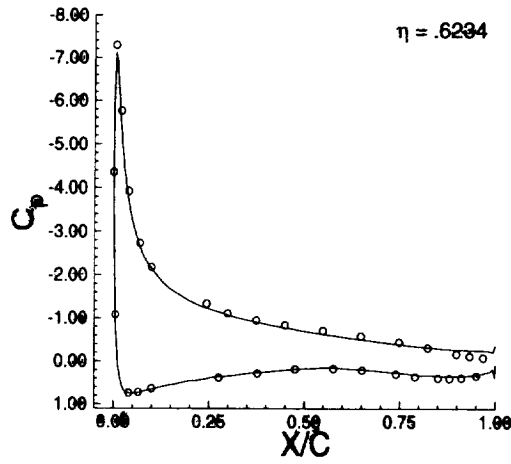
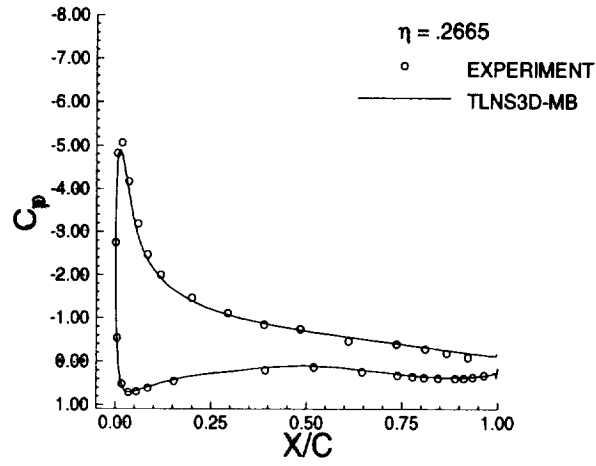


**Figure 34:** Comparison of computed and experimental full-span pressure distributions ( $M_\infty = .20$ ,  $\alpha = 12.55^\circ$ ,  $Re = 4.20 \times 10^6$ ).

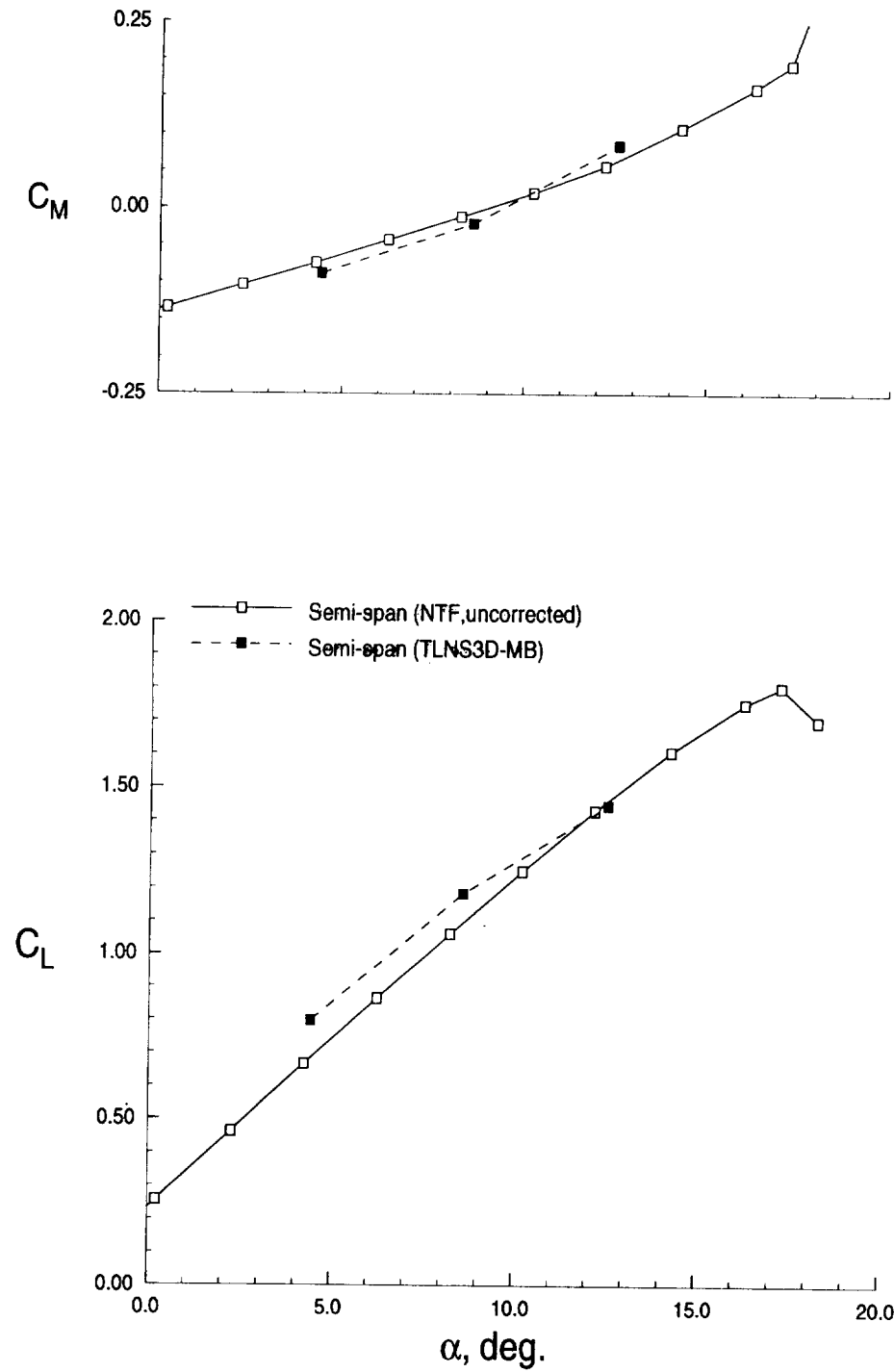


**Figure 35:** Comparison of computed and experimental semi-span lift and pitching moment coefficients ( $M_\infty = .20$ ,  $Re = 4.20 \times 10^6$ ).

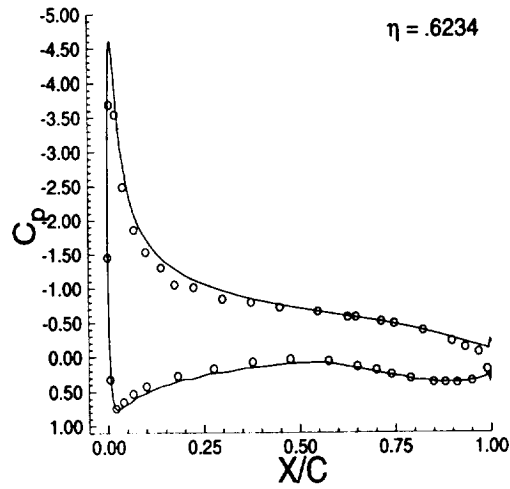
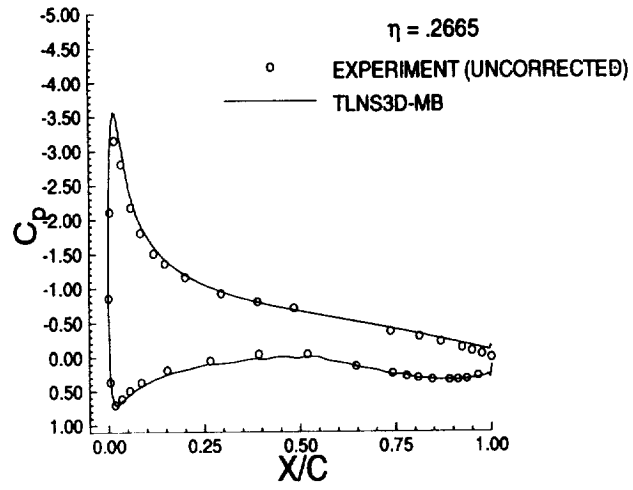


**Figure 36:** Comparison of computed and experimental semi-span pressure distributions ( $M_\infty = .20$ ,  $\alpha = 8.24^\circ$ ,  $Re = 4.20 \times 10^6$ ).

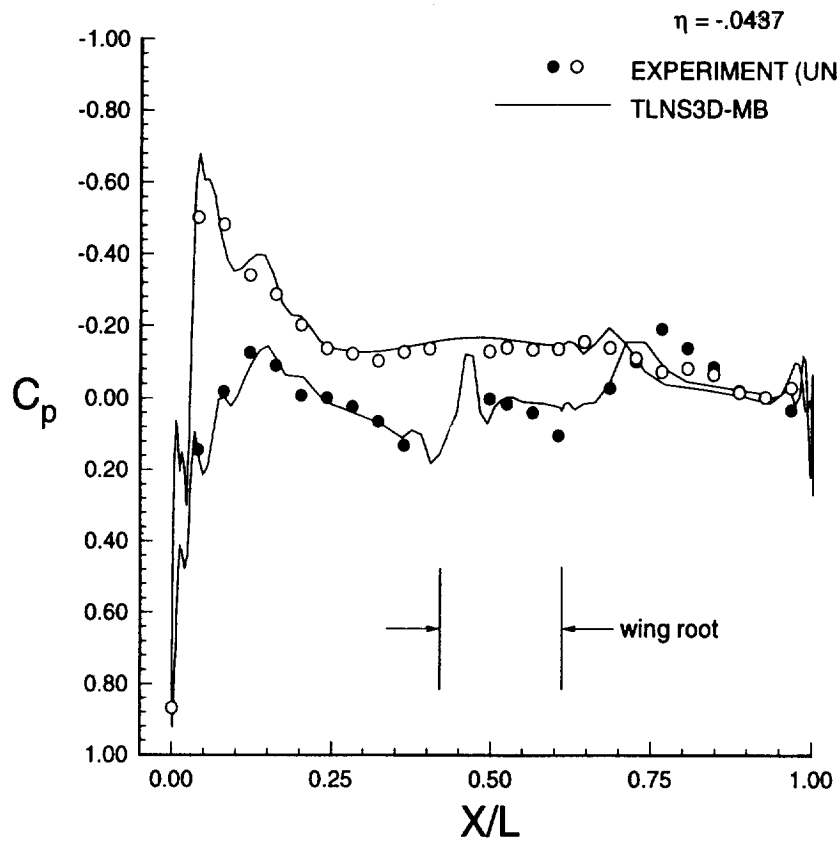


**Figure 37:** Comparison of computed and experimental semi-span pressure distributions ( $M_\infty = .20$ ,  $\alpha = 8.24^\circ$ ,  $Re = 4.20 \times 10^6$ ).

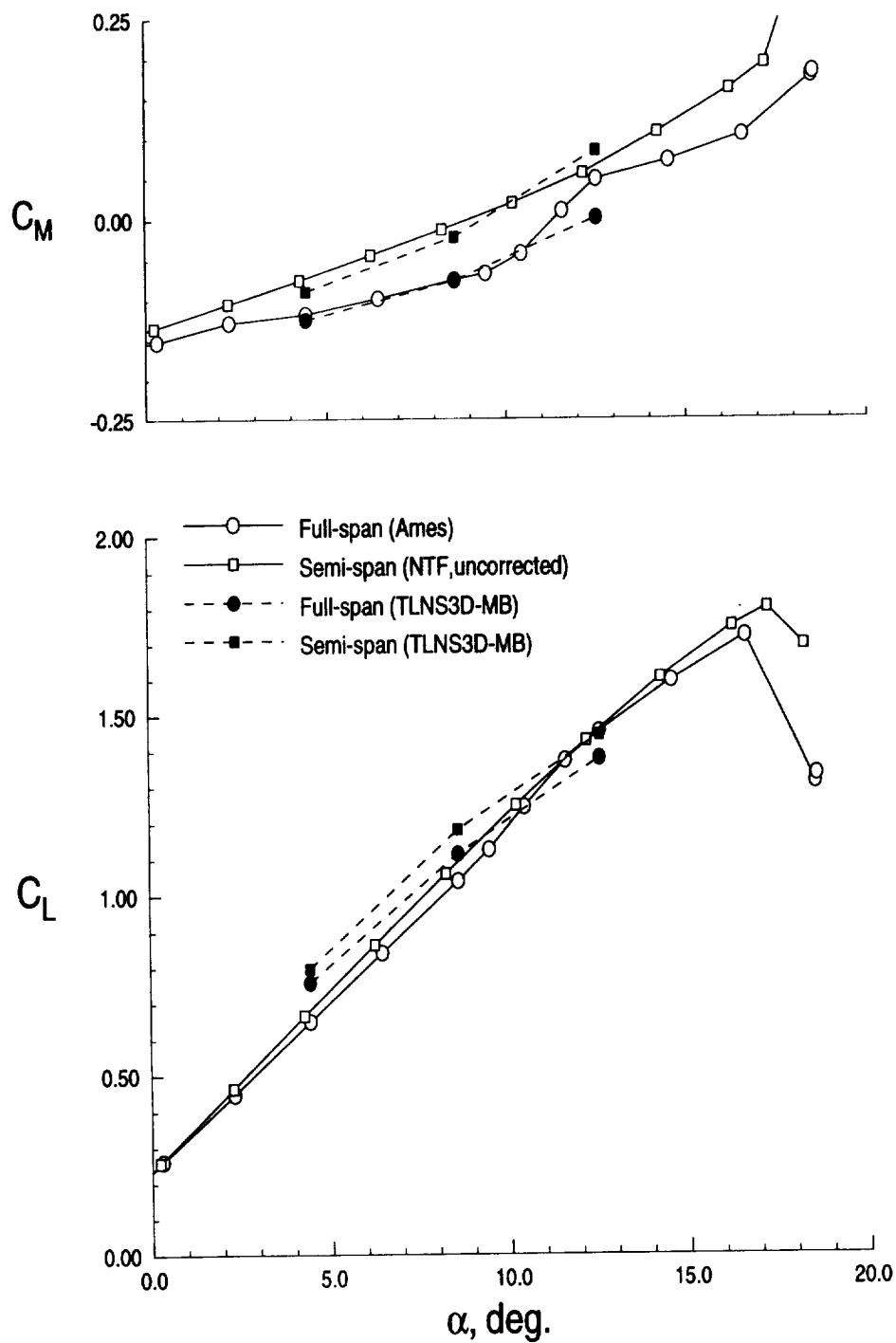


**Figure 38:** Comparison of full-span and semi-span lift and pitching moment coefficients ( $M_\infty = .20$ ,  $Re = 4.20 \times 10^6$ ).



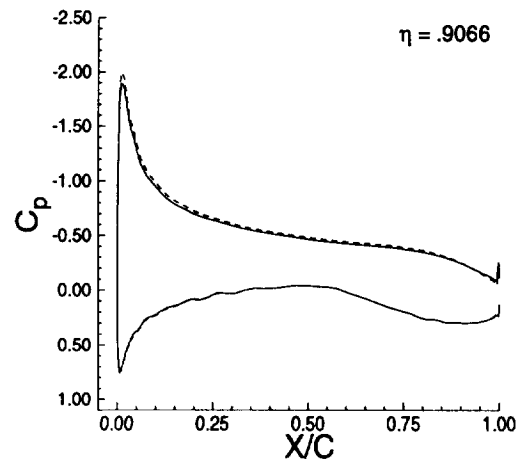
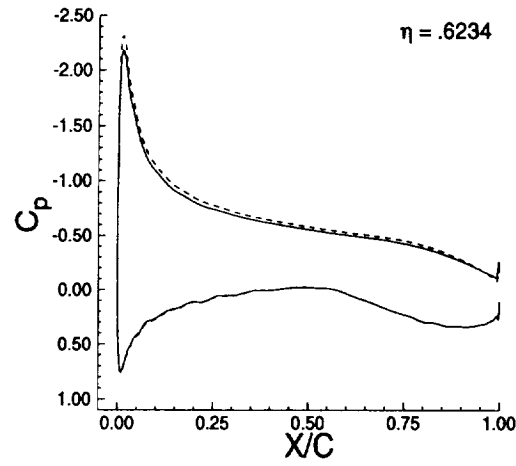
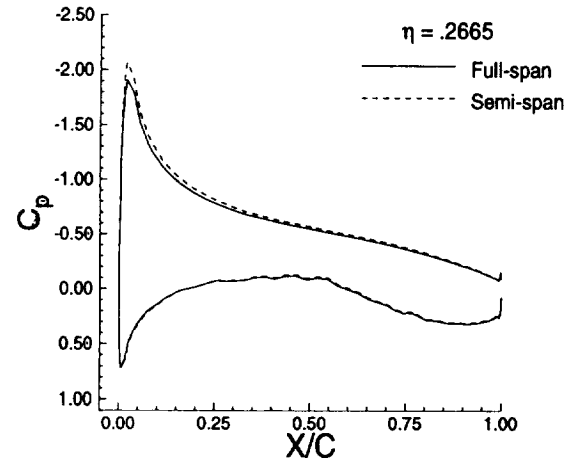


**Figure 39:** Comparison of computed full-span and semi-span pressure distributions ( $M_\infty = .20$ ,  $\alpha = 4.43^\circ$ ,  $Re = 4.20 \times 10^6$ ).

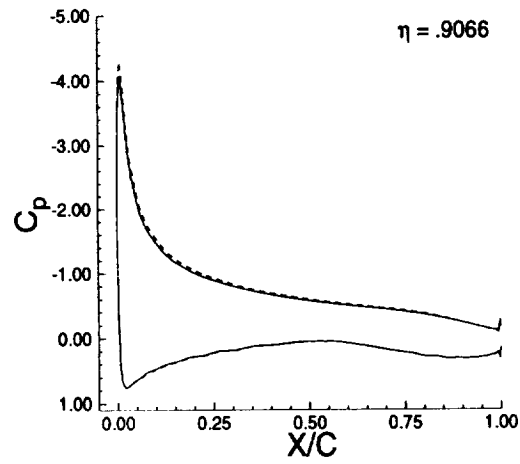
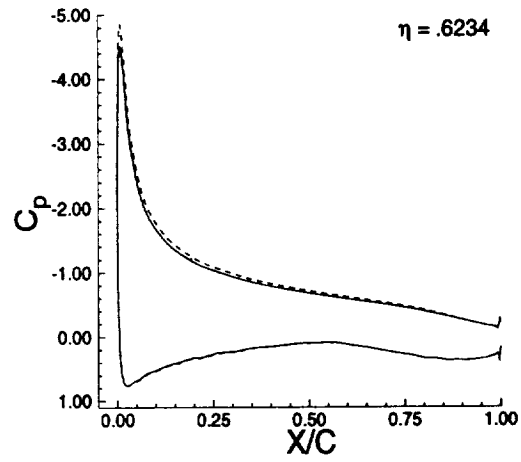
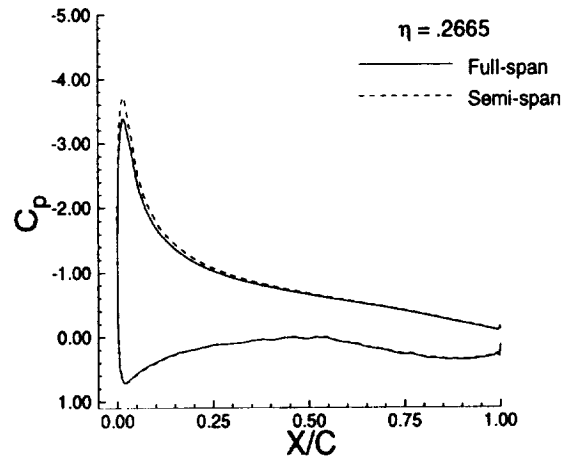


**Figure 40:** Comparison of computed full-span and semi-span pressure distributions ( $M_\infty = .20$ ,  $\alpha = 8.58^\circ$ ,  $Re = 4.20 \times 10^6$ ).

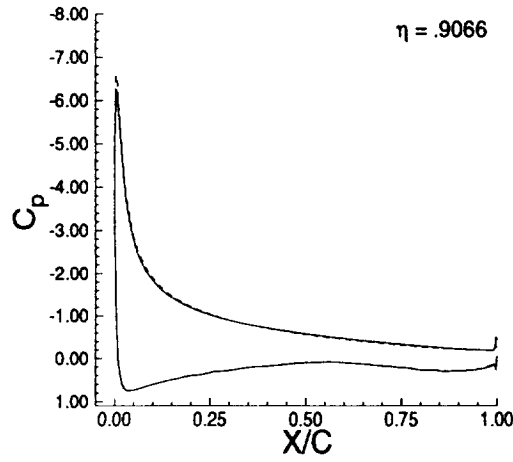
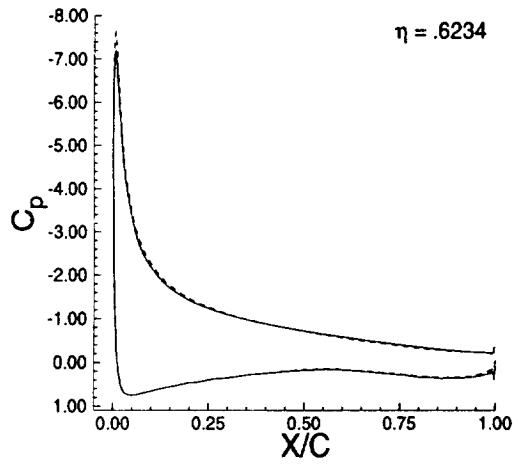
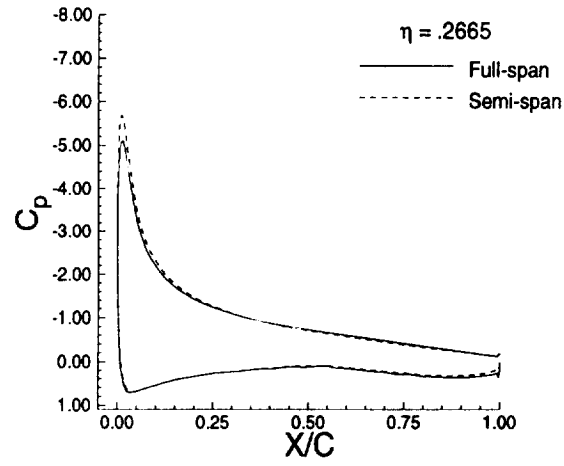


**Figure 41:** Comparison of computed full-span and semi-span pressure distributions ( $M_\infty = .20$ ,  $\alpha = 12.55^\circ$ ,  $Re = 4.20 \times 10^6$ ).

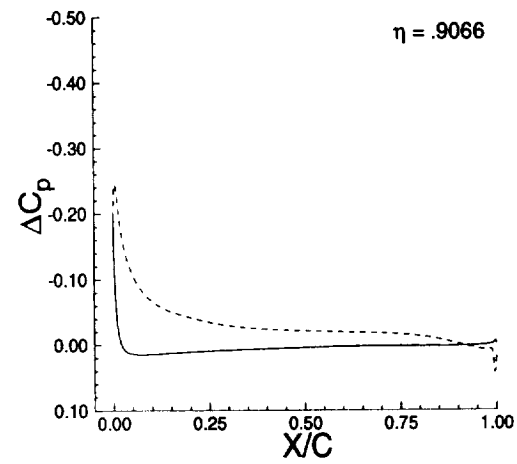
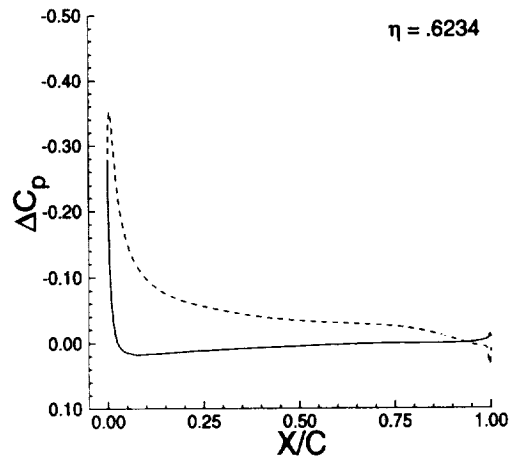
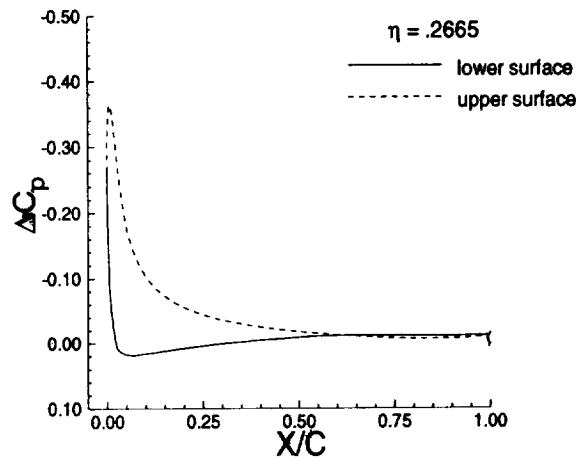


**Figure 42:** Computed differential wing pressure distributions ( $M_\infty = .20$ ,  $\alpha = 8.58^\circ$ ,  $Re = 4.20 \times 10^6$ ).

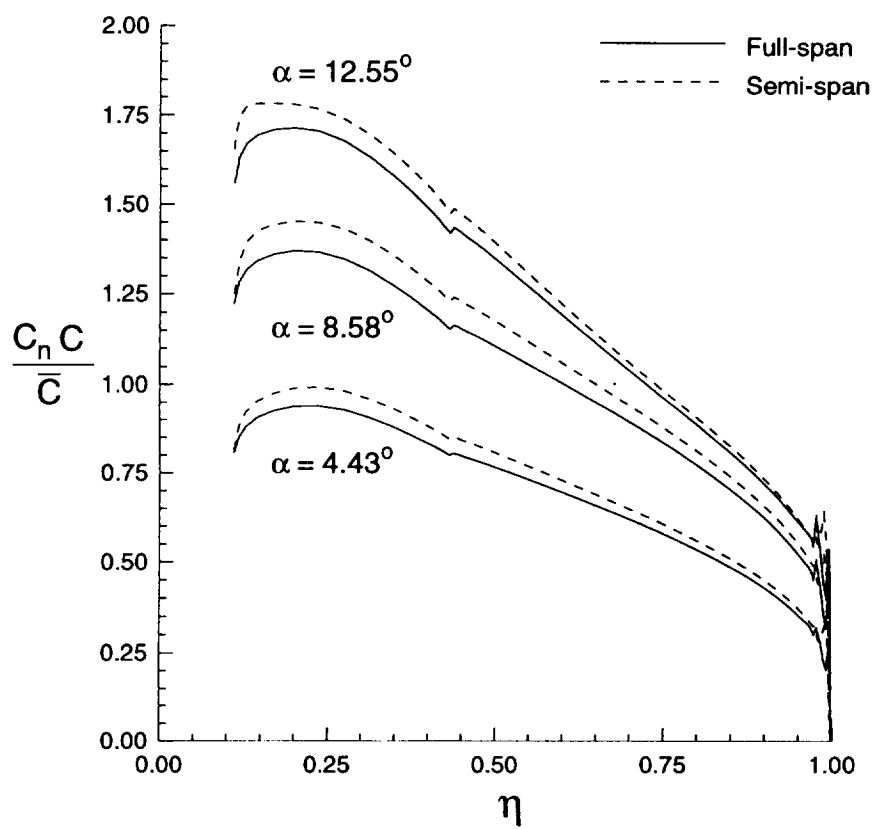


**Figure 43:** Comparison of computed spanload distributions ( $M_\infty = .20$  ,  $Re = 4.20 \times 10^6$ ).

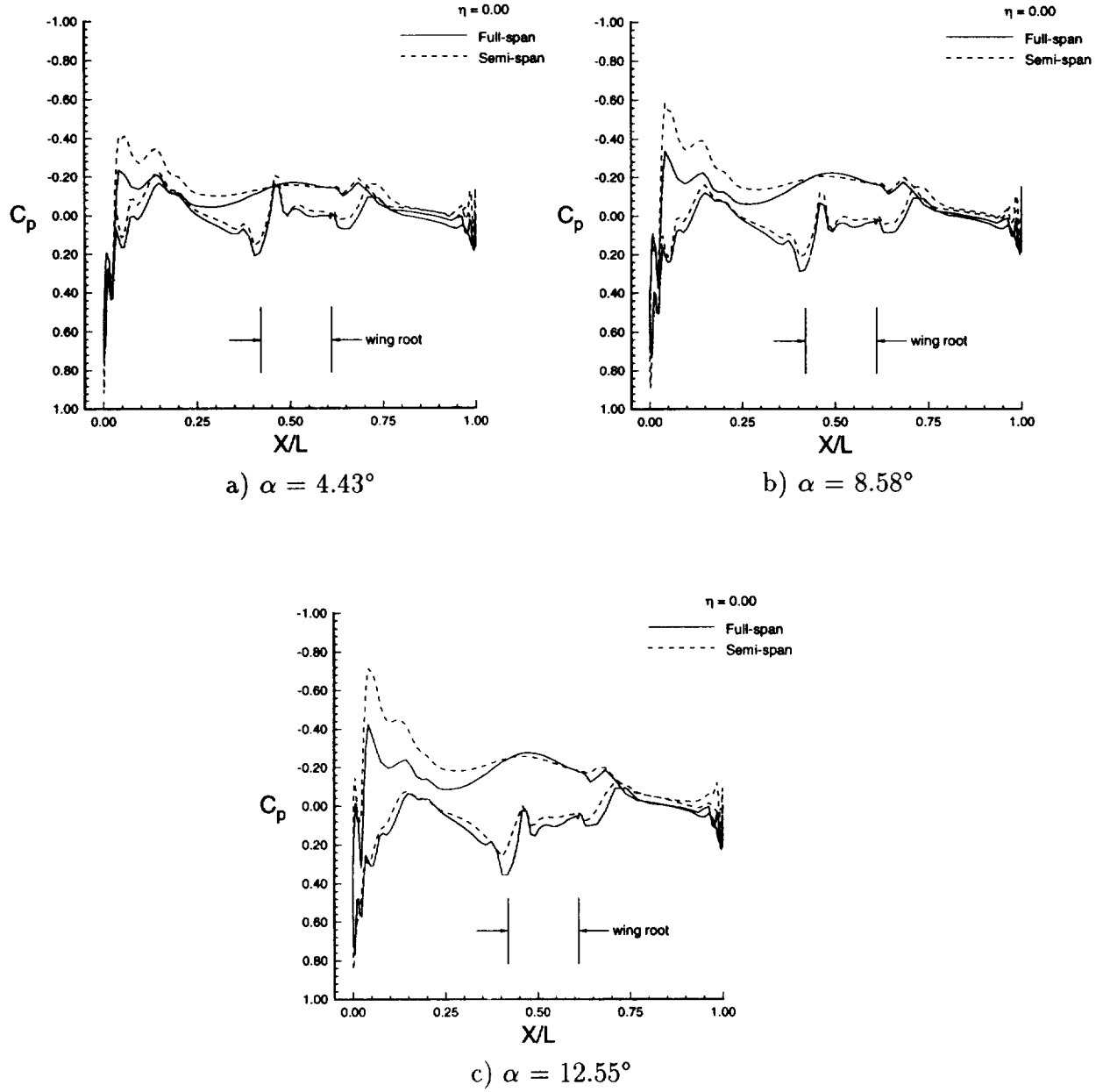
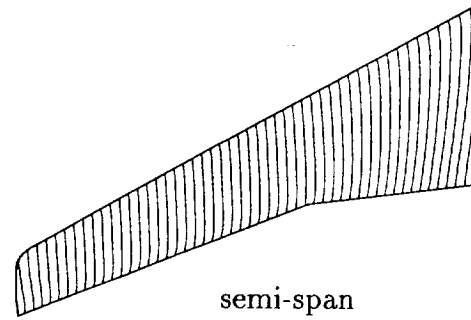
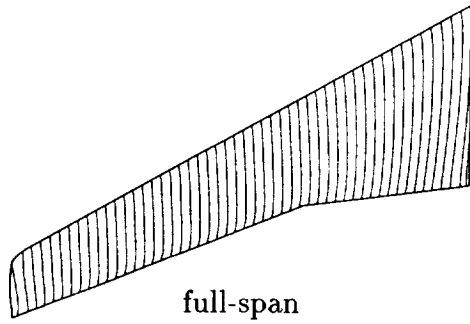
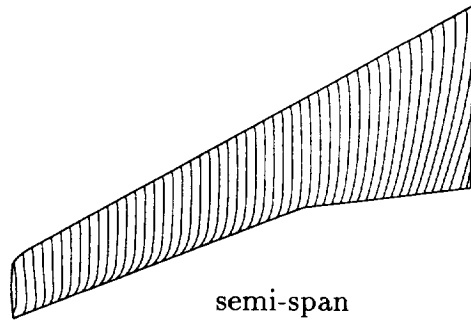
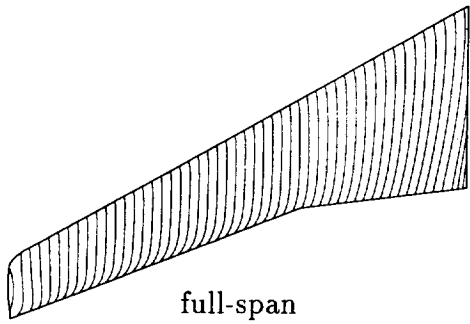


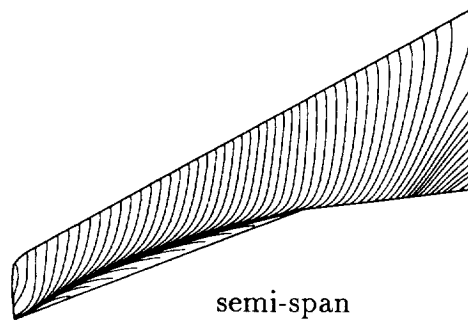
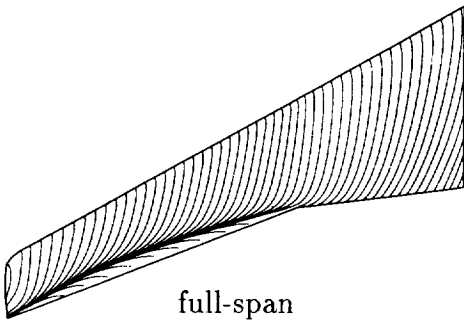
**Figure 44:** Comparison of computed full-span and semi-span fuselage centerline pressure distributions ( $M_\infty = 0.20$ ,  $Re = 4.20 \times 10^6$ ).



a)  $\alpha = 4.43^\circ$



b)  $\alpha = 8.58^\circ$

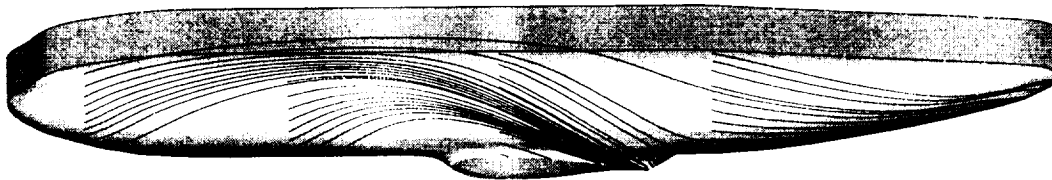


c)  $\alpha = 12.55^\circ$

**Figure 45:** Comparison of computed full-span and semi-span upper wing surface streamline patterns ( $M_\infty = 0.20$ ,  $Re = 4.20 \times 10^6$ ).



a) full-span



b) semi-span

**Figure 46:** Comparison of computed full-span and semi-span fuselage streamline patterns ( $M_\infty = 0.20$ ,  $\alpha = 12.55^\circ$ ,  $Re = 4.20 \times 10^6$ ).



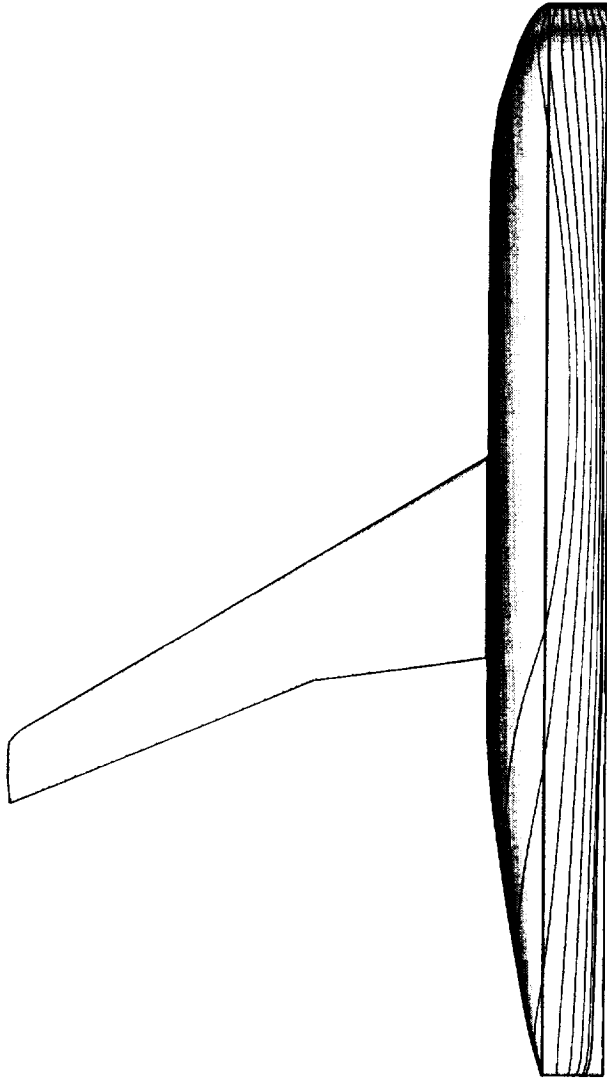
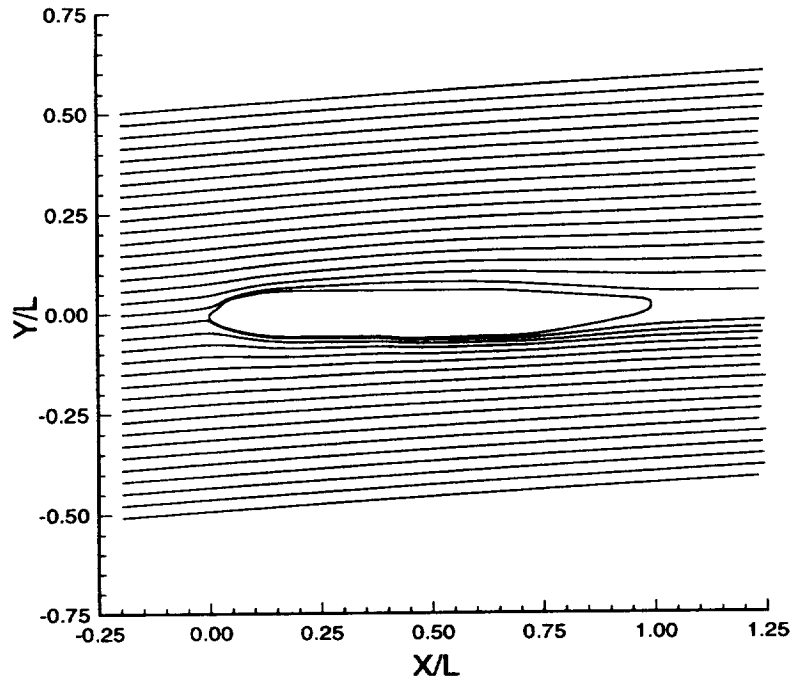
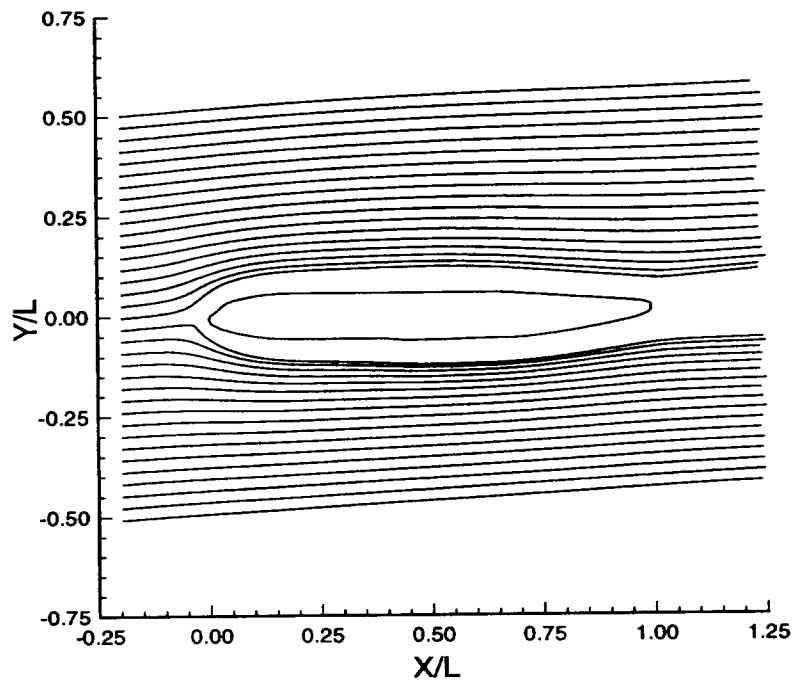


**Figure 47:** Planform view of streamline patterns on upper surface of semi-span configuration ( $M_\infty = 0.20$ ,  $\alpha = 12.55^\circ$ ,  $Re = 4.20 \times 10^6$ ).

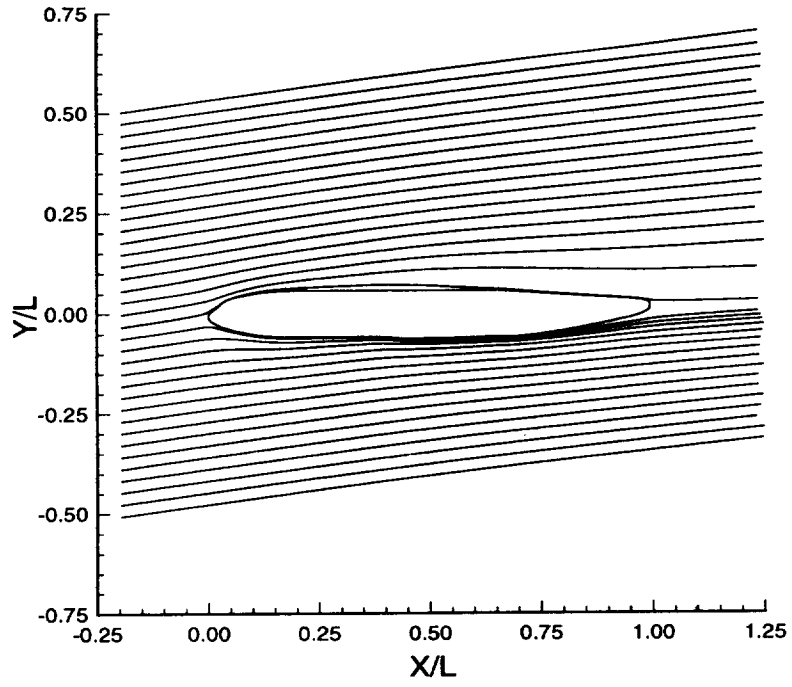


a) full-span

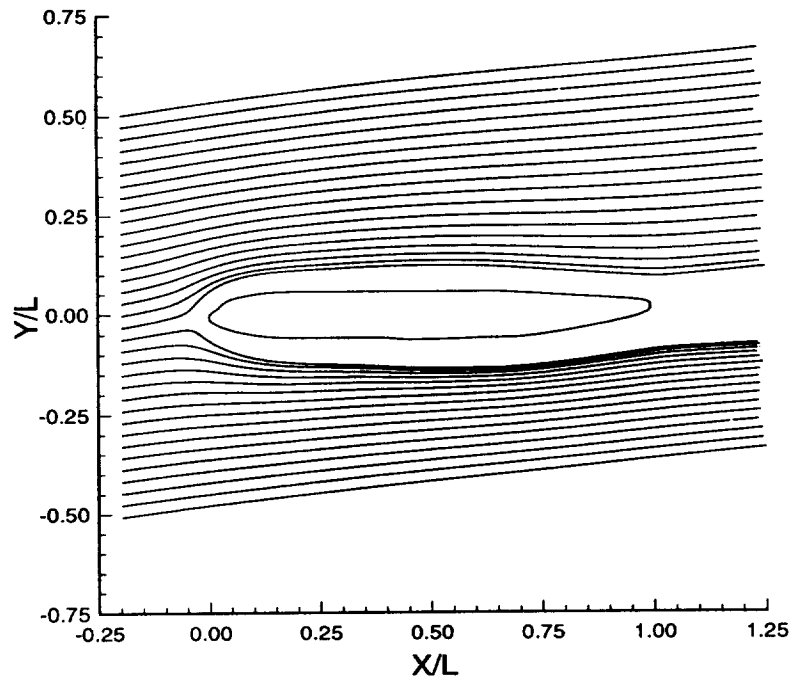


b) semi-span

**Figure 48:** Comparison of computed full-span and semi-span root plane streamline patterns ( $M_\infty = .20$ ,  $\alpha = 4.43^\circ$ ,  $Re = 4.20 \times 10^6$ ).

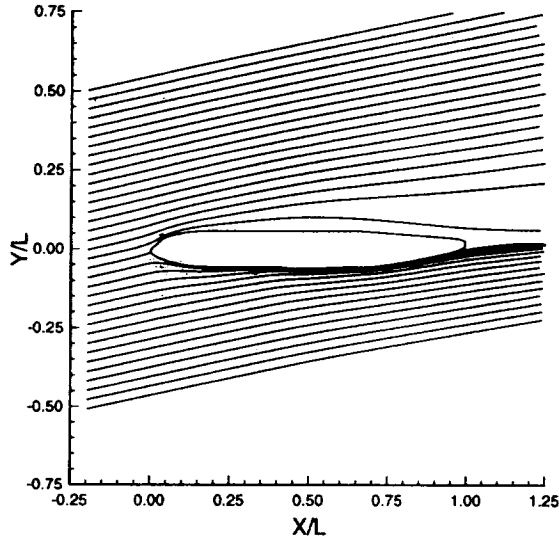


a) full-span

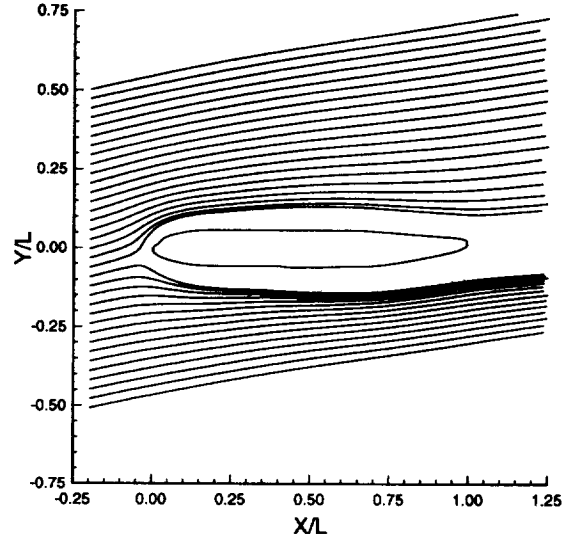


b) semi-span

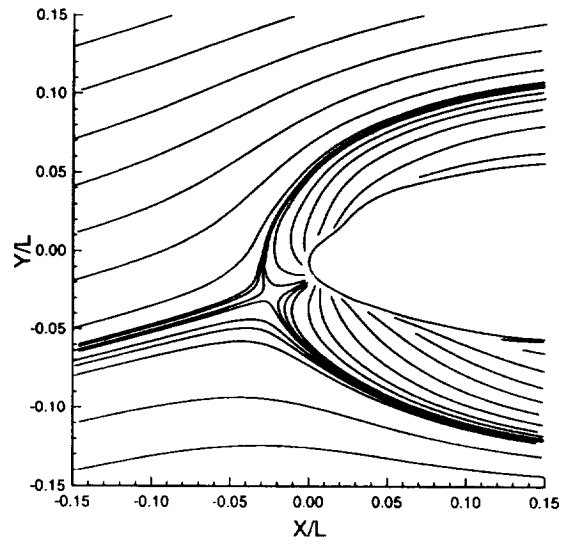
**Figure 49:** Comparison of computed full-span and semi-span root plane streamline patterns ( $M_\infty = .20$ ,  $\alpha = 8.58^\circ$ ,  $Re = 4.20 \times 10^6$ ).



a) full-span



b) semi-span



c) semi-span nose region

**Figure 50:** Comparison of computed full-span and semi-span root plane streamline patterns ( $M_\infty = .20$ ,  $\alpha = 12.55^\circ$ ,  $Re = 4.20 \times 10^6$ ).

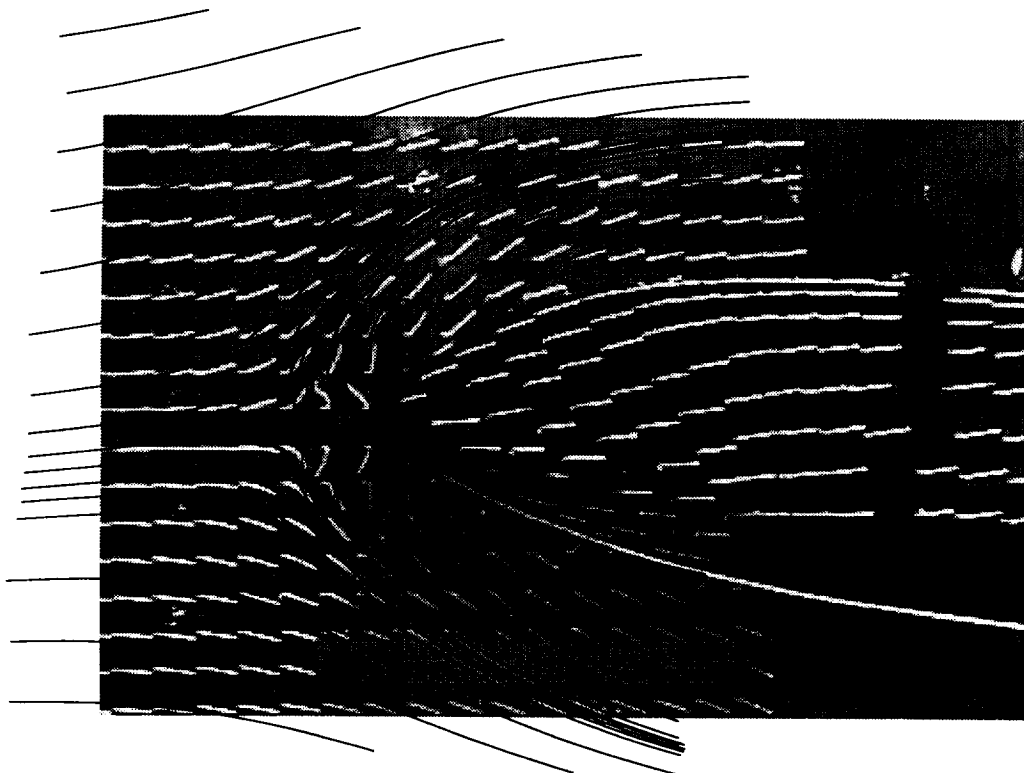


**Figure 51:** Comparison of computed sidewall streamline pattern and experimental tuft visualization results ( $M_\infty = .20$ ,  $\alpha = 8.24^\circ$ ,  $Re = 4.20 \times 10^6$ ).

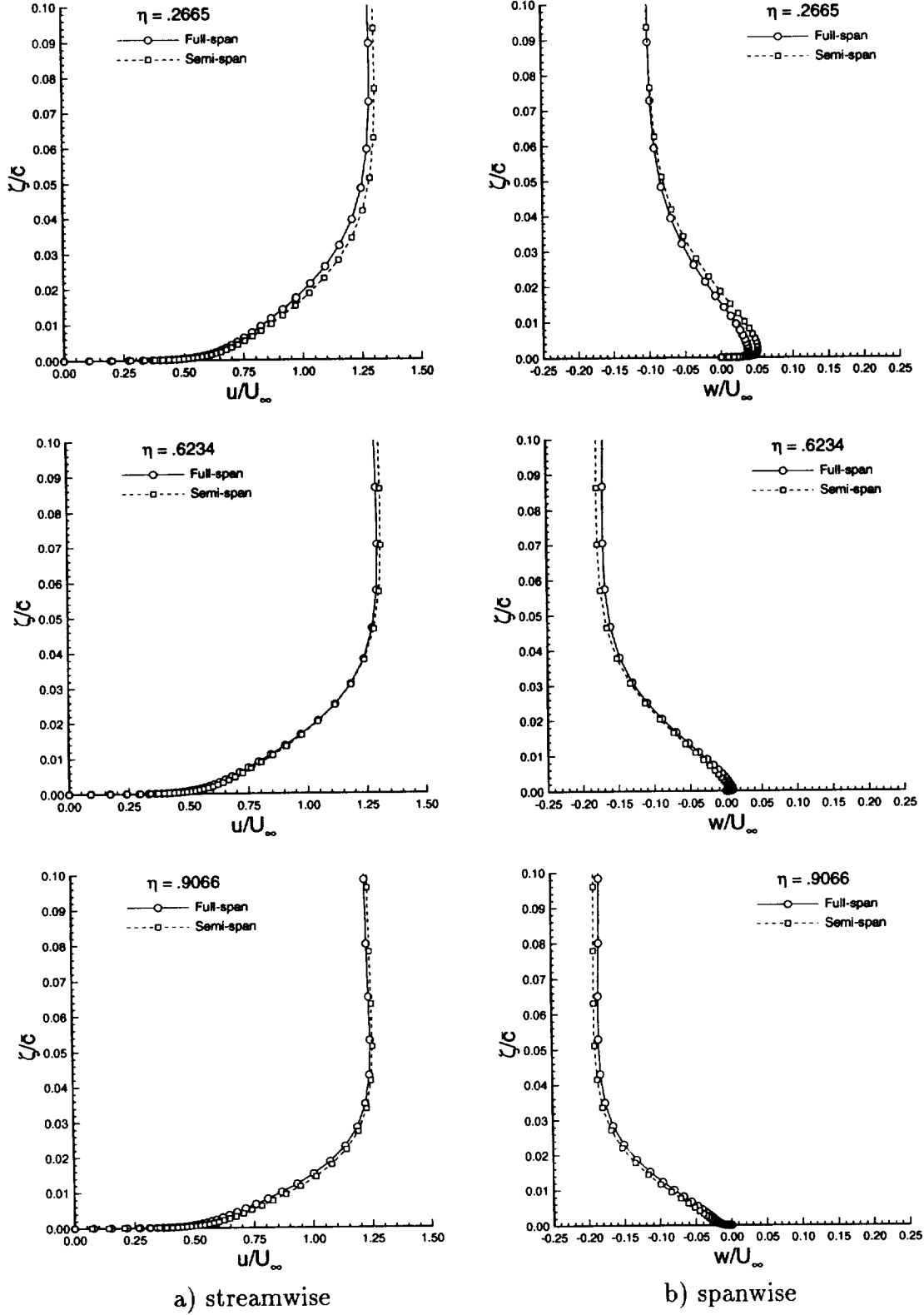


**Figure 52:** Comparison of full-span and semi-span upper surface wing velocity profiles at  $x/c = 0.50$  ( $M_\infty = 0.20$ ,  $\alpha = 8.58^\circ$ ,  $Re = 4.20 \times 10^6$ ).

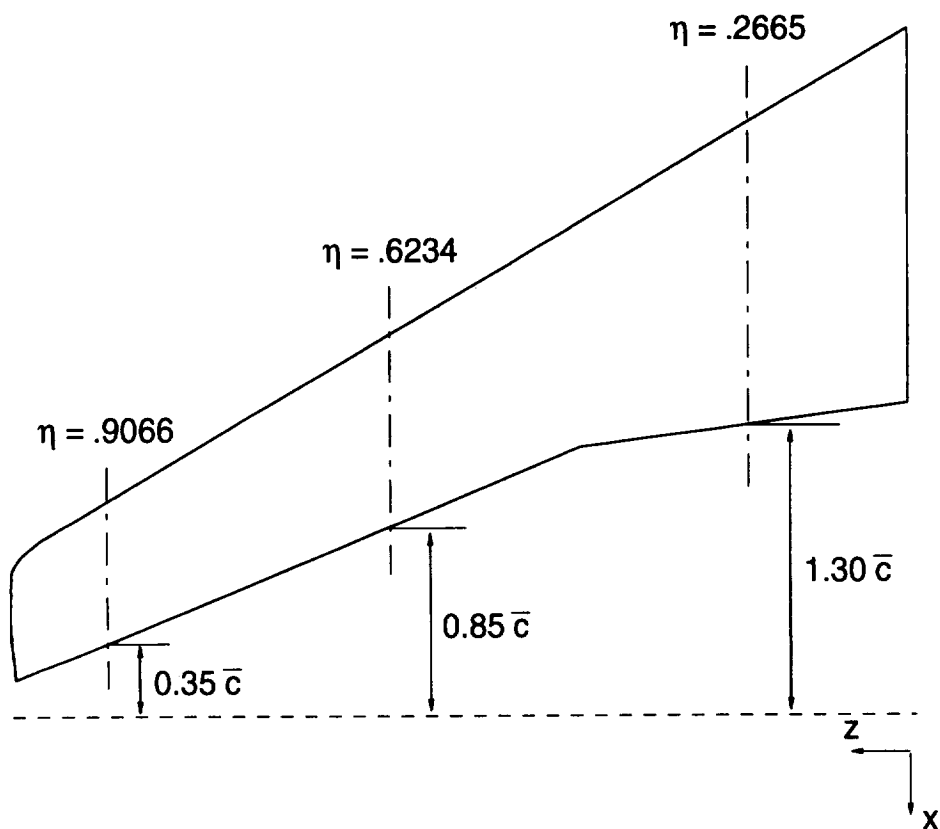


**Figure 53:** Location of wake velocity profile comparisons.

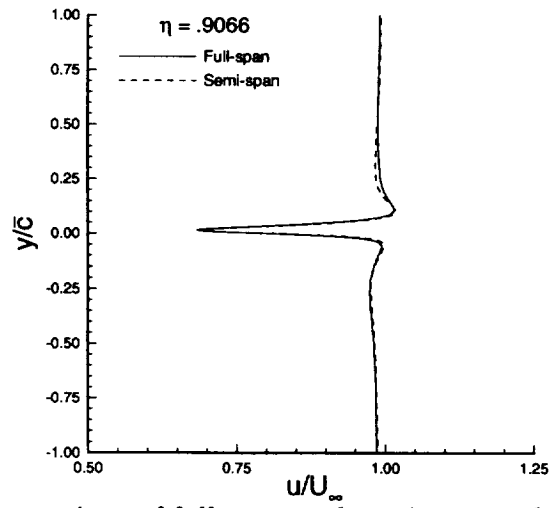
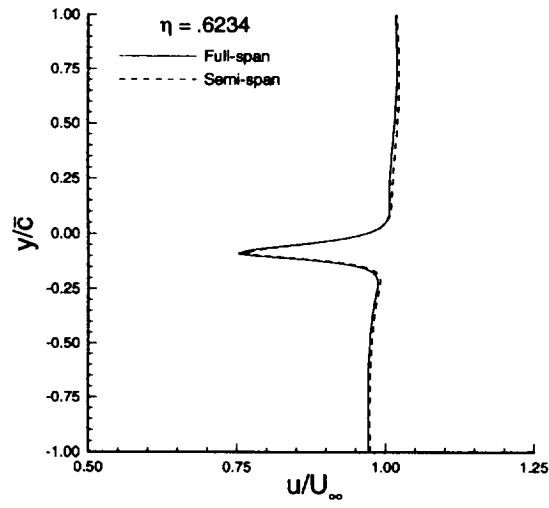
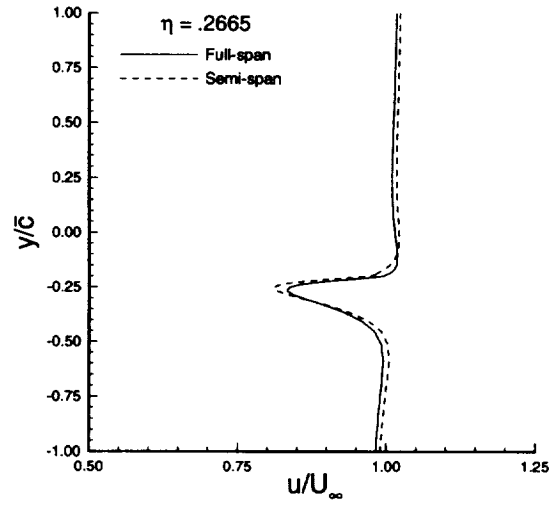


**Figure 54:** Comparison of full-span and semi-span wake velocity profiles ( $M_\infty = .20$ ,  $\alpha = 8.58^\circ$ ,  $Re = 4.20 \times 10^6$ ).



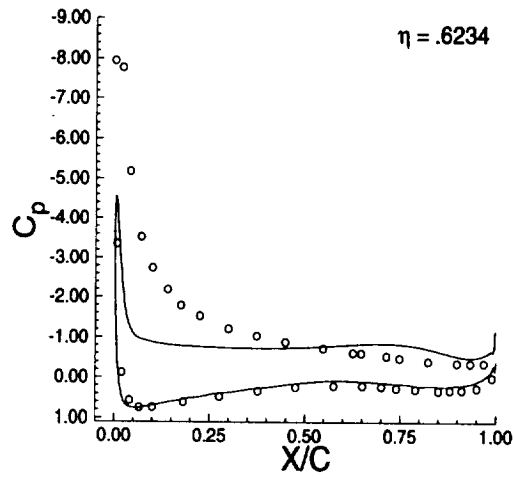
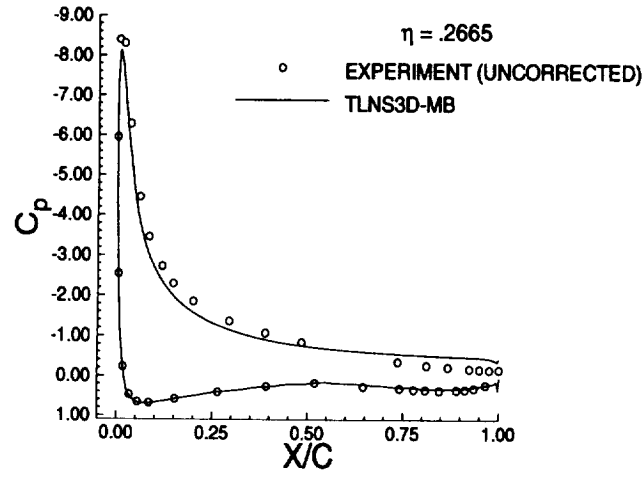


**Figure 55:** Comparison of computed and experimental semi-span pressure distributions ( $M_\infty = .20$ ,  $\alpha = 18.25^\circ$ ,  $Re = 4.20 \times 10^6$ ).

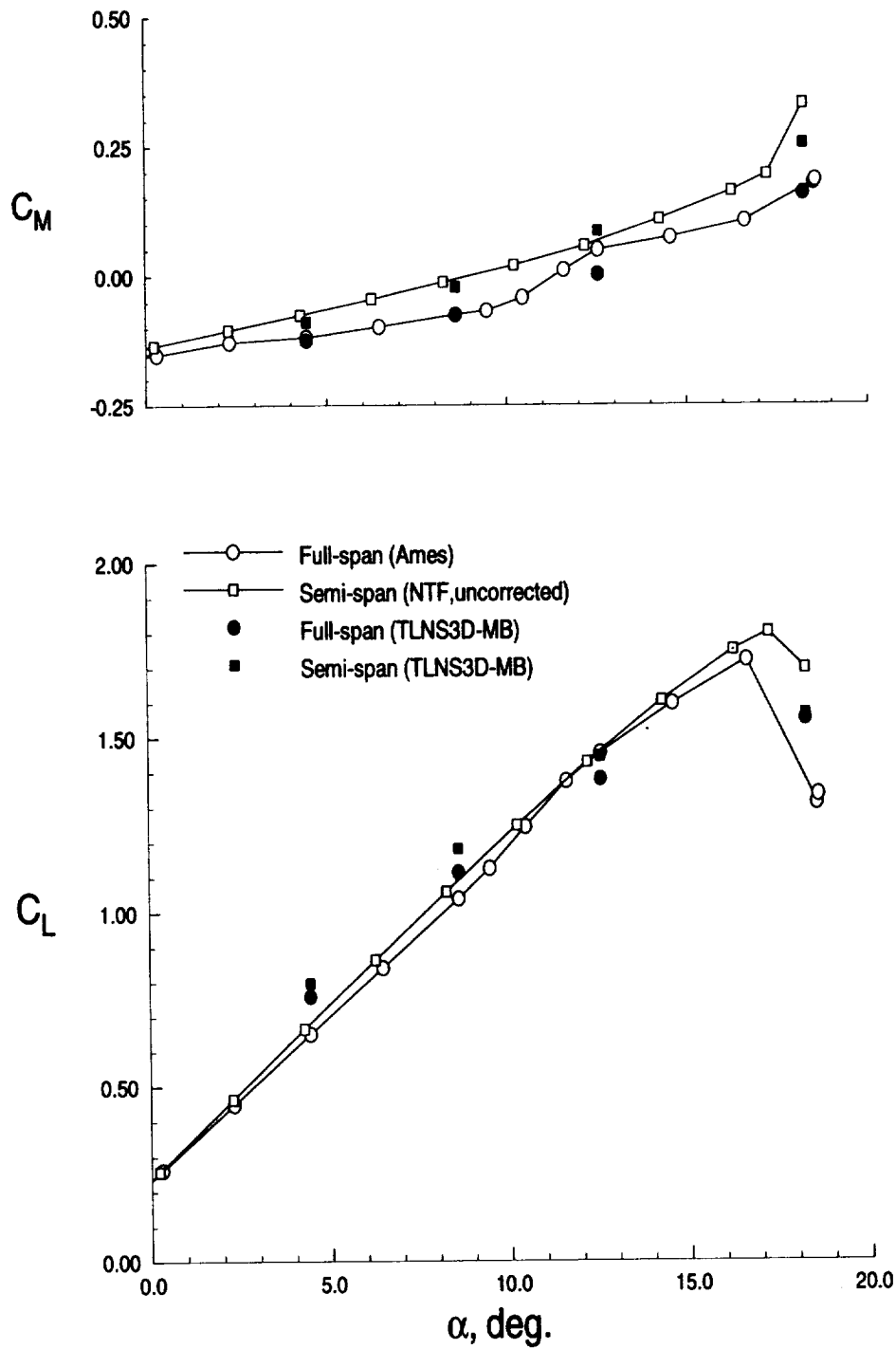


**Figure 56:** Comparison of full-span and semi-span lift and pitching moment coefficients ( $M_\infty = .20$ ,  $Re = 4.20 \times 10^6$ ).

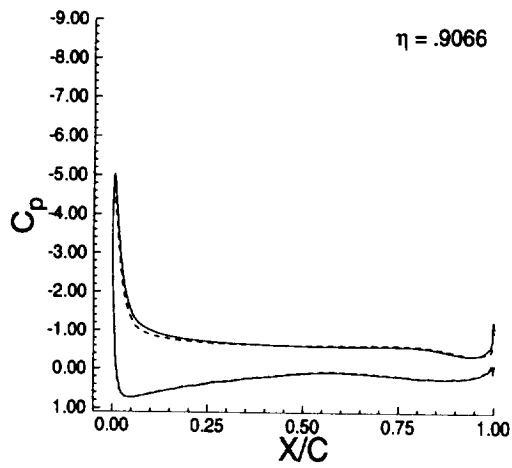
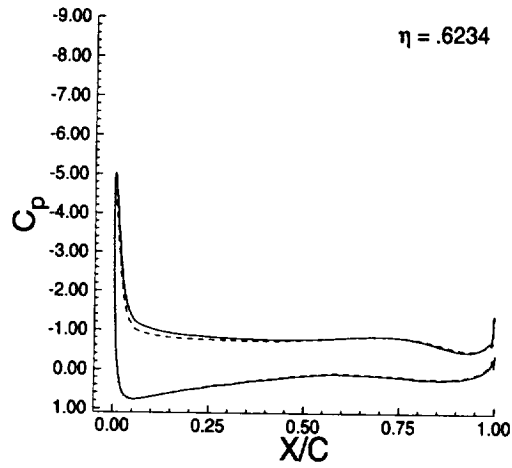
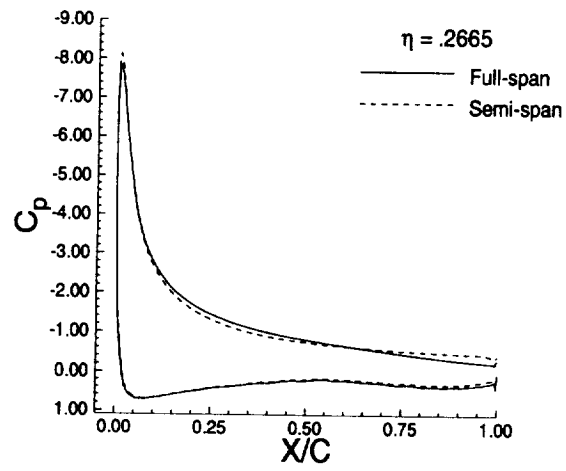


**Figure 57:** Comparison of computed full-span and semi-span pressure distributions ( $M_\infty = .20$ ,  $\alpha = 18.25^\circ$ ,  $Re = 4.20 \times 10^6$ ).

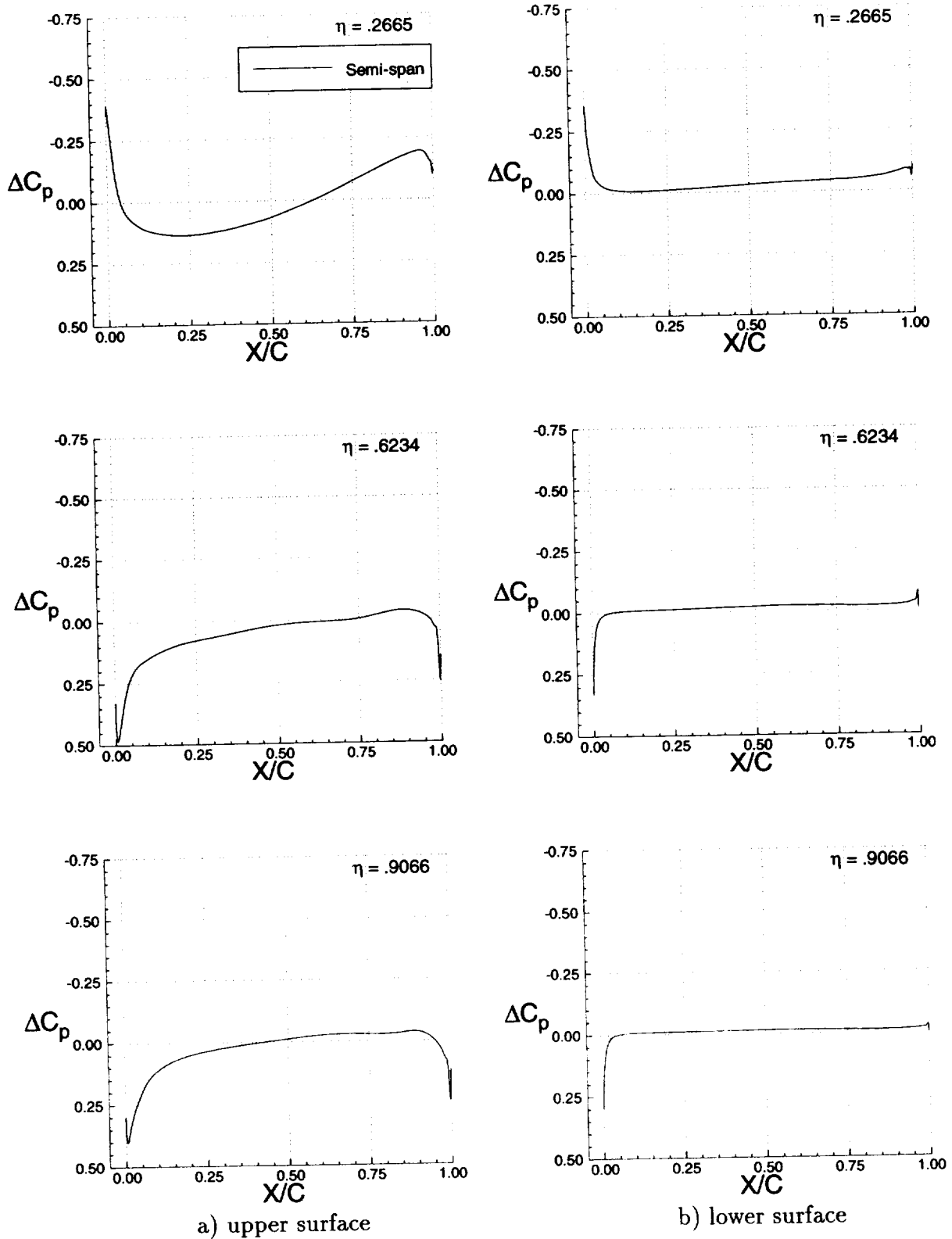
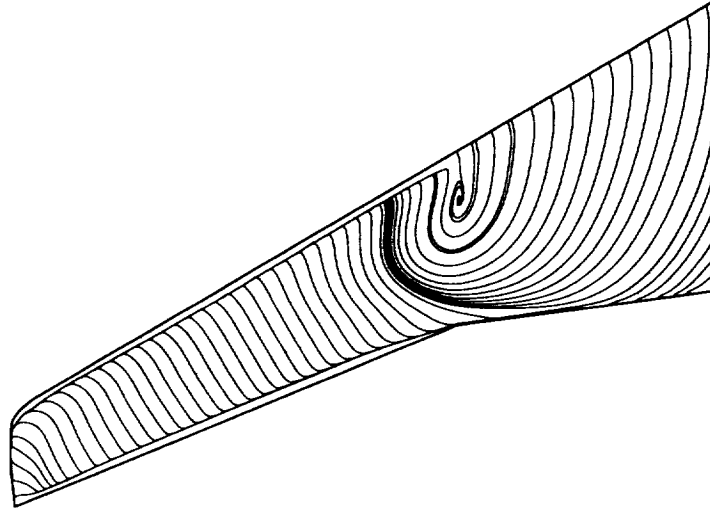


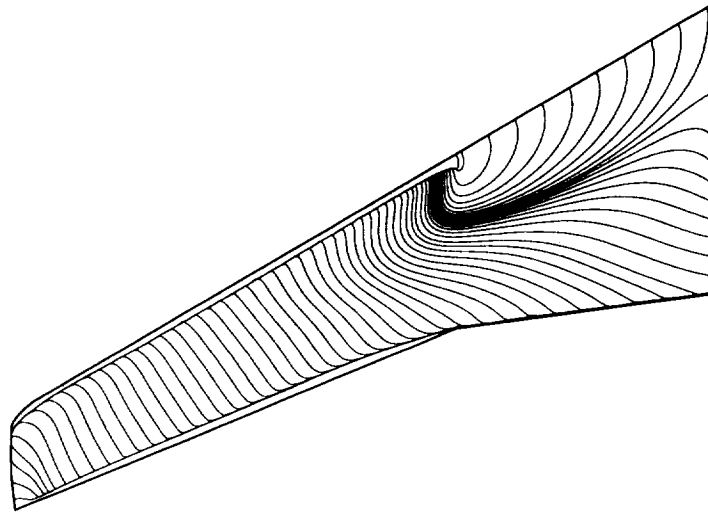
**Figure 58:** Computed differential wing pressure distributions ( $M_\infty = 0.20$ ,  $\alpha = 18.25^\circ$ ,  $Re = 4.20 \times 10^6$ ).



**Figure 59:** Comparison of computed full-span and semi-span fuselage centerline pressure distributions ( $M_\infty = .20$ ,  $\alpha = 18.25^\circ$ ,  $Re = 4.20 \times 10^6$ ).

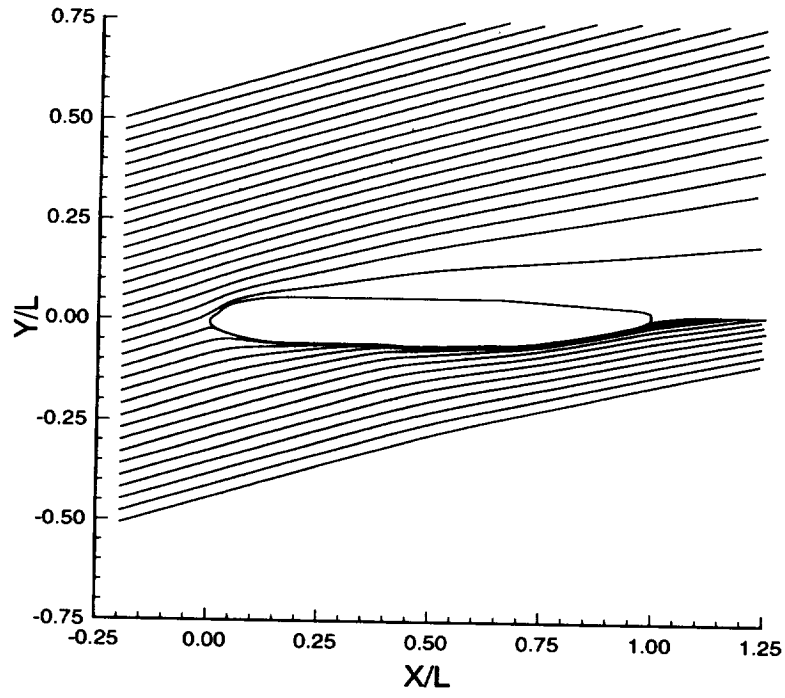


a) full-span

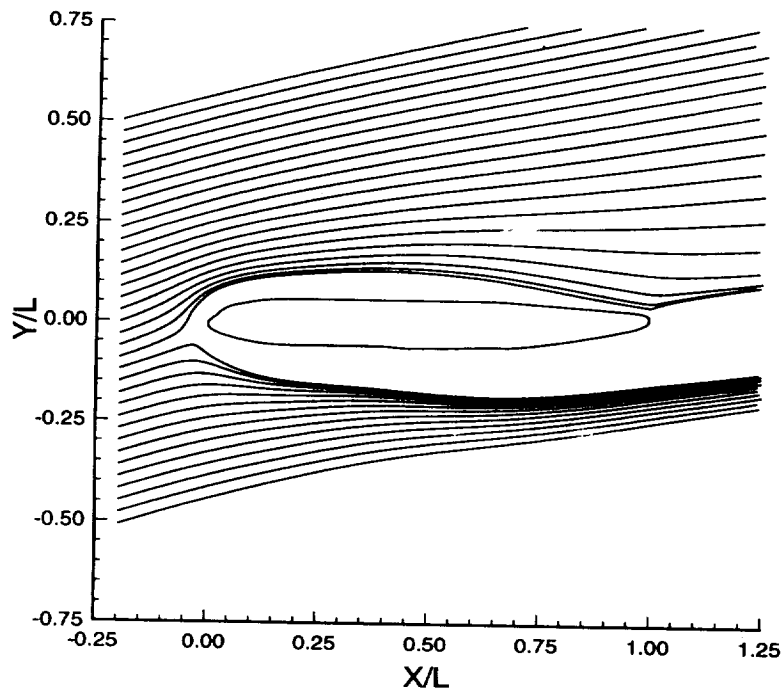


b) semi-span

**Figure 60:** Comparison of computed upper wing surface streamline patterns ( $M_\infty = .20$ ,  $\alpha = 18.25^\circ$ ,  $Re = 4.20 \times 10^6$ ).

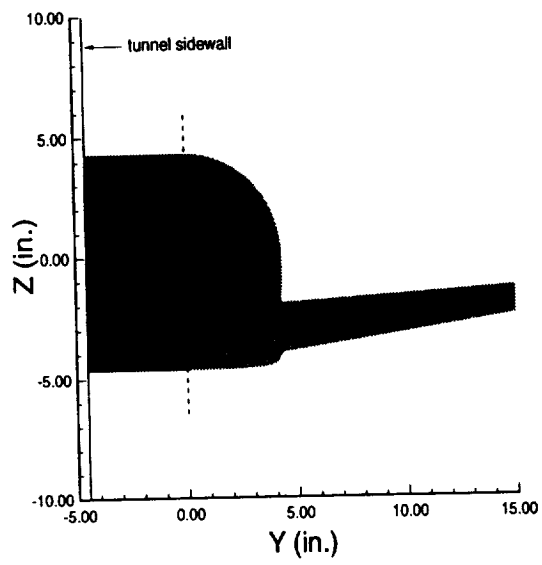


a) full-span

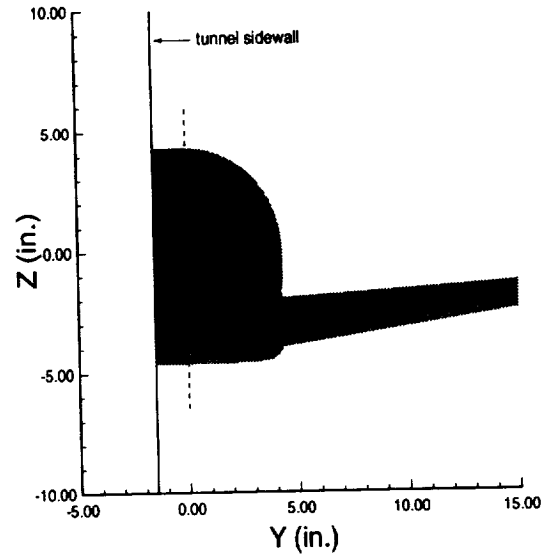


b) semi-span

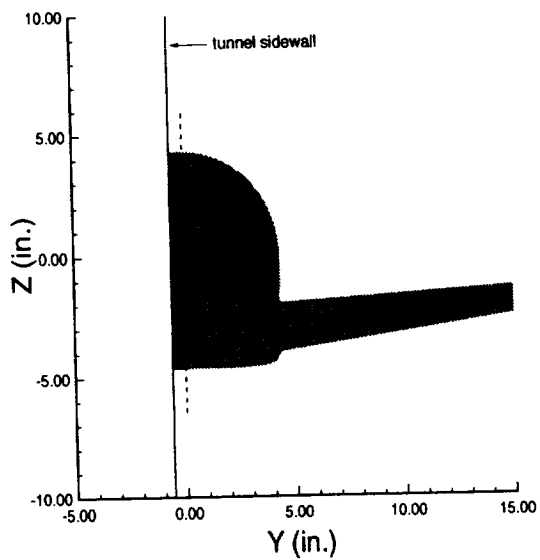
**Figure 61:** Comparison of root plane streamline patterns ( $M_\infty = 0.20$ ,  $\alpha = 18.25^\circ$ ,  $Re = 4.20 \times 10^6$ ).



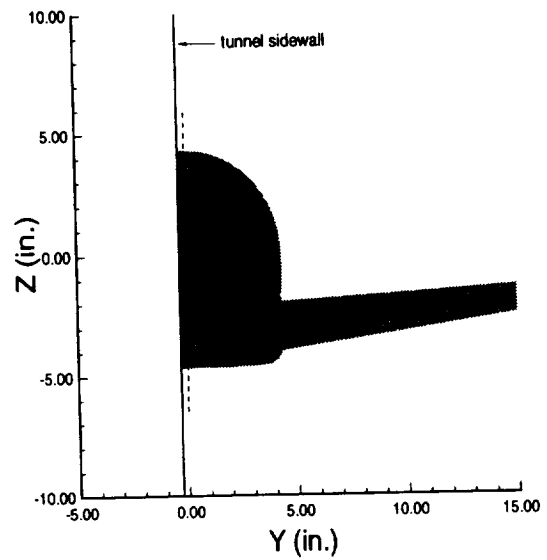
a)  $h = 15\delta^*$



b)  $h = 5\delta^*$



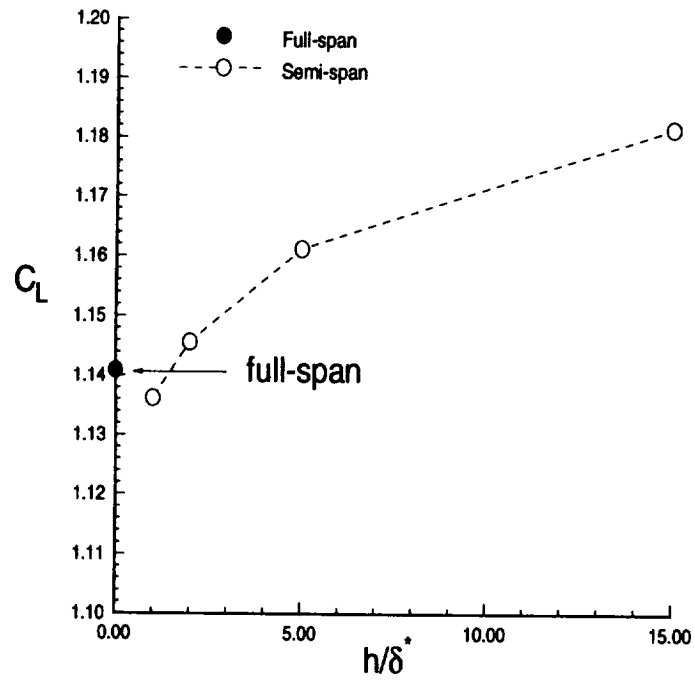
c)  $h = 2\delta^*$



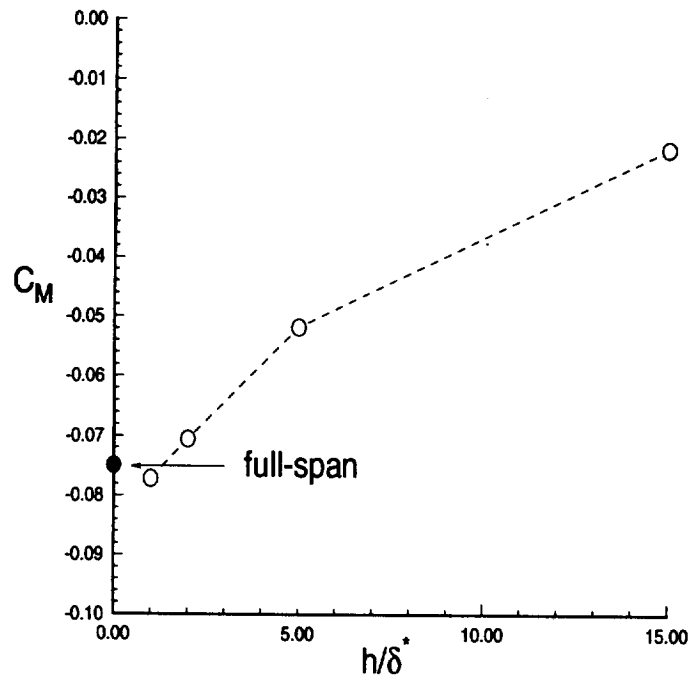
d)  $h = 1\delta^*$

**Figure 62:** Frontal view of various stand-off heights examined.





a) lift coefficient



b) pitching moment coefficient

**Figure 63:** Influence of stand-off height on lift and pitching moment coefficients ( $M_\infty = 0.20$ ,  $\alpha = 8.58^\circ$ ,  $Re = 4.20 \times 10^6$ ).

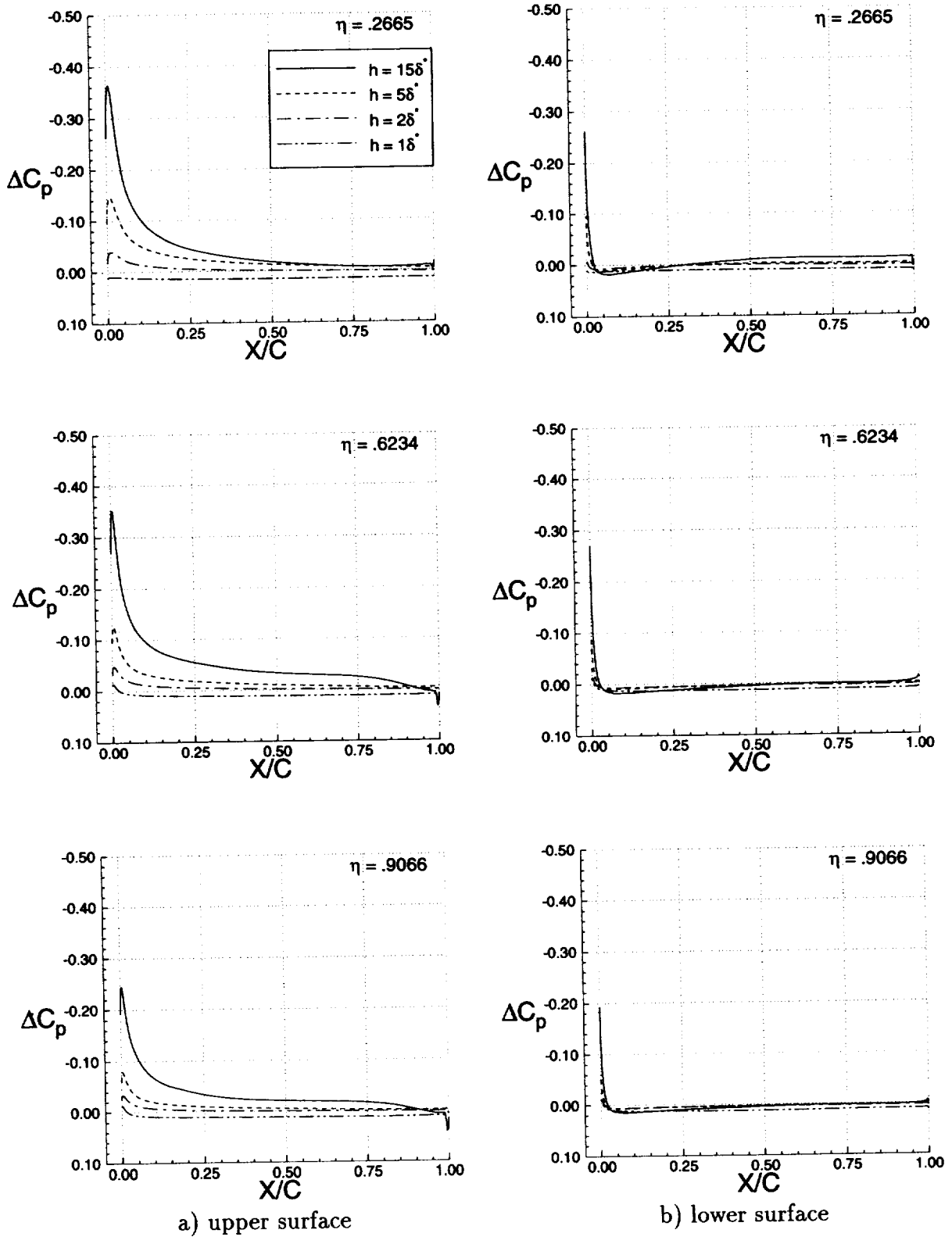


**Figure 64:** Influence of stand-off height on differential wing pressure distributions ( $M_\infty = 0.20$ ,  $\alpha = 8.58^\circ$ ,  $Re = 4.20 \times 10^6$ ).

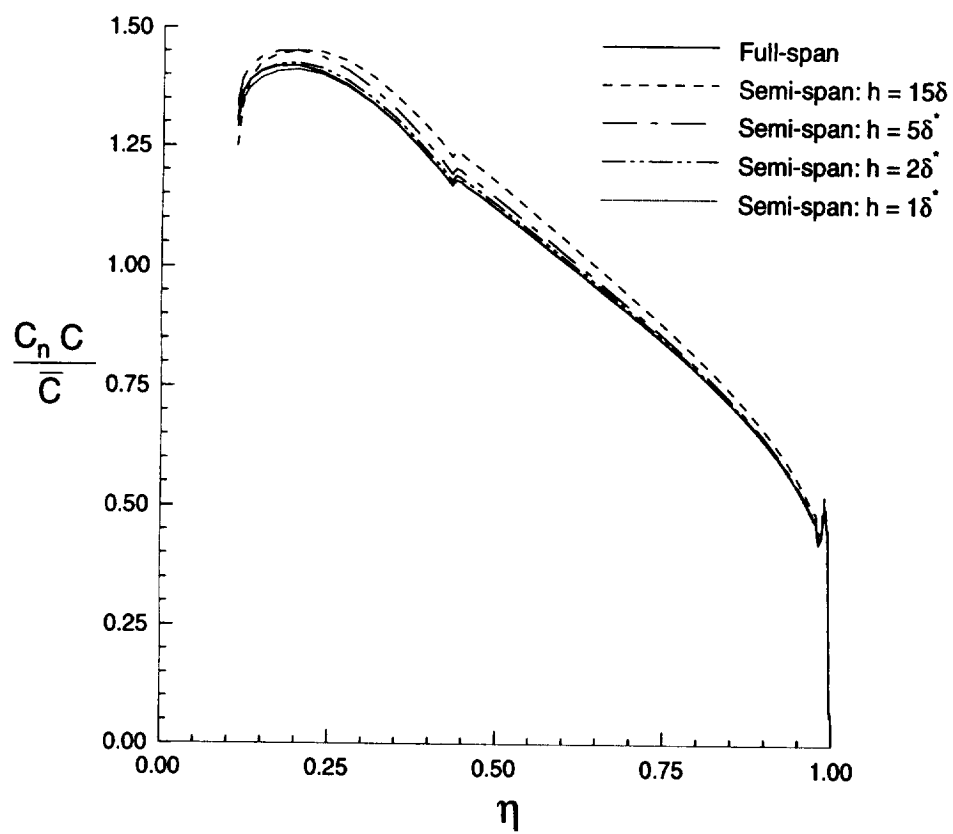
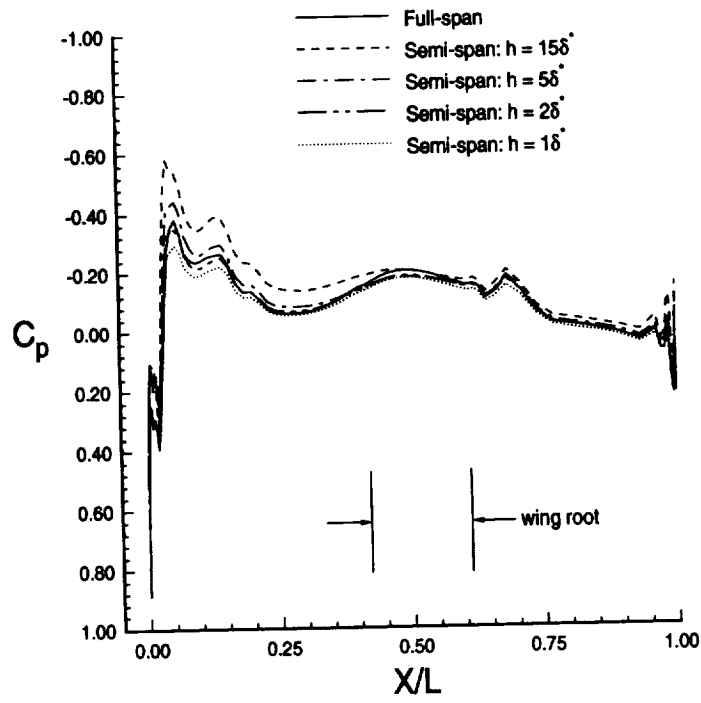
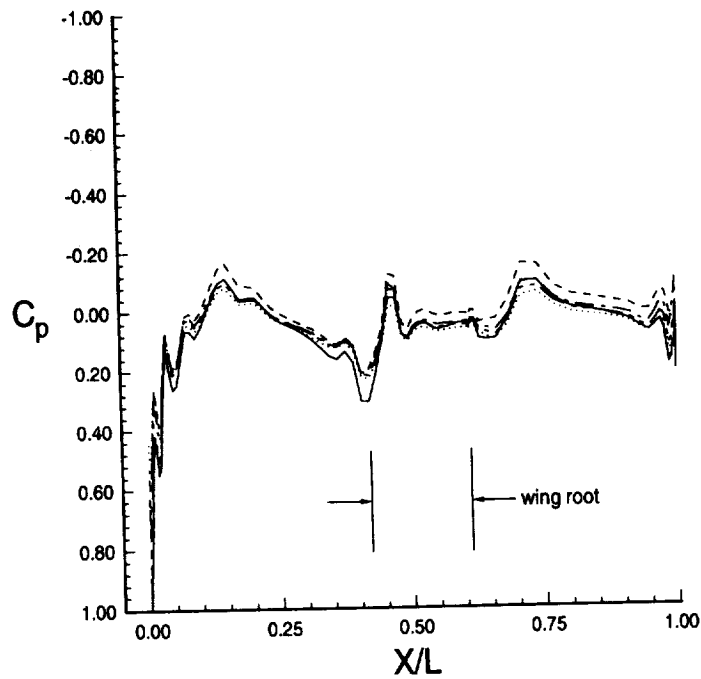


**Figure 65:** Influence of stand-off height on spanload distribution ( $M_\infty = 0.20$ ,  $\alpha = 8.58^\circ$ ,  $Re = 4.20 \times 10^6$ ).

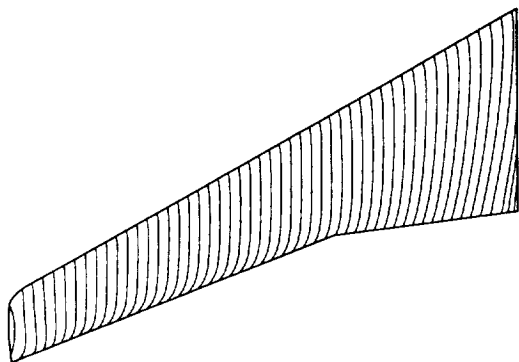


a) upper surface

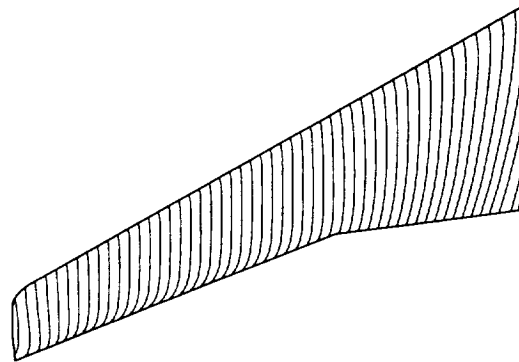


b) lower surface

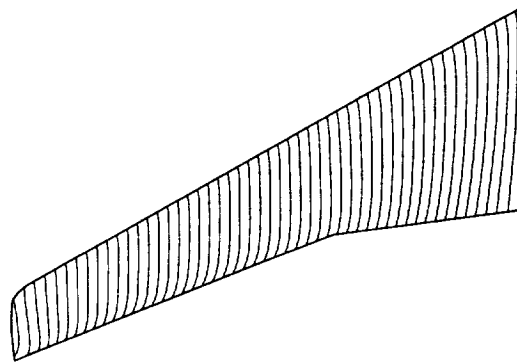
**Figure 66:** Influence of stand-off height on fuselage centerline pressure distribution ( $M_\infty = 0.20$ ,  $\alpha = 8.58^\circ$ ,  $Re = 4.20 \times 10^6$ ).



a) full-span



b) semi-span:  $h = 15\delta^*$

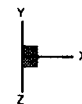


c) semi-span:  $h = 2\delta^*$

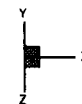
**Figure 67:** Influence of stand-off height on wing upper surface streamline patterns ( $M_\infty = 0.20$ ,  $\alpha = 8.58^\circ$ ,  $Re = 4.20 \times 10^6$ ).



a) full-span

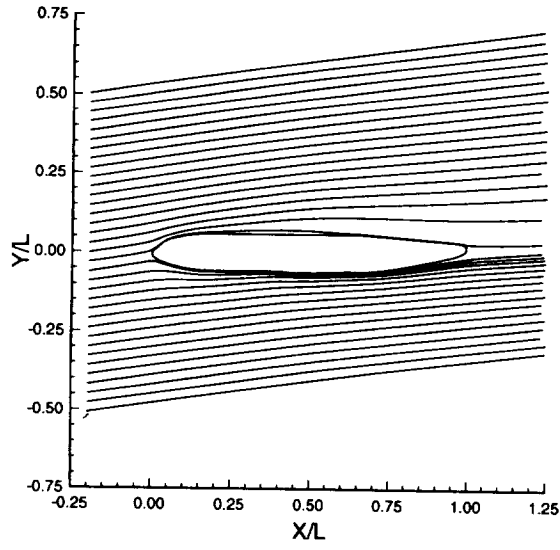


b) semi-span:  $h = 15\delta^*$

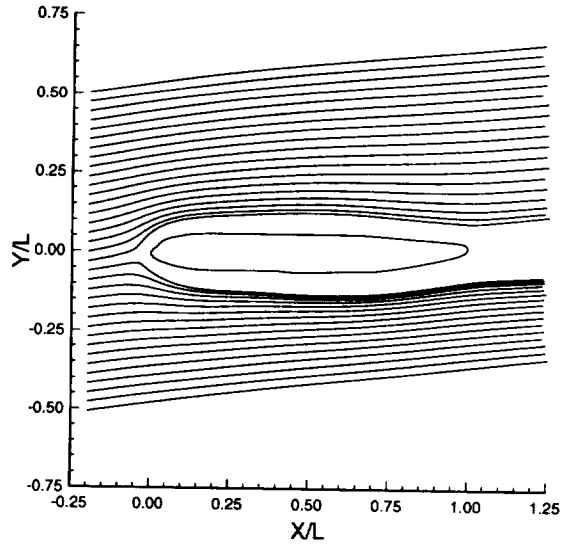


c) semi-span:  $h = 2\delta^*$

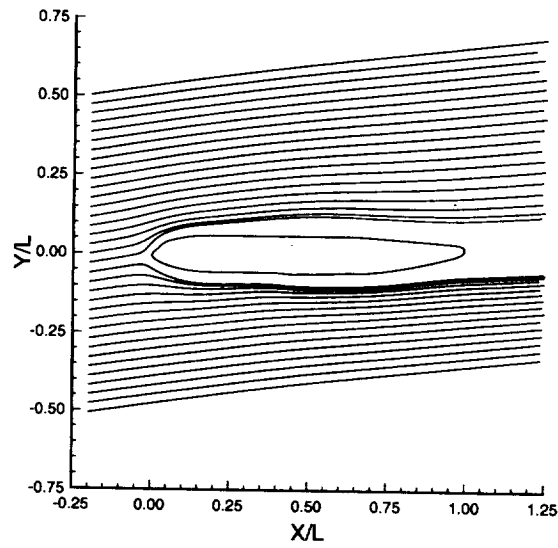
**Figure 68:** Influence of stand-off height on fuselage streamline pattern ( $M_\infty = 0.20$ ,  $\alpha = 8.58^\circ$ ,  $Re = 4.20 \times 10^6$ ).



a) full-span



b) semi-span:  $h = 15\delta^*$



c) semi-span:  $h = 2\delta^*$

**Figure 69:** Influence of stand-off height on root plane streamline patterns ( $M_\infty = 0.20$ ,  $\alpha = 8.58^\circ$ ,  $Re = 4.20 \times 10^6$ ).

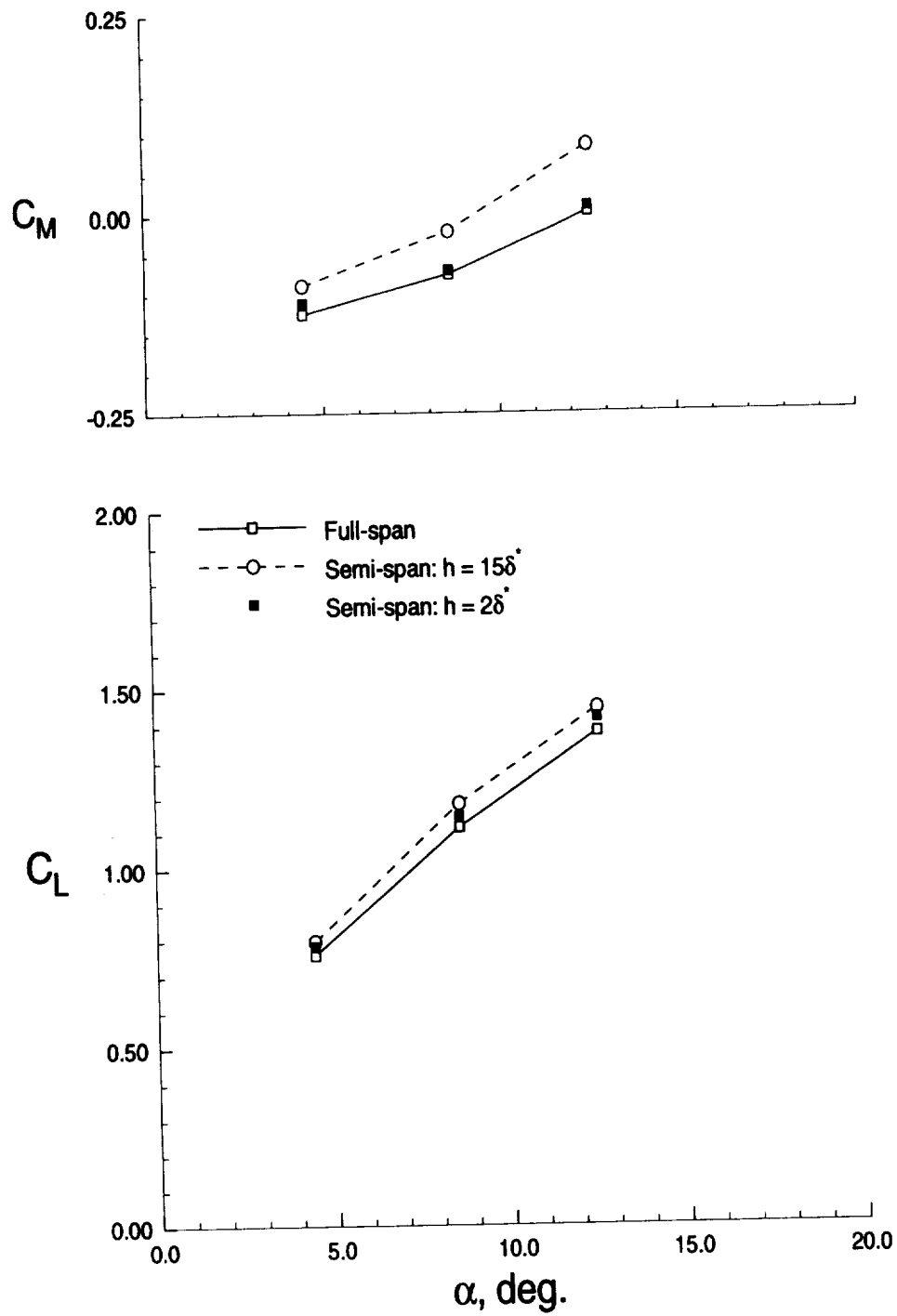


**Figure 70:** Influence of stand-off height on semi-span lift and pitching moment coefficients ( $M_\infty = .20$ ,  $Re = 4.20 \times 10^6$ ).



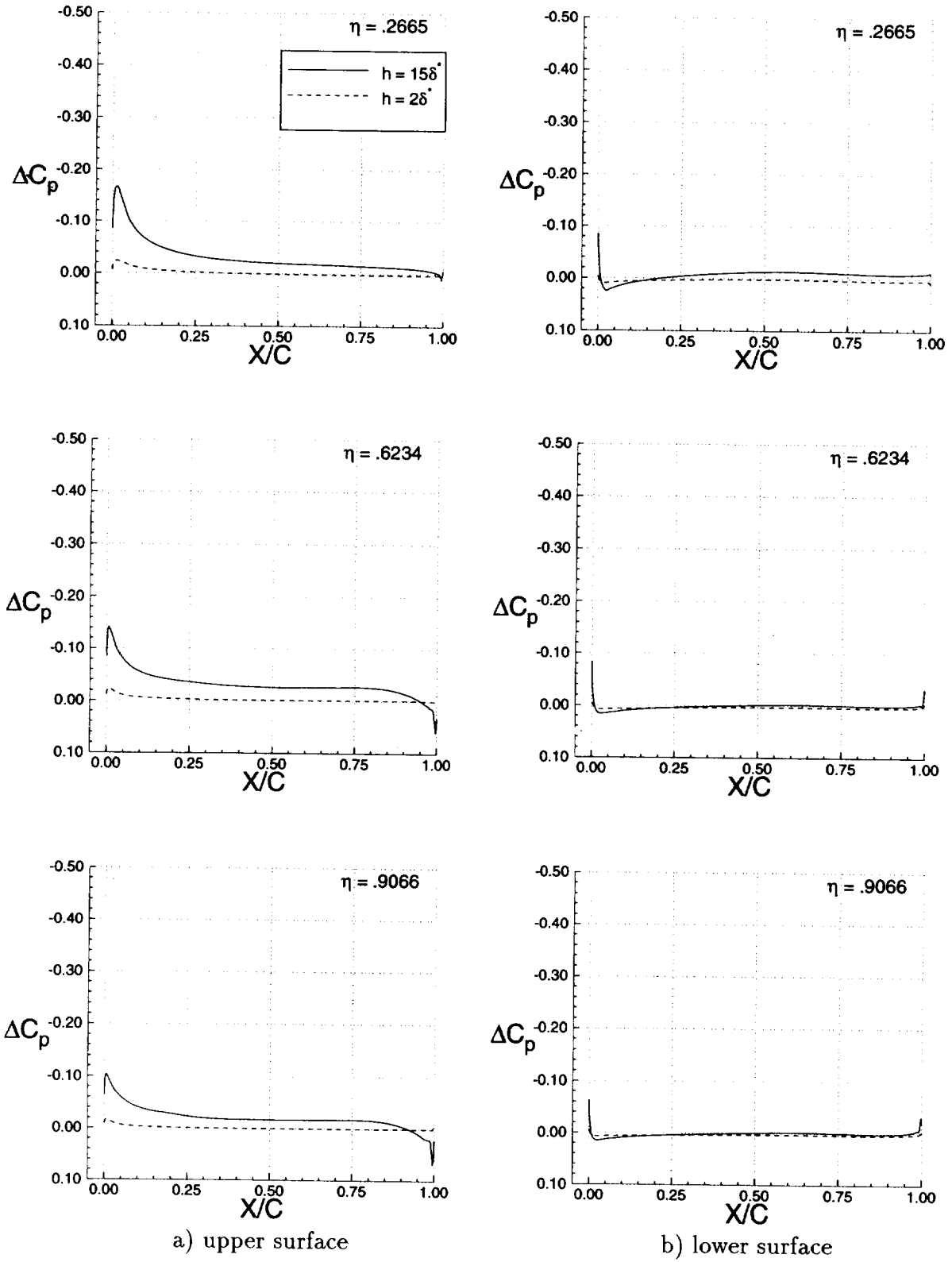


**Figure 71:** Influence of stand-off height on differential wing pressure distributions ( $M_\infty = 0.20$ ,  $\alpha = 4.43^\circ$ ,  $Re = 4.20 \times 10^6$ ).

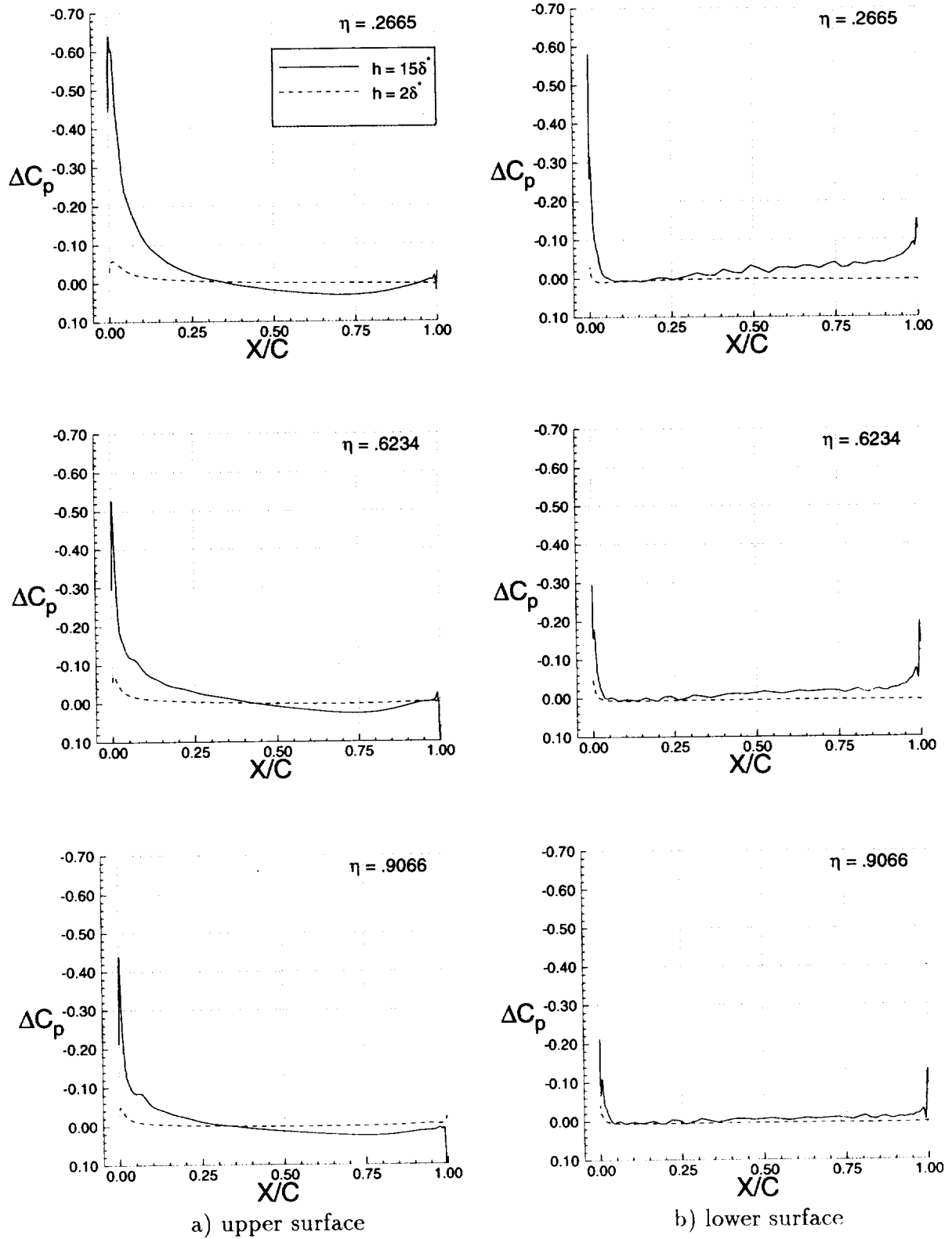


**Figure 72:** Influence of stand-off height on differential wing pressure distributions ( $M_\infty = 0.20$ ,  $\alpha = 12.55^\circ$ ,  $Re = 4.20 \times 10^6$ ).

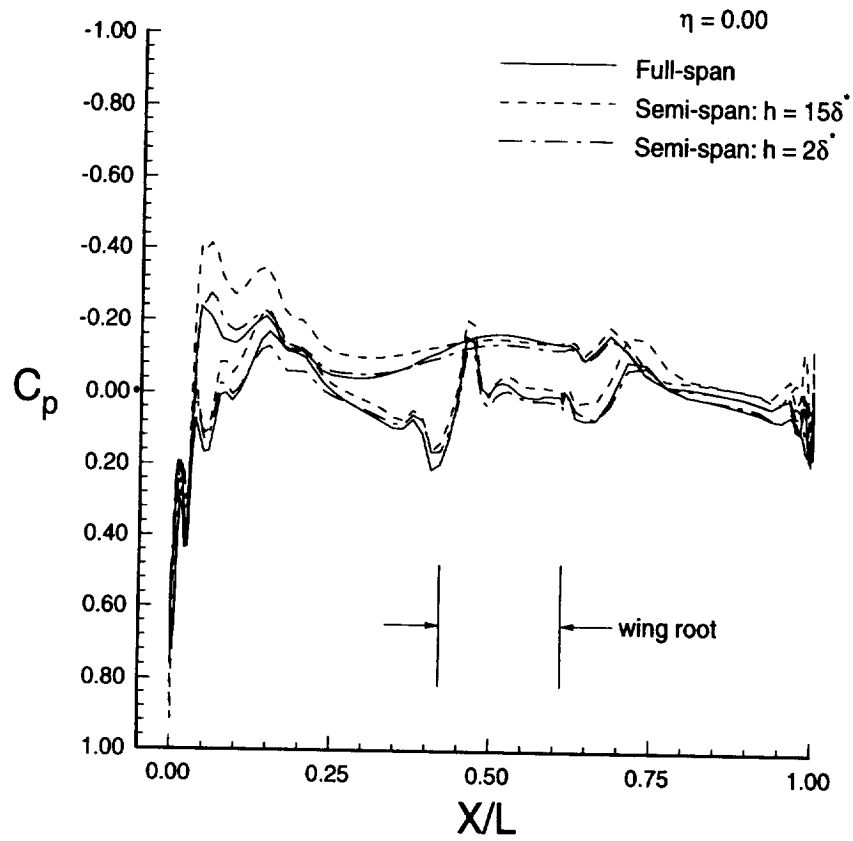


**Figure 73:** Influence of stand-off height on fuselage centerline pressure distribution ( $M_\infty = 0.20$ ,  $\alpha = 4.43^\circ$ ,  $Re = 4.20 \times 10^6$ ).

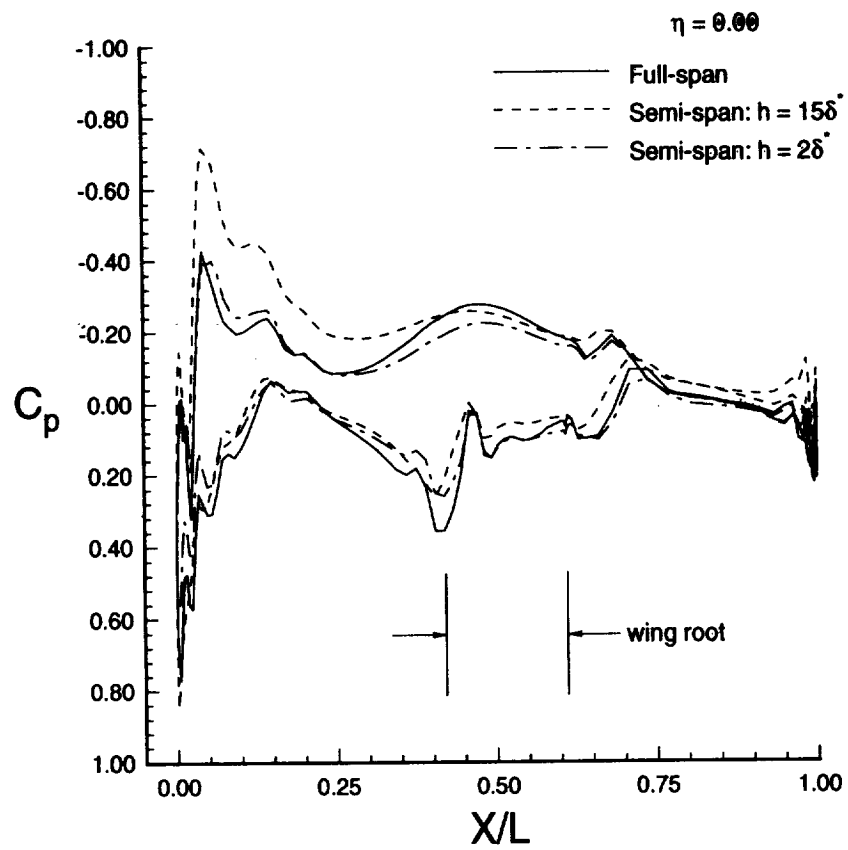
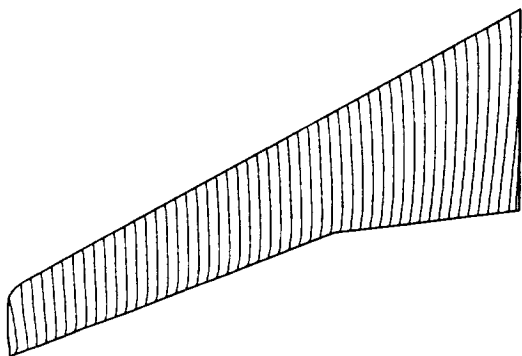
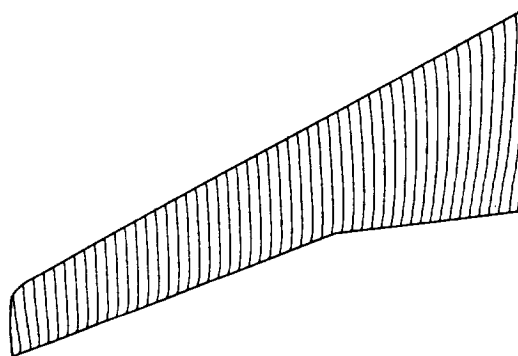


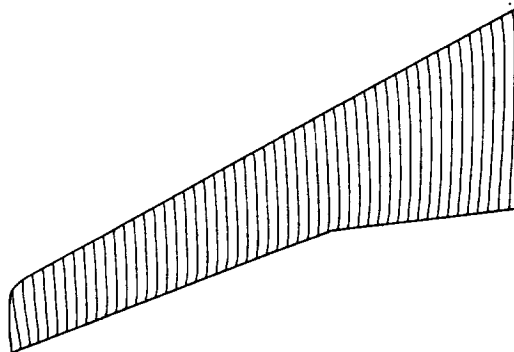
**Figure 74:** Influence of stand-off height on fuselage centerline pressure distribution ( $M_\infty = 0.20$ ,  $\alpha = 12.55^\circ$ ,  $Re = 4.20 \times 10^6$ ).



a) full-span

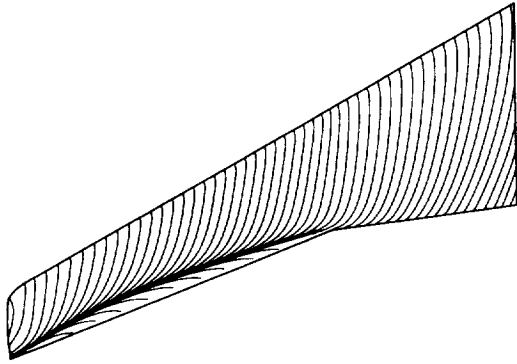


b) semi-span:  $h = 15\delta^*$

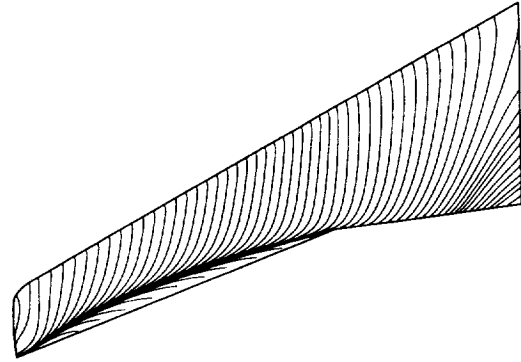


c) semi-span:  $h = 2\delta^*$

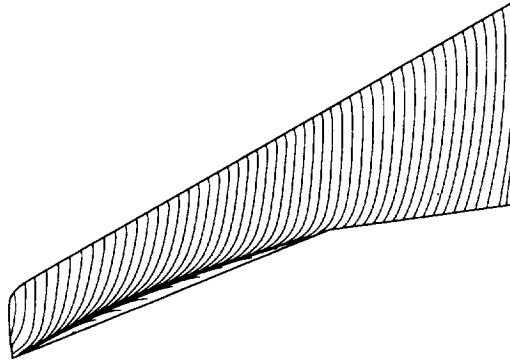
**Figure 75:** Influence of stand-off height on wing upper surface streamline patterns ( $M_\infty = 0.20$ ,  $\alpha = 4.43^\circ$ ,  $Re = 4.20 \times 10^6$ ).



a) full-span



b) semi-span:  $h = 15\delta^*$



c) semi-span:  $h = 2\delta^*$

**Figure 76:** Influence of stand-off height on wing upper surface streamline patterns ( $M_\infty = 0.20$ ,  $\alpha = 12.55^\circ$ ,  $Re = 4.20 \times 10^6$ ).

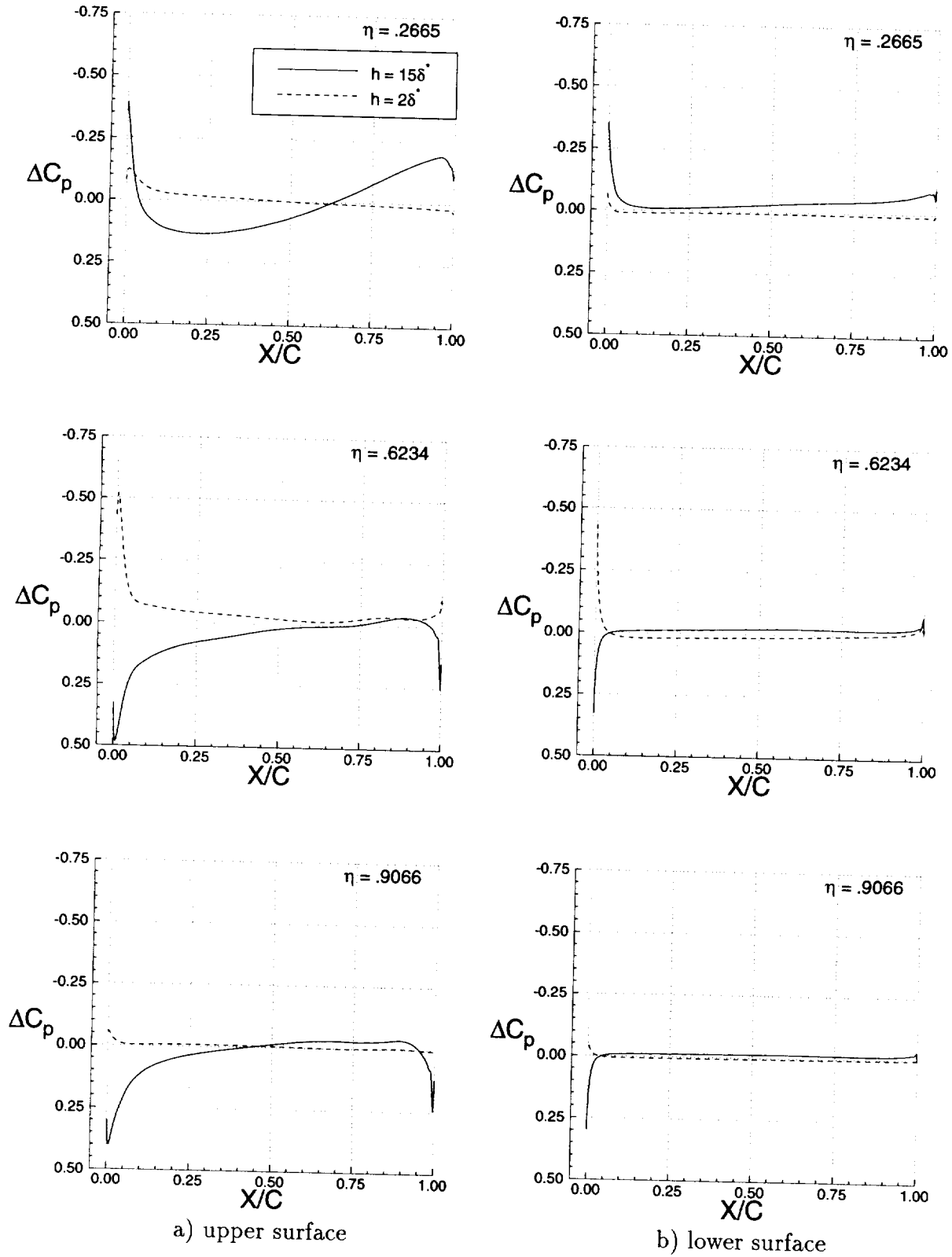


**Figure 77:** Influence of stand-off height on differential wing pressure distributions ( $M_\infty = 0.20$ ,  $\alpha = 18.25^\circ$ ,  $Re = 4.20 \times 10^6$ ).

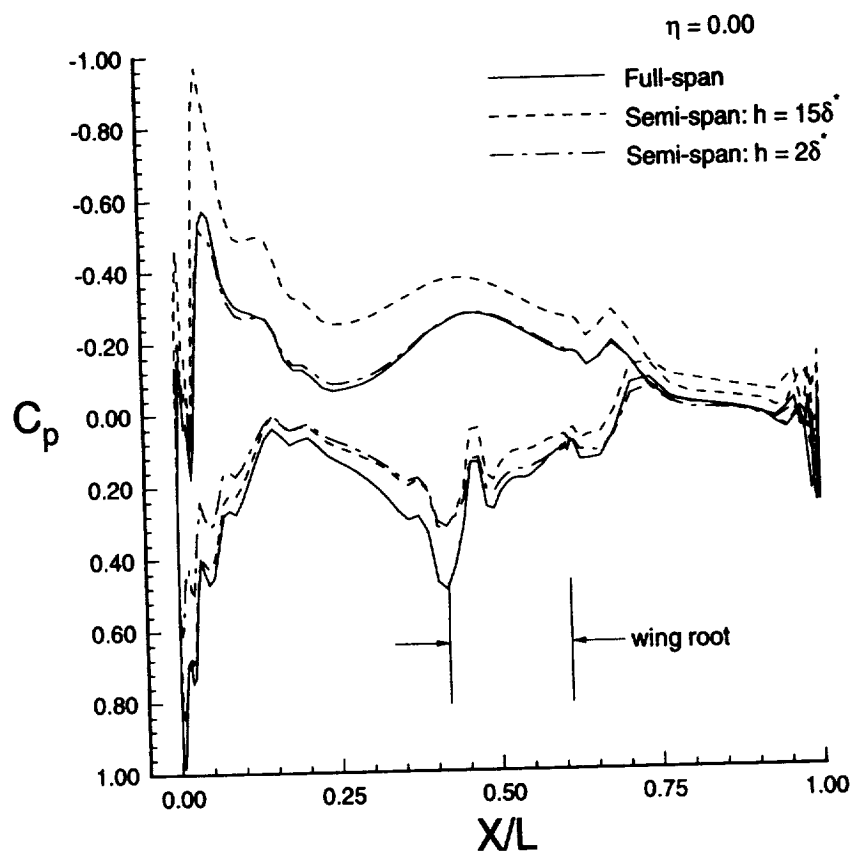
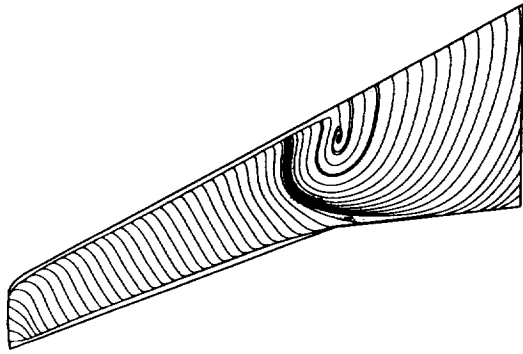
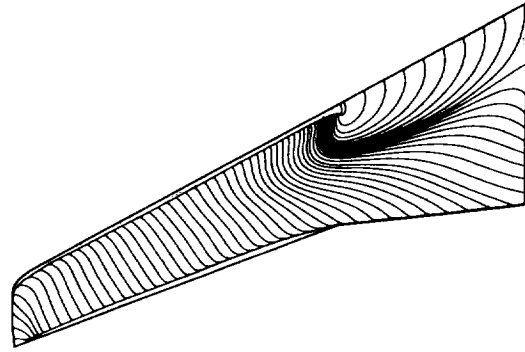


**Figure 78:** Influence of stand-off height on fuselage centerline pressure distributions ( $M_\infty = 0.20$ ,  $\alpha = 18.25^\circ$ ,  $Re = 4.20 \times 10^6$ ).

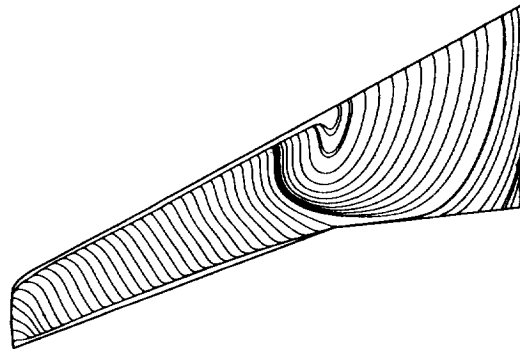




a) full-span



b) semi-span:  $h = 15\delta^*$



c) semi-span:  $h = 2\delta^*$

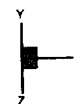
**Figure 79:** Influence of stand-off height on upper wing surface streamline patterns ( $M_\infty = 0.20$ ,  $\alpha = 18.25^\circ$ ,  $Re = 4.20 \times 10^6$ ).



a) full-span

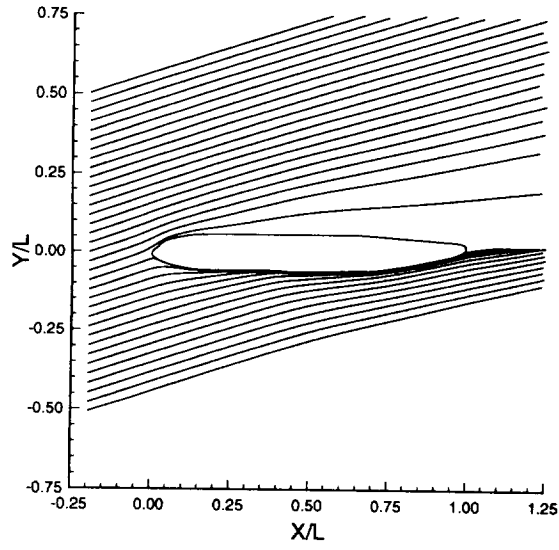


b) semi-span:  $h = 15\delta^*$

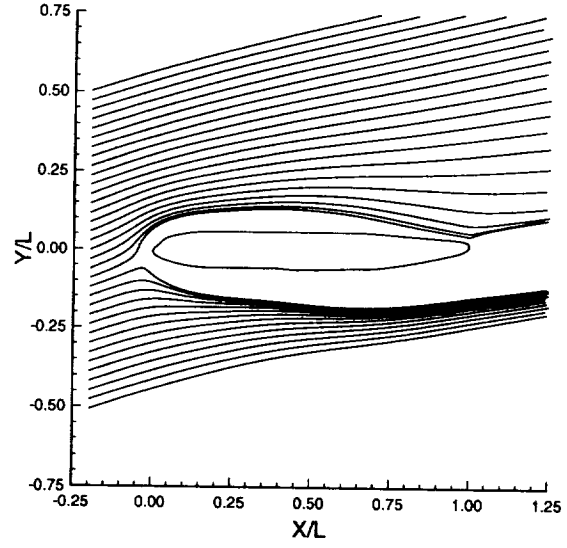


c) semi-span:  $h = 2\delta^*$

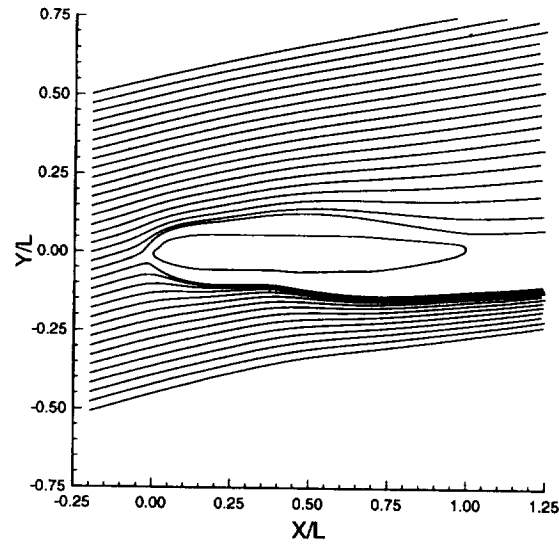
**Figure 80:** Influence of stand-off height on fuselage streamline pattern ( $M_\infty = 0.20$ ,  $\alpha = 18.25^\circ$ ,  $Re = 4.20 \times 10^6$ ).



a) full-span

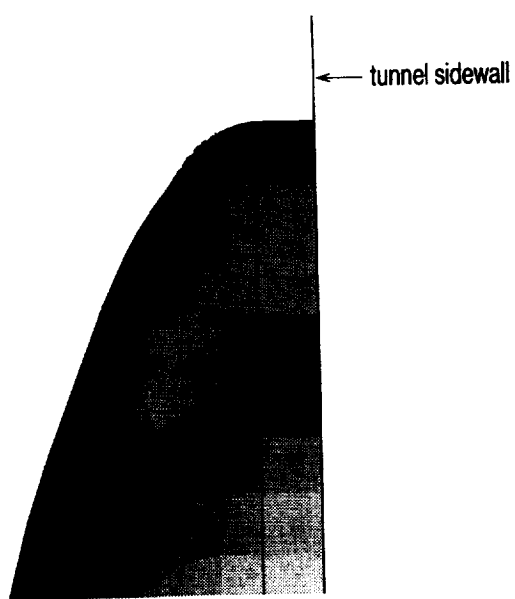


b) semi-span:  $h = 15\delta^*$

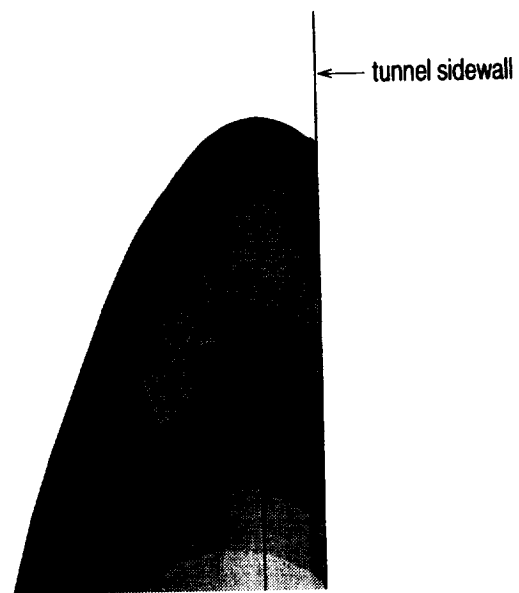


c) semi-span:  $h = 2\delta^*$

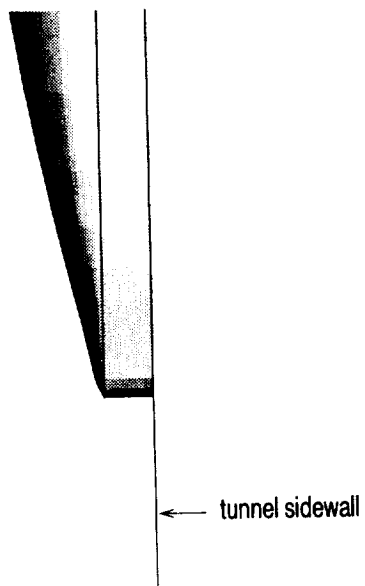
**Figure 81:** Influence of stand-off height on root plane streamline patterns ( $M_\infty = 0.20$ ,  $\alpha = 18.25^\circ$ ,  $Re = 4.20 \times 10^6$ ).



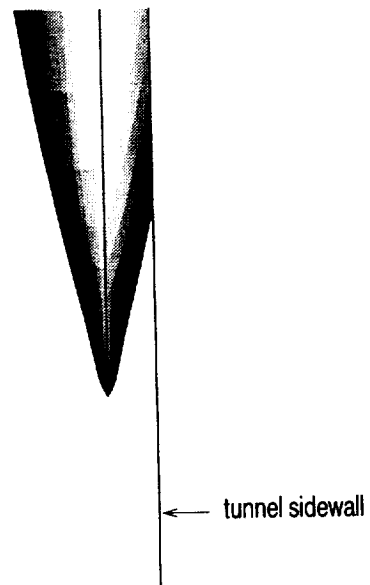
a) nose, 2-D stand-off



b) nose, 3-D stand-off

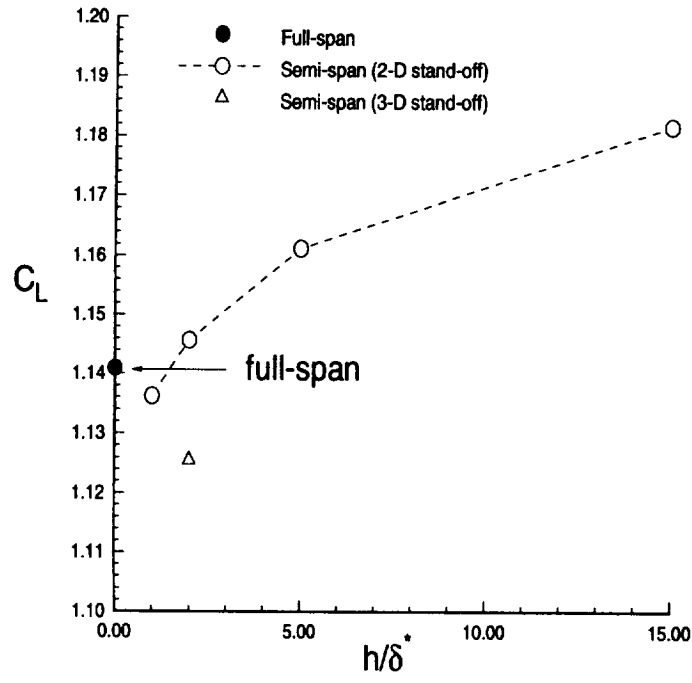


c) tail, 2-D stand-off

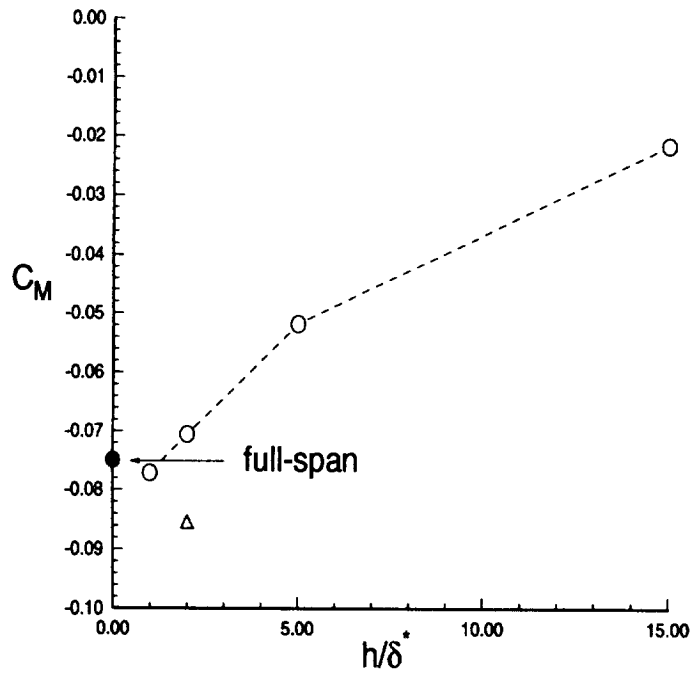


d) tail, 3-D stand-off

**Figure 82:** Comparison of 2-D and 3-D stand-off geometries.



a) lift coefficient



b) pitching moment coefficient

**Figure 83:** Influence of stand-off shape on lift and pitching moment coefficients ( $M_\infty = 0.20$ ,  $\alpha = 8.58^\circ$ ,  $Re = 4.20 \times 10^6$ ).

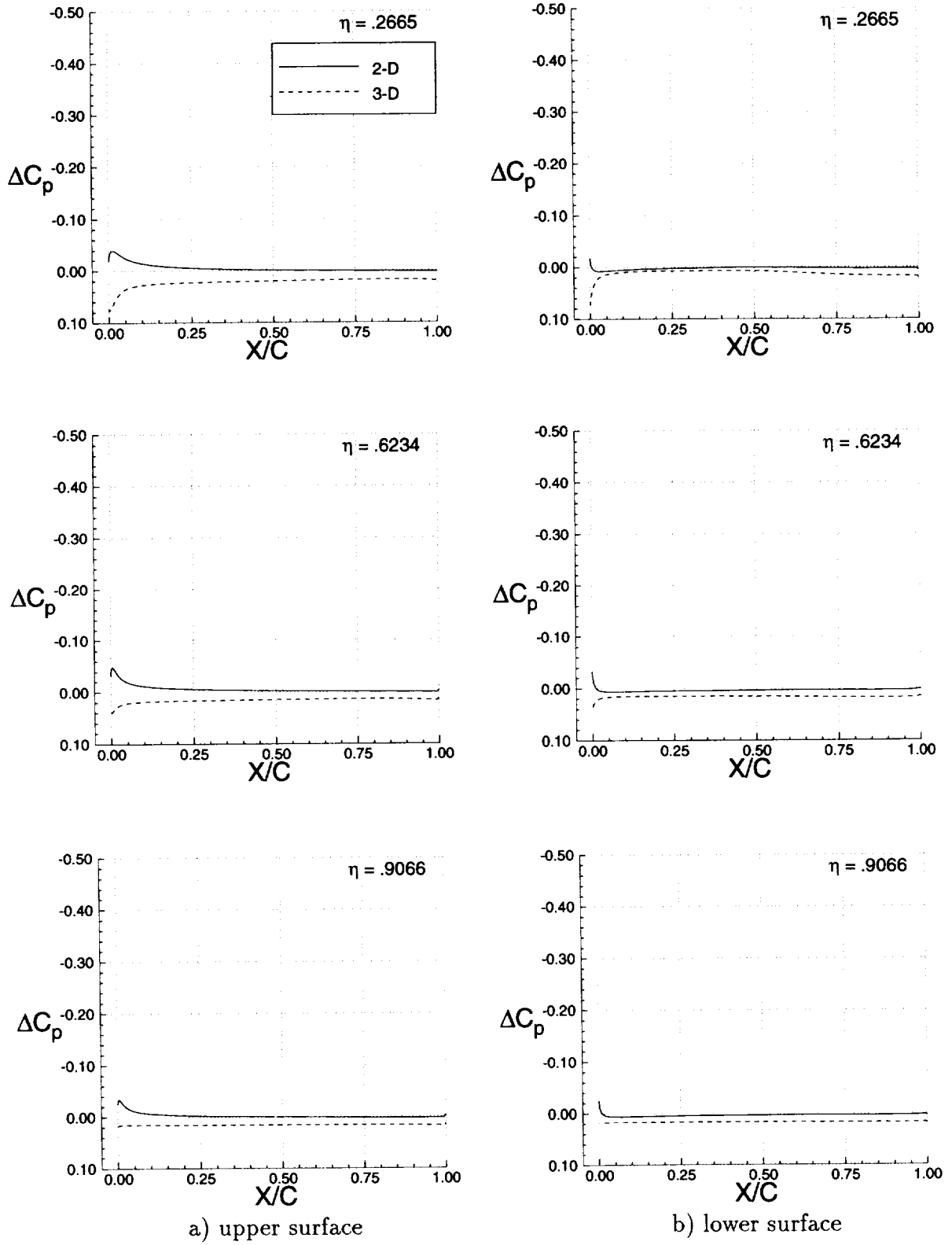
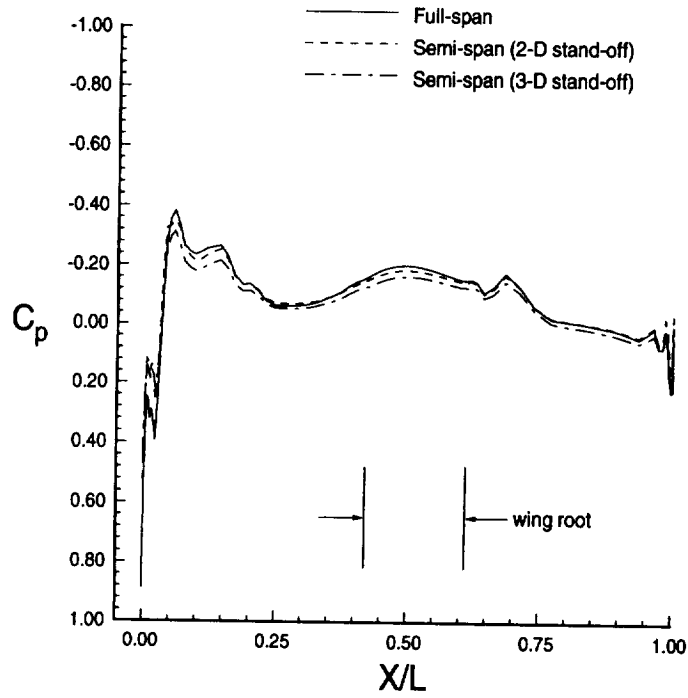
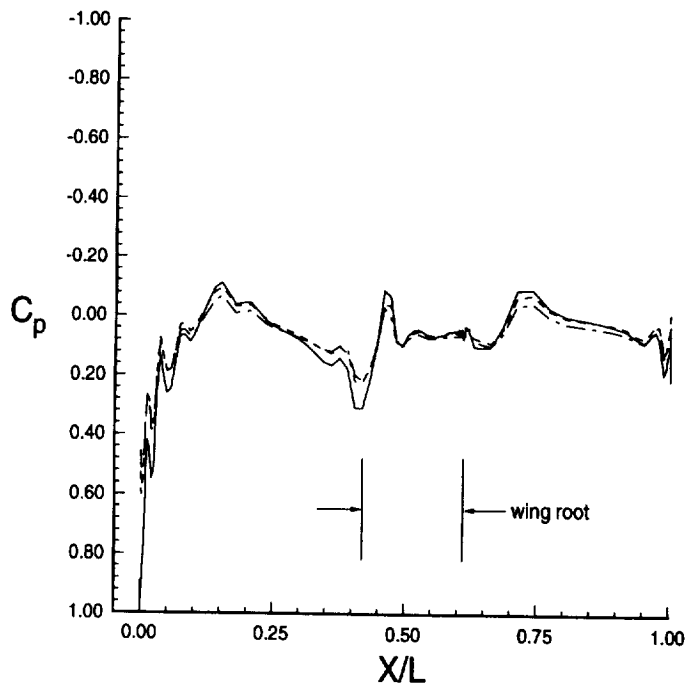


**Figure 84:** Influence of stand-off shape on differential wing pressure distributions ( $M_\infty = 0.20$ ,  $\alpha = 8.58^\circ$ ,  $Re = 4.20 \times 10^6$ ).

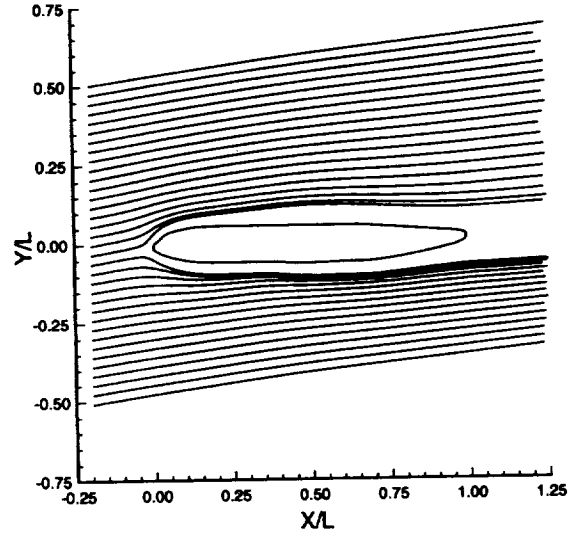


a) upper surface

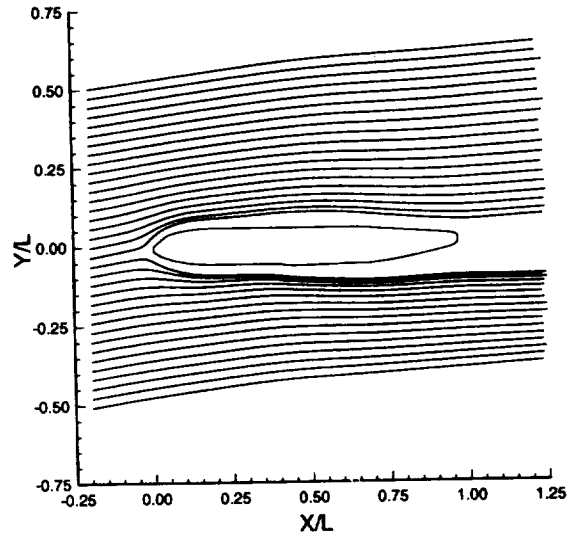


b) lower surface

**Figure 85:** Influence of stand-off shape on fuselage centerline pressure distribution ( $M_\infty = 0.20$ ,  $\alpha = 8.58^\circ$ ,  $Re = 4.20 \times 10^6$ ).



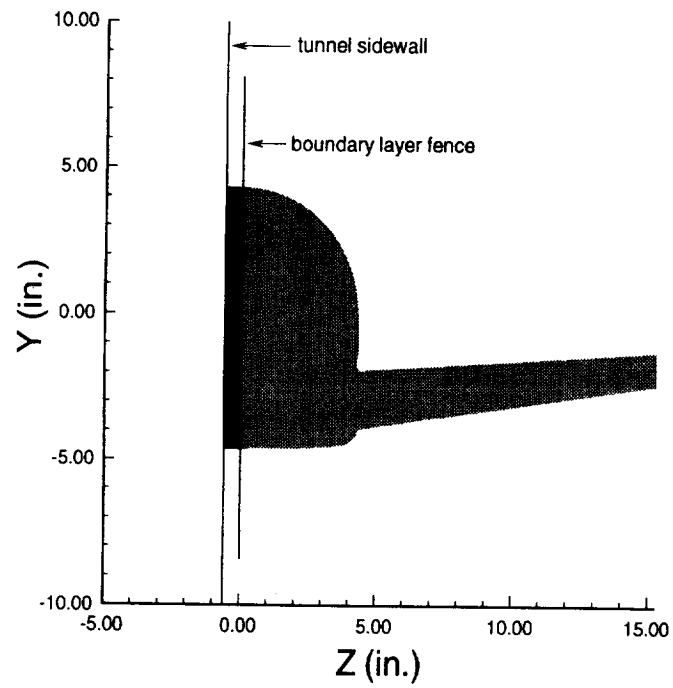
a) 2-D stand-off



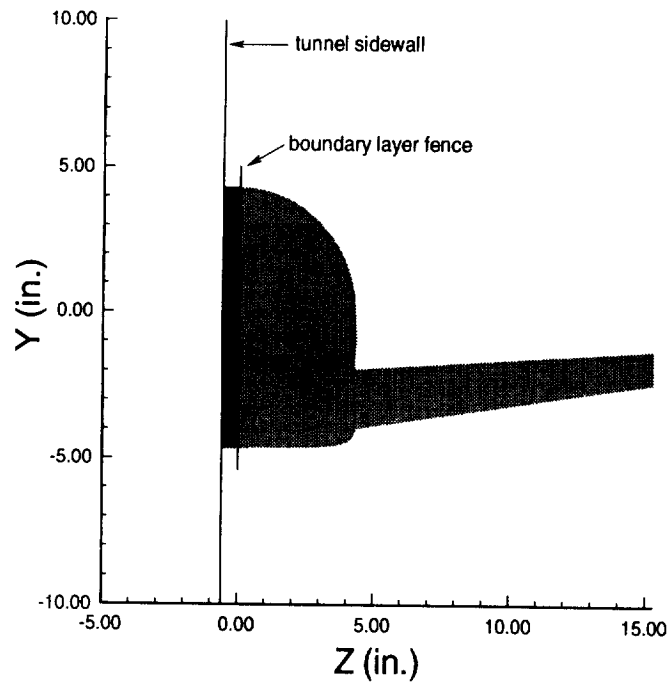
b) 3-D stand-off

**Figure 86:** Influence of stand-off shape on root plane streamline patterns ( $M_\infty = 0.20$ ,  $\alpha = 8.58^\circ$ ,  $Re = 4.20 \times 10^6$ ).





a)  $h_f = 4.00$  inches.



b)  $h_f = 0.75$  inches.

**Figure 87:** Frontal view of stand-off boundary layer fences.

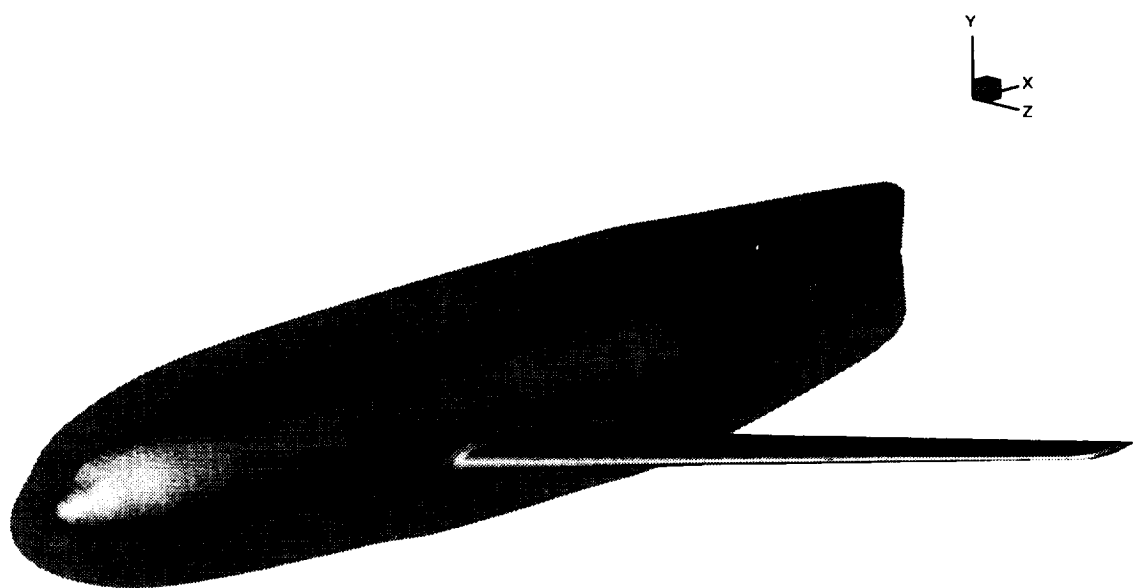
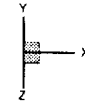
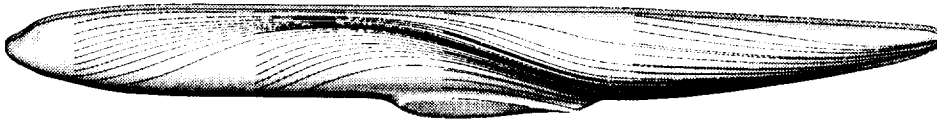


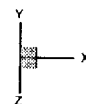
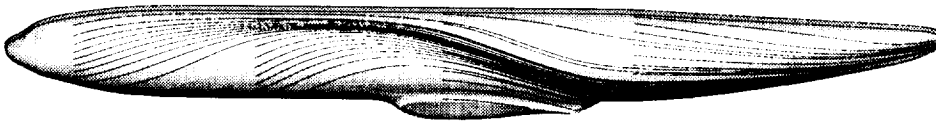
**Figure 88:** Oblique view of 4.0 inch stand-off boundary layer fence.



a) full-span



b) semi-span:  $h_f = 0.00\text{in.}$



c) semi-span:  $h_f = 4.00\text{in.}$

**Figure 89:** Comparison of fuselage streamline patterns ( $M_\infty = 0.20$ ,  $\alpha = 12.55^\circ$ ,  $\text{Re} = 4.20 \times 10^6$ ).

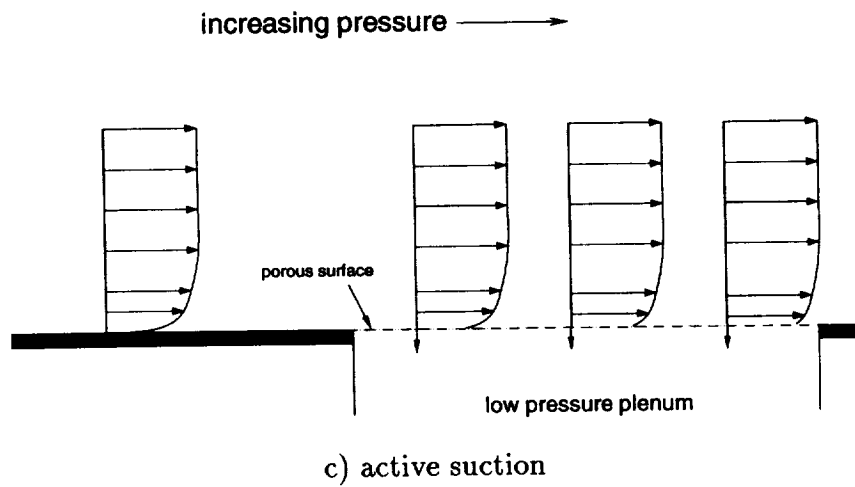
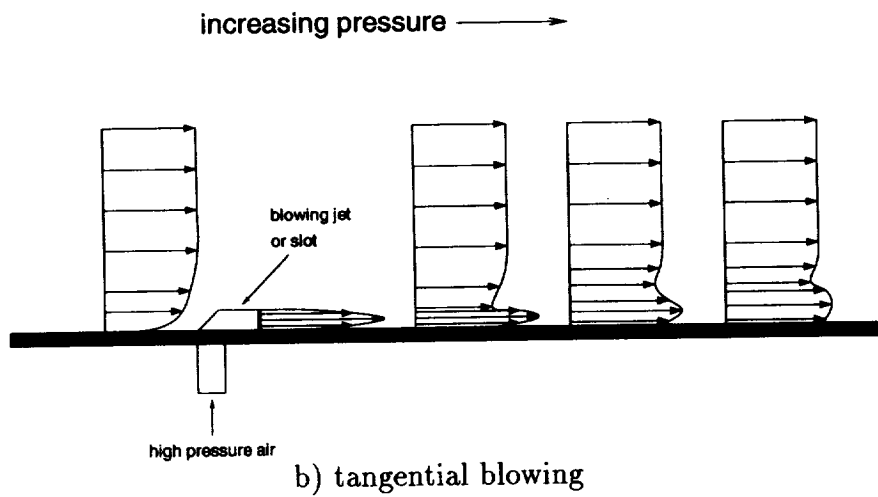
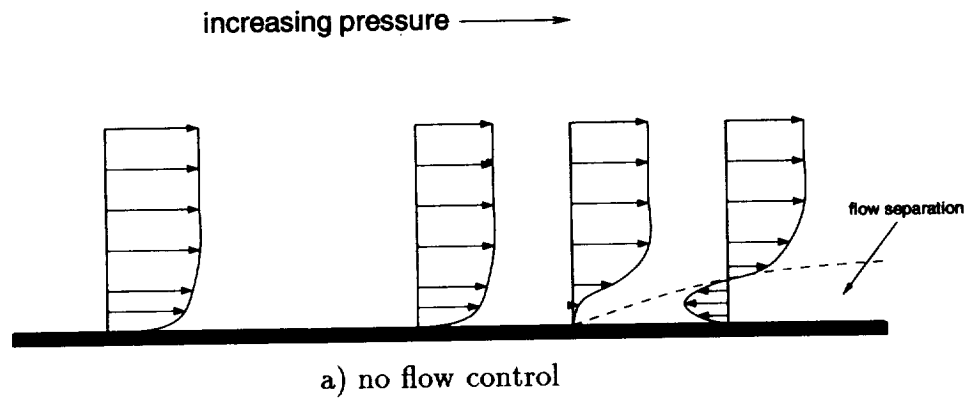


**Figure 90:** Comparison of boundary layer control techniques.

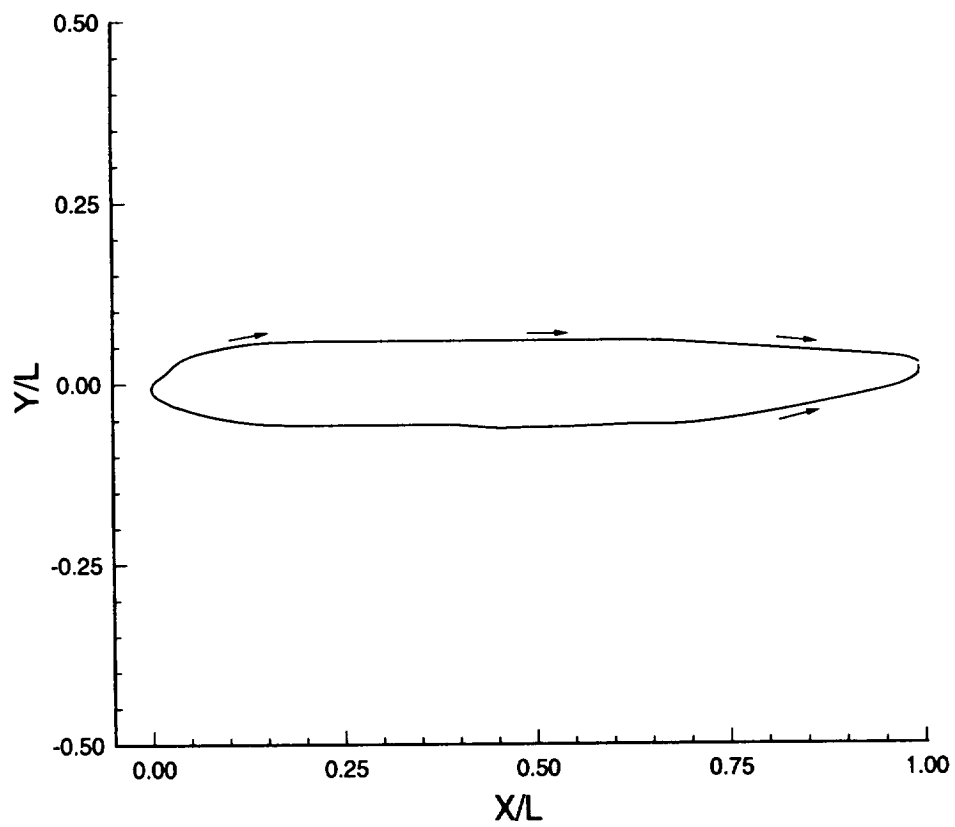


**Figure 91:** Location of juncture region blowing jets.

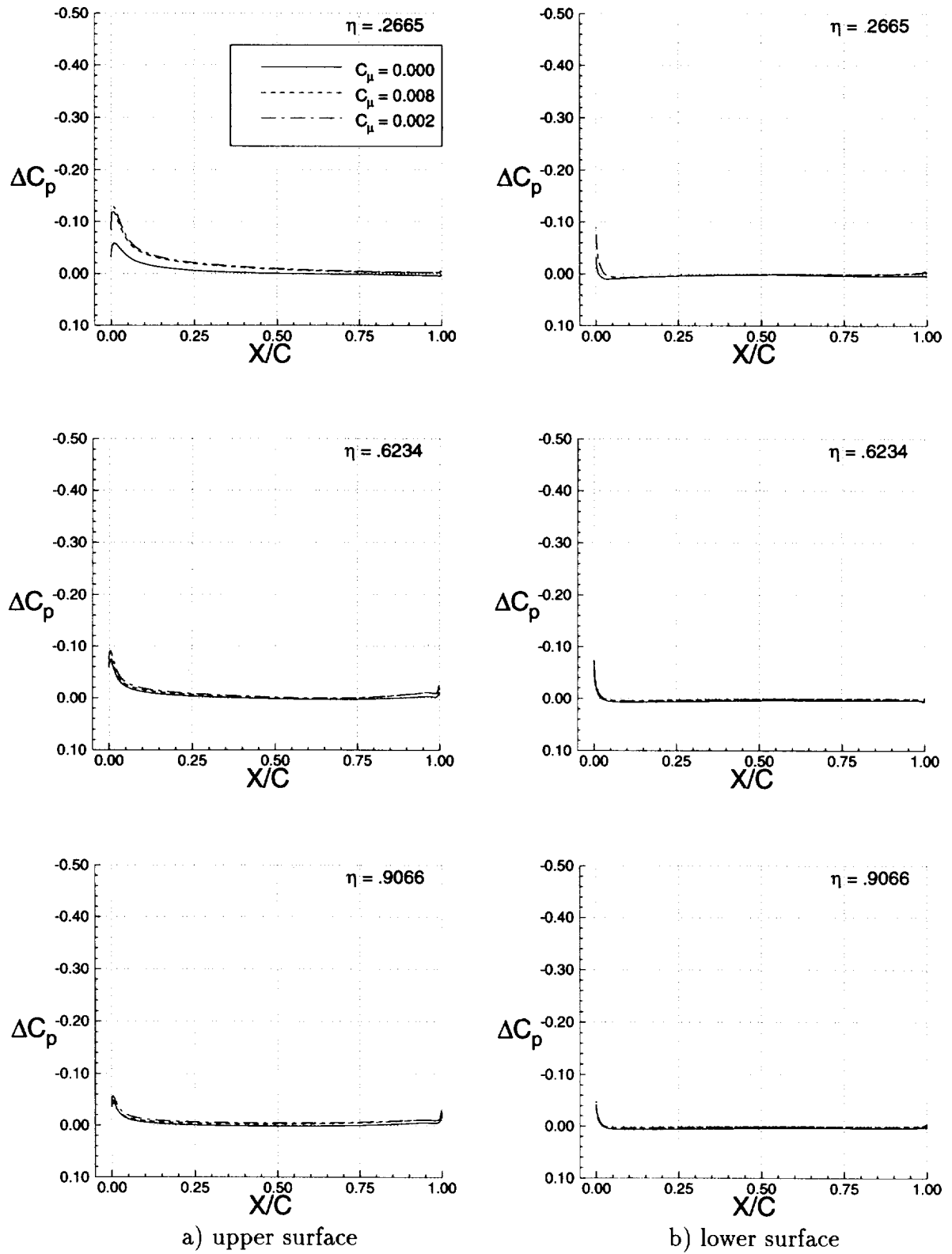


**Figure 92:** Influence of juncture blowing jets on differential wing pressure distributions ( $M_\infty = 0.20$ ,  $\alpha = 12.55^\circ$ ,  $Re = 4.20 \times 10^6$ ).

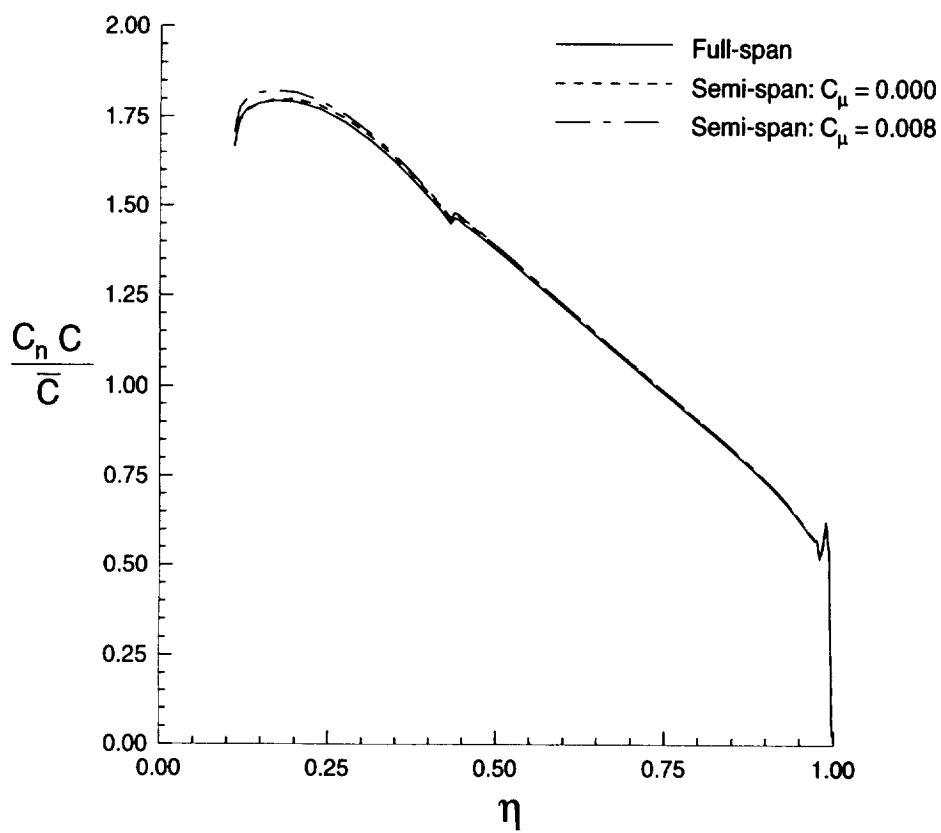


**Figure 93:** Influence of juncture blowing jets on spanload distribution ( $M_\infty = 0.20$ ,  $\alpha = 12.55^\circ$ ,  $Re = 4.20 \times 10^6$ ).





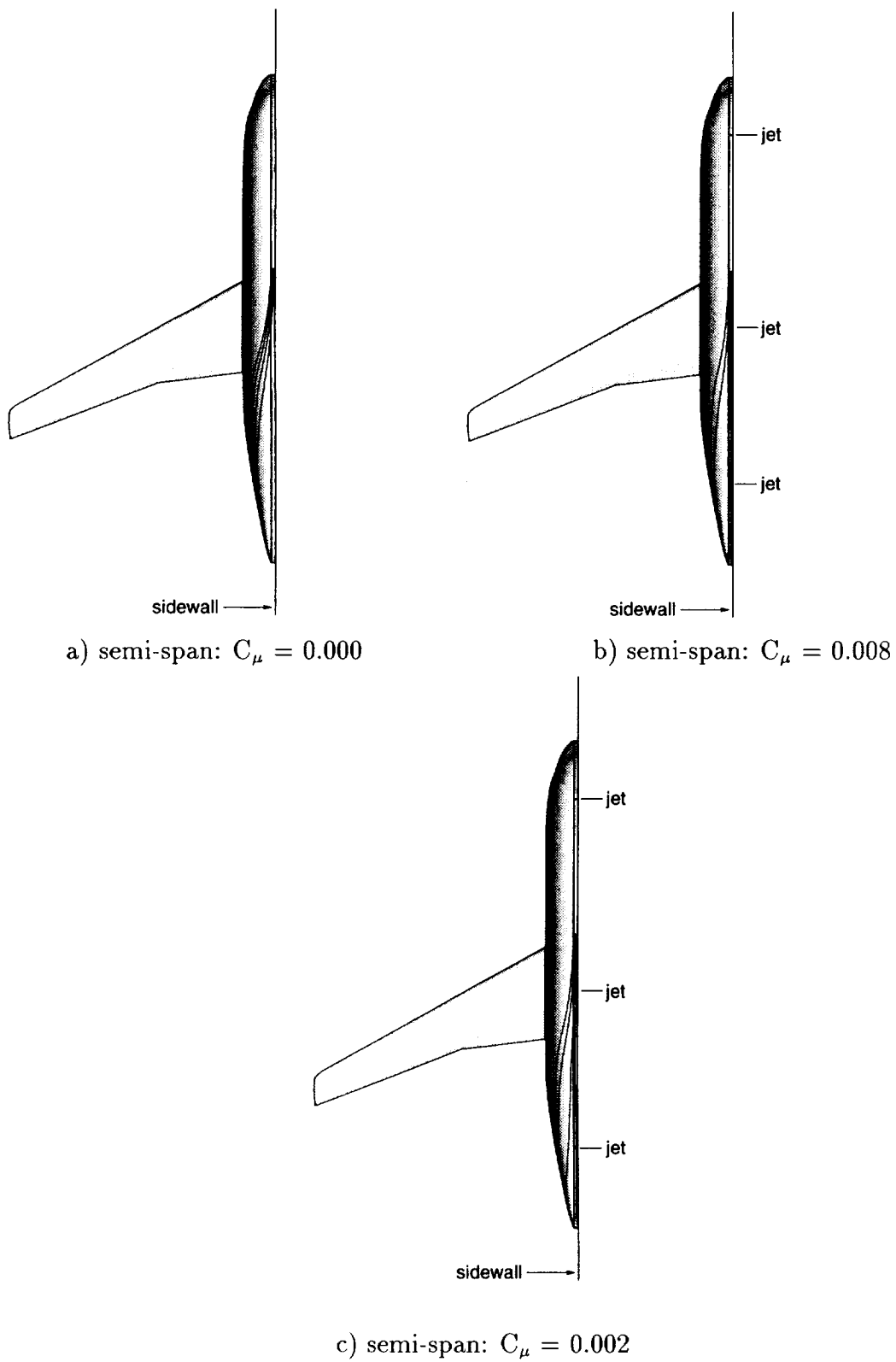
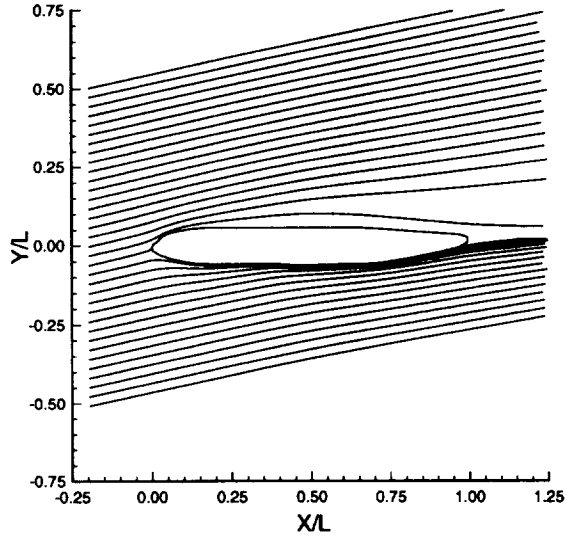
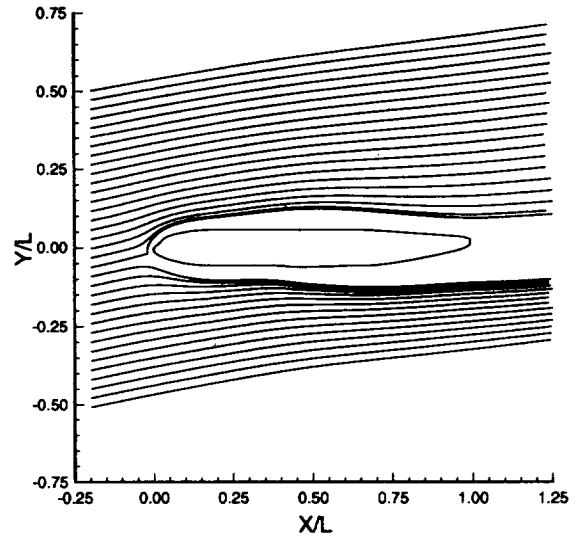


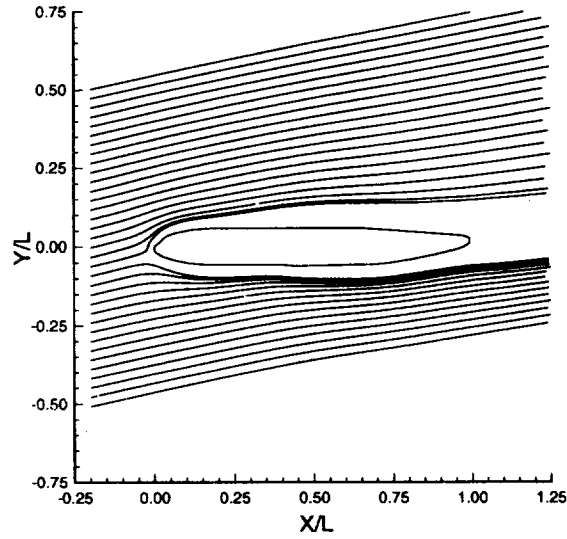
**Figure 95:** Influence of juncture blowing jets on upper fuselage streamline patterns ( $M_\infty = 0.20$ ,  $\alpha = 12.55^\circ$ ,  $Re = 4.20 \times 10^6$ ).



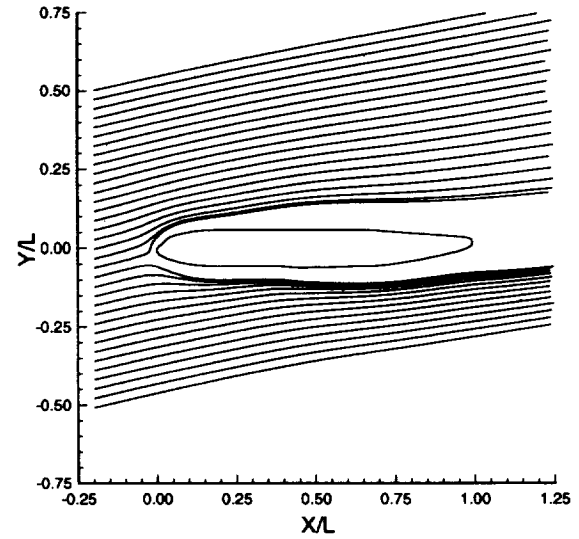
a) full-span



b) semi-span:  $C_\mu = 0.000$

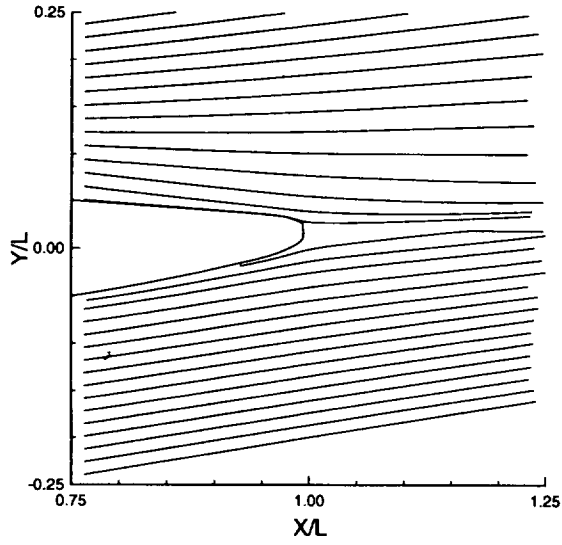


c) semi-span:  $C_\mu = 0.008$

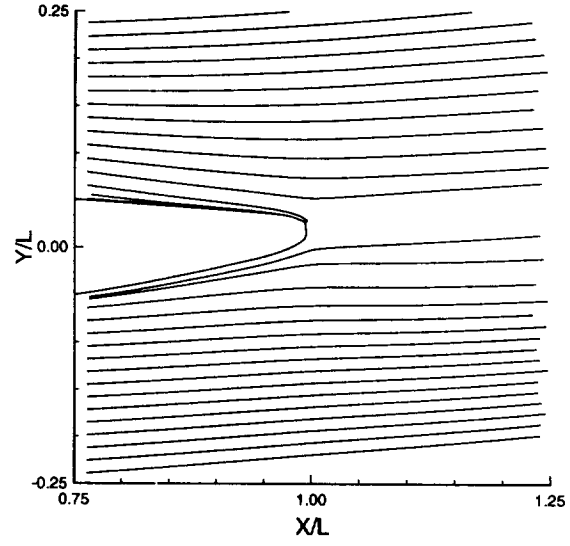


d) semi-span:  $C_\mu = 0.002$

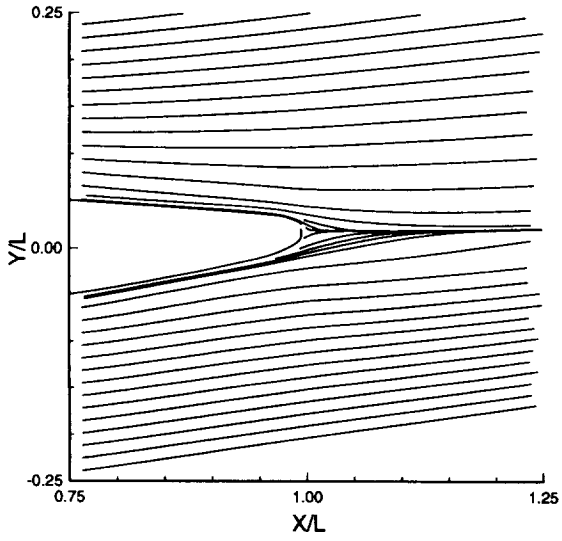
**Figure 96:** Influence of juncture blowing jets on root plane streamline patterns ( $M_\infty = 0.20$ ,  $\alpha = 12.55^\circ$ ,  $Re = 4.20 \times 10^6$ ).



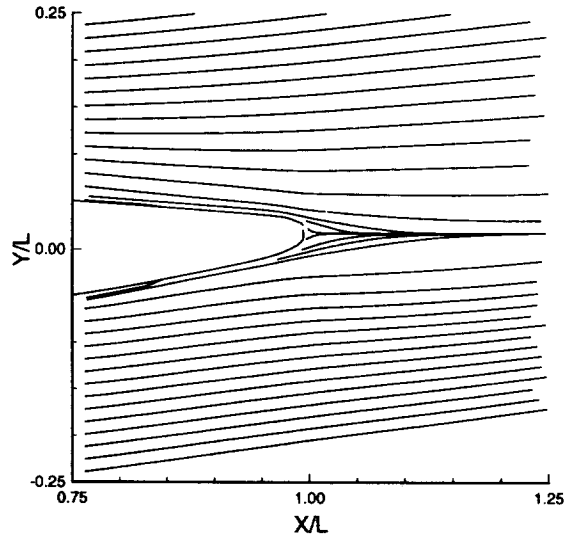
a) full-span



b) semi-span:  $C_\mu = 0.000$



c) semi-span:  $C_\mu = 0.008$



d) semi-span:  $C_\mu = 0.002$

**Figure 97:** Influence of juncture blowing jets on aft root plane streamline patterns ( $M_\infty = 0.20$ ,  $\alpha = 12.55^\circ$ ,  $Re = 4.20 \times 10^6$ ).

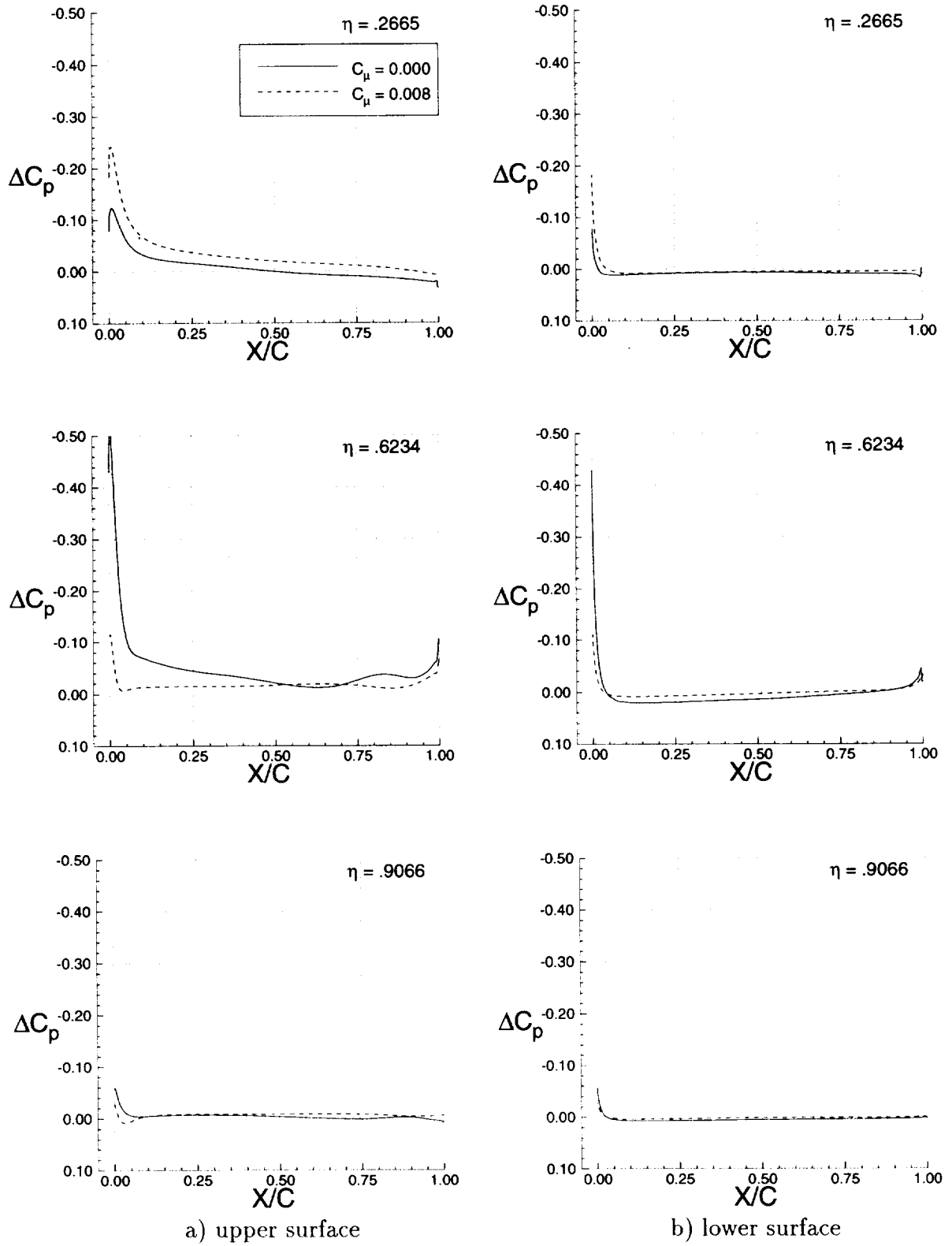


**Figure 98:** Influence of juncture blowing jets on differential wing pressure distributions ( $M_\infty = 0.20$ ,  $\alpha = 18.25^\circ$ ,  $Re = 4.20 \times 10^6$ ).

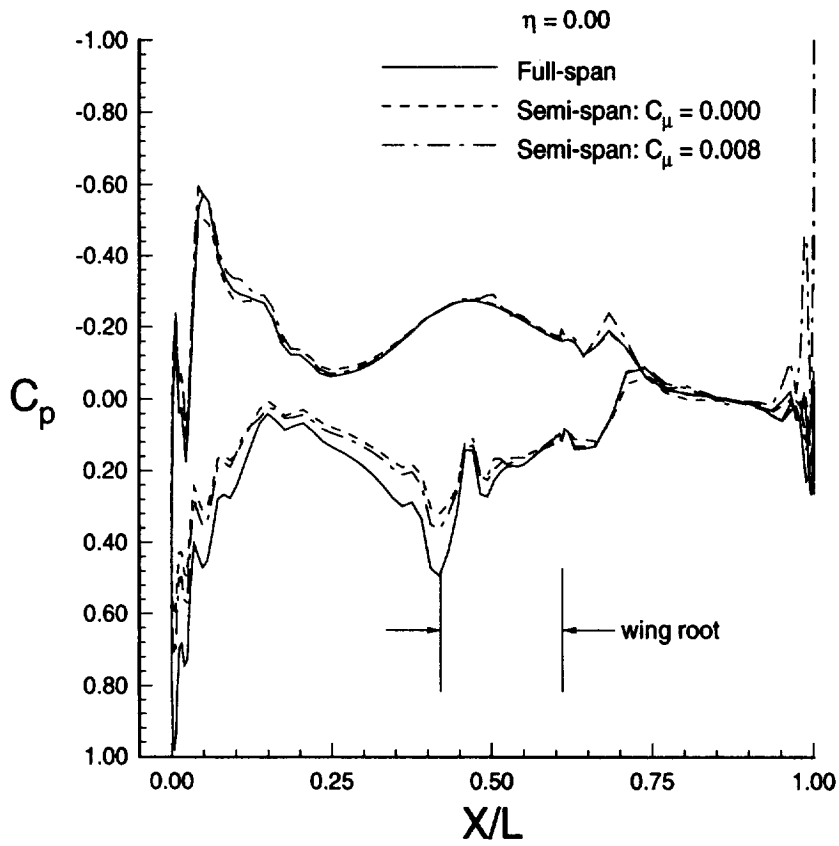
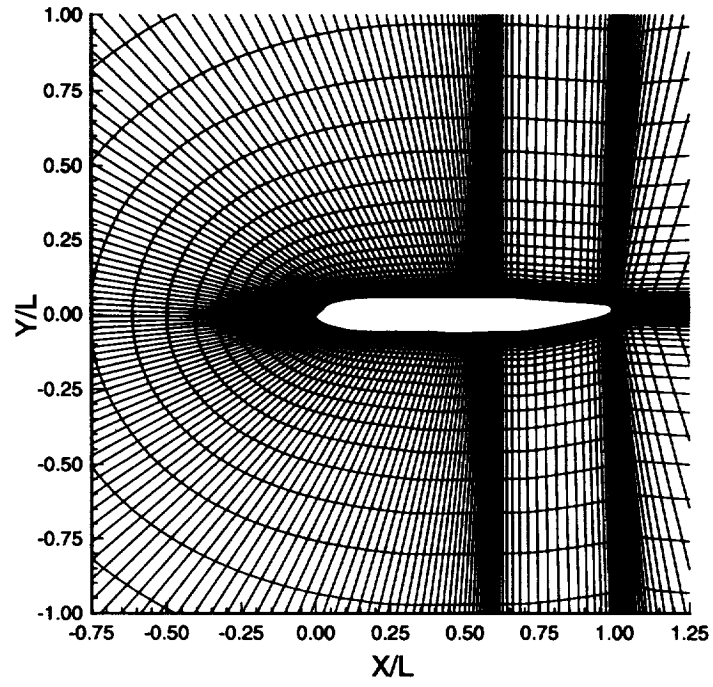
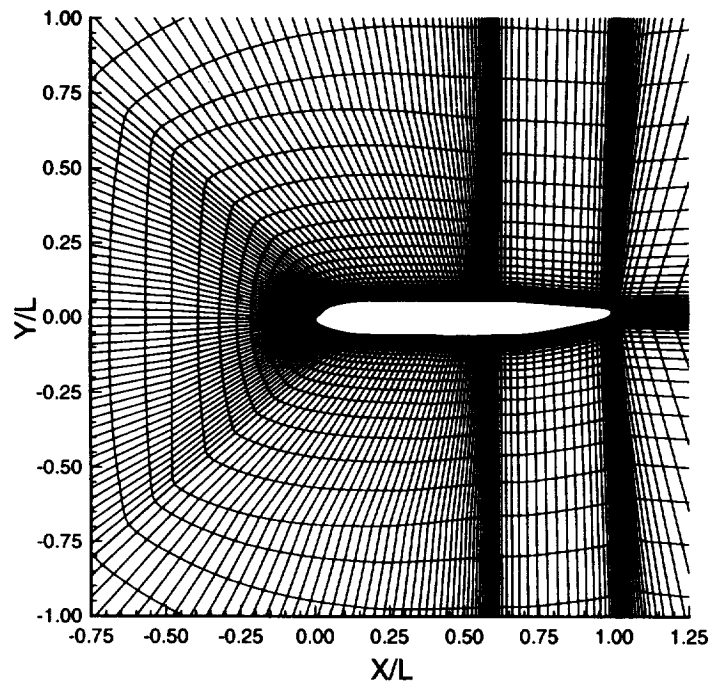


**Figure 99:** Influence of juncture blowing jets on fuselage centerline pressure distribution ( $M_\infty = 0.20$ ,  $\alpha = 18.25^\circ$ ,  $Re = 4.20 \times 10^6$ ).

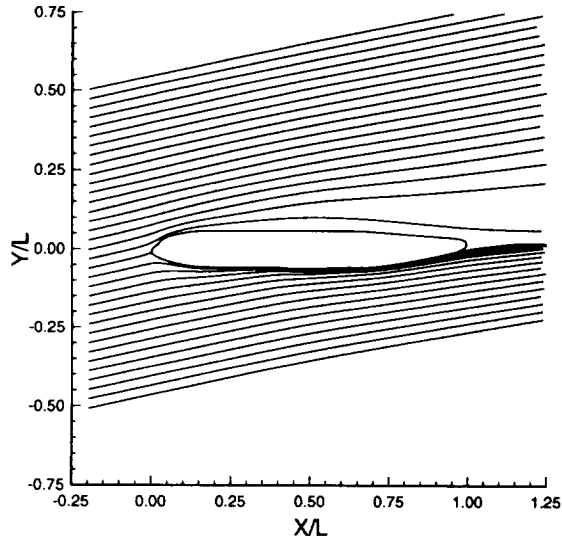


a) original grid

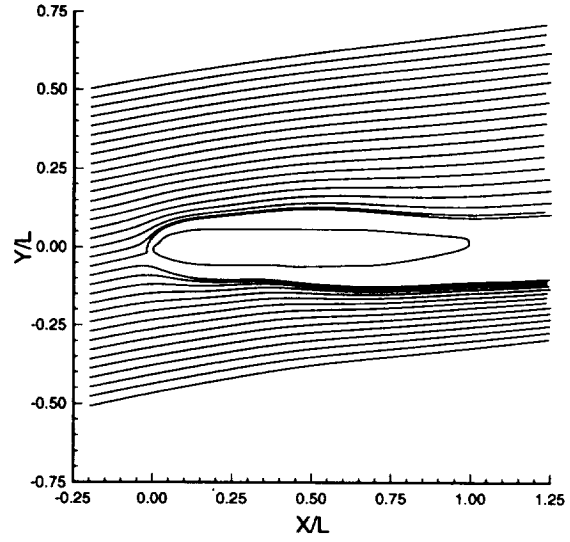


b) modified grid

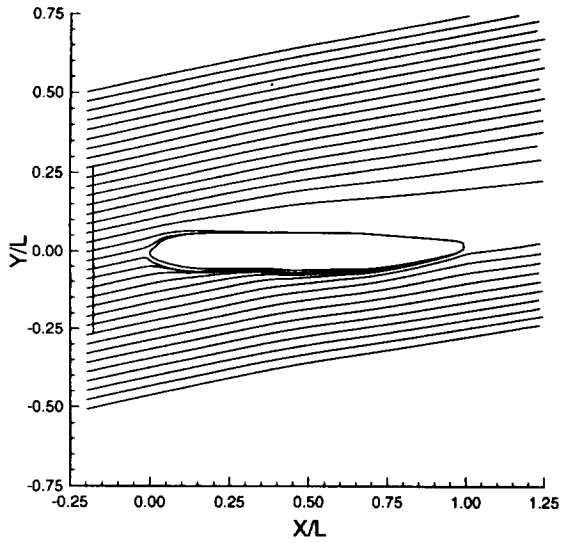
**Figure 100:** Root plane grid modifications for upstream blowing simulations.



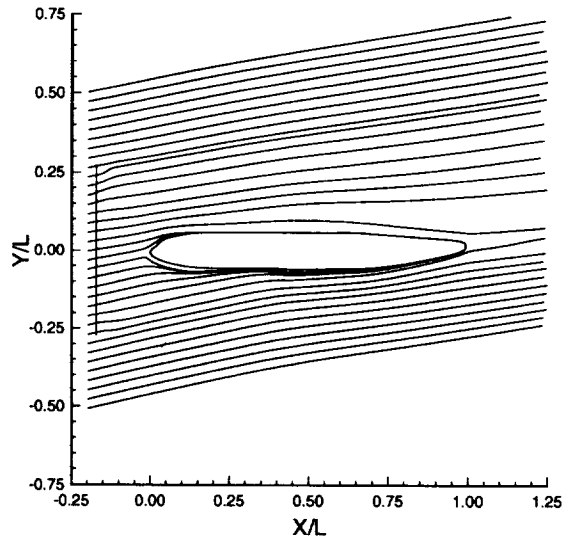
a) full-span



b) semi-span:  $C_\mu = 0.000$

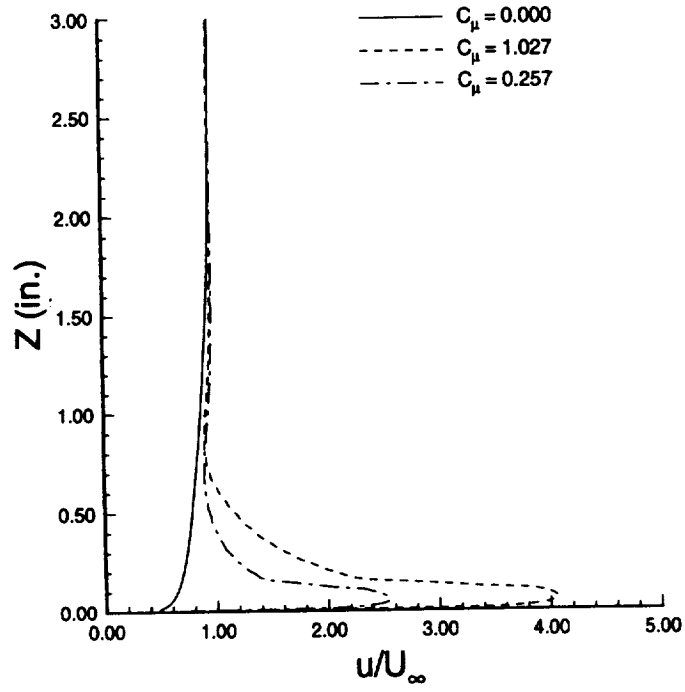


c) semi-span:  $C_\mu = 1.027$

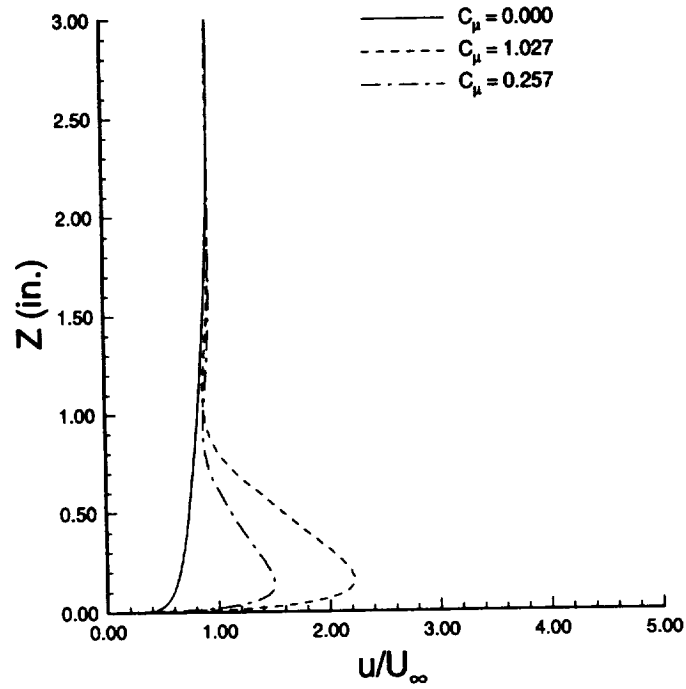


d) semi-span:  $C_\mu = 0.257$

**Figure 101:** Influence of upstream blowing on root plane streamline patterns ( $M_\infty = 0.20$ ,  $\alpha = 12.55^\circ$ ,  $Re = 4.20 \times 10^6$ ).



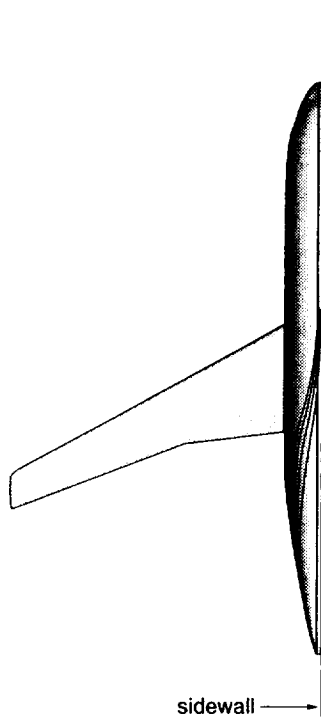
a)  $X/L = -0.25$



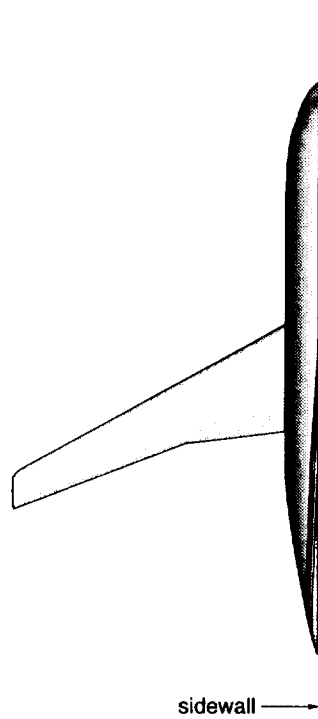
b)  $X/L = -0.125$

**Figure 102:** Influence of upstream blowing on sidewall boundary layer profiles along  $Y/L = 0.00$  ( $M_\infty = 0.20$ ,  $\alpha = 12.55^\circ$ ,  $Re = 4.20 \times 10^6$ ).

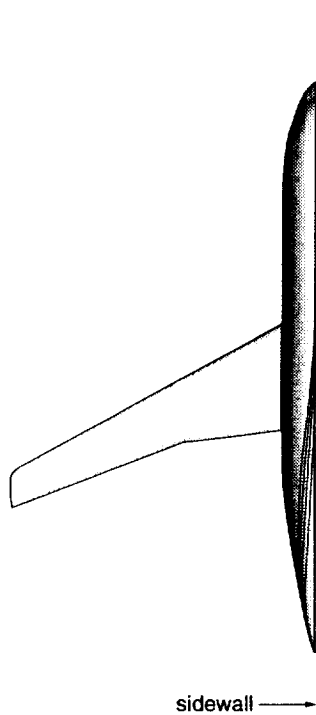




a) semi-span:  $C_\mu = 0.000$

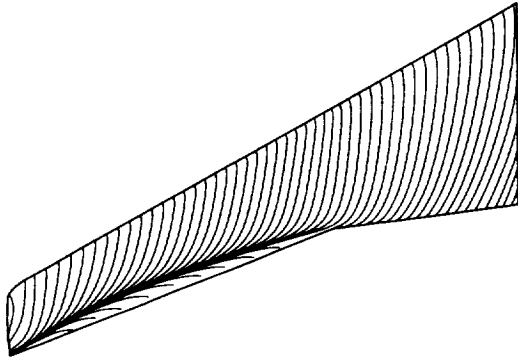


b) semi-span:  $C_\mu = 1.027$

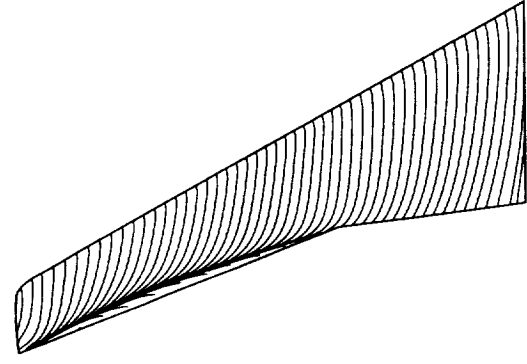


c) semi-span:  $C_\mu = 0.257$

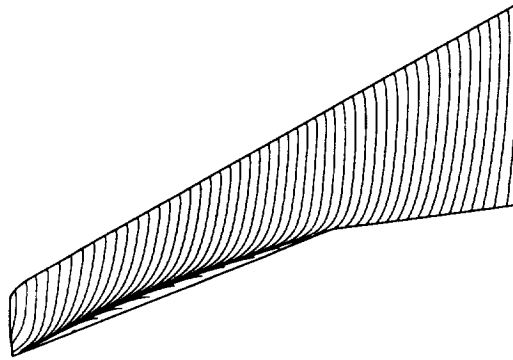
**Figure 103:** Influence of upstream blowing on upper fuselage streamline patterns ( $M_\infty = 0.20$ ,  $\alpha = 12.55^\circ$ ,  $Re = 4.20 \times 10^6$ ).



a) full-span

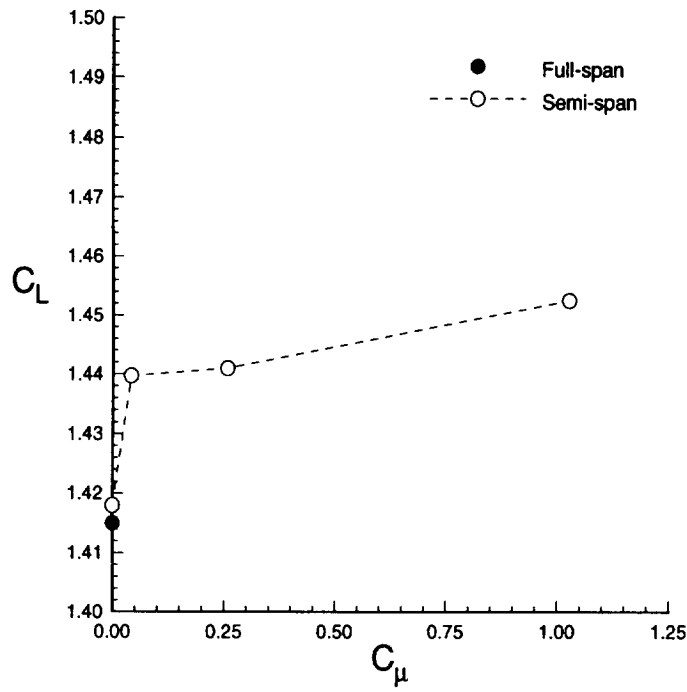


b) semi-span:  $C_\mu = 0.000$

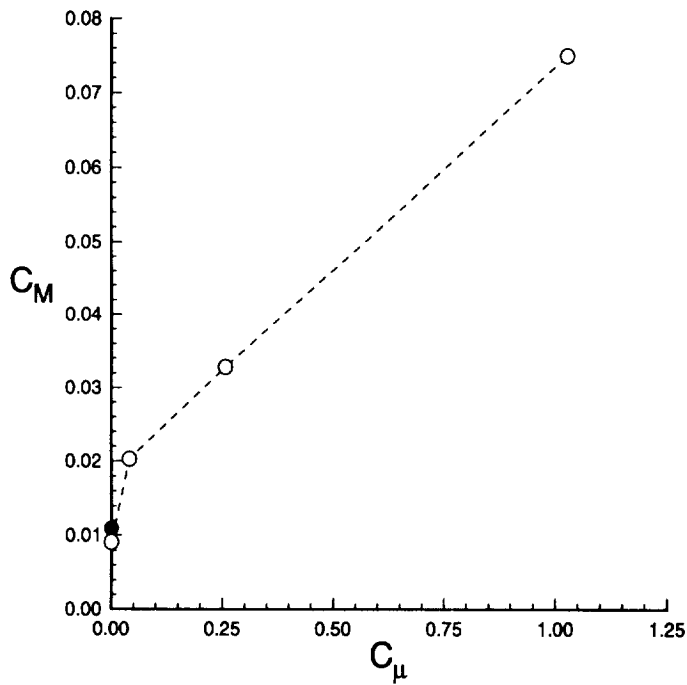


c) semi-span:  $C_\mu = 1.027$

**Figure 104:** Influence of upstream blowing on wing upper surface streamline patterns ( $M_\infty = 0.20$ ,  $\alpha = 12.55^\circ$ ,  $Re = 4.20 \times 10^6$ ).

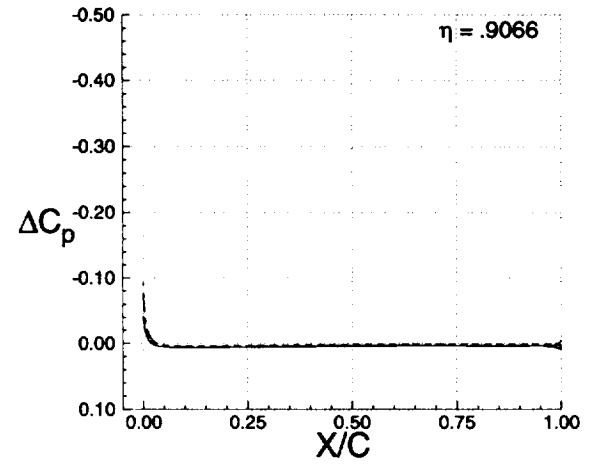
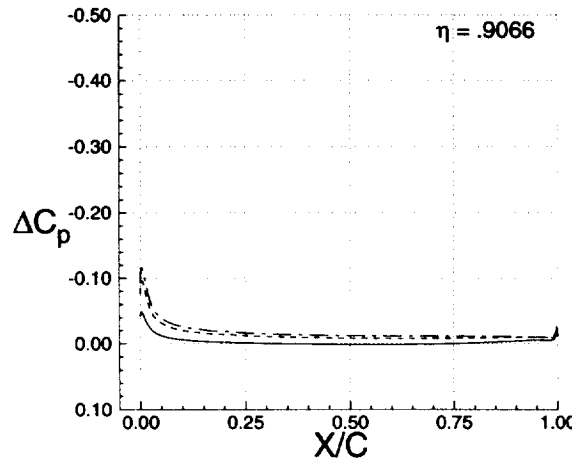
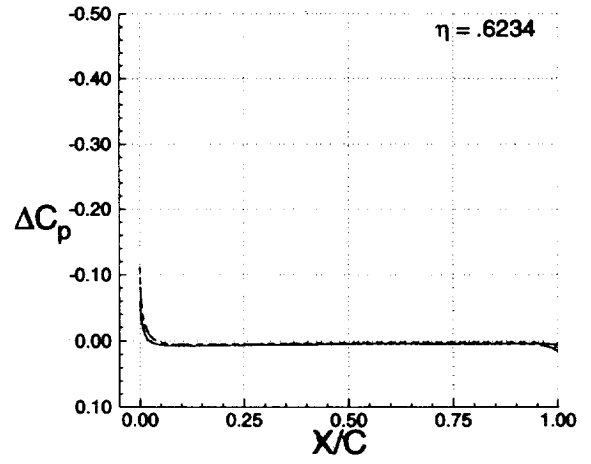
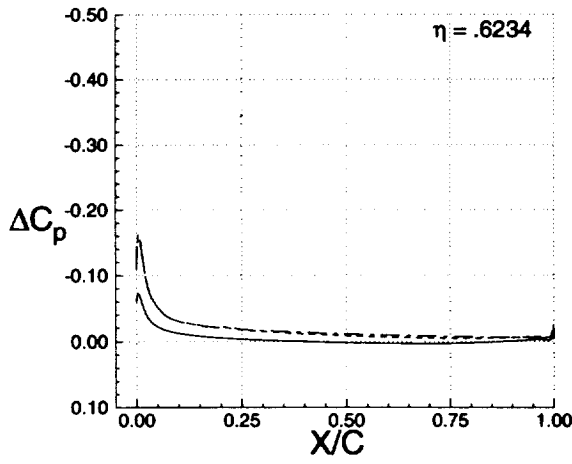
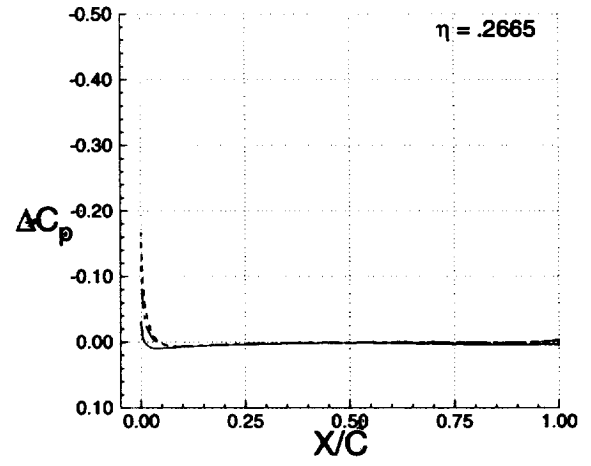
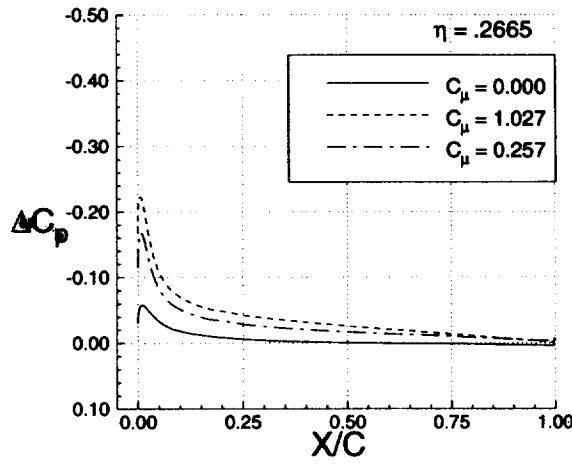


a) lift coefficient



b) pitching moment coefficient

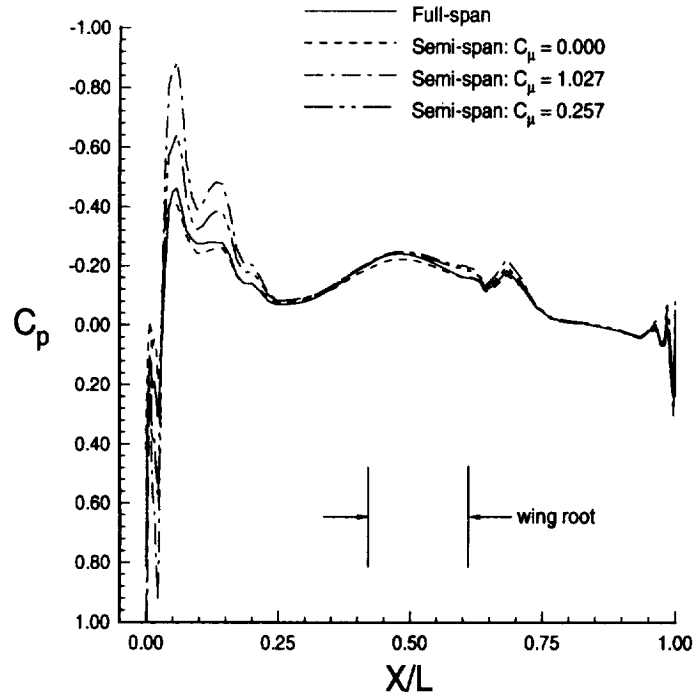
**Figure 105:** Influence of upstream blowing on lift and pitching moment coefficients ( $M_\infty = 0.20$ ,  $\alpha = 12.55^\circ$ ,  $Re = 4.20 \times 10^6$ ).



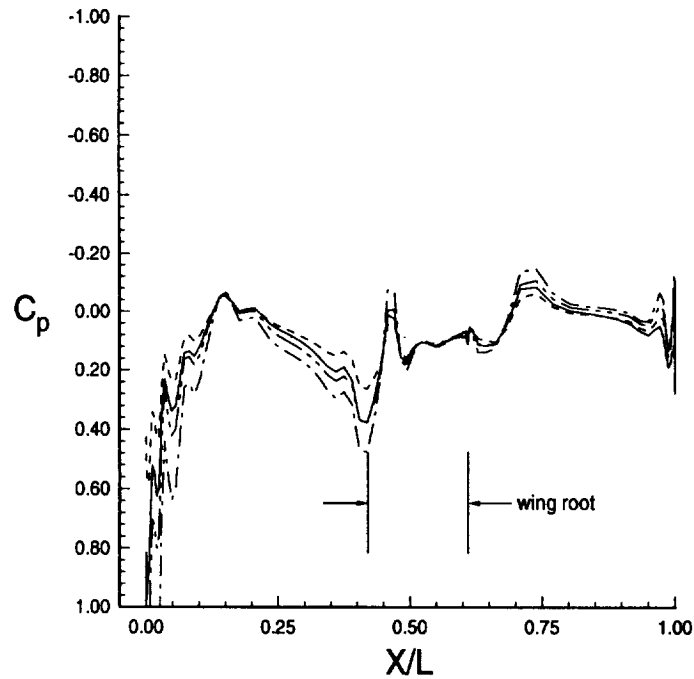
a) upper surface

b) lower surface

**Figure 106:** Influence of upstream blowing on differential wing pressure distributions ( $M_\infty = 0.20$ ,  $\alpha = 12.55^\circ$ ,  $Re = 4.20 \times 10^6$ ).



a) upper surface



b) lower surface

**Figure 107:** Influence of upstream blowing on fuselage centerline pressure distribution ( $M_{\infty} = 0.20$ ,  $\alpha = 12.55^\circ$ ,  $Re = 4.20 \times 10^6$ ).

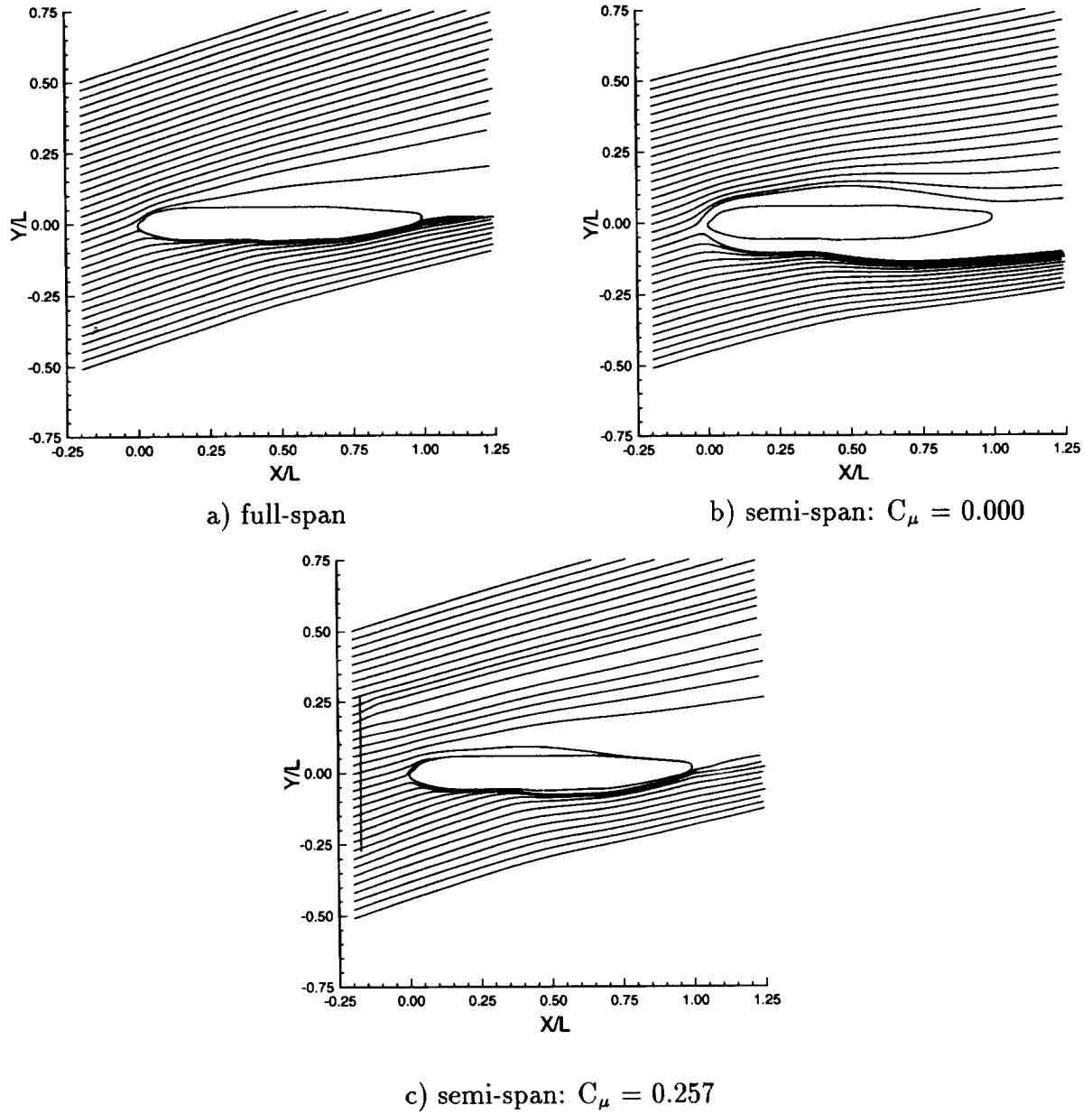
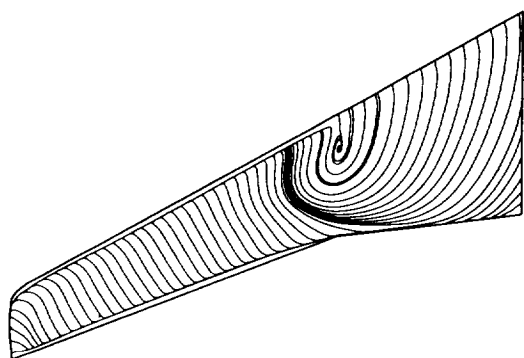
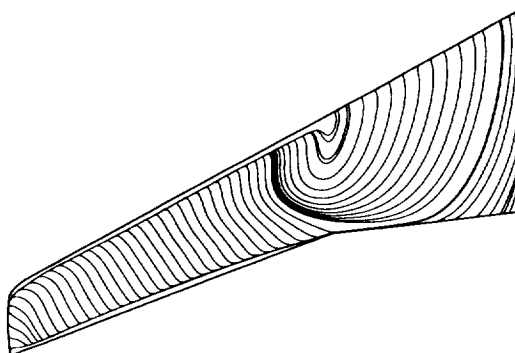


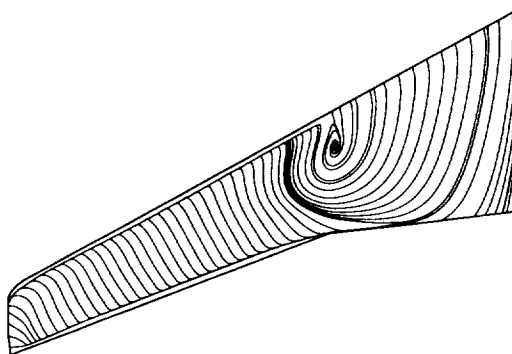
**Figure 108:** Influence of upstream blowing on root plane streamline patterns ( $M_\infty = 0.20$ ,  $\alpha = 18.25^\circ$ ,  $Re = 4.20 \times 10^6$ ).



a) full-span



b) semi-span:  $C_\mu = 0.000$



c) semi-span:  $C_\mu = 0.257$

**Figure 109:** Influence of upstream blowing on wing upper surface streamline patterns ( $M_\infty = 0.20$ ,  $\alpha = 18.25^\circ$ ,  $Re = 4.20 \times 10^6$ ).

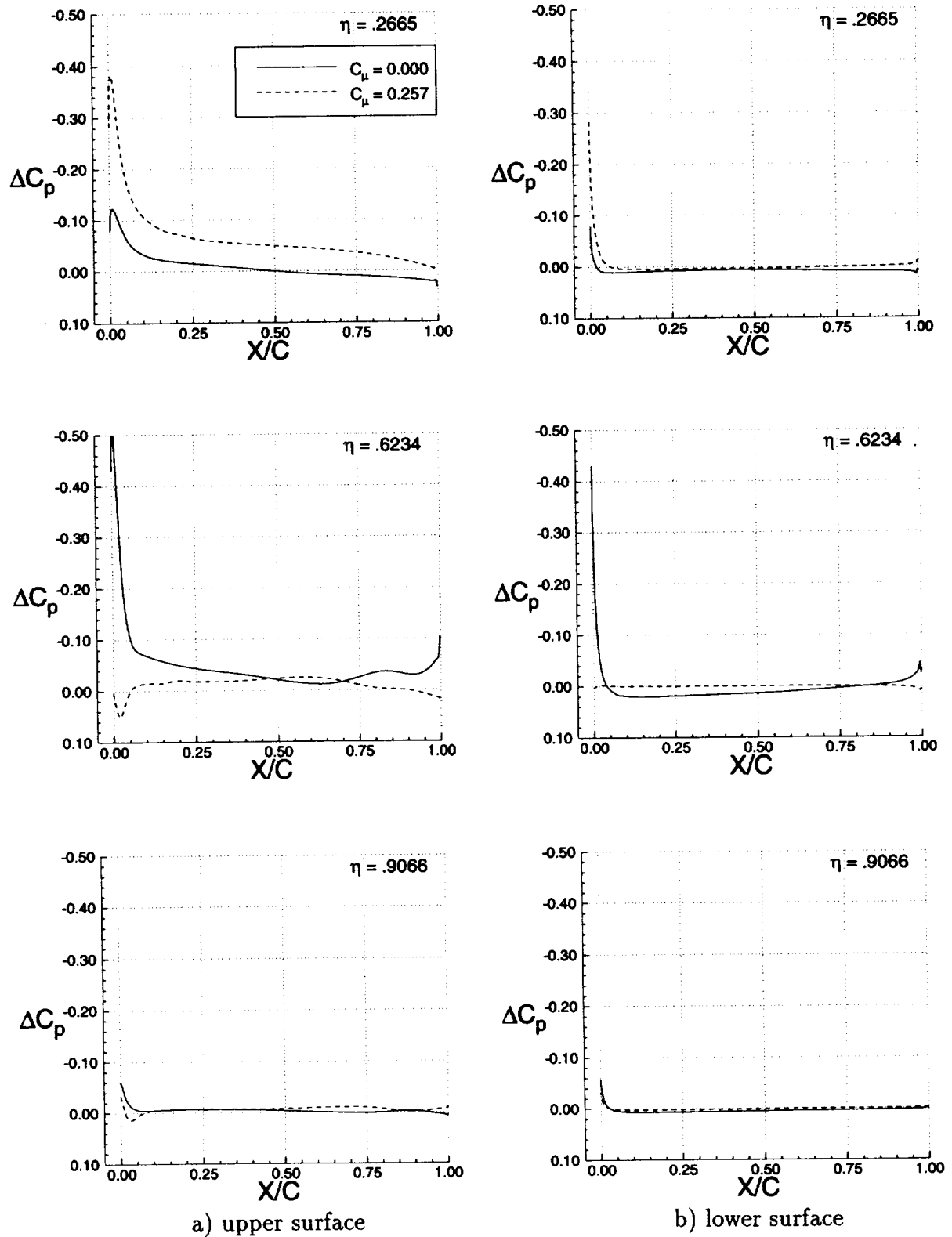


**Figure 110:** Influence of upstream blowing on differential wing pressure distributions ( $M_\infty = 0.20$ ,  $\alpha = 18.25^\circ$ ,  $Re = 4.20 \times 10^6$ ).



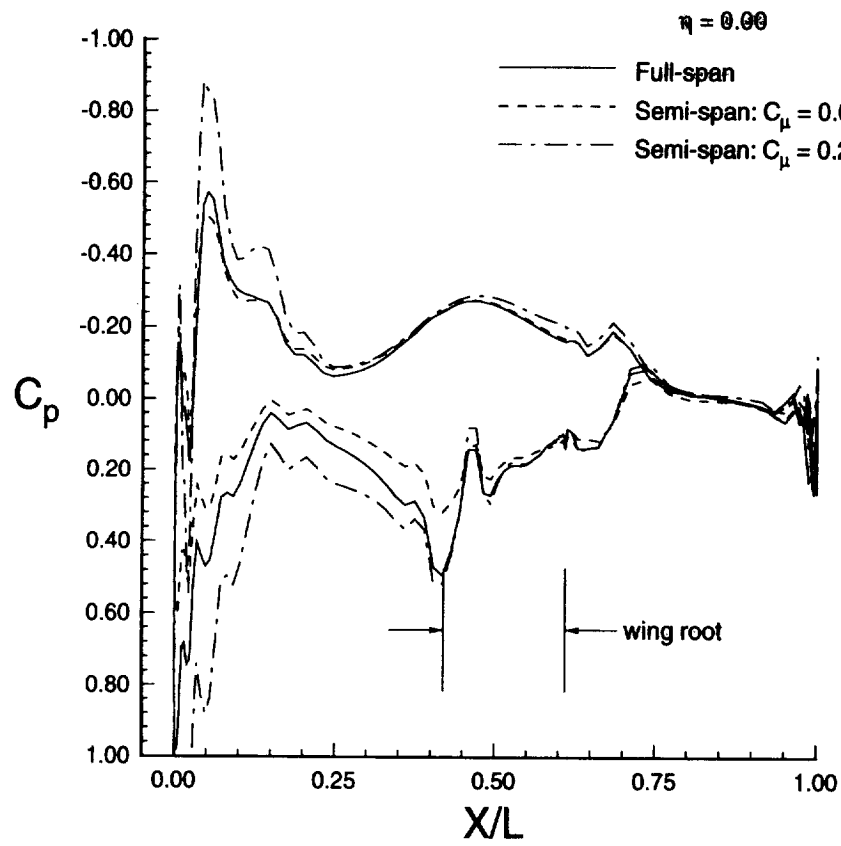


**Figure 111:** Influence of upstream blowing on fuselage centerline pressure distribution ( $M_\infty = 0.20$ ,  $\alpha = 18.25^\circ$ ,  $Re = 4.20 \times 10^6$ ).

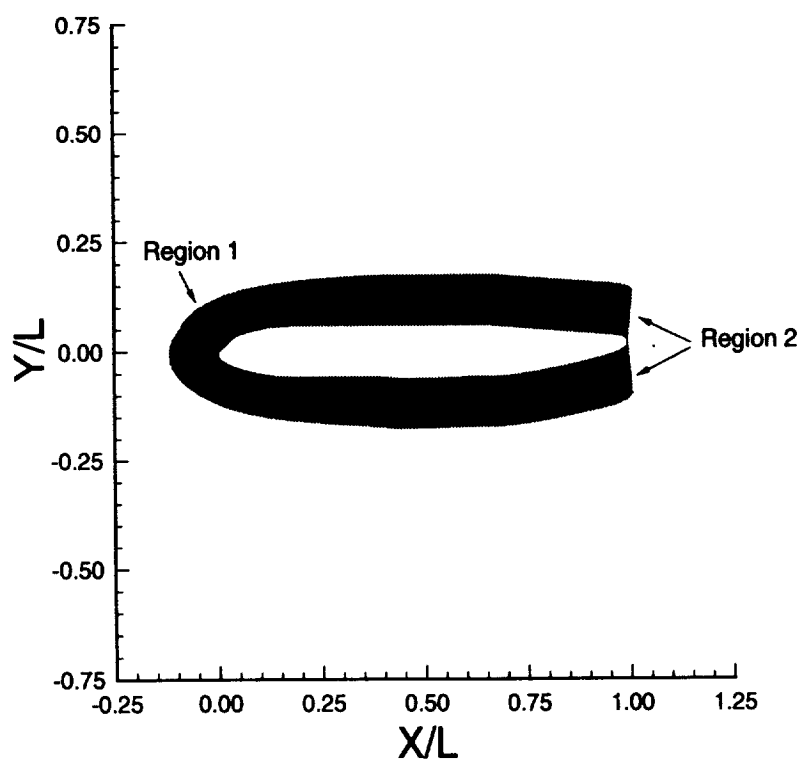
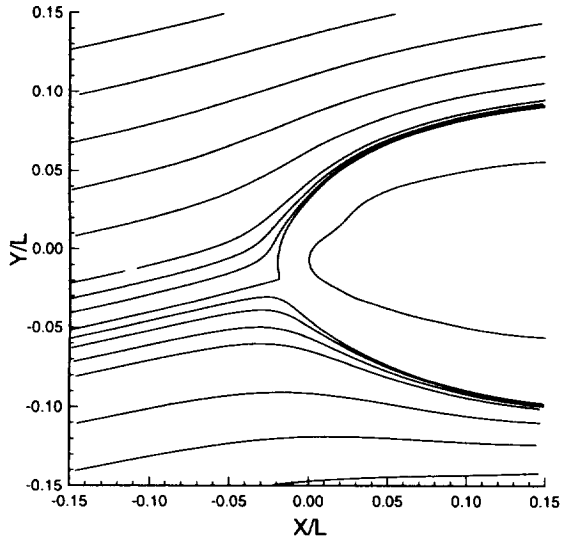
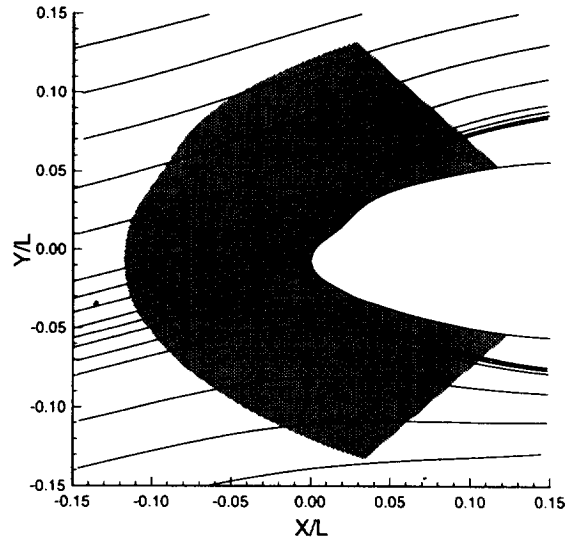


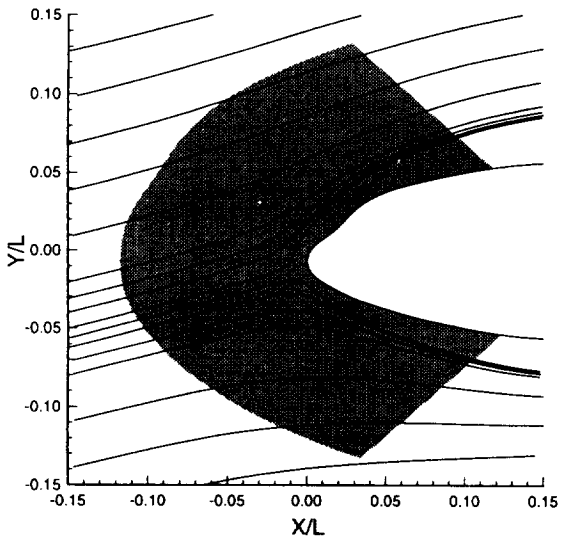
**Figure 112:** Location of sidewall suction regions.



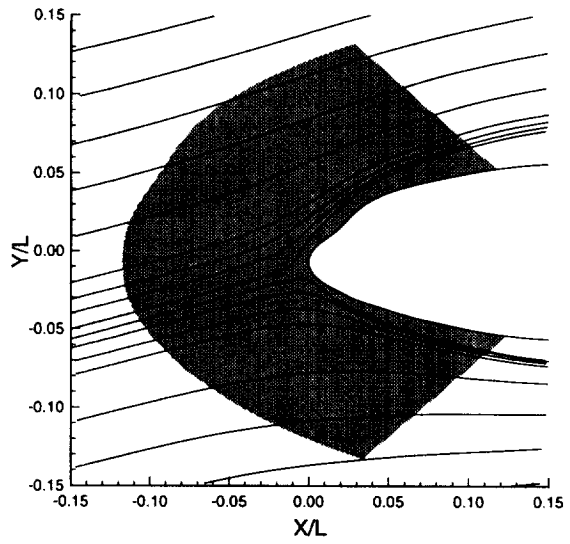
a) semi-span:  $C_q = 0.000$



b) semi-span:  $C_q = -0.005$



c) semi-span:  $C_q = -0.010$



d) semi-span:  $C_q = -0.020$

**Figure 113:** Influence of nose region sidewall suction on root plane streamline patterns ( $M_\infty = 0.20$ ,  $\alpha = 12.55^\circ$ ,  $Re = 4.20 \times 10^6$ ).

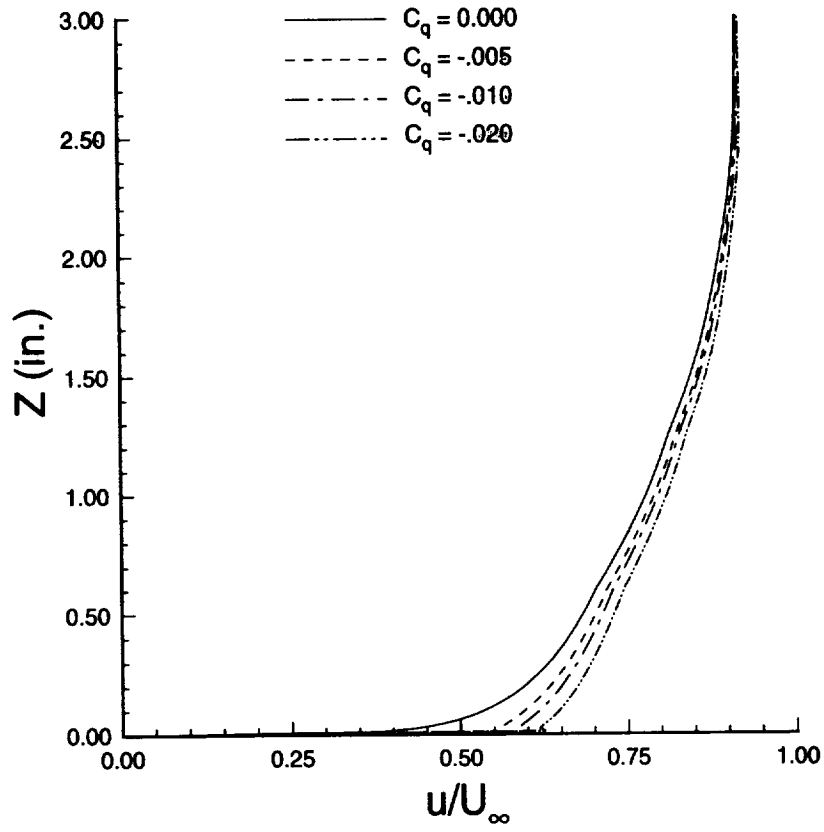
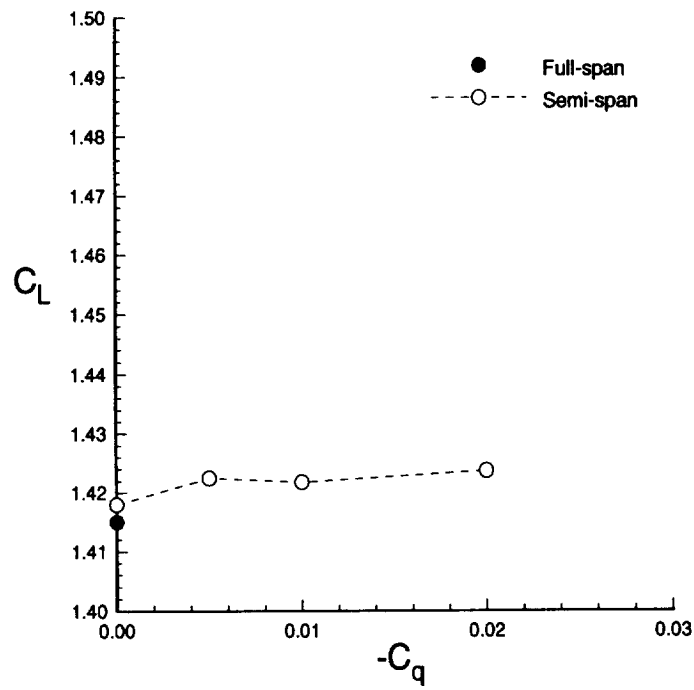
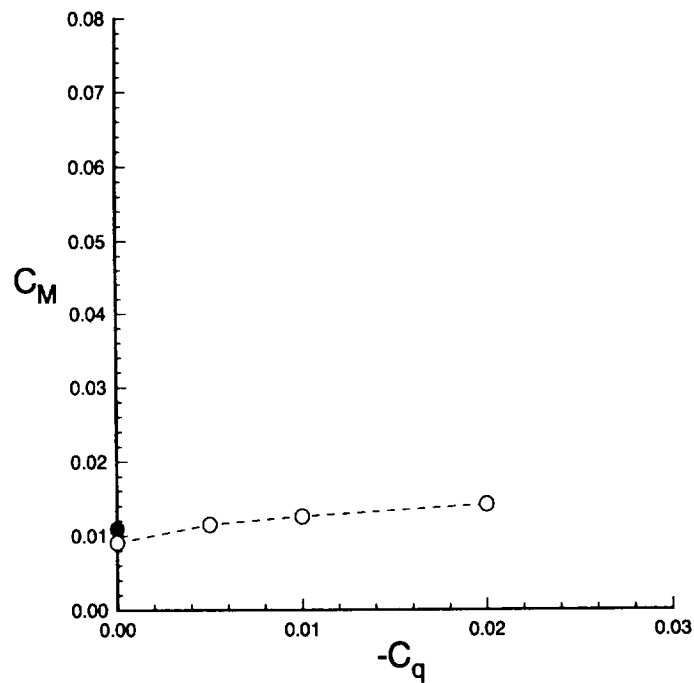


**Figure 114:** Influence of nose region sidewall suction on sidewall boundary profiles at  $y/L = 0.00$ ,  $X/L = -.06$  ( $M_\infty = 0.20$ ,  $\alpha = 12.55^\circ$ ,  $Re = 4.20 \times 10^6$ ).



a) lift coefficient



b) pitching moment coefficient

**Figure 115:** Influence of nose region sidewall suction on lift and pitching moment coefficients ( $M_\infty = 0.20$ ,  $\alpha = 12.55^\circ$ ,  $Re = 4.20 \times 10^6$ ).

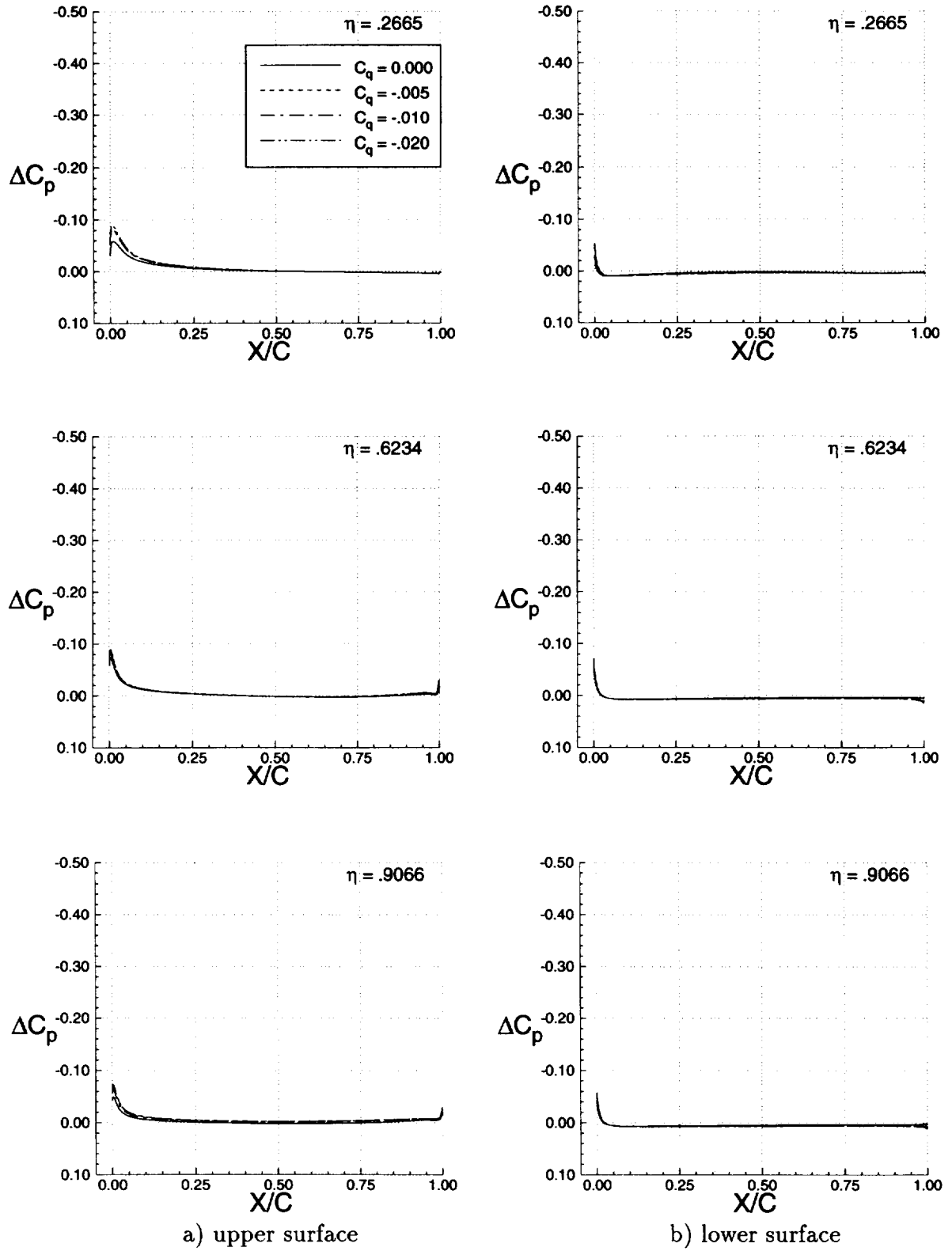


**Figure 116:** Influence of nose region sidewall suction on differential wing pressure distributions ( $M_\infty = 0.20$ ,  $\alpha = 12.55^\circ$ ,  $Re = 4.20 \times 10^6$ ).

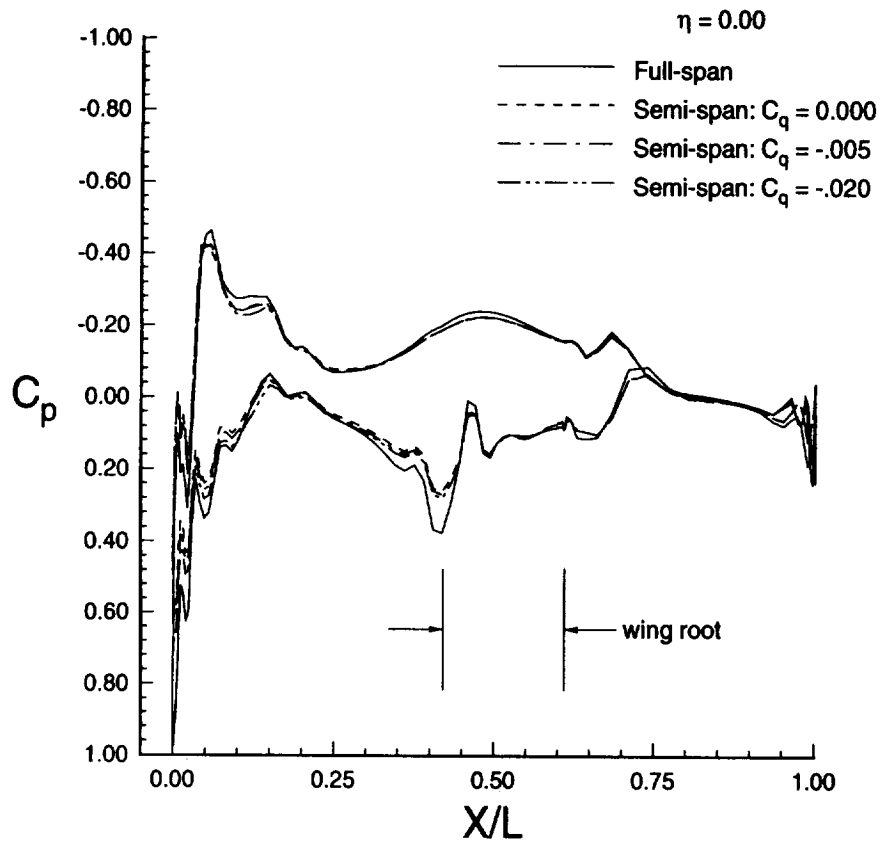
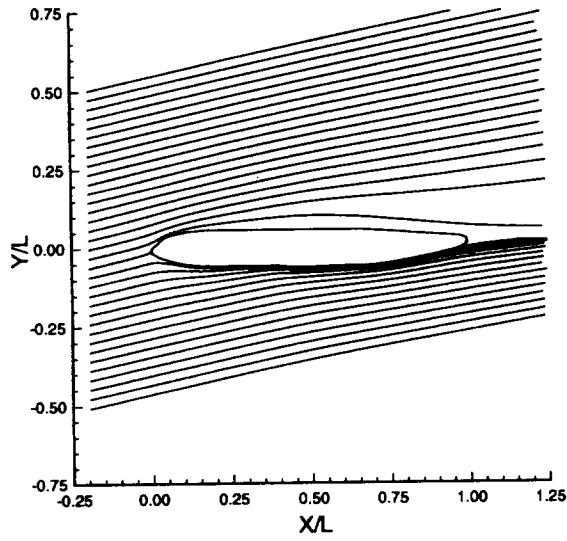
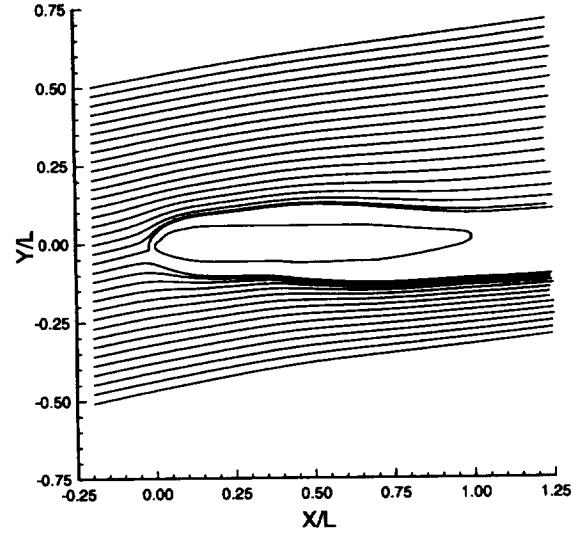


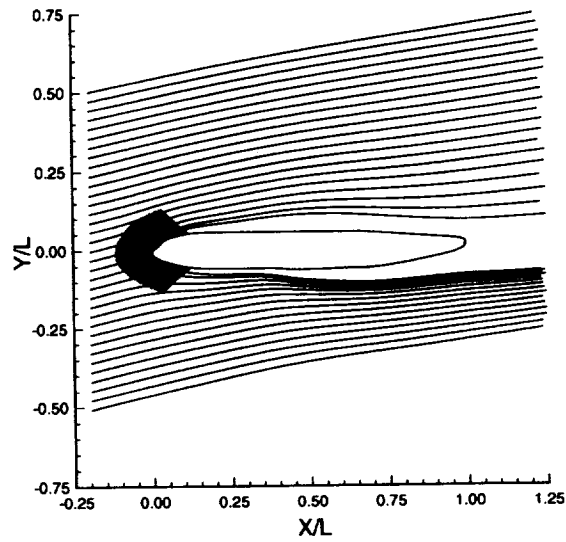
**Figure 117:** Influence of nose region sidewall suction on fuselage centerline pressure distribution ( $M_\infty = 0.20$ ,  $\alpha = 12.55^\circ$ ,  $Re = 4.20 \times 10^6$ ).



a) full-span



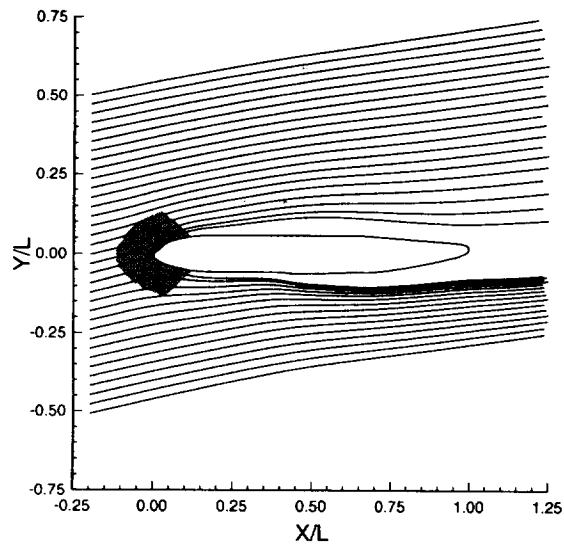
b) semi-span:  $C_q = 0.000$



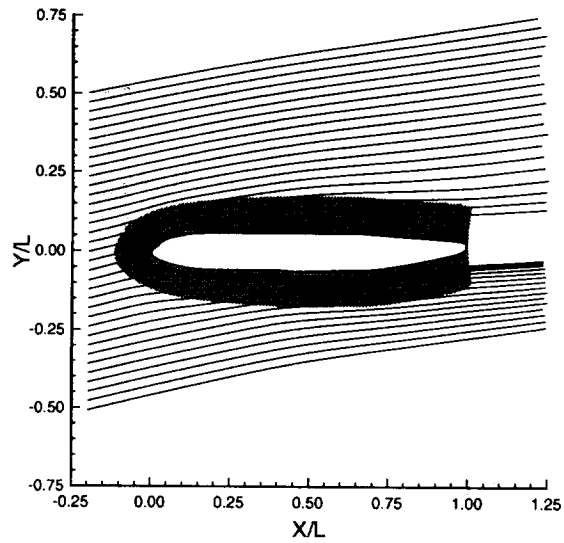
c) semi-span:  $C_q = -.020$

**Figure 118:** Influence of nose region sidewall suction on root plane streamline patterns ( $M_\infty = 0.20$ ,  $\alpha = 12.55^\circ$ ,  $Re = 4.20 \times 10^6$ ).

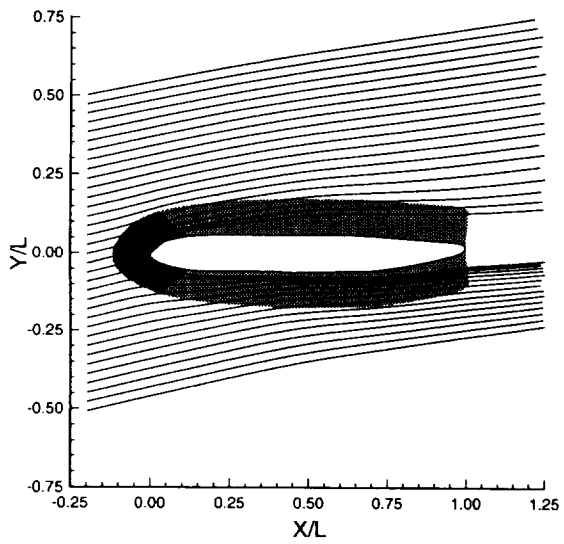




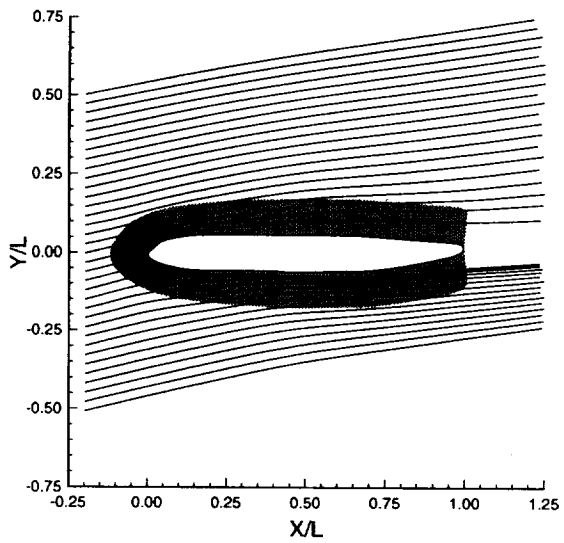
a) semi-span:  $C_q(2) = 0.000$



b) semi-span:  $C_q(2) = -0.020$

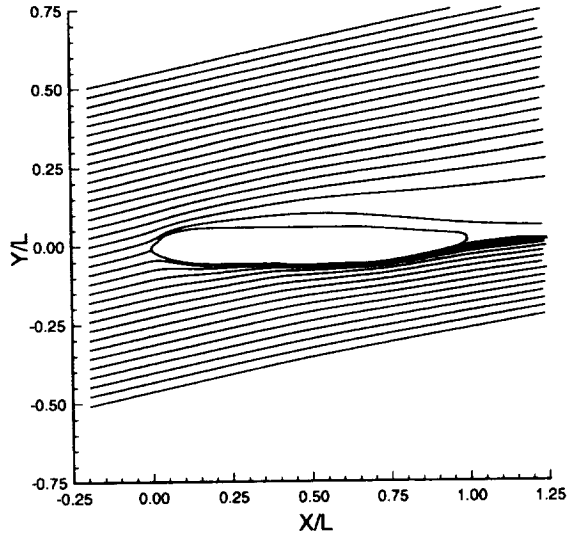


c) semi-span:  $C_q(2) = -0.010$

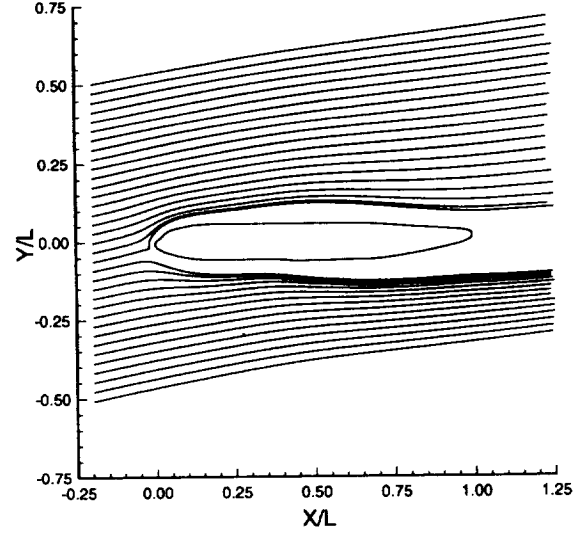


d) semi-span:  $C_q(2) = -0.005$

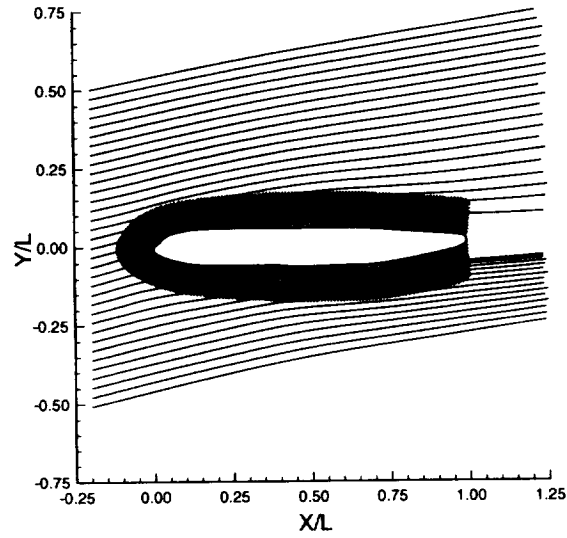
**Figure 119:** Influence of juncture region sidewall suction on root plane streamline patterns,  $C_q(1) = -0.020$  ( $M_\infty = 0.20$ ,  $\alpha = 12.55^\circ$ ,  $Re = 4.20 \times 10^6$ ).



a) full-span

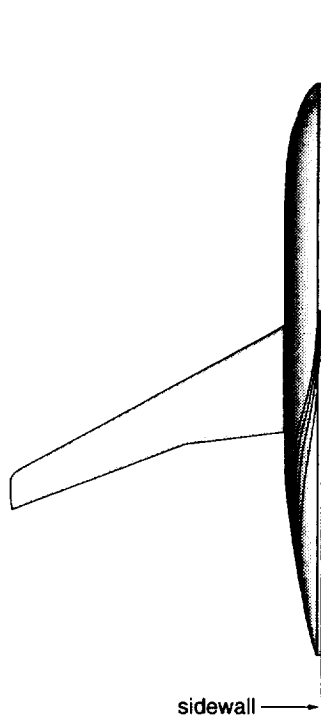


b) semi-span:  $C_q = 0.000$

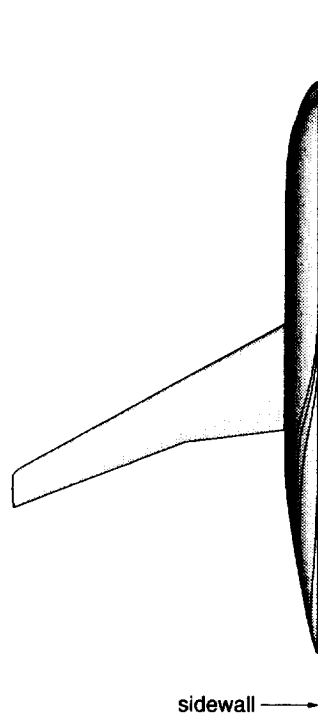


c) semi-span:  $C_q(1) = -.020$ ,  $C_q(2) = -.005$

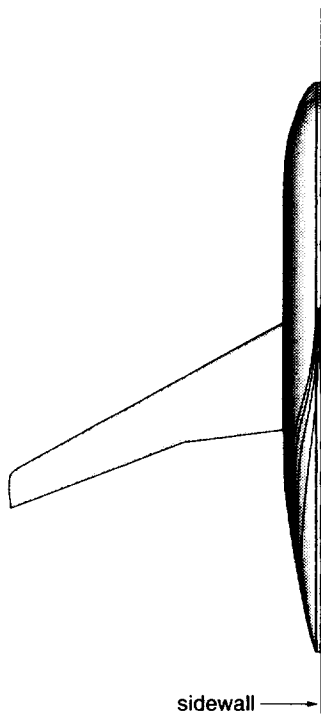
**Figure 120:** Comparison of root plane streamline patterns ( $M_\infty = 0.20$ ,  $\alpha = 12.55^\circ$ ,  $Re = 4.20 \times 10^6$ ).



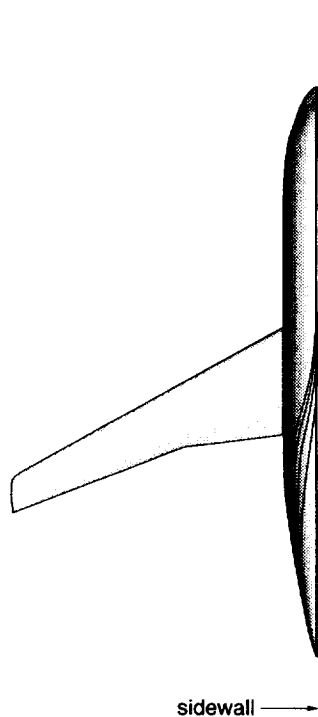
a) semi-span:  $C_q = 0.000$



b) semi-span:  $C_q(2) = -.020$



c) semi-span:  $C_q(2) = -.010$



d) semi-span:  $C_q(2) = -.005$

**Figure 121:** Influence of juncture region suction on upper fuselage streamline patterns  $C_q(1) = -.020$  ( $M_\infty = 0.20$ ,  $\alpha = 12.55^\circ$ ,  $Re = 4.20 \times 10^6$ ).

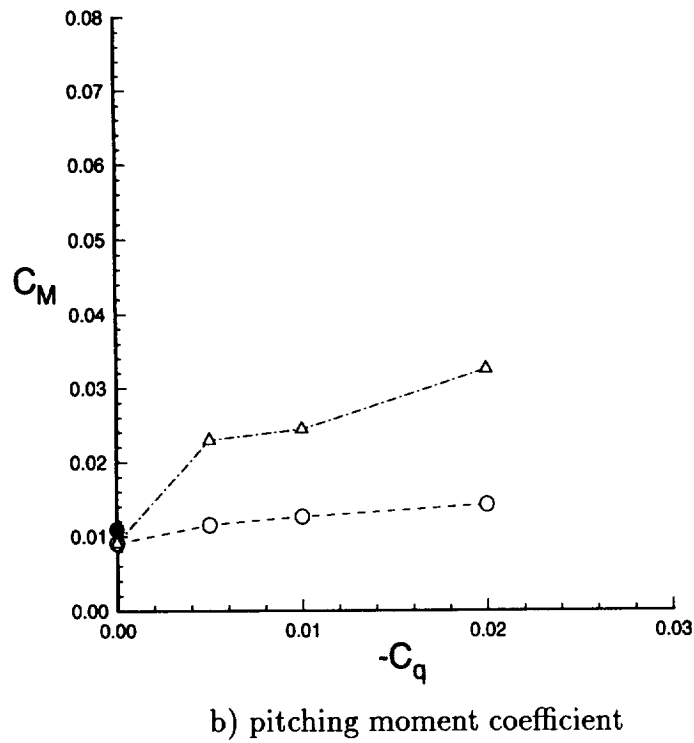
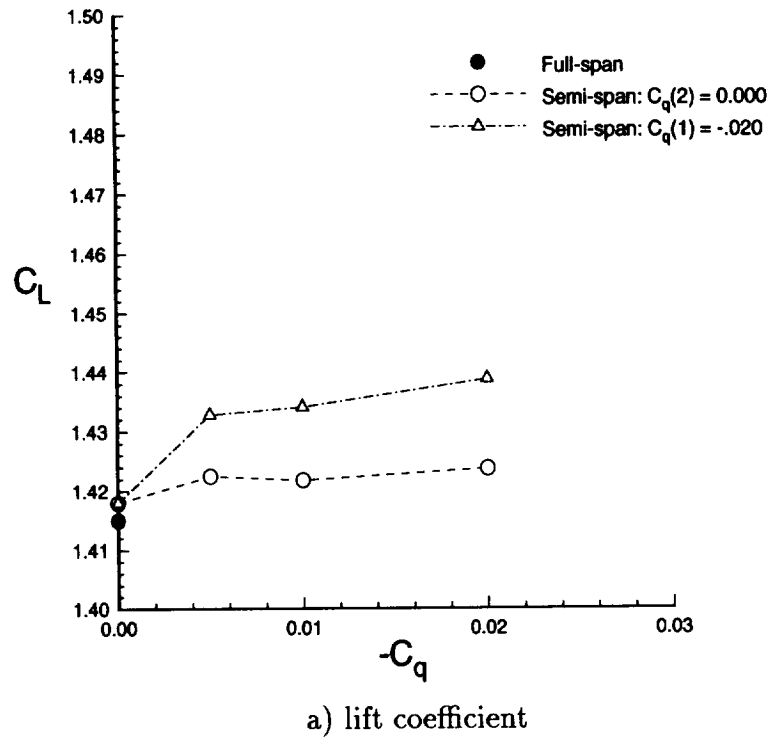


**Figure 122:** Influence of sidewall suction on lift and pitching moment coefficients ( $M_\infty = 0.20$ ,  $\alpha = 12.55^\circ$ ,  $Re = 4.20 \times 10^6$ ).

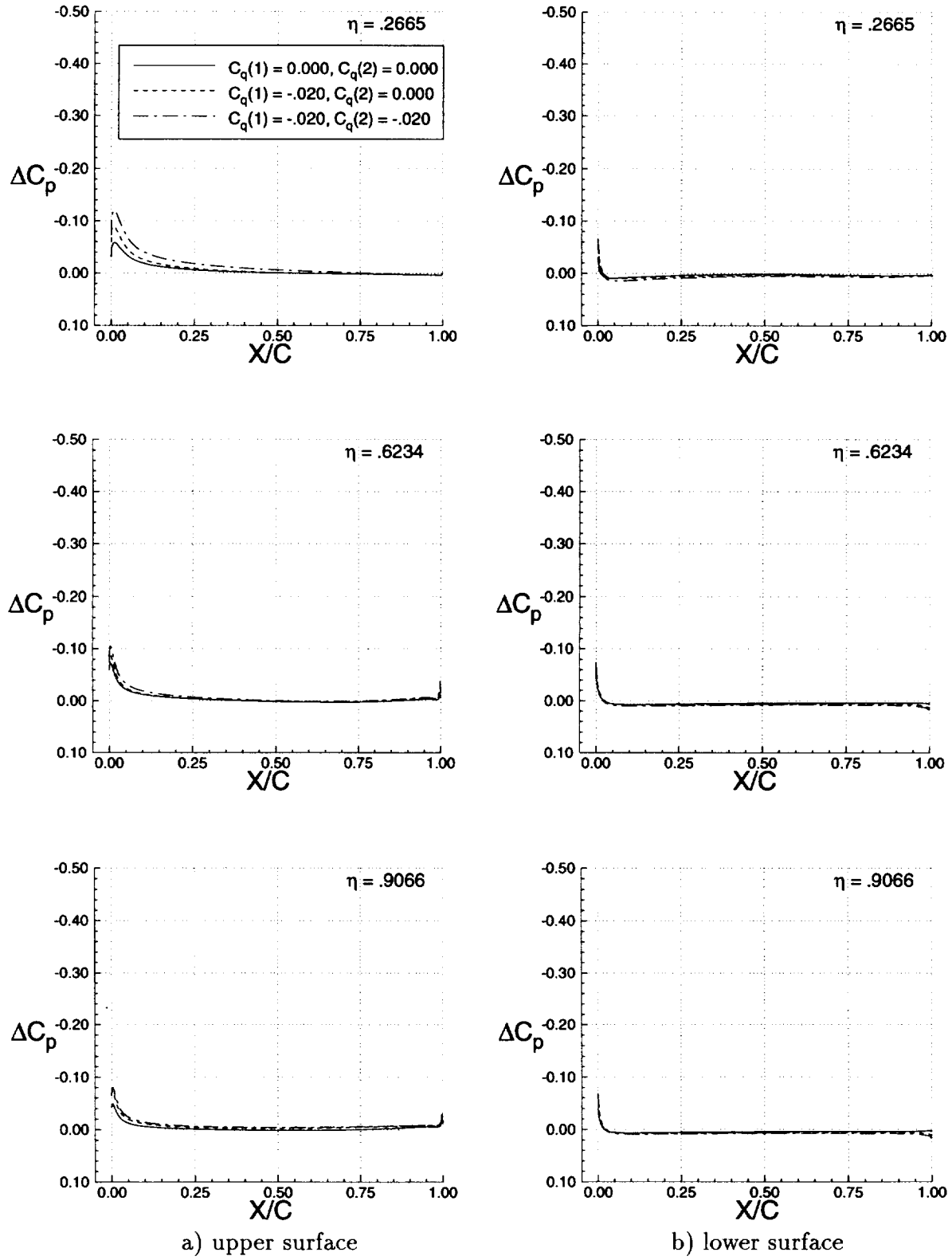


**Figure 123:** Influence of sidewall suction on differential wing pressure distributions ( $M_\infty = 0.20$ ,  $\alpha = 12.55^\circ$ ,  $Re = 4.20 \times 10^6$ ).

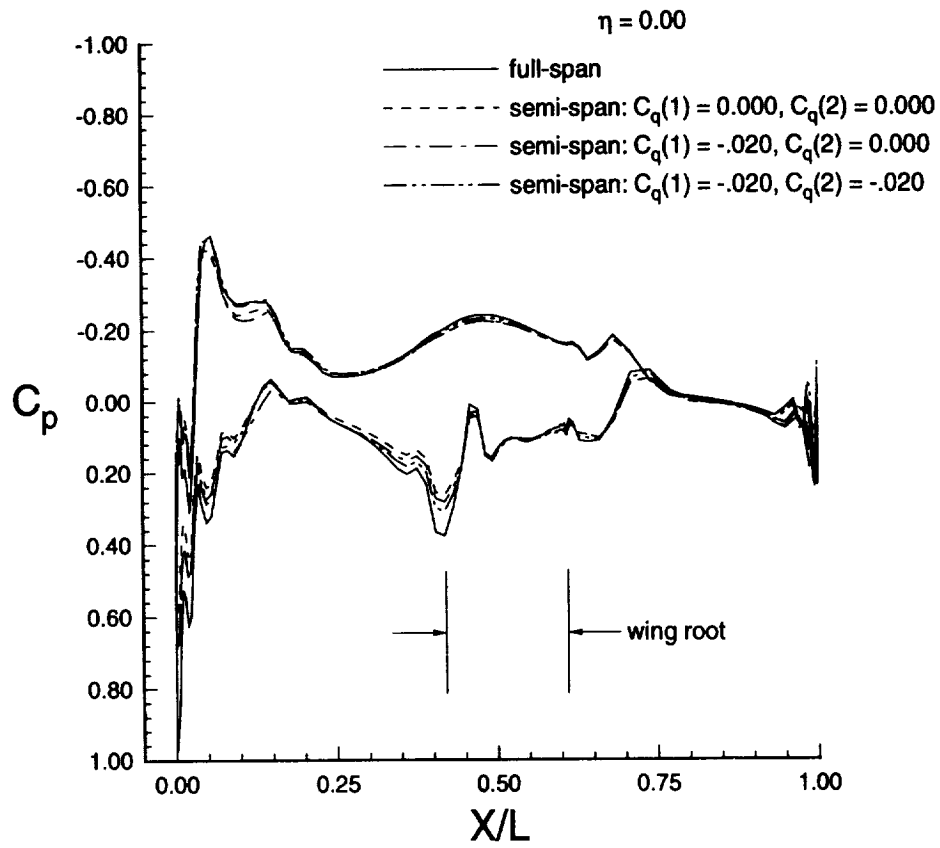
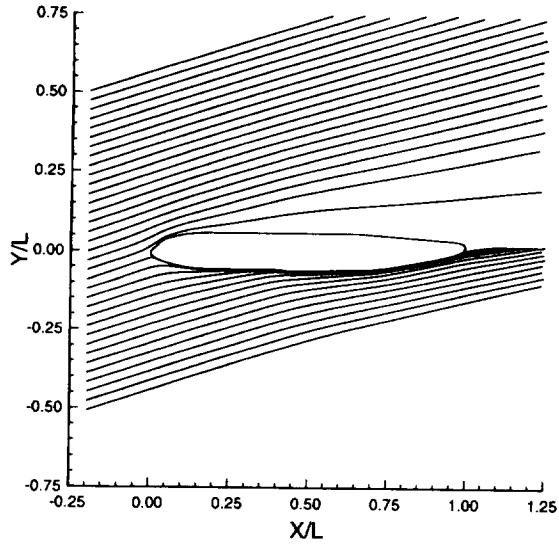
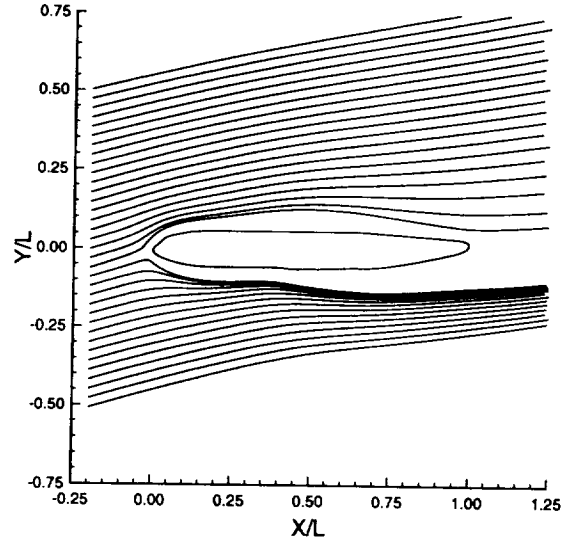


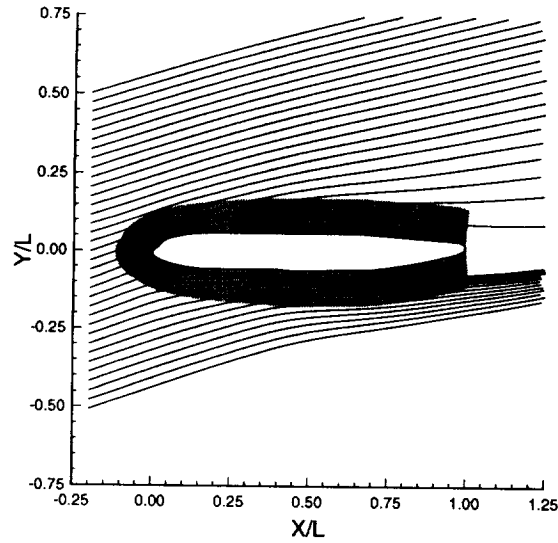
**Figure 124:** Influence of sidewall suction on fuselage centerline pressure distribution ( $M_\infty = 0.20$ ,  $\alpha = 12.55^\circ$ ,  $Re = 4.20 \times 10^6$ ).



a) full-span

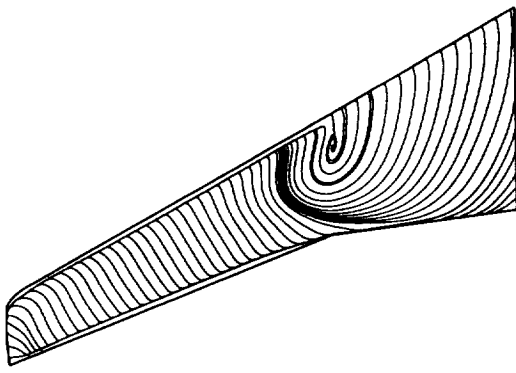


b) semi-span:  $C_q = 0.000$

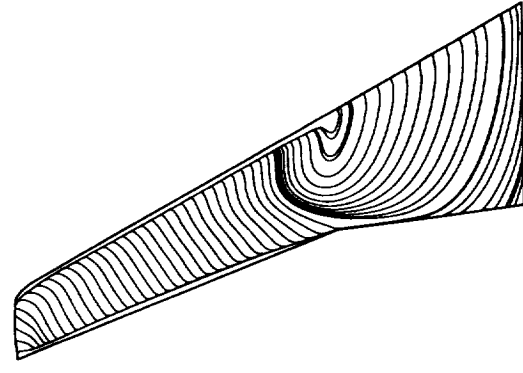


c) semi-span:  $C_q(1) = -.020$ ,  $C_q(2) = -.005$

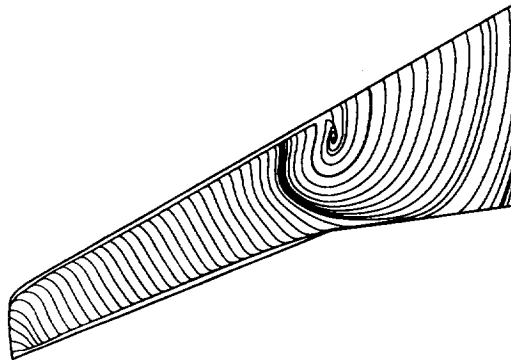
**Figure 125:** Comparison of root plane streamline patterns ( $M_\infty = 0.20$ ,  $\alpha = 18.25^\circ$ ,  $Re = 4.20 \times 10^6$ ).



a) full-span



b) semi-span:  $C_q = 0.000$



c) semi-span:  $C_q(1) = -.020$ ,  $C_q(2) = -.005$

**Figure 126:** Influence of sidewall suction on wing upper surface streamline patterns ( $M_\infty = 0.20$ ,  $\alpha = 18.25^\circ$ ,  $Re = 4.20 \times 10^6$ ).



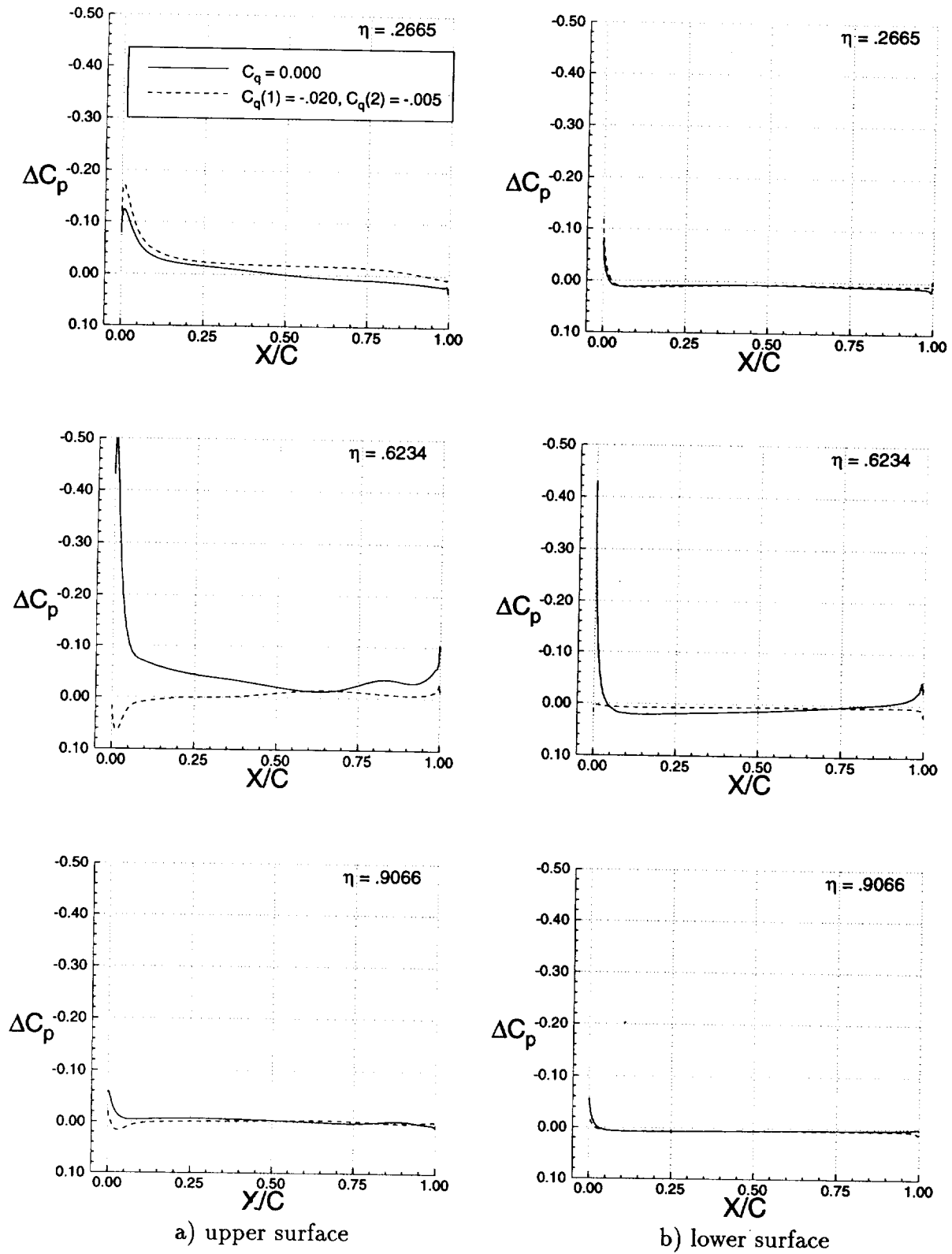


**Figure 127:** Influence of sidewall suction on differential wing pressure distributions ( $M_\infty = 0.20$ ,  $\alpha = 18.25^\circ$ ,  $Re = 4.20 \times 10^6$ ).

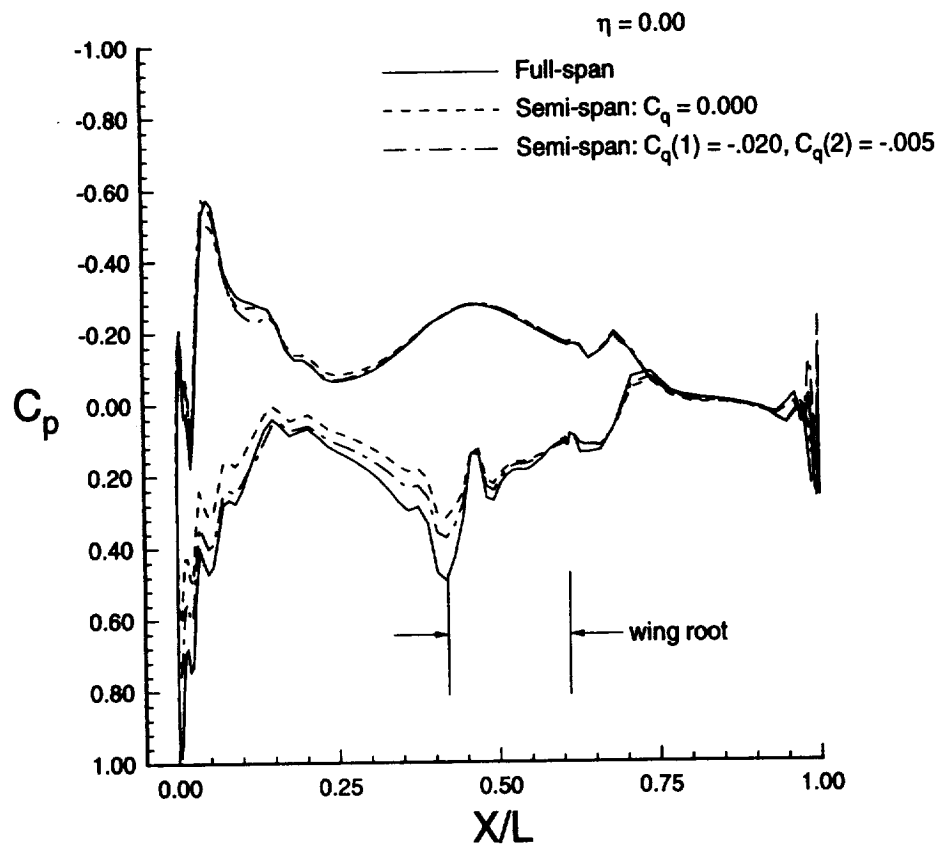
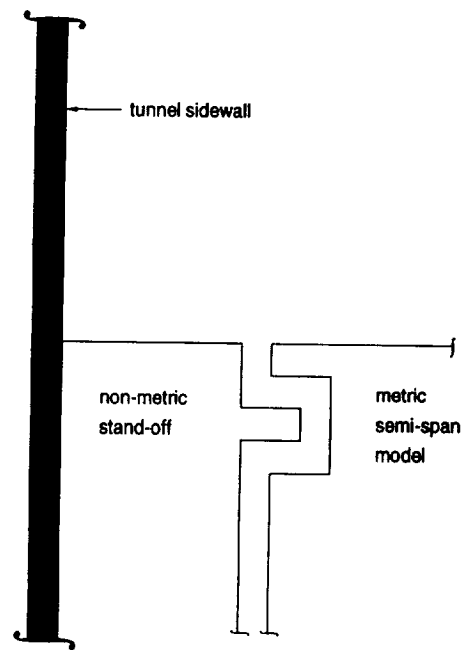
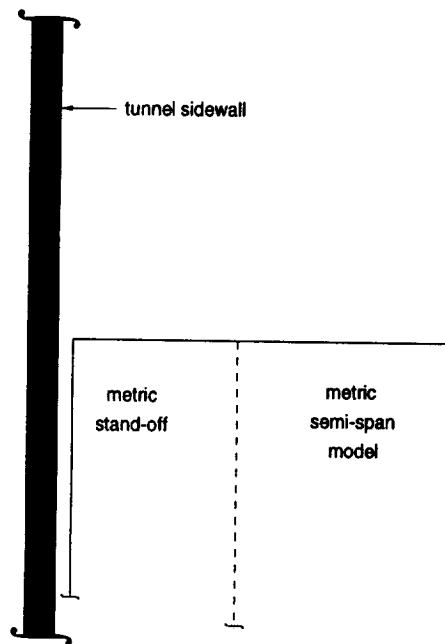


**Figure 128:** Influence of sidewall suction on fuselage centerline pressure distribution ( $M_\infty = 0.20$ ,  $\alpha = 18.25^\circ$ ,  $Re = 4.20 \times 10^6$ ).



a) non-metric stand-off



b) metric stand-off

**Figure 129:** Comparison of semi-span model mounting techniques.

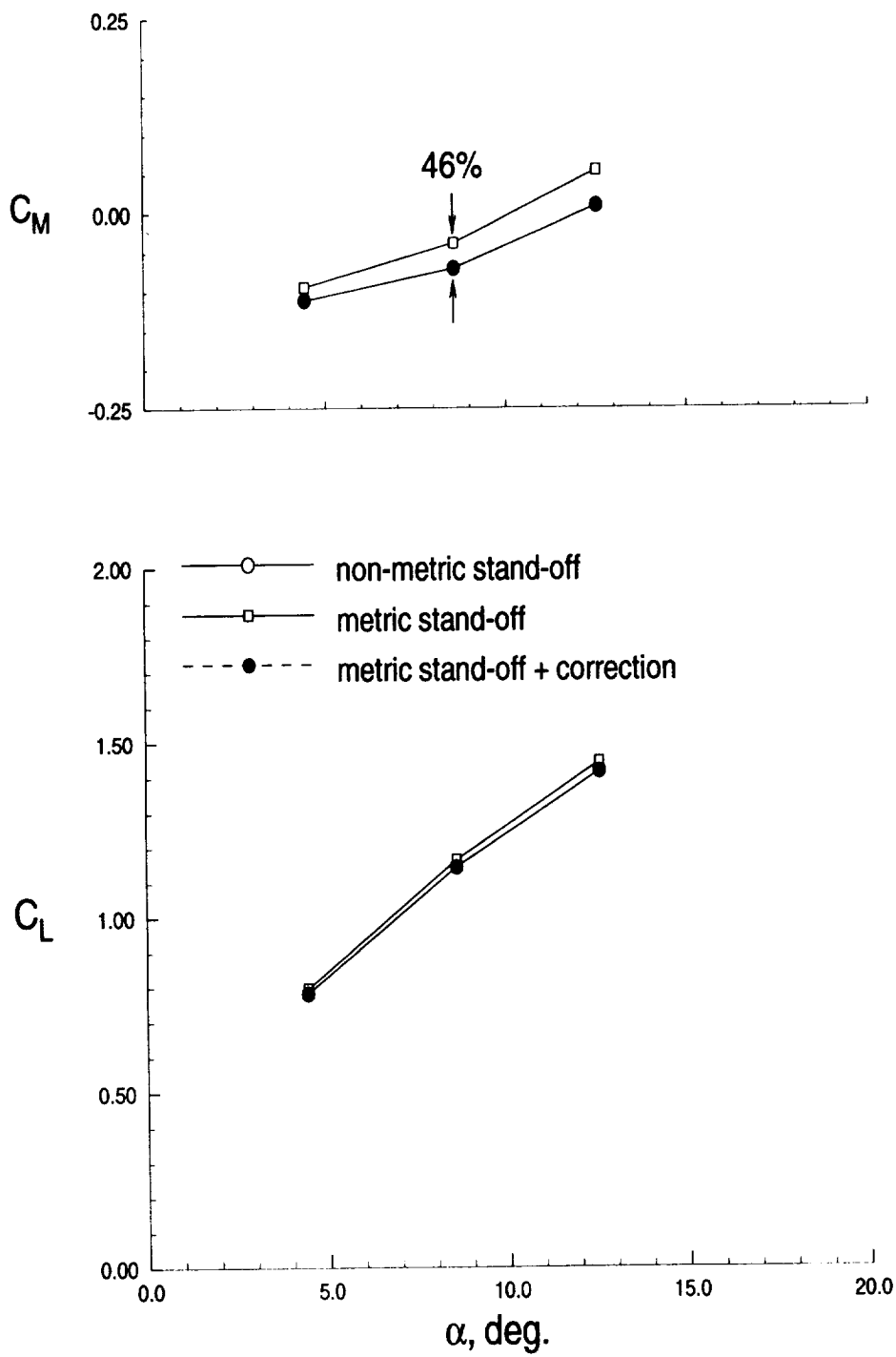


**Figure 130:** Demonstration of metric stand-off correction procedure ( $M_\infty = 0.20$ ,  $Re = 4.20 \times 10^6$ ).

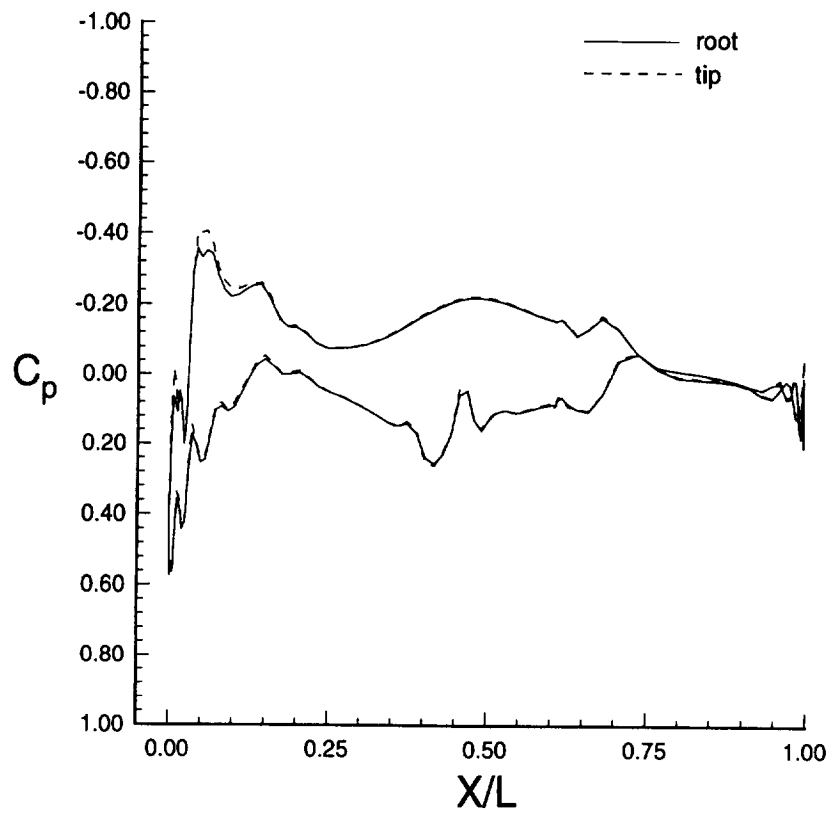


**Figure 131:** Comparison of computed stand-off pressure distributions ( $M_\infty = 0.20$ ,  $\alpha = 12.55^\circ$ ,  $Re = 4.20 \times 10^6$ ).

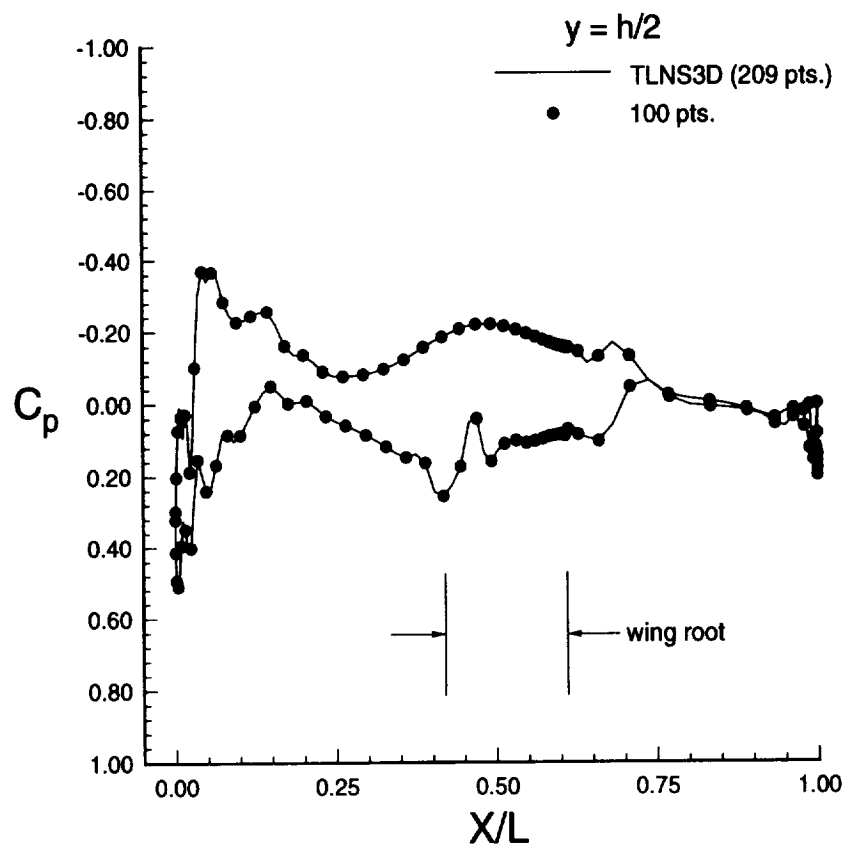
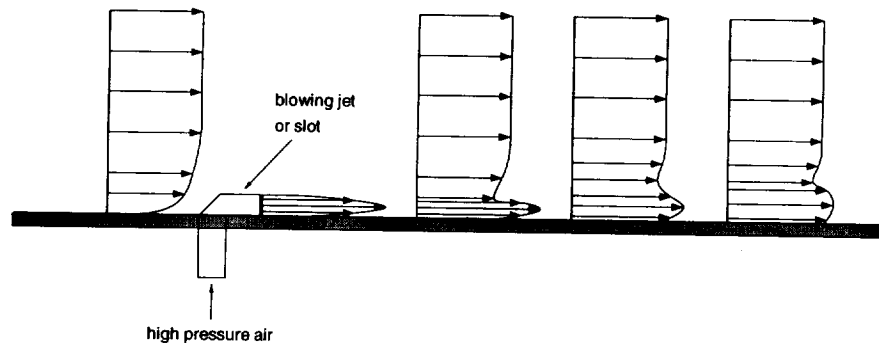
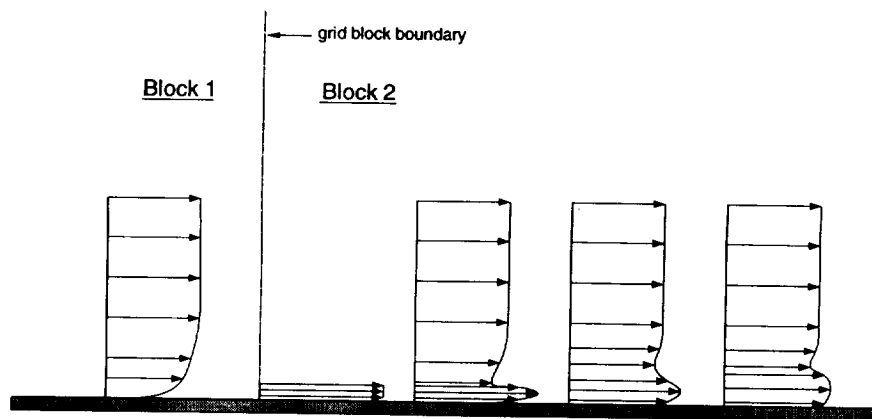


**Figure 132:** Proposed pressure tap distribution on metric stand-off.



a) actual blowing jet



b) simulated blowing jet

**Figure 133:** Comparison of actual and simulated tangential blowing jets.

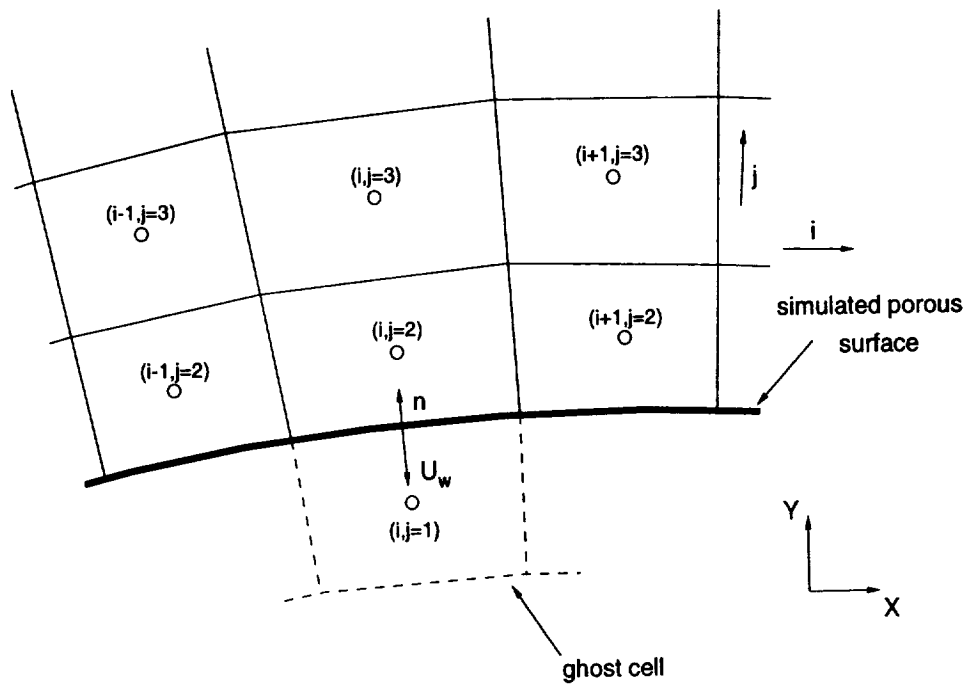


**Figure 134:** Nomenclature for porous surface boundary condition.



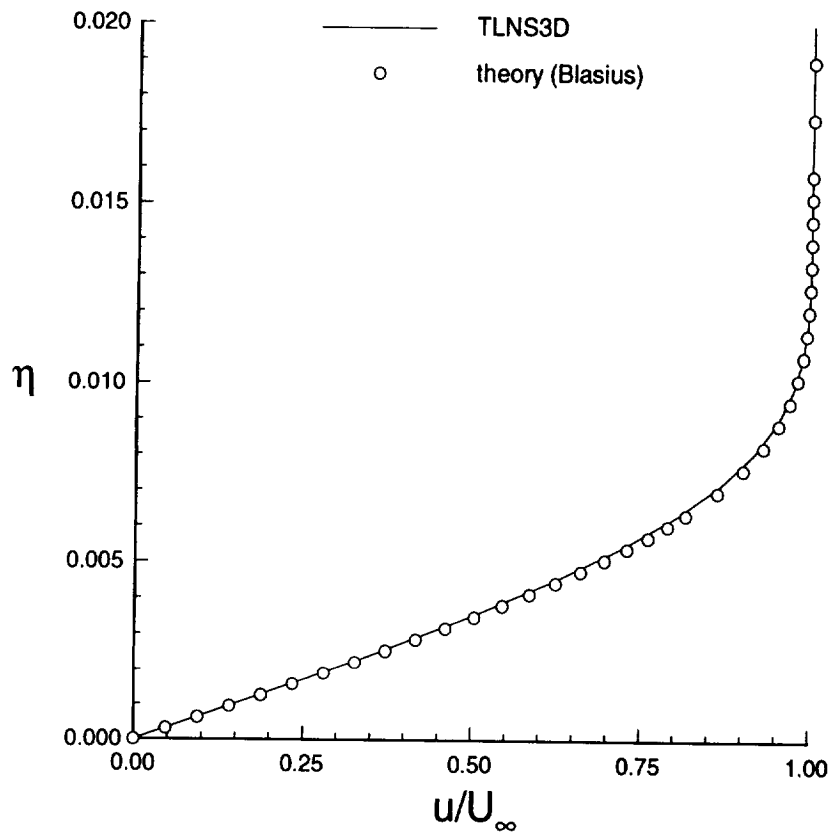


**Figure 135:** Comparison of computed and theoretical laminar flat plate velocity profiles ( $Re_x = 0.50 \times 10^6, C_q = 0.000$ ).

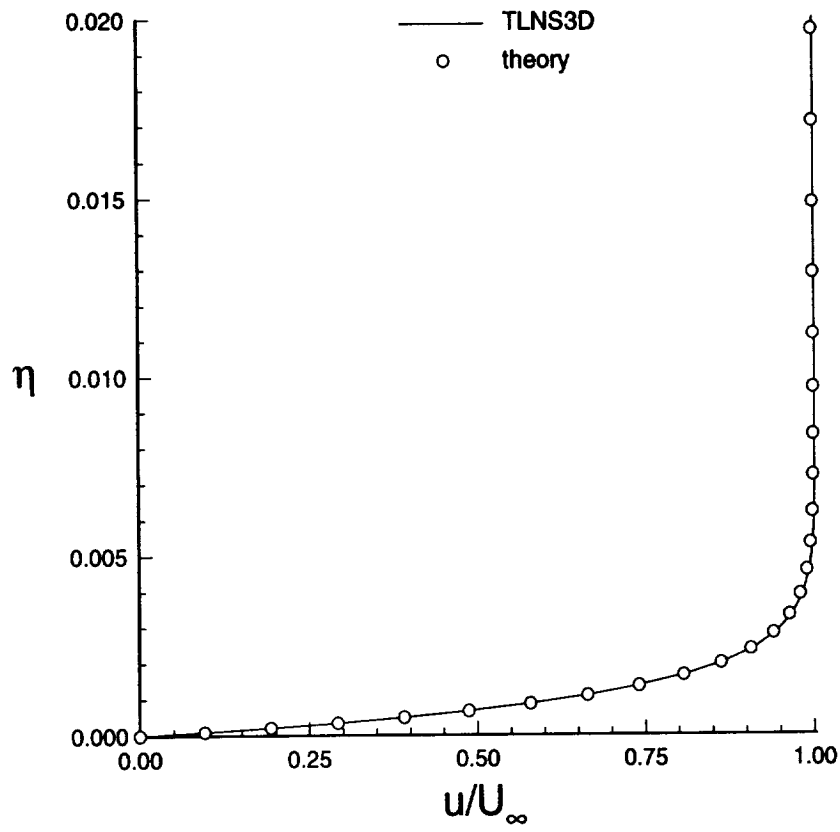


**Figure 136:** Comparison of computed and theoretical laminar flat plate velocity profile ( $Re_x = 0.50 \times 10^6, C_q = -.010$ ).

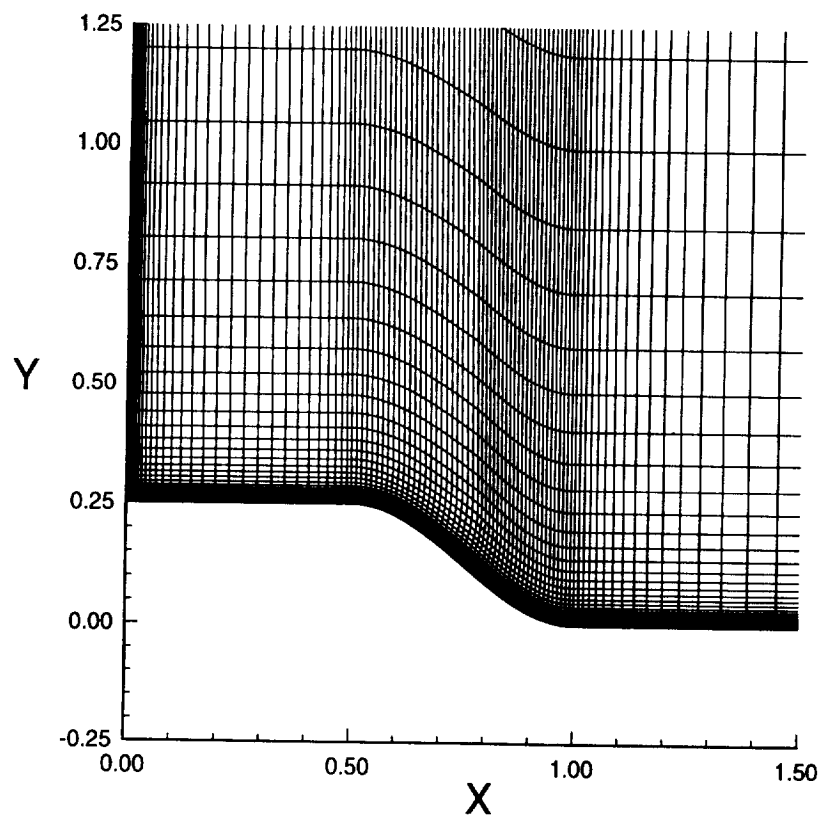
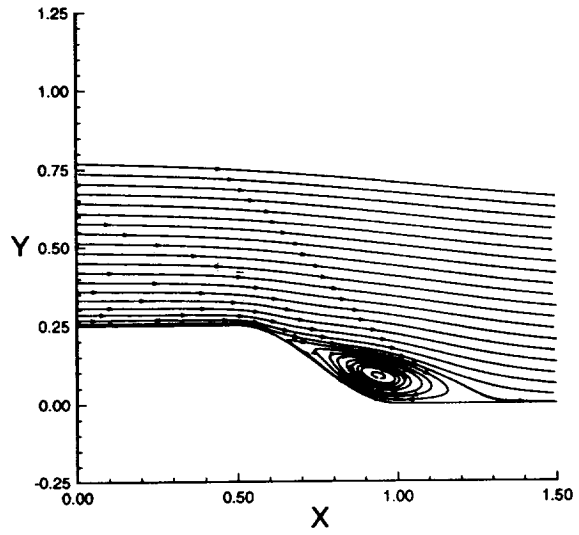
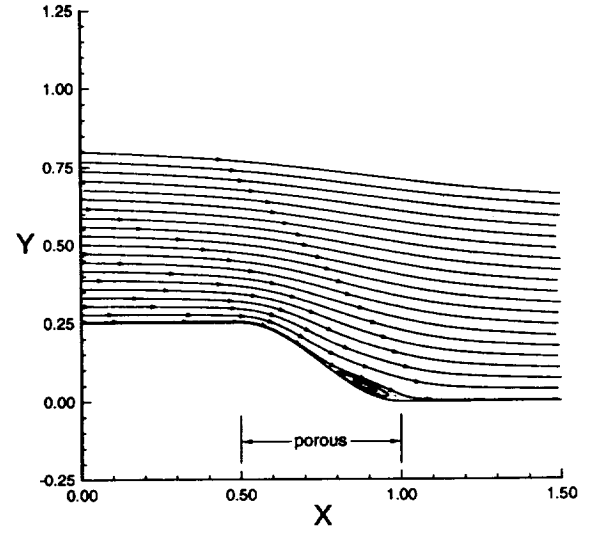


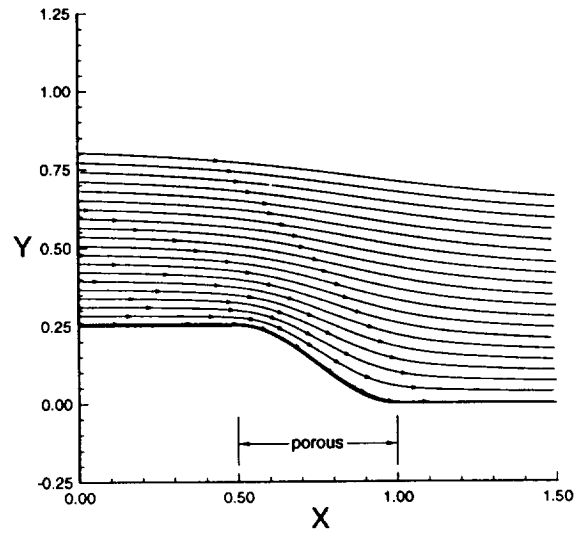
**Figure 137:** Partial view of backward facing sinusoidal ramp grid.



a)  $C_q = 0.000$



b)  $C_q = -.0005$



c)  $C_q = -.010$

**Figure 138:** Influence of suction on backward facing sinusoidal ramp flow ( $M_\infty = 0.20$ ,  $Re/\ell = 2.00 \times 10^6$ ).



REPORT DOCUMENTATION PAGE			Form Approved OMB No. 0704-0188	
Public reporting burden for this collection of information is estimated to average 1 hour per response, including the time for reviewing instructions, searching existing data sources, gathering and maintaining the data needed, and completing and reviewing the collection of information. Send comments regarding this burden estimate or any other aspect of this collection of information, including suggestions for reducing this burden, to Washington Headquarters Services, Directorate for Information Operations and Reports, 1215 Jefferson Davis Highway, Suite 1204, Arlington, VA 22202-4302, and to the Office of Management and Budget, Paperwork Reduction Project (0704-0188), Washington, DC 20503.				
1. AGENCY USE ONLY (Leave blank)		2. REPORT DATE March 1996		3. REPORT TYPE AND DATES COVERED Contractor Report
4. TITLE AND SUBTITLE Computational Analysis of Semi-span Model Test Techniques			5. FUNDING NUMBERS NCC1-169  WU 505-59-85-01	
6. AUTHOR(S) William E. Milholen II; Ndaona Chokani				
7. PERFORMING ORGANIZATION NAME(S) AND ADDRESS(ES) North Carolina State University Department of Mechanical and Aerospace Engineering Raleigh, NC 27695-7910			8. PERFORMING ORGANIZATION REPORT NUMBER	
9. SPONSORING / MONITORING AGENCY NAME(S) AND ADDRESS(ES) National Aeronautics and Space Administration Langley Research Center Hampton, VA 23681-0001			10. SPONSORING / MONITORING AGENCY REPORT NUMBER  NASA CR-4709	
11. SUPPLEMENTARY NOTES The information presented in this report was offered in partial fulfillment of the requirements for the first author's Doctor of Philosophy Degree, NCSU, Raleigh NC, 1995. Langley Technical Monitor: L.E. Putnam				
12a. DISTRIBUTION / AVAILABILITY STATEMENT  Unclassified - Unlimited Subject Category 02			12b. DISTRIBUTION CODE	
13. ABSTRACT (Maximum 200 words)  A computational investigation was conducted to support the development of a semi-span model test capability in the NASA LaRC's National Transonic Facility. This capability is required for the testing of high-lift systems at flight Reynolds numbers. A three-dimensional Navier-Stokes solver was used to compute the low-speed flow over both a full-span configuration and a semi-span configuration. The computational results were found to be in good agreement with the experimental data. The computational results indicate that the stand-off height has a strong influence on the flow over a semi-span model. The semi-span model adequately replicates the aerodynamic characteristics of the full-span configuration when a small stand-off height, approximately twice the tunnel empty sidewall boundary layer displacement thickness, is used. Several active sidewall boundary layer control techniques were examined including: upstream blowing, local jet blowing, and sidewall suction. Both upstream tangential blowing, and sidewall suction were found to minimize the separation of the sidewall boundary layer ahead of the semi-span model. The required mass flow rates are found to be practicable for testing in the NTF. For the configuration examined, the active sidewall boundary layer control techniques were found to be necessary only near the maximum lift conditions.				
14. SUBJECT TERMS semi-span model, Navier-Stokes solutions, stand-off height, metric stand-off, local blowing jets, upstream blowing slot, sidewall suction, National Transonic Facility			15. NUMBER OF PAGES 227	
			16. PRICE CODE A11	
17. SECURITY CLASSIFICATION OF REPORT unclassified	18. SECURITY CLASSIFICATION OF THIS PAGE unclassified	19. SECURITY CLASSIFICATION OF ABSTRACT unclassified	20. LIMITATION OF ABSTRACT	



\_\_\_\_\_